Photovoltaics with Silicon Nanoparticles

Der Fakultät für Ingenieurwissenschaften,
Abteilung Elektrotechnik und Informationstechnik
der Universität Duisburg-Essen

zur Erlangung des akademischen Grades

Doktor der Ingenieurwissenschaften

angenommene Dissertation

von

Martin Meseth
aus
Dieburg

1. Gutachter: Prof. Dr. Roland Schmechel
2. Gutachter: Prof. Dr. Franz-Josef Tegude
Tag der mündlichen Prüfung: 08.12.2014

Darmstadt, 20. Januar 2015

Contents

Chapter 1

Motivation

To satisfy the demand for more and more energy all around the world the extension of traditional energy sources such as coal, oil and gas stands in contrast to the struggle against the climate change, i.e. the reduction of greenhouse gas (GHG) emissions, such as carbon dioxide. Several governments have already passed commitments, to reduce their GHG emission. The European Union, for example, has pledged to reduce the emission of GHGes by 20% below the niveau of 1990 until the year 2020 and by at least 80% until 2050. [Agency2010, EU-Commission2011]

To fulfill these ambitious aims, the amount of wasted energy has to be reduced by increasing the energy efficiency. In parallel to this, a change towards sustainable, renewable primary energy sources, such as hydroelectric, wind and solar power as well as biogas is necessary. (Since the focus of this work is on photovoltaics (PVs), here only challenges regarding PVs are addressed.)

During the year 2010 a global PV capacity of 40GW of PV modules has been installed. [Ardani2011] Among these, PV cells based on silicon (Si) as absorbing material still make the biggest market share of $\approx$ 87%. Si as such, is a reasonable material for PV applications, as it shows a theoretical maximum conversion efficiency of up to 30% which is near the absolute maximum for homojunction solar cells. [Shockley1961] Further, Si is abundant, non toxic and well-investigated and Si PV cell modules show a long term stability (20 to 30 years). The downside of Si PV cells, however, are their comparably high costs. So, in order to make the politically demanded installation of solar cells interesting for investors, too, their costs per watt peak ($/Wp) have to decrease. Thus, today's challenge of PV industry and great topic of Si PV research is to decrease the $/Wp. Since the absorber still makes a significant share for Si PV cells, the idea of this work is a cost reduction due to the absorber.

One of several routes towards this goal are thin film PV cells. Although they exhibit a lower conversion efficiency, these PV cells have the potential to decrease the $/Wp ratio, due to the much lower production costs. While most Si thin film research is based on amorphous Si that has to be deposited in vacuum, the future's aim of this thesis is to use Si nanoparticles (NPs) for the absorbing layer instead. NPs can be dispersed, thus making them printable without the necessity of vacuum. Therefore, cheap and simple techniques can be applied to deposit the NPs to create thin film PV cells.

The primary focus of this thesis is to create PV cells that are made partly from Si NPs, which has to be seen as an intermediate step towards to future's goal. Today, pn-junctions in Si substrates are typically realized by ion implantation or diffusion techniques. Ion implantation is applied to create precise doping profiles but the process has to be performed in vacuum and a thermal treatment is mandatory, making it expensive. [Krause2002, Young1980, Ellmer1992, Meseth2013, Beneking1991, ch. 4.3] For dopant incorporation into the substrate by diffusion a

thermal treatment is performed after dopant-deposition. The doping sources can be gaseous, liquid or solid and for the thermal treatment, different heat sources, such as furnaces, rapid thermal annealing units, wide spectral lamps or lasers are applied. [Sameshima1987, Ogane2009, Bet2006, Fogarassy1981, Fahrenbruch1983, Mandelkorn1973, Edwards2008, Sah1995, p. 385 f.] Another widely used and low cost diffusive doping process in PVs is the screen printing of aluminium (Al) pastes followed by thermal annealing. [Rauer2011] However, due to the different thermal expansion coefficients of Si and Al, wafer bowing is observed if the substrate's thickness is reduced to lower the material costs. [Schneider2001]

The main attempt of this thesis is therefore to replace common dopant sources by highly doped Si NPs. Due to the printability this process leads to potential cost reductions and for the Al diffusion technique, this attempt has to potential to prevent wafer bowing. The technique of using Si NPs for PVs is not absolutely new, as a similar way is already successfully commercialized by DuPont™ Innovalight™. [Scardera2011] However, publications on this process are rare or secret. In this work lasers are used for the thermal diffusion step due to their localized nature of energy deposition.

An investigation of cost efficiency and the industrial applicability of the presented processes is not part of this work. However, potential for reduction in production costs is supposed due to low production costs of the Si NP material. [Huelser2011] Furthermore, by scaling up the setup, lasers have the potential for a fast and cheap commercial production.

The structure of this work is as follows: The theoretical background is given in chapter 2, the used materials are introduced in ch. 3 and the experimental methods are presented in ch. 4. Thereafter the experimental results are discussed: First the main investigations of laser doping of Si substrates on crystalline (ch. 5) and multi crystalline Si (ch. 6) are presented. This is followed by first attempts to create diodes and PV cells made of Si NPs as the absorbing layer solely: In ch. 7 results from spark plasma sintering of Si NPs are discussed and in ch. 8 first investigations of laser annealed Si NP thin films on non-conductive substrates are presented. A summarizing conclusion with an outlook for the future is given at the end (ch. 9).

Chapter 2

Theory

In this chapter the basic theoretical backgrounds which are essential to understand the discussions in the experimental chapters are presented in short. However, it is made no claim to be complete or exhaustive, but instead has to be seen as a compact theoretical introduction. As the aim of this work is the realization of photovoltaic (PV) devices from nanoparticles, chapter 2.1 focuses on the theory of PVs and ch. 2.2 overviews different approaches to realize PV cells from today's standard towards future PV cells. Finally, a short introduction in lasers and the interaction of laser light with mater is presented in ch. 2.3, because sample processing using lasers is a major part of this work.

2.1 Basics on photovoltaics

The PV effect describes the direct conversion of light into electrical power. In fig. 2.1 the fundamental processes for PV action are sketched for a homojunction semiconductor solar cell according to the commonly used energy band model and under the assumption that only one photon is absorbed in the space charge region[1]:

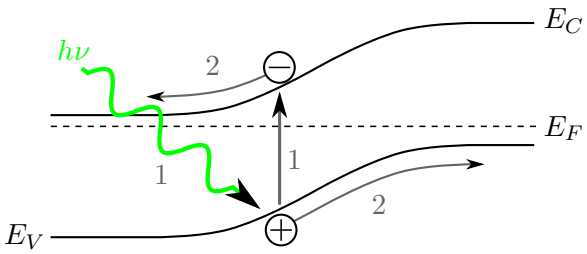

Figure 2.1: Fundamental processes in an illuminated PV cell

1. Photon absorption and charge carrier excitation:
   Light can be absorbed by the material, if the photon energy $E_{h\nu}$ is at least as big as the band gap energy $E_g \leq E_{h\nu}$. The absorbed photon energy immediately excites an electron into the conduction band and leaves a hole in the valence band.

[1] Quasi-Fermi levels are not shown here, as the influence of the two charge carriers on the energy bands is expected to be negligible.

2. Charge carrier drift / diffusion:
   Due to the gradient of the electrical field in the space charge region, the charges drift into the oppositely doped regions: holes to the p-type and electrons to the n-type region. After having left the space charge region, the charge carriers diffuse due to the concentration gradients until they reach the respective metal contacts. Here they can be extracted and can do work in an externally electrical circuit.

Beside these ideal processes, several loss mechanisms, such as radiative and non-radiative recombination or trapping of charge carriers, can occur. This leads to a reduction of the effective carrier lifetime and in consequence to a decreased cell's efficiency. By minimizing defects such as unintentional impurities or lattice imperfections these losses can be reduced.

To characterize PV cells, the most often used method is the voltage dependent current measurement ($I(U)$), because it is fast and can be realized rather simple on the one hand. On the other hand, from these measurements most of the important characteristics can be derived. The $I(U)$ measurements are performed in the dark and under illumination using light of specific characteristics. For terrestrial applications an AM1.5G irradiance (according to IEC 904-3) is used which exhibits a power density of 100mW/cm^2. [Wuerfel2005, p. 23] The lower part of figure 2.2 shows the idealized $I(U)$ characteristics of a PV cell in the dark (black line) and under illumination (red line) and are discussed in the following.

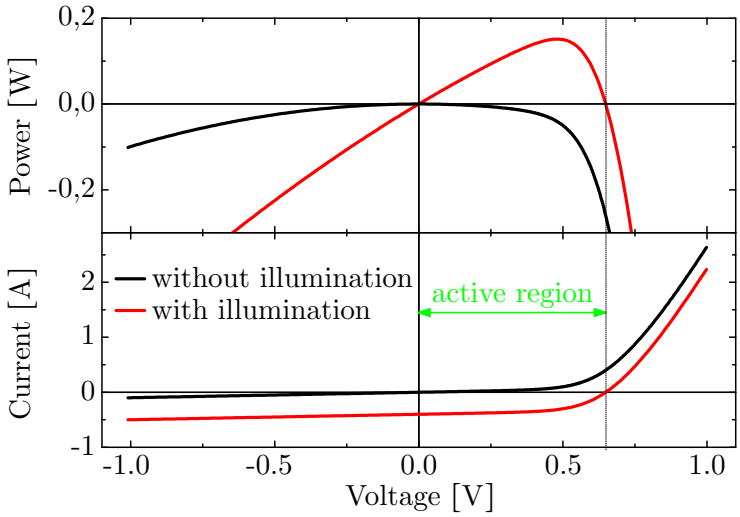

Figure 2.2: $I(U)$ characteristic (bottom) and extractable power ($P = -I \cdot U$, top) of an idealized PV diode in the dark (black lines) and under illumination (red)

2.1.1 Current voltage characterization of pn-diodes in the dark

The $I(U)$ characteristic of a PV cell without illumination is the same as of a diode. Therefore, it can be described by Shockley's diode equation [Shockley1949]:

$$I(U) = I_D = I_0 \left(\exp\left[\frac{e \cdot U}{n \cdot k_B \cdot T} \right] - 1 \right) \tag{2.1}$$

Here I_D, I_0, e, n, k_B and T stand for the diode's current, the diode's saturation current, the elemental charge, the diode's ideality factor, the Boltzmann's constant and the temperature, respectively.

The ideality factor is a measure for the quality of the diode: If charge carrier recombination appears only in the junction region, the ideality factor is $n = 1$; if it appears only in the bulk, it is $n = 2$. [Sze2007] Usually both mechanisms are present in a diode; consequently, the ideality factor varies in between both values. [Sah1957]

Since in a real diode resistances and shunts are present, the $I(U)$ characteristics often differ significantly from the idealized model. It is therefore usually replaced by an equivalent circuit as shown in fig. 2.3a: A resistor R_{ser} is connected in series with a parallel connection of a shunt resistor R_{shu} and an ideal diode. The resulting $I(U)$ characteristic can be written as follows:

$$\begin{aligned} I = I_D + I_{shu} &= I_0 \left(\exp\left[\frac{e \cdot U_D}{n \cdot k_B \cdot T} \right] - 1 \right) + \frac{U_D}{R_{shu}} \\ &= I_0 \left(\exp\left[e \cdot \frac{U - R_{ser} \cdot I}{n \cdot k_B \cdot T} \right] - 1 \right) + \frac{U - R_{ser} \cdot I}{R_{shu}} \end{aligned} \tag{2.2}$$

Here D, ser and shu indicate that the values are linked to the diode, the series resistor and the shunt resistor, respectively. Since PV cells usually are large-area devices, the resistances are often presented in units of Ωcm^2. If area-related resistances are presented in this work, the area used for calculation is the whole interface pn-junction area.

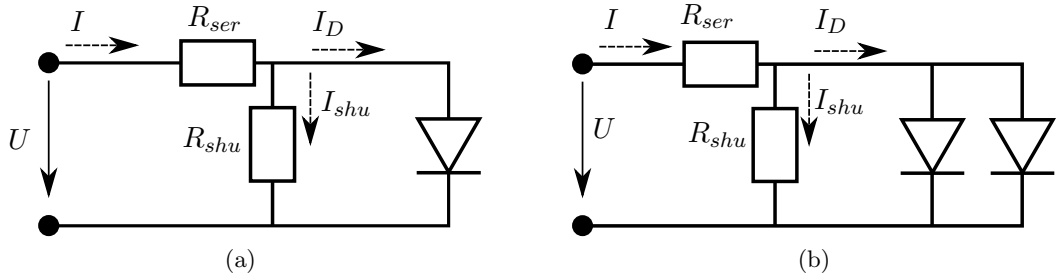

Figure 2.3: Equivalent circuits of the one-diode (left) and the two-diode model

Using this model, still deviations can occur, because the ideality factor can change with the applied voltage. [Sah1957, Steingrube2011] This dependency is considered if a second diode, which differs from the first regarding the ideality factor and the saturation current, is added in parallel (see fig. 2.3b).

2.1.2 Current voltage characterization of pn-diodes under illumination

The $I(U)$ characteristic of an illuminated PV diode is similar to the one in the dark, only reduced by an almost constant current, the short circuit current I_{sc}. It builds up due to the conversion of photons into free charge carriers (and the shunting of the device). For standard solar cells and typical illumination densities up to a few suns it is proportional to the light power.

Due to the conversion of photons, an electromotive force (EMF) can be used to provide electrical power P to an external circuit. As can be obtained from the upper part of fig. 2.2, a power is only provided in between $U = 0\text{V}$ and the open circuit voltage U_{oc} (the active area - marked with the green double arrow). Using the maximum power P_{mpp} the fill factor FF can be calculated [Wuerfel2005, p. 124]:

$$FF = \frac{P_{mpp}}{I_{sc} \cdot U_{oc}} = \frac{I_{mpp} \cdot U_{mpp}}{I_{sc} \cdot U_{oc}} < 1 \tag{2.3}$$

It is one measure of the device's quality. Due to the exponential nature of the diode current, FF is always smaller than unity; for Si PV cells Granek announced a theoretical maximum of $FF < 85\%$. [Granek2009]

The power conversion efficiency η is the ratio of the maximum extracted power to the incident, optical power P_{opt}:

$$\eta = \frac{P_{mpp}}{P_{opt}} \tag{2.4}$$

According to the detailed balance limit described by Shockley and Queisser the maximum efficiency for a Si solar cell is limited to $\approx 30\%$. [Shockley1961] Nowadays record efficiencies for homojunction c-Si solar cells of $(25.0 \pm 0.5)\%$ have been obtained, showing the small gap to the theoretical maximum. [Green2014]

Due to the EMF the equivalent circuits of fig. 2.3 have to be extended by a current source in parallel to the diode(s), as shown in fig. 2.4 for the one-diode model. Consequently, also eq. (2.2) has to be adapted by subtracting a current due to the photovoltaic effect I_{phot}:

$$I = I_D + I_{shu} - I_{phot} = I_0 \left(\exp\left[\frac{U - R_{ser} \cdot I}{n \cdot k_B \cdot T} \right] - 1 \right) + \frac{U - R_{ser} \cdot I}{R_{shu}} - I_{phot} \tag{2.5}$$

Since in a typical PV cell, the ratios R_{ser}/R_{shu} and I_0/I_{phot} are very small, it can be approximated that $I_{phot} \approx I_{sc}$. Therefore usually only I_{sc} is used for corresponding calculations.

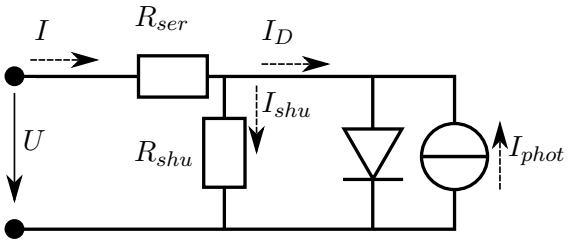

Figure 2.4: One diode equivalent circuit of an illuminated PV cell

2.2 Photovoltaic designs: from thick layers to nanoparticles

Since Becquerel's observation of the photovoltaic (PV) effect, lots of research resulted in a multitude of products. [Becquerel1839] Nowadays the absorbing layer of most of the sold PV products are homojunctions (see fig. 2.1 for the band scheme) made of crystalline or multicrystalline silicon (c-Si or mc-Si). A sketch of a simple PV cell is shown in fig. 2.5:

1. A grid-structured metal contact is established at the front of the cell such that most of the incoming light enters the layers below.

2. Below the front contact, a semiconductor pn-junction is established in parallel to the surface; the polarity depends on the cell design.

3. A large-area contact is coated at the back of the cell.

Although in the past decades the prices for PV modules reduced significantly, the costs to generate electrical power by PVs is still higher than by conventional fossil energy sources. [EnergyAndClimateDep2012, USEnergyAdmin2013, Swanson2006] Consequently, research and development still seeks for cheaper technologies. In the following a short overview of nowadays approaches to replace c-Si or mc-Si as absorbing layers are presented. Comparisons in the text refer to Si technologies if not stated otherwise.

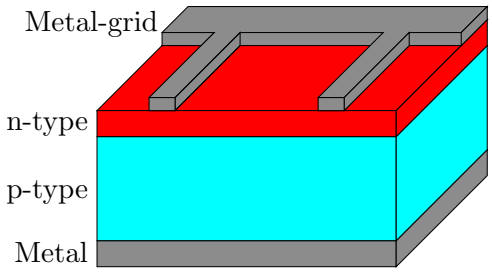

Figure 2.5: Simple PV cell

2.2.1 Organic materials for photovoltaics

Organic semiconductors are one potential material class to create cheap PV cells. Due to high absorption coefficients only very thin films ($\lesssim 1\mu m$) are needed and the materials can be deposited by simple coating techniques or by ink-jet or role-to-role printing. Consequently, production and material costs are comparably small and the final product can be light weighting. As these cells can also be prepared on flexible substrates, they have the potential to open up new markets and applications.

The absorbing layer of an organic PV cell is usually formed by a bulk heterojunction of two different materials. In the past decade many research activities focused on P3HT (poly(3-hexylthiophene)) and PCBM ([6,6]-phenyl-C_{61}-butyric acid methyl ester). [Koster2008, Kroon2008] However, conversion efficiencies of only $\sim 5.3\%$ are reached for this material combination. [Cheng2013] In 2012 Mitsubishi Chemicals designed an organic record cell with a power conversion efficiency of up to 11%. Unfortunately, the press statement, does not give any clues, what kind of material is used for it. [Green2014, Nozawa2012]

The current, major disadvantage of this type of PV cell is the poor long-term stability. [McConnell2004] The materials either oxidize when in contact with air or they degenerate because of photolytic and / or photochemical reactions. [Sagadevan2013, Joergensen2012]

2.2.2 Direct band gap materials for photovoltaics

Due to conservation of momentum, in an indirect band gap semiconductor (e.g. Si, Ge, GaP, AlAs) an additional phonon is required to absorb a photon, that exhibits an energy of the band gap's energy or little above it. For direct band gap semiconductors, in contrast, a phonon is not needed. Consequently, the light absorption coefficient α of a direct semiconductor is a much steeper function for energies close to the band gap energy. [Sze2007, p. 665] Additionally, some direct semiconductors exhibit absorption coefficients that are up to one order of magnitude higher than Si. So, in order to create a PV cell from these semiconductors with a comparable efficiency as Si cells, the absorbing layer can be much thinner. Besides the positive cost effects, the thinner layer has also the advantage of reduced charge carrier recombination in the cell.

Therefore, direct-bandgap semiconductors, such as III-V (e.g. GaAs), II-VI (e.g. CdTe) or quaternary compound semiconductors (e.g. CIGS) currently are under investigation as absorbing layer. In the following, these are discussed in short.

III-V semiconductors

Among the III-V semiconductors, gallium arsenide (GaAs) and their combination with elements such as P, Al, In, Sb are well studied. The major driving force for these investigations is the possibility to tune the energy band gap by changing the material composition. [Sze2007, p. 57] The doping of GaAs is different to the doping of Si, because dopants can replace both elements in their sublattices. Group IV elements, for example, can be donors or acceptors, depending on whether Ga or As is replaced. Nevertheless, mainly due to the solubility of certain atoms in the sublattices doping is feasible. [Bozel2006, p. 503] Consequently, it is also possible to create pn-junctions and PV cells.

Since the band-gap of GaAs is very well matched to the solar spectrum, maximum efficiencies of up to 30% are possible. [Sze2007, p. 724] In 2011, Kayes et al. published a record cell with an efficiency of 27.6% made of GaAs. [Kayes2011] To date, this material is still the material of the record cell for homojunction solar cells ($28.8\% \pm 0.9\%$). [Green2014, NREL2013] However, high costs and the toxicity of the material prevent GaAs solar cells to enter the market for terrestrial applications. In contrast, if less weight is more important than low costs, GaAs PV cells are a reasonable choice of material, e.g. for space applications such as the MidSTAR-1 satellite, that is launched on March 9, 2007.

II-VI semiconductors

This class of material is dominated by cadmium telluride (CdTe) if it comes on PVs. According to Isshiki and Wang, CdTe is the only II-VI compound semiconductor, in which p- and n-type doping can be controlled easily by donor or acceptor impurities. [Isshiki2006, p. 831] Nevertheless, the most important[2] approach for CdTe PV makes use only of a p-doped CdTe layer in combination with an n-type CdS layer. [Strevel2013, Dharmadasa2002] CdTe has a band gap that is close to the optimum for terrestrial PVs, in consequence conversion efficiencies of almost 30% are theoretically possible. [Sze2007, p. 724] According to Gloeckler et al., record efficiencies of up to 19% ($19.6\% \pm 0.4\%$) are already realized. [Gloeckler2013, Green2014]

Although both elements are quite rare in the earth's crust and therefore comparably expensive, CdTe PV cells have entered the market in the past few years. [Mortimer1976] This development is driven especially by the manufacturer FirstSolar and it is possible because only a little amount of the material is needed. [FirstSolar2012, Kosyachenko2010] An investigation about the emissions created during the life cycle of PV cells made of different absorber materials shows, that CdTe-technology is favorable when compared with Si. However, it has to be mentioned, that the difference between PV technologies is small, when compared with conventional, fossil energy technologies. [Fthenakis2008] Nevertheless, the intrinsic toxicity of CdTe material is still a crucial point for these materials and complete recycling needs to be guaranteed.

CIGS

In the past 20 years copper indium gallium (di)selenide (CIGS) has become famous in the field of thin film PVs. Its chemical formula is $CuIn_xGa_{1-x}Se_2$ and by varying x from 1 to 0 the band gap can be tuned from 1.0eV to 1.7eV. The major reason, why this material has such a great impact on PVs is found in its exceptionally high absorption coefficient of $10^5 cm^{-1}$ for wavelengths $\lambda < 800nm$. [Stanbery2002]

[2] The biggest thin film Solar cell manufacturer *FirstSolar* published this approach, making it the most important at the moment.

The fundamental device design of a CIGS cell is as follows [Hedstroem1993, Chirila2011]:

Soda lime glass | Mo (~ 800nm) | CIGS (3000nm) | CdS (~ 20nm) | ZnO (~ 300nm)

The glass stabilizes the thin and fragile film. The large area coated, back contact is made of molybdenum, because it forms an interface layer of $MoSe_2$ during growth, creating a quasi-ohmic contact. The space charge region builds up in between the p-type absorber CIGS and the n-type CdS. For the front contact ZnO is used, because it is transparent and conducting.

Although rare elements are needed for this material combination, several products have successfully entered the market. For example, the Manz AG offers inflexible modules with conversion efficiencies of 14.6% and Global Solar sells a flexible product with a power conversion efficiency of 12.6%. [ManzAG2012, GlobalSolar2012] The actual record conversion efficiency for CIGS cells is $(19.8 \pm 0.6)\%$, which on the one hand is only two thirds of the maximum. But on the other hand it has to be considered, that the research on CIGS is comparably young. [Green2014] Thus, further improvements can be expected in the near future.

2.2.3 Nano structures for photovoltaics

By nano structuring the surfaces of a PV cell, its efficiency can be increased significantly. Lots of research has focused on the creation of anti reflection layers on the front side of a PV cell. Nowadays, the standard approach is to create an anti reflection layer by coating, e.g. sputter deposition of SiN. The layer's thickness and refractive index are chosen such that reflection losses of the important light spectrum are minimized.

Besides this bottom-up method, top-down methods are investigated, too. Already in the 1970^{th} researchers have realized, that optical reflections can be reduced down to 1%, if the surface is textured. [Stephens1977, Nguyen2013] Approaches to texture the surface are anisotropic etching of Si using alkaline solutions (c.f. ch. 4.2.1), local metal-catalyzed wet chemical etching, sputtering and reactive ion etching. [Seidel1990, Koynov2006, Koynov2007, Gittleman1979, Ruby2001] Especially the sputtering and the ion etching have become famous recently and fancy names like "nano grass" or "black silicon" are created for the resulting material. [Shieh2011, Nguyen2013] The newly arose interest is a result from improvements in sputter techniques from display production, which have the potential to apply this technique in an economic way.

2.2.4 Nanoparticles for photovoltaics

By adjusting the size of semiconducting NPs, the bandgap can be tuned for optimal spectral light absorption due to quantum confinement (QC). [Dingle1974, Ekimov1985, Ochoa1996, Arizpe-Chavez2000] Additionally, the absorption is enhanced because the QC effect increases the oscillation strengths. [ERKC2009]

Since NP-films can be created by simple coating techniques, handling costs are comparably small. Among the NPs, the cadmium chalcogenides (CdS, CdSe and CdTe) are maybe the best-studied materials. [Hodes1987, Wang2011a] However, devices with absorbers made of NPs solely have not exceeded conversion efficiencies of 5% so far. [Gur2005]

Otherwise, different concepts are under investigation that make use of NPs. In the following, hybrid photovoltaics, the dye sensitized solar cells ("Grätzel cells") and certain other concepts are presented in short.

Hybrid photovoltaics

In comparison to inorganic semiconductors, organic semiconductors show comparably low mobilities. As the mobility is a crucial factor to realize efficient organic PV cells, idea has come up, to combine both materials; i.e. to create hybrid PV cells. [Boucle2007] Semiconducting NPs made of CdTe or TiO_2 have shown great enhancement of the power conversion efficiency and are of great interest, as the absorbed spectrum can be changed by changing the particle size due to QC. [Greenham1996, Helgesen2010, Shukla2011] Nevertheless, scientist still reach for a breakthrough regarding high efficiencies.

Dye sensitized solar cells

In the early 1990^{th}, the research group of M. Grätzel has invented this new type of solar cell [ORegan1991]: A 10µm thick layer of 15nm diameter TiO_2 NPs are coated and shortly sintered on a conductive glass that is coated with a transparent conductive oxide (TCO). The NPs are covered with a monolayer of a dye ($RuL_2(\mu\text{-}(CN)Ru(CN)\tilde{L}_2)_2$, where L and $\tilde{L}$ stand for 2,2'bipyridine-4,4'-dicarboxylic acid and for 2,2'bipyridine, respectively) and the space between these layers and the counter electrode (Pt or TCO coated glass) is filled with a redox electrolyte (iodine/triiodine).

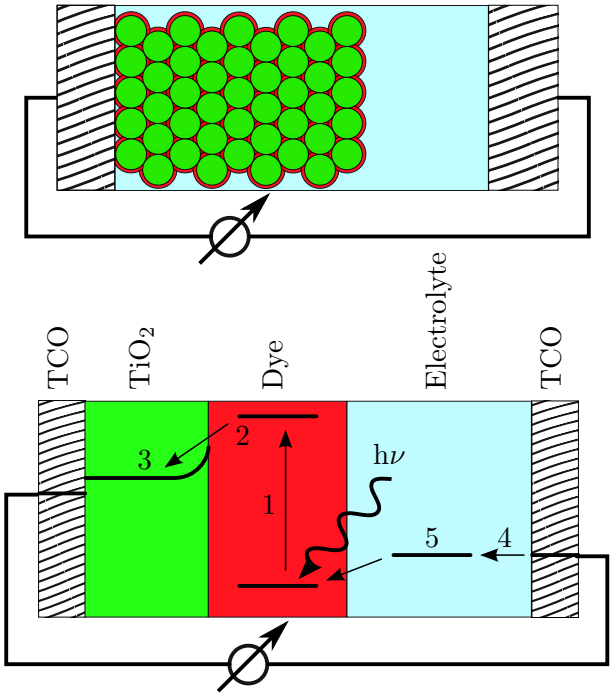

Figure 2.6: After ref. [ORegan1991]: Scheme of dye sensitized PV cell (top) and energy band scheme (bottom) including photon absorption (1) and electron current (2-5)

TiO_2 has a band gap between 3.02eV and 3.23eV (phase dependent). [Graetzel1985] Consequently, only photons of $\lesssim 400$nm can be absorbed by TiO_2. In contrast, the dye's absorption spectrum increases almost linearly from $\approx 0\%$ at ≈ 700nm to its maximum at ≈ 550nm. [ORegan1991] By absorbing a photon in the dye monolayer, an electron gets excited and transfers from the dye to a TiO_2 NP and the back electrode. Via an external current it reaches the

counter electrode and (via the electrolyte) the dye[3] (see fig. 2.6).

The great advantage of this type of solar cell are the low costs as well as the simple design which can be flexible, too. While the first publication gave a conversion efficiency of 7.12%, nowadays maximum conversion efficiencies of 11.9% have been measured. [Kawai2013, Green2014]

Other concepts

Metallic NPs are also used to improve cell efficiency of organic PV cells. [Atwater2010] On the one hand, particles with a big diameter (> 50nm) are used as scattering centers for the light in order to increase the mean optical path through the absorber and thus the device efficiency. On the other hand, smaller particles (5nm to 20nm) are identified as light absorbers creating plasmon resonance. [Sha2011] Due to the plasmonic nearfield, the organic layer's effective absorption cross-section and thus the exciton dissociation are increased. [Stratakis2013]

Furthermore, NPs are currently under investigation to effectively increase the permittivity of the organic semiconductor. The binding force of the exciton's charge carrier pair can be described by the Coulomb's force:

$$\vec{F}_C = \frac{q_e \cdot q_h}{4\pi \cdot \epsilon_0 \cdot \epsilon_r \cdot r^2} \cdot \frac{\vec{r}}{|\vec{r}|} \tag{2.6}$$

with q_e and q_h being the charge of the electron and the hole, ϵ_0 and ϵ_r being the permittivity of the vacuum and the relative permittivity and $\vec{r}$ being the distance between both charges, respectively. Consequently, a small permittivity results in a great binding force (for organic materials ϵ_r usually is in the range of 3 to 4). The proven idea is to incorporate nanoparticulate materials with high permittivities, such as $SrTiO_3$ with $\epsilon_r \sim 300$, to effectively reduce $\vec{F}_C$. [Engel2012, Engel2013, Hikita2010, p. 180]

2.2.5 Use of nanoparticles for this work

Although QC is also observed for Si, it is not of primary importance for this work. [Cullis1991, Proot1992, Buuren1993] Instead, the main reason to use Si NPs is the possibility to form homogeneous, thin films by spin coating of NP dispersions. These films are subsequently laser annealed in order to improve its electrical properties.

According to several theoretical and experimental investigations the melting point of small particles decreases with the particle's diameter. [Wautelet1990, Wautelet1991, Buffat1976, Goldstein1996, Couchman1977, Schierning2008] Thus, a reduction of the melting temperature for a decreased diameter as for NPs is expected. This can be beneficial, as less energy is needed to liquefy the NP thin film.

As mentioned earlier, the long-term objective of this work is to create cheap, printable, thin-film PV cells with the absorber made solely from NPs, e.g. by subsequently spin or spray coating and laser annealing of p-type and n-type NP layers. Most reports on electronic applications using Si NPs deal with thermoelectricity or hybrid PV. [Meseth2012a, Petermann2011, Pereira2007, Niesar2009, Dietmueller2009] Only little research is published about the preparation of conductive films made by Si NPs. [Watanabe2012] Thus, the aim of this thesis is to investigate the potential of Si nanoparticles for PV applications.

[3] This is a simplification; the electron leaving the front contact usually differs from the excited one.

2.3 Laser interactions with materials

In this section the fundamental principles and processes in a laser and the interaction of laser light with a material are described. Especially the chapter 2.3.2 mainly summarizes the first few chapters of the book "Laser-Beam Interactions with Materials: Physical Principles and Applications" by M. v. Allmen and A. Blätter. [Allmen1995] However, it primarily focuses on aspects which are relevant for this work.

2.3.1 Fundamental working principle of a laser

To create laser light, a population inversion of charge carriers has to be created in a so called active medium. In a two-level system electrons are excited from a lower energy level E_1 into a higher energy level E_2. The inversion is established, if more electrons are in E_2 than in E_1. One of the excited electrons will release its excitation energy by spontaneously emitting a photon of energy $E_{h\nu} = E_2 - E_1$ while relaxing to E_1. Due to stimulated emission of photons from the residual, excited electrons in the active medium the number of coherent photons multiplies. A resonator, consisting of two mirrors reflects the photons to increase the mean residence time in the active medium and thus their amplification.

In reality, two energy level lasers cannot exist, because a stationary population inversion cannot be realized (the probability of stimulated emission and absorption would become equal, consequently in best case population would be equal, too). Instead three or four (or even more) energy level lasers are used, where electrons are pumped from the absolute energy minimum E_0 to the absolute maximum E_3 (1 in fig. 2.7). By a very fast transition, the electrons relax into the upper laser energy level E_2 (2) where the mean lifetime usually is much higher than in E_3. From here, these electrons relax into the lower energy state E_1 by emitting a photon ($h\nu$, 3). This level exhibits again a very short lifetime, so that the electron finally relaxes back into E_0 (4).

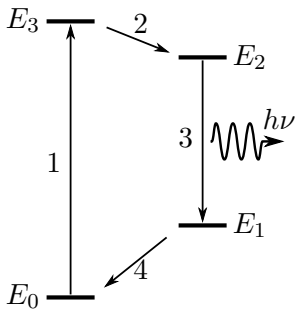

Figure 2.7: Energy scheme of a four level laser

Lasers are available in a wide spectral range, from x-ray wavelengths of free electron lasers in between 1.2Å (LINAC) and 47nm (FLASH) to the UV, the visible and the IR range. [Emma2010, Tiedtke2009, Matsumoto1990, Deutsch1981, Sameshima2005, Andrae1999, Dassow2000, Fogarassy1981, Hoeger2012, Ukawa2010, Tucci2008] Besides the wavelength, the pulse duration of a laser can vary from femtosecond pulses to continuous wave (cw) radiation and the power can vary by orders of magnitude. [Smith2011, Ehrlich1980]

2.3.2 Interaction of low power laser light with material

This subsection discusses interactions of laser light and mater for radiations that are weak enough not to perturb the states of electrons and atoms significantly. [Allmen1995] Fundamentally, laser radiation consists of electro magnetic (E-M) radiation. [Foerster2013, ch. 2] The electric part of this radiation is usually described by an oscillating electric field $\vec{E}$. For linearly polarized, monochromatic light of wavelength λ, propagating along x, the resulting equation is:

$$\vec{E} = \vec{E}_0 \cdot \exp\left[\imath \cdot \left(\frac{2\pi \cdot x}{\lambda} - \omega \cdot t\right)\right] \tag{2.7}$$

Here $\vec{E}_0$ and ω are the vectorial amplitude and the angular frequency of the electric field, $\imath$ is the imaginary unit and t is the time. The magnetic part of the radiation $\vec{H}$ is described analogous, however, $\vec{H}$ is always oriented perpendicular to $\vec{E}$. The amplitude of $\vec{H}$ can be related to E_0 by:

$$H_0 = n_{\Re} \cdot \epsilon_0 \cdot c_0 \cdot E_0 \tag{2.8}$$

Here $n_{\Re}$, ϵ_0 and c_0 are the refraction index[4] of the medium, the dielectric constant of the vacuum and the speed of light in vacuum, respectively.

With this, the energy flux per area A of the E-M wave ("irradiance" Irr) can be calculated by:

$$Irr = \left|\vec{E} \times \vec{H}\right| = n_{\Re} \cdot \epsilon_0 \cdot c_0 \cdot E_0^2 \tag{2.9}$$

Consequently, the total power of a laser beam is described by $P = Irr \cdot A$. The specification of Irr is useful only for a radiation that is constant in time. Else, e.g. for pulsed lasers, the integrated energy E or energy density $ED = E/A$ of a single pulse is given usually:

$$ED = \int_{t_0}^{t_e} Irr(t)\mathrm{d}t \tag{2.10}$$

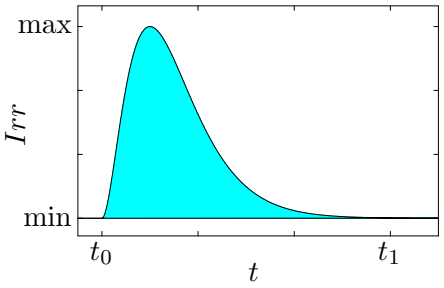

Figure 2.8: Schematic irradiance of a single laser pulse

Here t_0 and t_1 are the time of the pulse's beginning and end, respectively, as schematically displayed in fig. 2.8.

Fundamentals on absorption and reflection

If an E-M wave attains a material surface, it induces an oscillation of the material's electrons, creating a macroscopic polarization of the material. (For visible light the radiation only interacts with the valence electrons, because the nuclei of the atoms cannot follow the high frequencies and the energy is too small for electrons of inner electron shells. [Allmen1995, ch. 2]) The complex dielectric function, can be regarded as a "generalized response function of the material". [Allmen1995, p. 8] It results from the Maxwell equations:

$$\tilde{\epsilon} = \epsilon_r + \frac{\imath \cdot \sigma}{\epsilon_0 \cdot \omega} \tag{2.11}$$

Here ϵ_r, σ and ω are the dielectric constant (for the case of an isotropic and nonmagnetic material), the materials conductivity and the frequency of the light. For an idealized material with N_e bound electrons showing only one single resonance at a frequency ω_0, $\tilde{\epsilon}$ can be described by [Allmen1995, p. 9]:

$$\tilde{\epsilon} = 1 + \frac{N_e \cdot e^2}{m_e \cdot \epsilon_0} f_{osc} \frac{\omega^2 - {\omega_0}^2 + \imath \cdot \Gamma \cdot \omega}{(\omega^2 - {\omega_0}^2)} \tag{2.12}$$

Here f_{osc}, m_e and Γ are the oscillator strength, the electron mass and the damping constant. While f_{osc} is a measure for the probability of the transition, Γ stands for the width of the resonance. In a real material, there does not exist only one resonance; instead, eq. (2.12) has to be replaced by a sum over all possible resonances.

[4] A loss-free material is assumed; thus only the real part of the complex refractive index is considered.

However, the material can either transmit, reflect or absorb the wave. If the light is transmitted, the irradiance is not influenced by the material, therefore it is not considered here. The influences of the other two possibilities depend on the complex refractive index:

$$\tilde{n} = n_{\Re} + \imath \cdot n_{\Im} \tag{2.13}$$

where $n_{\Re}$ is the real part and $n_{\Im}$ the imaginary part of the refractive index, which is related to $\tilde{\epsilon}$ by $\tilde{n}^2 = \tilde{\epsilon}$. [Allmen1995, p. 7]

Reflection The ratio r of reflected to incident irradiance can be calculated from the Fresnel equations. At a surface between two materials with refractive indices $\tilde{n}_1$ and $\tilde{n}_2$ it holds:

$$r = \left(\frac{\tilde{n}_1 - \tilde{n}_2}{\tilde{n}_1 + \tilde{n}_2}\right) \cdot \left(\frac{\tilde{n}_1 - \tilde{n}_2}{\tilde{n}_1 + \tilde{n}_2}\right)^* \tag{2.14}$$

(The sign * symbolizes the complex conjugation.) For the case of a material in vacuum ($\tilde{n}_2 = 1$) this reduces to:

$$r = \left(\frac{\tilde{n}_1 - 1}{\tilde{n}_1 + 1}\right) \cdot \left(\frac{\tilde{n_1}^* - 1}{\tilde{n_1}^* + 1}\right) = \frac{\left(n_{1,\Re} - 1\right)^2 + {n_{1,\Im}}^2}{\left(n_{1,\Re} + 1\right)^2 + {n_{1,\Im}}^2} \tag{2.15}$$

Absorption Because of the fundamental law of energy conservation, the part that is neither reflected nor transmitted gets absorbed in the material. The absorption can be defined by Lambert-Beer's law: After passing a distance x of a material with an absorption coefficient α, the initial irradiance Irr_0 reduces to:

$$Irr(x) = Irr_0 \cdot \exp\left[-\alpha \cdot x\right] \tag{2.16}$$

Another definition of α results from the extinction coefficient (imaginary part of $\tilde{n}$):

$$\alpha = \frac{4\pi \cdot n_{\Im}}{\lambda} = \frac{1}{a_{abs}} \tag{2.17}$$

Here x, λ and a_{abs} are the propagation distance, the wavelength and the absorption length, respectively.

For most nonmetals there are two different types of absorption in the UV-VIS-NIR spectrum: Interband absorption, i.e. the excitation of an electron (and a hole) from the valence (conduction) band into the conduction (valence) band, and high-frequency optical phonon absorption. While the former are present only for energies above the band gap, the latter are found at much lower energies. [Allmen1995, p. 9-10]

Regarding their absorption semiconductors can be divided in direct and indirect semiconductors. While α is a very steep function of the wavelength for the former, it rises much lower for the latter ones, because due to conservation of momentum an additional phonon is mandatory for the absorption. Schematically, this is displayed in fig. 2.9, showing the valence and the conduction band energy of an indirect semiconductor as a function of

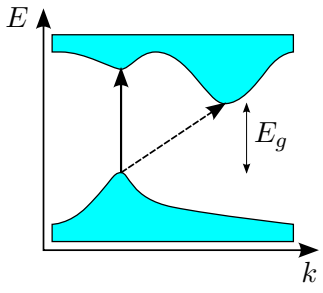

Figure 2.9: Scheme of an indirect band

the wave vector as well as a phonon-assisted transition (dashed arrow) and a direct transition (solid arrow). For example, at room temperature the indirect band gap of Si is 1.1eV and the direct gap is ≥ 3.4eV.

It has to be mentioned, that impurities and defects in the material can increase the absorption due to states inside the host materials band gap.

2.3.3 Interaction of high power laser light with material

In this thesis, the laser light mostly exhibits a high power, making an extension of the above mentioned theory necessary. As the radiation alters the properties of the material significantly, the dielectric function is no more constant in time. This mostly affects the properties that depend on the temperature. The most important ones are: The charge carrier density, the band gap, the thermal and electrical conductivity as well as reflectivity and absorptivity.

Anyway, the excitation does not necessarily need photon energies above the conduction band edge. [Boyd1984] Due to resonant coupling to high- frequency phonons, IR-laser light heats semi-conducting material. [Allmen1995, p. 10] Since the number of free, intrinsic carriers N_{fic} depends on the absolute temperature T [Sze2007, ch. 1.4]:

$$N_{fic} \propto T^{3/2} \cdot \exp\left[-\frac{T_0}{T}\right] \tag{2.18}$$

the increased temperature leads to an increased number of free charge carriers, which leads to an increased absorption coefficient, which increases the temperature and so on. Nevertheless absorption of photons with energies ≥ E_g is much more efficient.

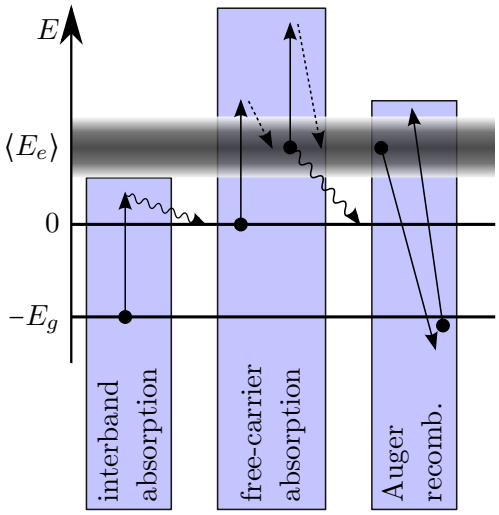

Figure 2.10: Scheme of photon absorption for high laser intensities; after [Allmen1995]

Mainly because of the high concentration of coherent photons of a laser beam, much more free charge carriers are present in the conduction band (for electrons) or valence band (holes) than under low intense radiation. These carriers can recombine, diffuse or they may get excited to even higher states. For pulsed laser annealing the energy absorbed by free carriers can exceed the amount of energy absorbed by the lattice. [Allmen1995, p. 22] Thus collisions among carriers begin to dominate collisions with the lattice and the carriers start to behave like a plasma. When the carriers relax, the energy difference is transfered into heat, increasing the lattice temperature.

Figure 2.10 schematically displays the before mentioned for electrons: By interband absorption of a photon with an energy above the band gap E_g electrons are excited into the conduction band - symbolized by solid, vertical arrows. Here they rapidly ($\sim 10^{-12}$s) relax to the conduction band edge ($E = 0$) - symbolized by the oscillating arrows. By absorbing another photon, a free electron is lifted high into the conduction band, from where it relaxes in a lifetime of $\sim 10^{-14}$s (symbolized by dashed arrows) to the average plasma energy of $\langle E_e \rangle$. Those electrons absorbing another photon here, relax after a similar time period back into $\langle E_e \rangle$.

Further, the Auger recombination is shown briefly. It is the prominent recombination mode for semiconductors at high concentrations of excited carriers. Typical time scales for Auger recombination are $\sim 10^{-9}$s.

2.3.4 Choosing the right laser parameters

Besides the absolute irradiation time, the wavelength, the pulse duration and the intensity determine the influence of the laser on the irradiated material. This makes it is hard to compare the influence of different lasers on a material with each other. However, some general trends can be observed:

1. By increasing the laser intensity or the irradiation time, the material is warmed, heated, melted, evaporated, ablated or sublimated. [Baeuerle2000, p. 4 f.]

2. The influence of the wavelength depends on the material due to the material dependent absorption coefficient. (In principle for Si α reduces with λ in the visible range.)

3. By reducing the pulse duration the heat diffusion length $l_{T,diff}$ and thus the depth dependent influence on the material gets reduced.

A first order approximation of the heat diffusion, using Fick's second law results in:

$$l_{T,diff} = \sqrt{D_T \cdot \tau_{pulse}} \tag{2.19}$$

Here, D_T and τ_{pulse} are the thermal diffusion constant and the duration of the pulse. The dependence of the heat diffusion length on the pulse duration for amorphous Si (a-Si) and c-Si at 300K and 1400K is shown in fig. 2.11 as a log-log plot, illustrating the strong dependency. [Ribeiro1995, Devlen1992, Cruz-Orea1994, Hull1999, ch. 4.6] Consequently lasers with a short pulse duration are used typically, if only a surface near processing is desired, whereas continuous radiation results in deeper, even more bulk-like processes.

Regarding solar cell fabrication, lasers are applied for different processes like hole drilling, doping or edge isolation. [Rezek1999, Andrae1999, Deutsch1981, 4JETTechnologies] In order to drill holes, e.g. for rear surface emitter solar cells, the respective material is explosively evaporated using high intense lasers with nano- to femtosecond pulses. [Ahn2012] For doping, lasers are used to locally heat the substrate which is coated with a layer containing the respective doping atoms. [Hasegawa2010, Matsumoto1990, Narayan1978]

An advantage of lasers for their application in industry are the different, available beam profiles, such as line or square profiles. Thus, the energy can be deposited exactly where it is wanted, without any unattended heating of surrounding areas as in ovens, for example.

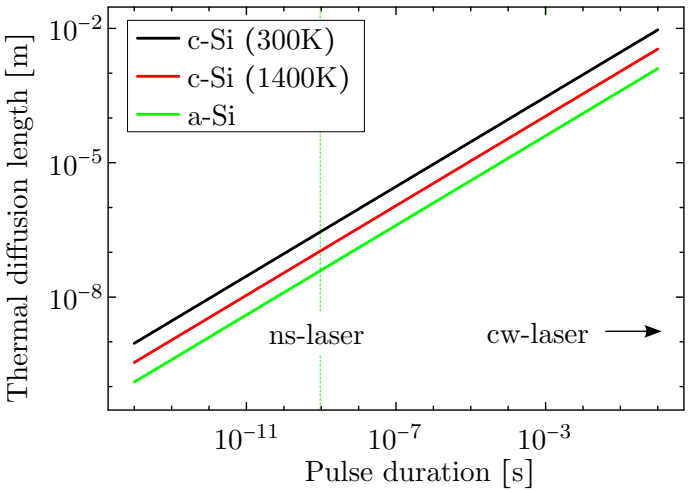

Figure 2.11: Simple estimation of thermal diffusion length for c-Si and a-Si

Chapter 3

Materials

In this chapter the materials which are used throughout the work are presented. Since this work focuses on Si and Si nanoparticles (NPs), these materials are discussed first. This is followed by sections on the used substrates and contacting metals.

3.1 Silicon and Silicon nanoparticle synthesis

Primarily due to the technological improvements gained from integrated circuits in the last half century, today Si is the by far most prominent semiconductor. [Moore1965, Rupp2011, Salvadeo2012] Nowadays it is possible to create ultra purified crystalline Si (c-Si). [Luque2005, ch. 5 & 6] Intrinsic c-Si is an indirect semiconductor that exhibits an electric band gap of 1.12eV, an electron affinity of 4.05eV and a diamond crystal structure with a lattice constant of 5.431Å (all at 300K). [Sze2007, p. 790] Typically, boron or phosphorous is used to realize p-type or n-type doping, which form energy states at 44meV from the valence band and 46meV from the conduction band, respectively. [Sze2007, p. 23] The relation between resistivity ρ and boron concentration N:

$$\rho_{boron} = \frac{1.305 \cdot 10^{16}}{N} \frac{\Omega}{\mathrm{cm}^2} + \frac{1.133 \cdot 10^{17}}{N \cdot \left(1 + (2.58 \cdot 10^{-19} \cdot N)^{-0.737}\right)} \frac{\Omega}{\mathrm{cm}^2} \tag{3.1}$$

is shown in fig. 3.1 with the relation for phosphorous. [Bulucea1993]

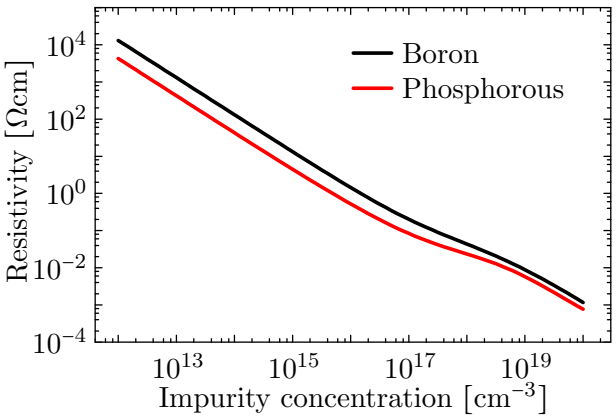

Figure 3.1: Resistivity-impurity relation according to Bulucea [Bulucea1993]

3.1.1 Si nanoparticle synthesis

The Si NPs used throughout this work are produced by decomposing the precursor gas silane ($SiH_4 \Rightarrow Si+2H_2$) in a mixture of inert carrier gases. [Wiggers2001, Petermann2011, Huelser2011] To dope the NPs, diborane (p-type) or phosphine (n-type) are added to the precursor gas, resulting in typical, final doping concentrations of ≈ 1at%. [Petermann2011, Meseth2012a, Meseth2013a] All NPs are provided by the Institute for Combustion and Gasdynamics of the University of Duisburg-Essen.

The energy required for the decomposition is delivered either via heated walls (see ch. 3.1.1) or via a microwave generator (ch. 3.1.1). The respective reactors are called "hot wall reactor" (HWR) and "microwave reactor" (MWR). After decomposition the Si atoms subsequently nucleate, coagulate and grow, forming the primary NPs. Especially in the HWR, these NPs can further sinter or / and coagulate with other NPs, forming hard or / and soft agglomerates.

Nanoparticles from the hot wall reactor

The HWR is designed for high NP production rates ~ kg/h. [Huelser2011] The Si NPs synthesis is done in a tubular HWR by spray pyrolysis. Using a nitrogen flow as carrier gas, the precursors are fed into the reactor consisting of six heating zones and a total heating length of 1m. The furnace temperature is set to 1050°C and the reactor pressure is adjusted to 400mbar. The particles are transported by the gas flow into a separator and collected on porous stainless filters. After production the material is automatically filled into plastic containers by back purging the filter. [Meseth2013a, Huelser2011, Wiggers2001] Due to safety reasons resulting from the toxic phosphine used for n-type doping, with this method, only p-type NPs can be fabricated. In fig. 3.2a a scanning electron microscope (SEM) top view image of HWR NPs on c-Si is shown. According to this, the particles exhibit a disc- or flake-like structure with diameters ~ 100nm. Dynamic light scattering (DLS) measurements of dispersed NPs result in particle diameters of ≈ 150nm. (The difference is attributed to the inaccuracy of the mathematical model to convert the DLS measurement into a particle size, as it assumes round particles.)

All HWR NPs used throughout this work are created by Dr. H. Orthner.

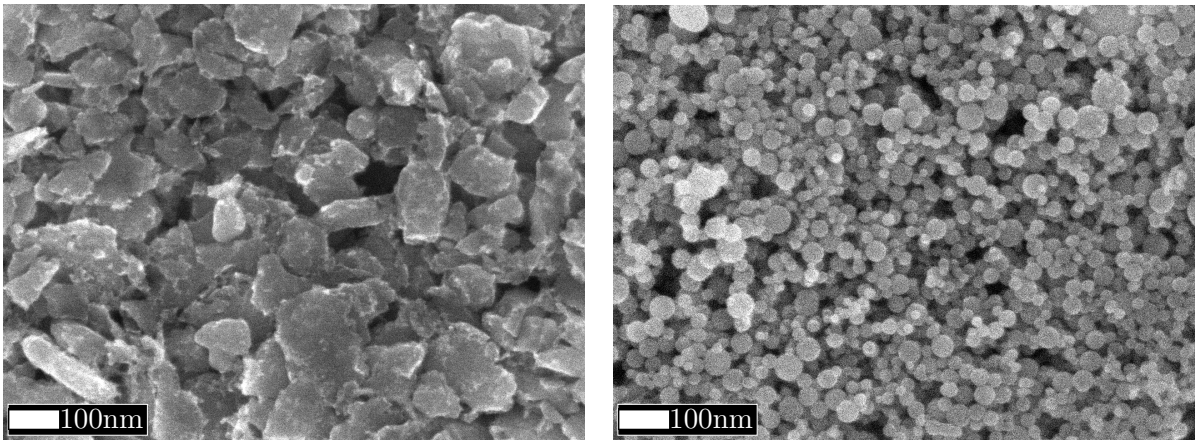

(a) Hot wall reactor nanoparticles (b) Micro wave reactor nanoparticles

Figure 3.2: SEM images of NPs created by the HWR (left) and MWR process (right)

Nanoparticles from the microwave reactor

The reactor used for MWR NP synthesis is based on a Cyrannus plasma source by iplas and is combined with a 6kW microwave generator; for the NP production it is operated at 1.2kW. As carrier gases 2 – 6slm[1] of argon and 1 – 4slm of hydrogen are used. The flux of the precursor silane is adjusted to 0.15slm and the pressure inside the reactor is set to 80mbar. By decomposition of the precursor in the plasma at temperatures $\gg$ 1000K Si NPs are formed that exhibit mean diameters in the range of 10nm – 30nm as obtained by means of Brunauer-Emmett-Teller, scanning electron microscopy (SEM) and transmission electron microscopy (TEM) measurements.

Figure 3.2b shows a typical SEM image of a MWR NP-film. The particles all exhibit an almost perfectly round structure with diameters in between $\approx$ 50nm and $\approx$ 15nm.

Oxygen shell and dopant distribution

If the Si NPs are placed in ambient air, almost immediately an oxide shell with a thickness of 5Å to 20Å forms. [Schierning2011a, Petermann2011, Stegner2009] Since most of the sample handling and preparations of this work are done in air, it is concluded that all NPs exhibit such an oxide shell. While the boron doping is found to be homogeneously distributed in the NPs, for phosphorous doped NPs about 95% of the dopants accumulate in the shell. [Lechner2008, Stegner2009]

3.2 Substrates

In this section the used substrates are discussed, starting with the conductive (Si) materials and going to the non-conductive materials, i.e. glass and flexible polyimide.

3.2.1 Crystalline silicon substrates

All c-Si substrates used exhibit a {100}-crystal orientation and at least one polished surface, which is used for preparation. However, they varied in regard of the doping type and concentration as well as the surface treatment of the opposite side and the thickness. Nominally undoped ("intrinsic") substrates are purchased from Semiconductor Wafer Inc., Taiwan and doped samples from CrysTec. Therefore the respective properties are listed in each chapter, separately.

3.2.2 Glass substrates

For experiments on glass, simple, polished oxide-lime glass is used. It exhibits a thickness of 0.8mm to 1.0mm and is cut into squares of 26mm edge length. It is impossible to give a melting temperature for a glass; however, at temperatures above $\approx$ 600°C the viscosity of simple glass increases so much that it is easily formable.

3.2.3 Flexible substrates

For experiments on flexible substrates, the polyimide Kapton® is used. It exhibits a thickness of 0.05mm, a red-brown colour and withstands temperatures up to 400°C for a few minutes according to the supplier DuPont®. The substrates are cut into $\approx 11 \times 11\text{mm}^2$ samples out of a Kapton® sheet of DIN A4 size using scissors.

[1] slm = standard liter per minute

3.2.4 Standard cleaning process

The standard cleaning process for all substrate types consists of successive cleaning steps in acetone and isopropanol ultra sonic baths, each for 10min. Subsequently the respective sample is dried by blowing off the residual solvent using a nitrogen flow.

Oxide removal step

Throughout this work hexafluorosilicic acid (chemical formula: H_2SiF_6; short term HFS) is used to remove the oxygen on c-Si substrates and from NPs. By heating HFS (here a temperature of $\approx 90°C$ is chosen) it dissociates, creating a hydrofluoric acid (HF) containing solution, which selectively etches SiO_X. Fig. 3.3 shows the x-ray photoelectron spectroscopy (XPS) measurement of an HFS-etched (bottom) and an unetched sample. As the SiO_2 peak vanishes completely, it is concluded, that the amount of SiO_2 is significantly reduced by the HFS treatment.

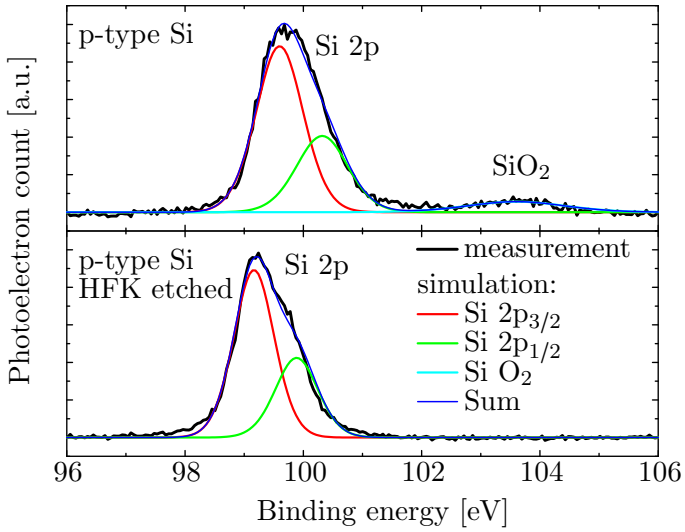

Figure 3.3: XPS spectrum of untreated (top) and HFK treated (bottom) c-Si sample (measurements by Dr. D. Krix, Experimental Physics, Prof. Dr. H. Nienhaus, University of Duisburg-Essen)

3.3 Contact materials

Contacts for electrical sample characterization are formed by thermal evaporation (see ch. 4.1.3) of gold (Au), silver (Ag) or aluminium (Al). The respective electron work functions are given in table 3.1.

Table 3.1: Work functions of the elements used for metal contacts. [Sharma2010, p. 12-121]

Plane	Gold (Au)	Silver (Ag)	Aluminium (Al)
{100}	5.47eV	4.46eV	4.20eV
{110}	5.37eV	4.52eV	4.06eV
{111}	5.31eV	4.74eV	4.26eV

Chapter 4

Experimental methods

This chapter presents the experimental methods used for sample preparation (ch. 4.1) and analysis (ch. 4.2). Standard methods are described only briefly.

4.1 Sample preparation

The first part of this section deals with the preparation of thin films by spin coating of Si nanoparticle (NP) dispersions and laser annealing of these films. In the second part, the preparation of bulk samples by spark plasma sintering of Si NPs is discussed. This is followed by a subsection about the contact formation on the prepared samples by physical vapor deposition for electrical characterization.

4.1.1 Preparation of thin film samples

Thin films of Si NPs are created by a dispersion based spin coating process. Further sample preparation includes the subsequent annealing of the film using either an infrared (IR) or an ultraviolet (UV) line-laser.

Creation of nanoparticle dispersions

NP dispersions are created by mixing up to 10wt.% of NPs with ethanol. Lechner has reported, that stable NP dispersions can also be created using chloroform, acetone, toluene and tetrahydrofurane. [Lechner2008a, p. 28] Here, ethanol is used due to easy handling and low costs. The mixture is milled in two steps using yttrium-stabilized zirconia (YSZ) beads (Netzsch-Beads Nano). For a pre-milling step, beads of 300µm diameter are used and for the main milling procedure beads of 100µm diameter are used. The milling consists of two steps, because this has resulted in best quality of the deposited film, c.f. ch. 5.1.

Two mills are applied: A "MicroCer" ball mill from Netzsch is used for dispersions of large volume. [NETZSCH2007] Here, the pre-milling step endures 30min at 1000r/min. In the following main milling step the frequency of rotation is changed from 1000r/min to 3000r/min in steps of 500r/min; each step lasting 30min. Since the utilized mill (of Institute for Combustion and Gasdynamics) stands in an open laboratory environment the dispersion gets in contact with air during the milling process.

For dispersions of smaller volume a Retsch MM 400 shaking mill is used. 3ml of the respective grinding beads and 4g of dispersion are filled in each air-sealed container. Using a milling

frequency of $30s^{-1}$, typically the pre-milling step is performed for 1h and the main milling step for 2h. The mill can be placed under a laboratory hood. Since toxic phosphine vaporizes if phosphorous doped NPs are in contact with ambient air, only the Retsch MM 400 mill is used to create dispersions of phosphorous doped NPs.

After the milling, dispersions are filtered using an MN 85/90 BF glass fibre filter without binder from Macherey-Nagel with an average retention capacity of 0.5µm.

Spin Coating

The resulting dispersions are deposited on substrates using a syringe equipped with a filter of 0.7µm pore size. The amount of dispersion is chosen such that the sample surface is covered completely. Immediately after deposition the rotation is started. The spin coating parameters (acceleration, maximum rotation) are varied throughout the work and are presented in the respective chapters.

Laser Annealing

For laser annealing a UV and an IR laser system, both from Lissotschenko Micro Optics (LIMO) are used. Both systems exhibit a top-hat - Gaussian laser profile (see fig. 4.2a) and are positioned using computer controlled x-, y- and z-positioning stages. The laser is always scanned in direction of the Gaussian profile, see fig. 4.2b. Table 4.1 summarizes the laser properties at the end of this subsection.

Ultraviolet laser The UV laser equipment is schematically presented in fig. 4.2c. It consists of an ATLEX-300-SI KrF excimer laser with a wavelength of 248nm and a pulse duration of 4ns – 6ns. The laser can be operated at repetition rates between 1Hz and 300Hz and at primary energies $6\text{mJ} \leq E_{prim} \leq 14\text{mJ}$. Using a semi-reflecting mirror, a small fraction of the laser light is reflected on a photo diode and the determined intensity is used by an internal regulating mechanism to adjust the primary energy. The energy at the sample's surface E_{sample} is controlled using a dielectric filter (Metrolux ML2100 in combination with a Metrolux ML8010 control unit).

With a beam homogenizer the originally rectangular beam profile ($4 \times 6\text{mm}^2$) is converted into a top-hat - Gaussian line profile of 10mm - 26µm (FWHM) which corresponds to an effective laser-area of $A_{eff} = 0.0026\text{cm}^2$. In dependence of the dielectric's filter angle $0° \geq \beta \geq 45°$ the transmission Tr can be approximated by:

$$Tr(\beta) = \frac{60.1\%}{1 + \exp\left[\frac{\beta - 31.5°}{3.36°}\right]} \tag{4.1}$$

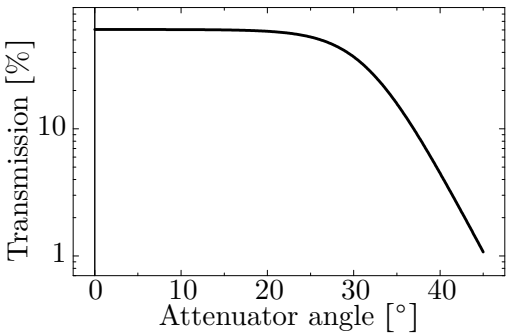

Figure 4.1: Attenuator's transmission

as is displayed in fig. 4.1. (Eq. (4.1) includes absorption and residual reflexion losses of the anti-reflex coated glass view port, that is mounted on top of the process chamber.) Here, the process chamber is mounted on a movable x-y-stage, and the focus plane of the laser line is adjusted using the movable z-axis that carries the focusing optic.

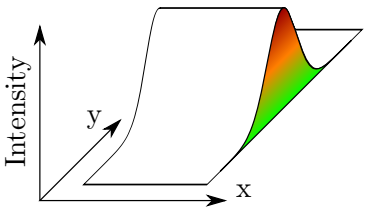

(a) Intensity profile of line lasers

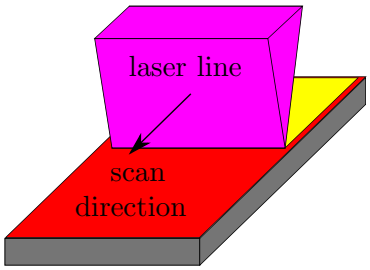

(b) Scan direction of line lasers

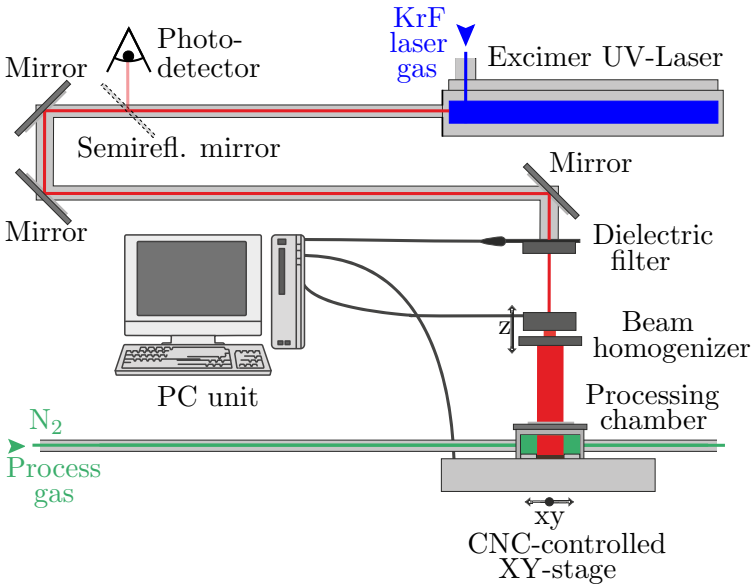

(c) Setup of the UV line laser [Kunze2012]

Figure 4.2: Scan direction of the line lasers and UV laser setup

To counteract confusion, the symbols used in regard of the UV laser experiments are shortly explained in the following:

1. E_{prim} symbolizes the primary energy of one pulse, at the exit of the excimer laser unit

2. $E_{sample} = Tr(\beta) \cdot E_{prim}$ symbolizes the energy of one pulse at the sample's surface

3. $\phi_{sample} = E_{sample}/A_{eff}$ symbolizes the mean energy density of one pulse at the sample's surface

Infrared laser A continuous-wave IR laser with a wavelength of 807.5nm, a spectral width of 6.8nm and a maximum laser power of 452W is used. This laser is equipped with a beam homogenizer, creating a top hat - Gaussian profile of 13.38mm - 52µm (FWHM) in the focus plane. The power can be set by the computer program and is adjusted by a regulating mechanism similar to the one discussed for the UV laser.

For the IR laser system the focusing optic is positioned in x-, y- and z-direction. Further, the substrates are placed on $1.5 \times 1.5\text{cm}^2$ (±0.25mm each direction) quartz glasses of (1.0 ± 0.1)mm thickness to thermally decouple the substrate from the metallic process chamber.

Processing chamber For laser annealing the samples are placed in a closed processing chamber. The laser beam is coupled onto the sample through a silica glass. For the UV laser a 7.5cm diameter view port, equipped with an anti-reflex coating for 248nm is used, for the IR laser a view port of 10cm diameter without anti-reflex coating is used. Both chambers can be flushed with gases - nitrogen and argon are used in order to prevent the samples from oxidation. [Behrenberg2012]

Table 4.1: Properties of the used laser systems

Laser unit	UV	IR
Wavelength	248nm	808nm
Pulse duration	5ns	continuous
Repetition rate	≥ 300Hz	continuous
Top-hat length	10mm	13.8mm
Gaussian FWHM	26µm	5µm

Rapid thermal annealing

For rapid thermal annealing processes an ULVAC-RICO MILA-5000 unit is used. High intense halogen lamps focus their light on the sample, creating temperature ramps of up to 50K/s. The process chamber is typically evacuated to a base pressure of $\sim 10^{-4}$mbar.

4.1.2 Preparation of bulk samples

Spark plasma sintering[1] (SPS) is a technique to rapidly heat and sinter powders, e.g. NPs. The biggest difference when compared to conventional sintering techniques is found in the origin of the heat, which builds up inside the sample due to Joule heating from the electrical current driven through the the powder. With this high heating and cooling rates of ~ 100K/s are possible, leading to a reduction of atom diffusion and of structural rearranging. [Schwesig2011] Consequently, by SPS of NPs, a nano structure can be obtained in bulk samples. In thermoelectrics, the SPS preparation technique nowadays is a standard preparation method. [Bux2009, Becker2012, Schwesig2011]

For sample processing NPs are filled in a cylindrical graphite die with an inner diameter of d = 20mm. The NPs are electrically isolated from the die's wall using a boron nitride layer. The sintering process is done in an argon atmosphere. A pressure of p = 38MPa is applied by two pistons in direction of the cylinder axis and is kept constant throughout the entire, following process. Due to the pressure, the powder is compacted to a density ≈ 50% of bulk Si. [Petermann2011] Subsequently a DC-current is driven through the pistons and consequently through the NPs, leading to a temperature increase in the powder. The temperature is measured using thermocouples and pyrometers. The heating rate is set to 100K/min until a maximum temperature of 1050°C is reached. This temperature is held constant for 3min before the sample is cooled down to room temperature with 100K/min. The sintered material's density reaches typical values of 95% to 98% of crystalline Si. [Schwesig2011, Schierning2011a, Petermann2011]. The sintered samples are sawed in pieces, grinded and polished using diamond polishing pastes.

For preparation an HP D 40 SPS unit by FCT-Systeme GmbH is utilized. During the process, the temperature, the pressure and the positions of the pistons are recorded at a sampling rate of 1s.

[1] Lately the term "spark plasma sintering" is found to describe the actual process incorrectly, since neither a plasma nor a spark is present. Different names like "Current-activated pressure-assisted densification", "DC-current sintering" or "field assisted sintering" are used instead. [Schwesig2011, Schierning2011a, Becker2012b]

4.1.3 Metal contact deposition

Metal contact deposition is performed by physical vapor deposition in an evaporation chamber from MBraun. In this chamber the samples are placed face downwards in a sample holder. About 30cm below it, a tungsten crucible filled with pieces of the respective metal is placed.

The evaporation process is usually started at a base pressure of $\sim 4 \cdot 10^{-6}$mbar by driving an electrical current through the tungsten crucible, which heats up and therefore melts / evaporates the respective metal. The current is controlled in order to obtain constant deposition rates in the range of 1Å/s – 4Å/s. Contact geometries are defined by shadow masks.

4.2 Sample analysis

Samples are analysed by investigating their structure (see ch. 4.2.1), their elemental composition (see ch. 4.2.2) and their electrical behaviour (see ch. 4.2.3). The corresponding methods are presented in the following.

4.2.1 Structural analysis

For structural analysis x-ray diffraction (XRD), scanning electron microscopy (SEM), dynamic light scattering (DLS), profilometry and transmission electron microscopy (TEM) are used. Further, a selective etching experiment is applied and is presented here.

X-ray diffraction

To analyze lattice constants as well as the sizes of crystallites x-ray diffraction (XRD) is applied. An X'pert Pro MPD (Multi Purpose Diffractometer) diffractometer from PANalytical using the characteristic $Cu\,K\,\alpha$ emission line is equipped. Since it has not been possible to separate the lines

1. $Cu\,K\,\alpha_1$ = 0.15405952nm [Maskil1988]
2. $Cu\,K\,\alpha_2$ = 0.15444256nm [Deutsch1981]

from another for low diffraction orders, a mean wavelength of λ_{Cu} = 0.1542nm is used for the calculations in this work. The accelerating voltage and the anode current are set to 40kV and 30mA, respectively. Measurements are performed in Θ - 2Θ geometry.

Lattice constant calculation To calculate the distances d between reflecting crystal planes, the Bragg-formula is used (see fig. 4.3). It correlates the constructive interference with d for the case of the glancing angle:

$$m \cdot \lambda = 2d \cdot \sin\left(\frac{2\Theta}{2}\right) \tag{4.2}$$

Here m is the diffraction order and λ is the wavelength of the x-ray radiation. The term $2\Theta/2$ is used since usually 2Θ is the value of the abscissa.

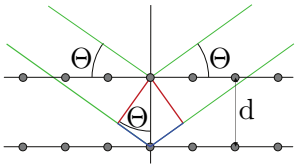

Figure 4.3: According to Bragg-formula

Crystallite size calculation From the position $2\Theta_{max}$ of a reflex of low diffraction order and from its full width at half maximum (FWHM) $\Delta 2\Theta$, it is possible to estimate the mean crystal size B perpendicular to the reflecting lattice plane. According to the Scherrer-formula B can be calculated by [Balaz2008]:

$$B_{Scherrer} = \frac{\lambda \cdot K}{\Delta 2\Theta \cdot \cos\left(\frac{2\Theta_{max}}{2}\right)} \tag{4.3}$$

Here λ represents the x-ray wavelength and K is a dimensionless form-factor taking into account the crystalline geometry; for cubic crystals $K \approx 0,94$. [Balaz2008] It has to be mentioned, that this method results only in a rough estimate and depends on the amount of available crystallites, amongst others.

Scanning electron microscopy

For SEM investigations a JEOL JSM7500-F field emission SEM is used. Accelerating voltages can be varied in between 1kV and 30kV; here it is usually set to 5kV. Furthermore, an EDX system, which will be specified in the following, is mounted in the SEM.

Profilometry

An AMBIOS XP-200 profilometer with a tip that exhibits an apex angle of 95° and a radius of 12.5µm is used. The stylus force is usually set to 0.1mg. The system has a maximum height resolution of 1nm and a planar resolution of 0.2µm is used. In order to estimate thicknesses of layers deposited on flat surfaces, the respective layer is scraped by pulling a razor blade over it and scanning rectangularly over the scratched line. From the height difference the thickness of the layer is derived. The profilometer is furthermore used to evaluate the roughness of surfaces or the three dimensional profile, while the latter is done by repeatedly performing line scans.

Transmission electron microscopy

By TEM the structure of cross sectional lamellae of several samples are characterized. The lamellae are prepared by the focused ion beam (FIB) technique using a Helios NanoLab 600 DualBeam from FEI [Meseth2013a]: In a first step, a 2.5µm thick Pt-layer is deposited on a 2µm × 10µm surface to protect the sample from possible ion beam damage. The surrounding area is then milled using a Ga ion beam. By this a cross sectional lamella of 6µm in height is left in the sample (see fig. 4.4a). After separating the lamella from the bulk it is thinned down to the final width $\lessapprox$ 100nm (see fig. 4.4c). To reduce the amount of residual Ga on the lamella's faces, the ion beam current is decreased during the latter process. For the subsequent characterization, TEM images as well as transmission electron diffraction (TED) micrographs are prepared.

The FIB preparation is performed by A. Beckel and M. Bartsch from the work group of Prof. Dr. A. Lorke and the TEM / TED measurements are done by A. Elsukova.

Selective etching experiments

To clarify the crystal structure of silicon surfaces, anisotropic KOH-etching experiments are performed. According to [Seidel1990] KOH etching rates in silicon differ up to a factor of 100

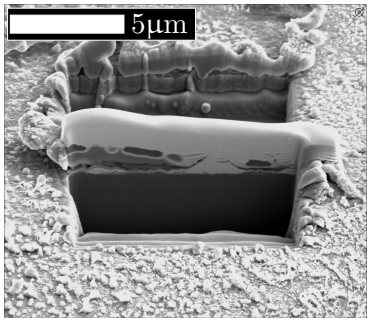

(a) Lamella in sample

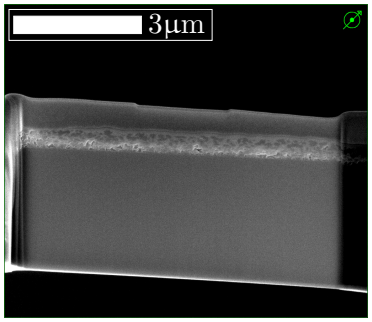

(b) Finished lamella - face view

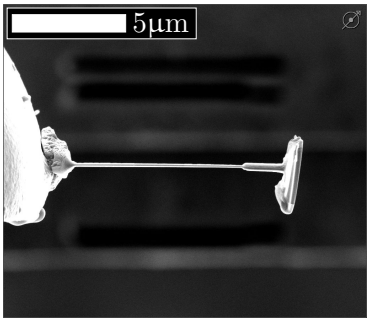

(c) Finished lamella - top view

Figure 4.4: Images from FIB-preparation: The image on the left shows the lamella before separation from the sample. The other images show a finished lamella

for the different crystal planes; whereat the {111} direction behaves like an etch stopping plane. For {100} silicon wafers KOH etching yields pyramidal structures of {111}-planes. For B doping concentration above 10^{19}cm^{-3} a respective etching is found to be challenging, as here borosilicate forms that acts as an etch stop. [MicroChemicals2012, Seidel1990a]

The experiments are performed by D. Behrenberg from the work group of PD. Dr. N. Hartmann.

4.2.2 Elemental characterization

The distribution of elements in the samples are analysed using scanning energy dispersive x-ray spectroscopy (EDX), secondary ion mass spectroscopy (SIMS), potential Seebeck microscopy and electrochemical capacitance-voltage measurements (ECV). While the former two methods give a direct elemental mapping, the latter two methods are indirect methods, as they can only determine the polarity and / or the doping density in a semiconductor. Further, the doping concentrations determined by the indirect (direct) methods are the concentrations of the activated (all) dopants.

Energy dispersive x-ray spectroscopy

The SEM is equipped with a Bruker XFlash 5030 energy dispersive x-ray (EDX) detector with a beryllium window. Due to the window only elements with an atomic number $N > 5$ can be detected. It is therefore impossible to detect B using EDX, here.

Secondary ion mass spectrometry

Elemental analysis is performed using secondary ion mass spectrometry (SIMS) working in time of flight (TOF) configuration and using a "Dual Beam Depth Profiling" mode. It consists of two alternating processes: On the one hand low energy beams of O^{2+} or Cs^- are used to sputter an area of $300\mu\text{m} \times 300\mu\text{m}$. The low energy is chosen in order to avoid forward implantation. The Cs^- ions are used if analysis is focused on oxygen or oxygen containing groups. On the other hand, high energy Bi^{1+} ion beams are used to analyze an area of $100 \times 100\mu\text{m}^2$ with a pixel resolution of 256×256. Bi^{1+} is chosen in order to maximize the mass resolution. The respective conditions are:

1. O_2^+ primary ion clusters: 2keV ion energy and 343nA target current

2. Cs^- primary ions: 0.5keV ion energy and 32nA target current

3. Bi_1^+ primary ion clusters: 30keV and 0.14pA or 30pA target current (negative or positive polarity of the analyzer, respectively in order to avoid edge contamination).

After the SIMS profiling the total crater depths are measured by means of an optical profiler (Sensofar PLμ neox). Depth scales are established by measuring the total sputter depths assuming linear sputter rates. The pressure during analysis are a few 10^{-9}mbar.

SIMS measurements are performed by Tascon GmbH for ION-TOF GmbH, both sited in Münster, Germany.

Scanning potential Seebeck microscopy

The scanning potential Seebeck microscopy is used to characterize the dopant distribution in semiconductors. The method is based on the thermoelectric effect: If a conductive material is heated, the mean velocity of the material's charge carriers increases. So, if a temperature gradient is found in this material, "fast" charge carriers diffuse from hot to cold regions, where their mean velocity decreases again. Consequently the charge carriers accumulate at the cold side and an electrical potential difference builds up along the gradient. Thus, by applying a temperature difference over an unknown material and measuring the thermoelectric voltage U_{TE} along this direction, the type of majority charge carriers can be determined. Moreover, it is found that the temperature difference ΔT and U_{TE} are proportional to each other:

$$U_{TE} = \Sigma \cdot \Delta T \tag{4.4}$$

with Σ being the the Seebeck coefficient. According to Snyder and Toberer for metals and degenerated semiconductors Σ is linked to the free charge carrier concentration N_{cc} [Snyder2008]:

$$\Sigma = \frac{2 \cdot {k_B}^2}{3 \cdot e \cdot \hbar^2} \cdot m^* \cdot T \cdot \left(\frac{\pi}{3 \cdot N_{cc}}\right)^{2/3} \tag{4.5}$$

$$\propto N^{-2/3} \tag{4.6}$$

Here, k_B, e, $\hbar$, m^* and N are the Boltzmann's constant, the elemental charge, the reduced Planck constant, the effective mass of the charge carrier and the doping concentration, respectively. Thus, by assuming that all dopants are ionized, the doping concentration can be calculated.

For the experiment a heated probe tip of diameter d = 3μm is placed on the surface of the sample under investigation. It creates a local, constant temperature difference between the probe tip and the sample of $\Delta T \approx 15.4$°C by feedback-loops using the temperatures measured by two T-type thermocouples; one at the tip and one at the sample. The thermoelectric voltage U_{TE} is determined by measuring the voltages of the Cu wires U_{Cu} and of the CuNi wires U_{CuNi} of the two thermocouples. [Ziolkowski2006] With the well known Seebeck coefficients for Cu Σ_{Cu} = 1.83μV/K [Sharma2010, p. 12-216] and for CuNi $\Sigma_{CuNi} \approx$ 40μV/K [Heikes1961, p. 316]

the sample's Seebeck coefficient Σ_S can be determined from the measurement:

$$U_{Cu} = (\Sigma_S - \Sigma_{Cu}) \cdot \Delta T \quad (4.7)$$

$$U_{CuNi} = (\Sigma_S - \Sigma_{CuNi}) \cdot \Delta T \quad (4.8)$$

$$\Sigma_S = \frac{U_{Cu}}{U_{CuNi} - U_{Cu}} (\Sigma_{Cu} - \Sigma_{CuNi}) + \Sigma_{Cu} \quad (4.9)$$

Using linear stages the sample is scanned with a step distance of dx = dy = 20µm in x- and y-direction and the Seebeck coefficient of each position can be determined.

Measurements are performed by P. Ziolkowski at the German Aerospace Centre (DLR) Cologne at room temperature.

Electrochemical capacitance voltage measurements

The electrochemical capacitance voltage (ECV) technique has been applied to determine depth dependent doping profiles of doped Si layers. For the measurements presented here, the sample surface is brought in contact with a 0.1mol/l solution of NH_4F. As a result, a Schottky barrier forms between the semiconductor and the electrolyte. The doping concentration is derived from the voltage dependent capacitance of the barrier (see eq. (4.15)). The electrolyte is furthermore used to stepwise etch the silicon. Thus, by measuring the carrier concentration after each etching step the doping profile of the wafer is determined.

Since measurements are performed by F. Kiefer of the work group of N.-P. Harder at the Institute for Solar Energy Research Hameln (ISFH) using a WEP CVP21 profiler, this method has been applied only seldomly. [Peiner1995, Bock2008]

4.2.3 Electrical characterization

For electrical characterization of the prepared samples, three main measurement methods are applied in this work and are presented in the following: First the conductance measurements are discussed. This is followed by the characterization methods of pn-diodes, namely the current-voltage ($I(U)$) and the capacitance-voltage ($C(U)$) measurement methods.

Conductivity measurements

For conductivity measurements the four point method is applied: A current is driven through the material by two outer contacts and the voltage difference between two inner contacts is measured (see fig. 4.5). Due to a high impedance of the voltmeter the contact resistance can be neglected and the material's conductivity is determined using the geometrical dimensions. [Schroder2006, Sze2007, Smits1958, Logan1967]

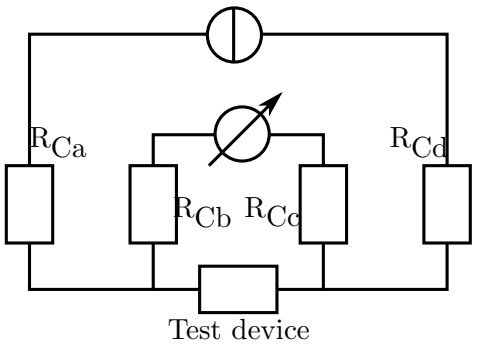

Figure 4.5: Four point measurement principle

In this work two different four point measurement geometries are used: On the one hand electrodes are evaporated, in a geometry as shown in fig. 4.6a. The distance of the inner electrodes is S = 100µm and the effective

electrode width is W = 7.4mm. If the material's thickness h is known, the conductivity can be calculated by:

$$\sigma = \frac{I \cdot S}{U \cdot W \cdot h} \tag{4.10}$$

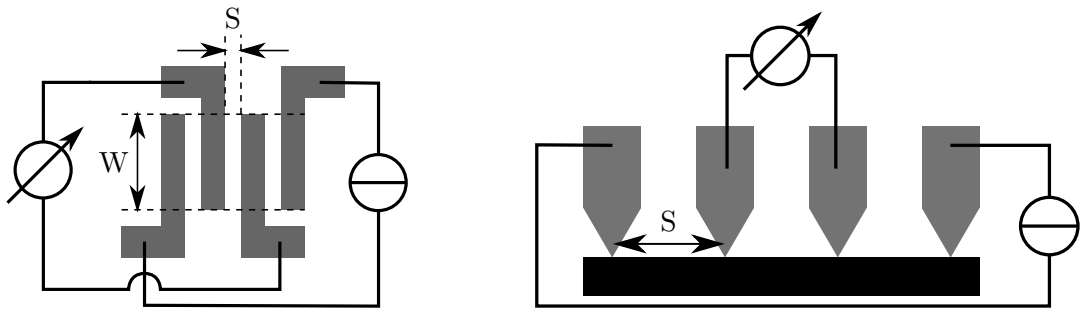

(a) Evaporated contacts (b) Pressed contacts

Figure 4.6: Designs of four point measurements using evaporated contacts (left) or standard probe (right)

On the other hand a standard four point measurement tool is used consisting of four tips made of tungsten carbide with a tip's end radius of 40µm that are mechanically placed on the material, c.f. fig. 4.6b. Since neighbouring probes exhibit a constant spacing (S = 1mm), the conductivity for this case is calculated by [Schroder2006]:

$$\sigma = \frac{\ln 2}{\pi} \frac{I}{U \cdot h} \tag{4.11}$$

A geometrical correction factor has not been considered for the presented measurements, as their influence on the measurement is less than 5% for the investigated sample geometries. [Schroder2006, Valdes1954, Smits1958]

Comparability of both four point measurement methods In order to prove, whether both methods are comparable, six silicon samples cut out of one wafer are measured first using the standard tool and conductivities are derived using eq. (4.11). Thereafter metal contacts as shown in fig. 4.6a are deposited on the samples and the conductivities are derived using eq. (4.10). In fig. 4.7 the resulting data is shown; black stars correspond to the standard method, red circles to the evaporated contact method.

Although the conductivities of both methods are in the same order, they differ by a constant factor of ≈ 3, even though the samples are exactly the same ones. Since the tip-based approach is standard in science and research, the derived values are expected to be in agreement with standard research. Consequently, it is assumed that eq. (4.10) is a too simple approach. Most probably the voltage drops over a longer distance than the assumed distance S.

However, the measurements show that for each setup the values are comparable to another. Therefore, in this work usually only conductances are presented as the result of four point measurements performed by the evaporated contact method, whereas conductivities are given for the standard method. All conductance and conductivity measurements are done using a Keithley SCS 4200 unit.

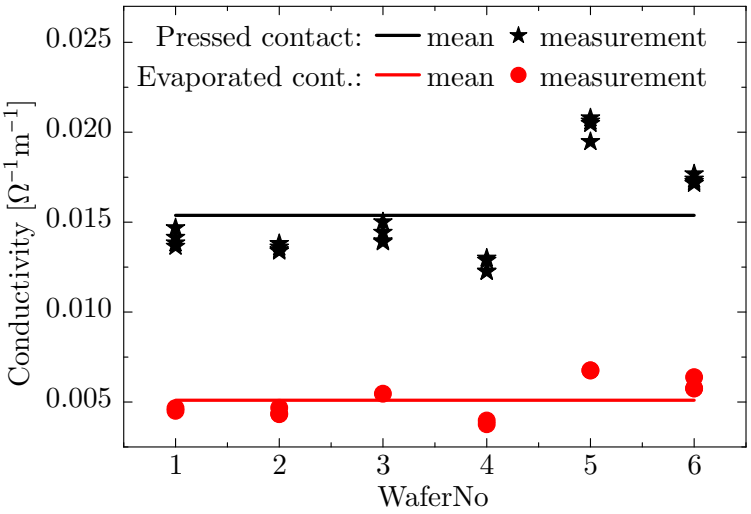

Figure 4.7: Comparison of electrical four point measurement results obtained by standard measurement (black stars) and by evaporated contacts (see fig. 4.6a, red circles)

Temperature dependent current-voltage measurements For temperature dependent current voltage measurements a two stage shielded, closed cycle He cryostat system by Janis (model: SHI-4H-5), utilizing an RDK 205D cold head by SHI and a CKW-21 He compressor by SHI, is used in combination with a LakeShore 336 temperature controller. For electrical characterization, the cryostat has six probes and the connected wires are twice shielded (triaxial cables). The temperature of the sample can be changed in between 5K and 450K. Measurements are performed at pressures of $\sim 10^{-4}$mbar.

Photovoltaic characterization of pn-junctions

The PV characteristics U_{oc}, I_{sc}, FF and η of pn-diodes are determined by $I(U)$ measurements using a Keithley 238 source measurement unit (SMU) in combination with a light source. Usually the applied voltage U is changed in between +1V and −1V in steps of 50mV. (If not stated otherwise, the area used for calculation of η is the processed sample area minus the contact area.)

Two light sources are used for illumination: A Wacom SolarSimulator creating a defined light flux density of $1000\mathrm{Wm}^{-2}$ close to the AM1.5 spectrum and a 1000W Hedler Jet-Lux halogen lamp (applied only for the SPS samples). For the power density at the sample's surface of the latter only an upper limit can be approximated by dividing the power by the exit's area A_{exit}:

$$\frac{P}{A_{exit}} = \frac{1000\mathrm{W}}{\pi \cdot 16\mathrm{cm}^2} = 199\,000\frac{\mathrm{W}}{\mathrm{m}^2} \tag{4.12}$$

Simulation of diode characteristics To extract more informations, the $I(U)$ graphs are fitted according to the one-diode model, see ch. 2.1. Since $I(U)$ is a recursive function (see eq. (2.2)) and since the unknown parameters n, R_{ser}, R_{shu} and I_0 are not independent of each other, the complete system can only be solved by numerical approximations.

In this thesis a Matlab fitting program is developed, which is based on a publication by Zhang et al. [Zhang2011, Kunert2013] Here, the problem of the recursive diode equation is

solved by using the "Lambert W" function $W(z)$:

$$z = W(z) \cdot e^{W(z)} \tag{4.13}$$

Optical beam induced current measurements

By optical beam induced current (OBIC) measurements a two dimensional graph of the short circuit current of PV pn-junctions is derived. The resulting map can help to identify process errors or disadvantages. For the measurement, the sample is mounted on an x-y-positioning table with a spatial resolution of 0.1µm and a repeating accuracy of 2µm. Monochromatic light is incorporated into the sample using fibre glass and reflecting optics and is created either by a 980nm laser or by a combination of a xenon discharge lamp (XDL) and a Newport Cornerstone 130 1/8m monochromator that filters wavelengths in between 400nm and 1000nm. A minimum spot size diameter of 3µm can be obtained using the laser and ≈ 10µm using the XDL-monochromator system. Further details on the used OBIC system can be found in a publication by Bitzer et al. [Bitzer2013]

The SMU used to measure I_{sc} is a Keithley 238 SMU. It is best described as a current source, that continuously adapts the current in order to ensure the applied voltage to be zero. For samples that exhibit a relatively small resistance, this results in inevitable time dependent measurement fluctuations. Due to this disadvantage, in ch. 7.3.3 instead of the current, the voltage is measured with a nano volt meter.

Since the OBIC measurement is performed by scanning parallel lines, starting at the top and running to the bottom, these time dependent fluctuations from the SMU are found as vertical lines in the OBIC graph.

Capacitance-voltage characterization

For pn-junctions, voltage dependent capacitance ($C(U)$) measurements are used to determine the build-in voltage and the doping concentration of the substrate: In the voltage dependent space charge region of width $w = w(U)$ of a pn-junction, the number of free charges is negligible. Analogue to the plate capacitor, a "depletion-layer capacitance per unit area" $C_D = C/A_1$ can be defined. [Sze2007, p. 85] By changing the applied voltage by $\mathrm{d}U$ a change in the depletion charge on each side of the pn-junction $\mathrm{d}Q_D$ occurs:

$$C_D = \frac{\mathrm{d}Q_D}{\mathrm{d}U} = \frac{\epsilon_0 \cdot \epsilon_r}{w(U)} \tag{4.14}$$

Here $\epsilon_0 = 8.854187 \cdot 10^{-12}\mathrm{F/m}$ and ϵ_r are the permittivity constant and the material's relative permittivity. For an abrupt, one sided junction, C_D is calculated by [Sze2007, p. 85]:

$$C_D = \sqrt{\frac{e \cdot \epsilon_0 \cdot \epsilon_r \cdot N}{2}} \cdot \left(U_{bi} - U - \frac{2 \cdot k_B \cdot T}{q}\right)^{-1/2} \tag{4.15}$$

Here U_{bi} and U are the build-in and the applied voltage. Consequently, by plotting $C_D^{-2}(U)$, N and U_{bi} can be derived by the slope and the extrapolation to $C_D^{-2} = 0$, respectively.

In this thesis, the $C(U)$ characterization of pn-junctions is done by superimposing an AC voltage U_{AC} on a DC voltage U_{DC}. While U_{DC} is used to bias the junction, the comparably small AC voltage U_{AC} is varied at a fixed frequency ω to determine the pn-junction's admittance

Y_{mat}. By comparing it with the admittance of a parallel connection of an ideal capacitor and an ideal resistor, the capacitance of the system is derived.

For the measurements, a Keithley SCS 4200 unit is used. The DC voltage is varied in the range of a few volts around 0V in steps of ≈ 10mV. The AC voltage is set to 20mV and the frequency is set to 1MHz or 100kHz, depending on the sample under test.

Chapter 5

Laser annealing of nanoparticle films on c-Si

In this chapter the feasibility to dope crystalline Si (c-Si) by laser annealing of coated thin films of highly doped Si nanoparticles (NPs) is investigated. Therefore in section 5.1, the film preparation is discussed. In the following chapters, NP coated Si substrates are laser annealed using a continuous wave infrared (cw IR) laser (ch. 5.2) or a pulsed ultraviolet (UV) laser (ch. 5.3). The resulting samples are investigated mainly by structural and electrical methods to judge the applicability of this method.

5.1 Realization of nanoparticle thin films

In order to create thin films, NPs are deposited onto c-Si substrates via a dispersion based spin coating process. In the following section the influence of the dispersion procedure and of the spin coating parameters are discussed. The films' thicknesses and roughnesses are determines by profilometry in order to evaluate how to form a closed, flat and homogeneous film which is essential for the subsequent processing.

5.1.1 Influence of dispersing procedure

The properties of the deposited film is greatly influenced by the way how to disperse the NPs. The figures 5.2 and 5.1 show profilometer measurements and photographs of NP thin films on Si and glass, respectively. (Glass substrates are used to visualize the difference better.) For all

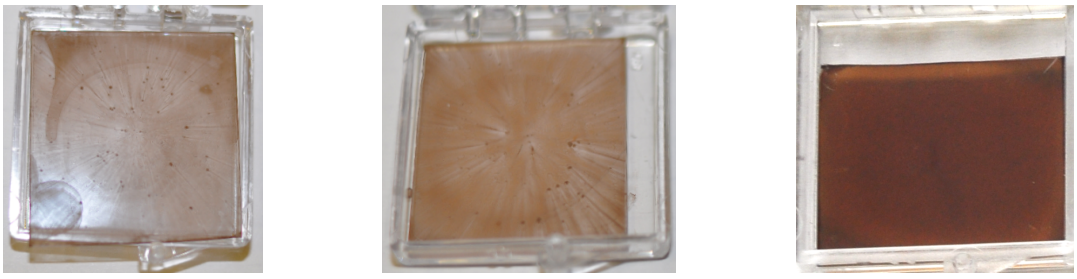

(a) Shaked (b) Ultrasonificated (c) Milled & filtered

Figure 5.1: Photographs of samples coated with NP dispersions of different dispersing procedures

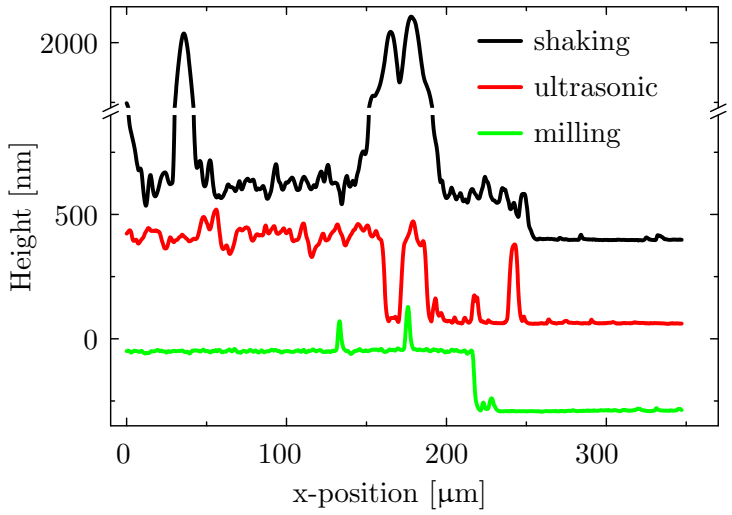

Figure 5.2: Profiles of spin coated NP films from dispersions created by simply shaking (black), by a high intense ultra sonic treatment (red) and by milling

samples, 2 000r/min and 1 088r/(min · s) are used as spin coating parameters. Dispersions are created by three different methods: By simply shaking the mixture with the hand (fig. 5.1a and black data of fig. 5.2), by a 3×10min high intensive ultra sonic treatment (fig. 5.1b and red data of fig. 5.2) and by milling for 2×60min using the Retsch MM 400 mill (fig. 5.1b and green data of fig. 5.1c). In order to determine the film thickness it is removed partly by scratching as can be seen on the right side in fig. 5.2.

The very unspecific procedure of shaking the mixture, results in an inhomogeneous thin film with a great amount of agglomerates, which can already be obtained in the photograph of fig. 5.1a. In profilometer scans, these agglomerates spike the average thickness of ≈ 200nm by up to 2.4µm. The average roughness in between the spiking agglomerates for this sample is $\chi_a \approx 25$nm.

Although the big agglomerates are reduced significantly for the sample prepared by the ultrasonificated dispersion, as can be obtained in fig. 5.1b, still an average roughness of $\chi_a \approx 26$nm is measured for this film, exhibiting an average thickness of ≈ 350nm.

The film created from the milled dispersion shows the smallest average roughness of $\chi_a \approx 3$nm at a film thickness of ≈ 240nm. The photographs in fig. 5.1c substantiate these results. In order to further reduce residual "comet tails", in the following experiments, the dispersions are filtered using a 0.7µm glass fiber filter assuring a good quality of the thin film.

5.1.2 Variation of spin coating parameters

In figure 5.3a the dependency of the layer thickness on the angular spin coating speed is shown for three samples, varying in the NP concentration of the dispersion from 10wt.% to 3wt.% and in the NP type. The acceleration is always set such, that after 1s the final angular speed is reached. According to the graph, the mean layer thickness decreases exponentially with the speed - independent of the NP concentration and type. It is the result of an increased centrifugal force and evaporation for increasing angular speeds. [Schubert2003] Thus, the layer thickness can be tuned very well towards thin layers. However, from the data it cannot be obtained that a high rotation speed reduces boundary effects at the edges and in the corners of the substrates

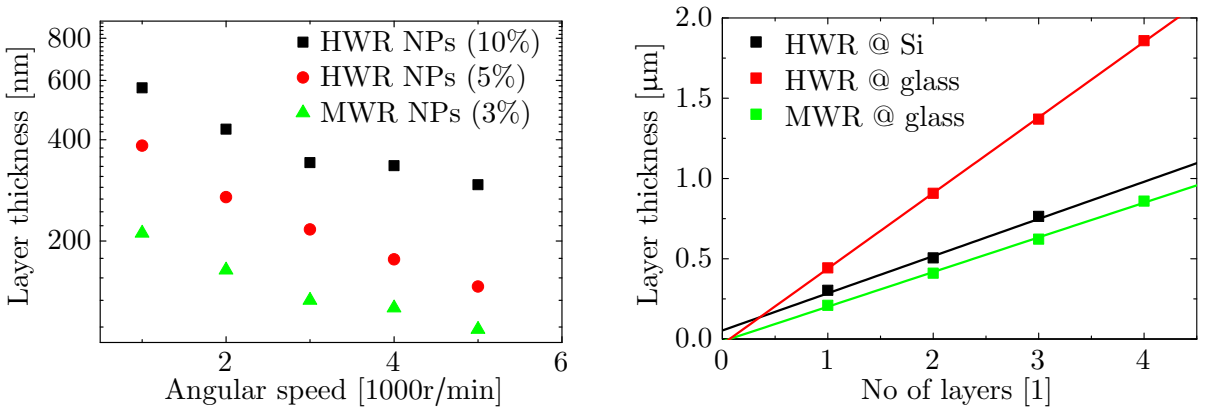

(a) Varied coating parameters (b) Repeated coatings

Figure 5.3: Thicknesses of spin coated NP layers varying the maximum angular speed (left) and the number of coatings (right), as well as NP concentration and type (see legends)

significantly. This, however, makes higher speeds favourable.

As already found in the fig. 5.3a an alternative to create thinner layers can be the reduction of the NP concentration. But, if the HWR NP concentration in the dispersion is reduced below ~ 5%, instead of a closed layer aggregates of particles are observed, as displayed in fig. 5.4 showing 3D profilometer scans of films from dispersions of 10wt.%, 1wt.% and 0.1wt.% HWR NPs in ethanol. The formation of aggregates is attributed to the surface tension of the ethanol and to drying effects, such as the coffee ring effect. [Deegan1997] The minimum NP concentration to create a closed film is expected in between 1% and 5%.

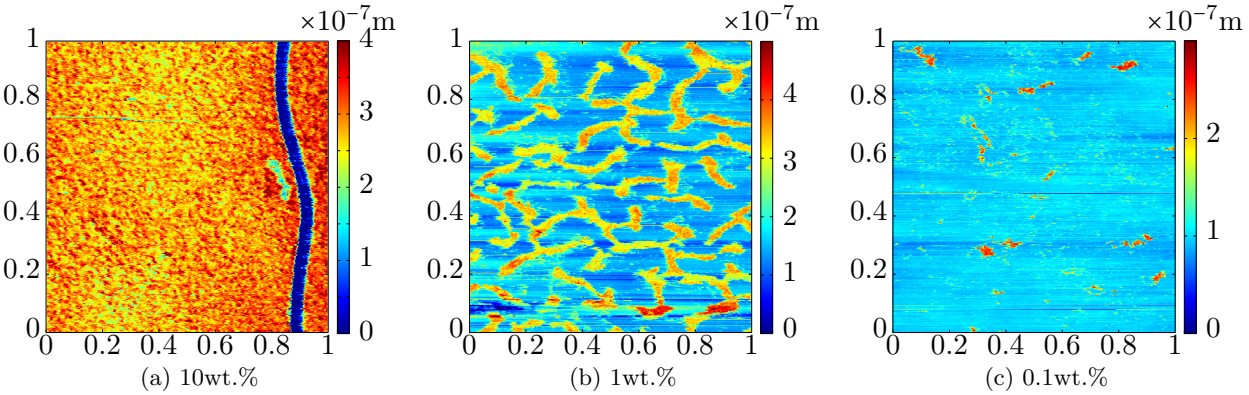

(a) 10wt.% (b) 1wt.% (c) 0.1wt.%

Figure 5.4: Profiles of films coated from dispersions of varying NP concentrations in ethanol; the blue line in the left figure is an intentional scratch - all surface areas are $1 \times 1\text{mm}^2$

Fig. 5.3b presents thickness measurements of multiple, repeatedly coatings. A linear dependence of the thickness on the number of coatings is found. Accordingly, the layer thickness can also be tuned sensitively towards thicker films.

If not stated otherwise, for the experiments presented in the following, the spin coating parameters are set to 2 000r/min and 2 000r/(min · s). This results in NP layers of ≈ 400nm thickness for typical 10wt.% HWR dispersions.

5.2 Infrared laser annealing of Si NP thin films on c-Si

For IR laser annealing experiments $1 \times 1\text{cm}^2$ and $1.5 \times 1.5\text{cm}^2$ nominally undoped ("intrinsic" $\sim 0.01\Omega^{-1}\text{cm}^{-1}$) Si substrates of 525µm thickness and one polished surface are used. The Si substrates are cleaned according the standard cleaning process followed by the standard hexafluorosilicic acid oxide removal step (see ch. 3.2.4). Subsequently boron doped HWR NPs are spin coated from a 10wt.% dispersion using the standard parameters on the polished surface.

The subsequent annealing process is performed using an IR laser with a maximum laser intensity (MLI) of 452W - c.f. ch. 4.1.1 - and consists of two steps: From preliminary experiments it is found that a pre-annealing step helps to reduce stress in the substrates and therefore decreases cracking or breaking. This step consists of 30 scans at 70% of MLI and scanning velocities of 10m/min, c.f. table 5.1 and is kept constant throughout the whole work. For the immediately following, main annealing step the intensity as well as the scanning speed are reduced to 40% of MLI and 300mm/min, respectively. Using these standard parameters the sample is scanned six times. In contrast to the pre-annealing scans, here the scanning direction is reversed after each scan (bidirectional).

Table 5.1: Standard parameters for IR laser annealing

Process	Pre-annealing	Main annealing
Used percentaged laser power	70	40
Scanning velocity / mm/min	10 000	300
Number of contiguous scans	30	6
Direction of scans	Unidirectional	Bidirectional

During the whole annealing procedure the chamber is flushed with an inert gas, usually argon (Ar) is used. The gas flow ($\geq$ 20l/min) is started 10s before the first laser irradiation to ensure, that residual gas contaminations are removed from the chamber's volume of $\approx$ 0.5L.

5.2.1 Structural investigations

Laser annealed samples are characterized structurally using photography, scanning electron microscopy (SEM), x-ray diffraction (XRD), transmission electron microscopy (TEM) and by an anisotropic etching experiment. These measurements are discussed in the following subsections.

Photography

Fig. 5.5 shows photographs of samples that are prepared according to the standard parameters, except that the main annealing laser intensity is varied according to the subscripted values. For all photographs, the scan direction is horizontally oriented. The first sample on the left shows an as deposited sample. (The scratch is made for profilometry measurements.)

The photographs indicate a clear relation between laser intensity and change of the surface: For low intensities a change in the colour from dark-brown (0% of MLI) to light-brown (25% of MLI) and to highly reflective silver (30% of MLI) is found. Although the colour does not change further for samples $\geq$ 35% of MLI, the morphology of the surface does: from a flat to an inhomogeneously waved surface. It is suggested that the laser intensity is high enough to melt a surface near layer and that the melting depth varies according to the laser intensity.

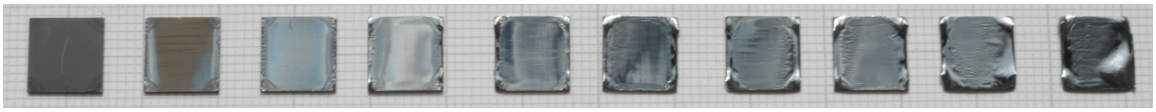

Figure 5.5: Photographs of annealed samples: the values indicate the main scan's laser intensity

Fig. 5.6 shows the photograph of a sample, that is annealed by scanning only once from the left to the right with a laser intensity of 50% of MLI. A significant change along the scan direction can be observed: While the right edge has been liquefied, the edge on the left seems to be rather unchanged. Furthermore, esp. near the right border a difference in the morphology and the surface colour is found. It seems as if the temperature is higher at the end of the laser scan.

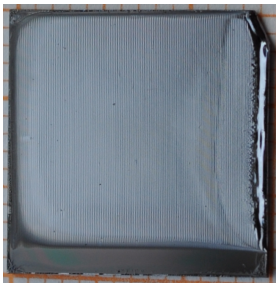

Figure 5.6: Photo of 1× scanned sample

This can be explained as follows: Before the scan the sample is expected to exhibit a homogeneous temperature distribution. Due to the laser irradiation the temperature increases primarily at the illuminated area. However, due to the high thermal conductivity of Si heat also diffuses in the rest of the sample. [Hull1999, ch. 4.5] Consequently, the average sample temperature at the beginning of each scan is lower, than at the end. Additionally, when the laser beam reaches the end of the sample, the heat diffusion gets constrained by the sample's edge, leading to a further temperature increase in that region.

For all of the annealed samples inhomogeneities at the left and the right border can be observed. Besides, the change at 25% of MLI is mainly observed in the colour and only for higher intensities deformations of the borders become visible. (The presence at both sides is a result of the bidirectional scan.)

Scanning electron microscopy

The photographs indicate, that a melting of the NPs occurs at laser intensities ≥ 30% of MLI. To clarify this, the melting process is investigated by SEM images of a sample annealed at 43% of MLI. Fig. 5.7 shows cross sectional SEM images taken from different positions along the top hat's direction: While the top most image results from a position of maximum laser intensity, the intensity is reduced to the bottom showing an as deposited Si NP thin film.

From the images it is found that by increasing the laser intensity, first NPs start to coalesce, forming bigger particles, then these wet the surface, leading to a significant densification of the highly porous NP film. At even higher intensities, the border between annealed NPs and the substrate vanishes. The formation of a closed, flat surface due to the NP melting is in line with the discussion according the photographs. Due to the morphology changes in fig. 5.5 a fusion of both materials due to melting of the NPs (and a surface near substrate layer) is supposed.

In fig. 5.8 top view SEM images of increasing magnification of a sample processed at standard parameters, are shown. The surface seems to be flat. However, white structures that are partly in contact with each other are found over the whole investigated area. These structures are not observed in the cross sectional images and their origin is not absolutely clear so far. It is suggested, that these structures are oxygen enriched areas, due to the higher brightness as a

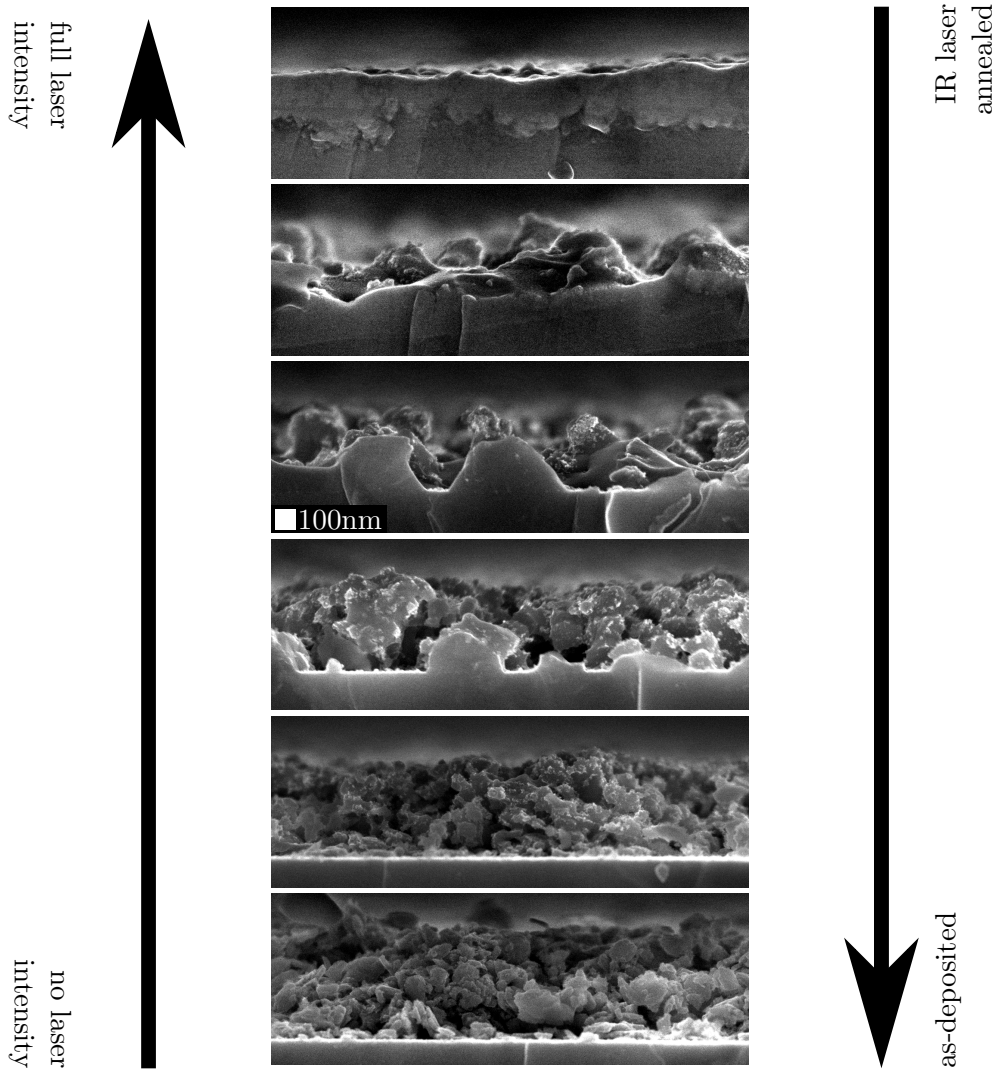

Figure 5.7: Cross sectional SEM images of IR laser annealed HWR NPs near the laser's top hat profile edge:
Top: at a position of full laser intensity;
Going down in the picture line: laser intensity is reduced;
Bottom: unannealed position (the scale bar holds for all images)

result from charging. EDX measurements of these structures do not show a significant difference in the oxygen signal. This may be due to their small volume and the resulting small EDX signal. (In ch. 5.2.2 these structures are discussed further using SIMS.)

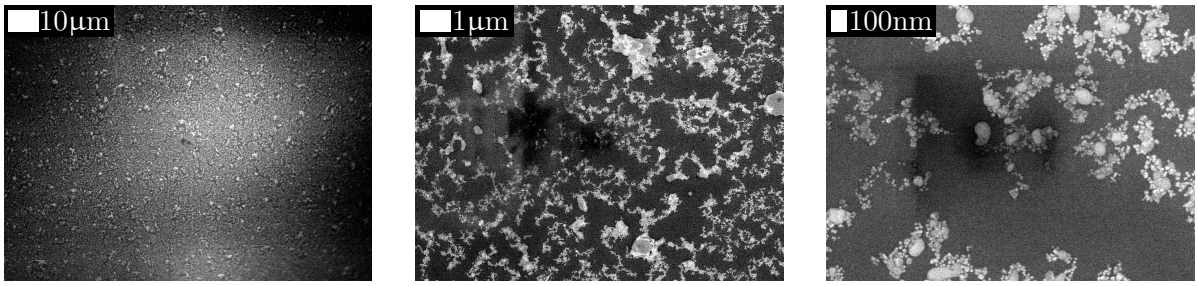

(a) Low magnification (b) Medium magnification (c) High magnification

Figure 5.8: Top view SEM images of an annealed sample; the magnification is increased from left to right (see scalebars)

X-ray diffraction measurements

To investigate the crystallinity of the annealed films XRD measurements are performed in $\Theta-2\Theta$ geometry over a range of $20° \geq 2\Theta \geq 120°$ in steps of $2\Theta = 0.01°$ for an uncoated reference substrate, an as deposited sample and two annealed samples (20% and 40% of MLI). The results are shown in fig. 5.9 as a semi logarithmic plot. The respective data are shifted along the y-axis for a better comparability.

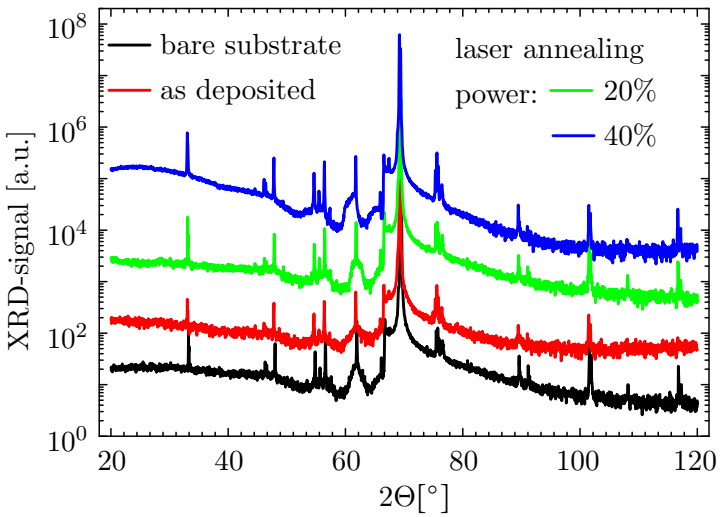

Figure 5.9: XRD measurements of an uncoated reference substrate (black), an as deposited substrate (red) and two laser annealed samples (20% and 40% of MLI - green and blue)

By comparing the diagrams it is found, that similar peaks of the substrate are observed for all samples. For all data the by far most prominent peak[1] at $\approx 69°$. For {100}-oriented Si only

[1]By taking a closer look at this peak, it splits in two peaks which is a result of the used radiation consisting of Cu-k-α_1 and Cu-k-α_2. [Deutsch1982, Maskil1988]

the 400-peak, which is found at 69.13°, is an allowed reflex for the used measurement geometry. [Ashcroft2007, Kittel2005, Birkholz2005, Hull1999, ch. 3.1] The facts that the annealing does not lead to any further peaks and that the 400-peak intensities have not changed significantly for the annealed samples indicate, that the annealed thin film re-solidifies either in the same crystalline orientation as the substrate or as an amorphous film.

Anisotropic etching experiment

Since the XRD measurements are not able to prove that the re-solidified layer is crystalline or amorphous, an intrinsic Si substrate is laser annealed using undoped HWR NPs in order to perform an anisotropic etching, c.f. ch. 4.2.1. For the experiment, annealed samples are immersed into diluted hydrofluoric acid in order to remove the surface oxide layer and subsequently placed in a KOH solution of 70 wt% H_2O, 20 wt% isopropanol and 10 wt% KOH at room temperature for 5min. The etched samples are analyzed using SEM in cross section geometry.

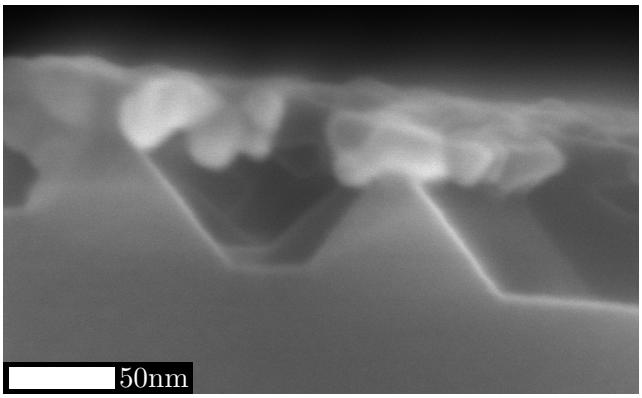

Figure 5.10: Cross sectional SEM image of a KOH etched annealed sample: A pyramidal structure is found in agreement with a crystalline {100}-surface orientation.

One resulting image is presented in fig. 5.10 showing the typical pyramidal structure of a KOH-etched {100}-surface oriented substrate. [Seidel1990] The particles on the pyramids' tops are expected to be residual SiO_X, that is not removed during the HF-etch. The presence of these pyramids is another indicator that the re-solidified layer is crystalline and of the same crystal orientation as the substrate.

Transmission electron microscopy

Since XRD measurements cannot clarify, whether the annealed thin film re-solidifies crystalline or amorphous and since it is further possible that the anisotropic etching removes the whole annealed layer and therefore gives the structure of the substrate, TEM and transmission electron diffraction (TED) measurements are performed for FIB-lamellae from two samples annealed at 30% and 50% of MLI. The faces of both lamellae exhibit a {110}-orientation. The figures 5.11 and 5.12 show the resulting TEM images.

For the sample annealed at lower energy (see fig. 5.11) the NP thin film consists of flake-like structures, which are similar to SEM cross sections of unannealed samples (c.f. fig. 5.7). It is therefore concluded, that the laser power is neither sufficient to completely melt the particles nor the substrate. From the image taken at highest magnification (fig. 5.11c) it is found that

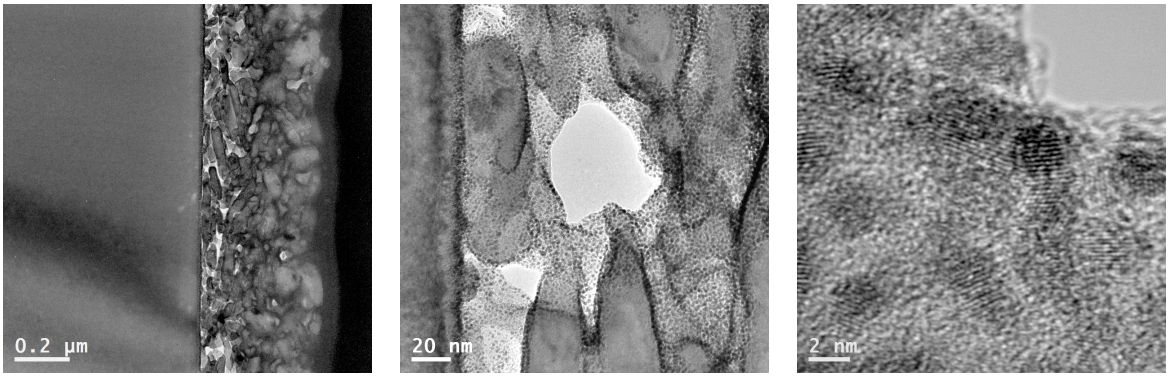

(a) Low magnification (b) Mid magnification (c) High magnification

Figure 5.11: TEM images of a sample, annealed at 30% of MLI; magnification increases from left to right

the typical, comparably big NPs of ~ 100nm consist of primary NPs of ≈ 2nm in diameter that are highly crystalline and statistically oriented. [Wiggers2001, Huelser2011]

Fig. 5.12a presents an HRTEM image of the sample annealed at high laser intensity at an inner part of the FIB lamella. A three-fold symmetry (55° – 70° – 55°, see green lines), which is typical for {110}-oriented diamond crystal structures like c-Si, can be observed all over the image. It is therefore concluded, that the annealed layer is of crystalline structure. (Brightness variations are attributed to the FIB preparation.) In fig. 5.12b an HRTEM cross section image

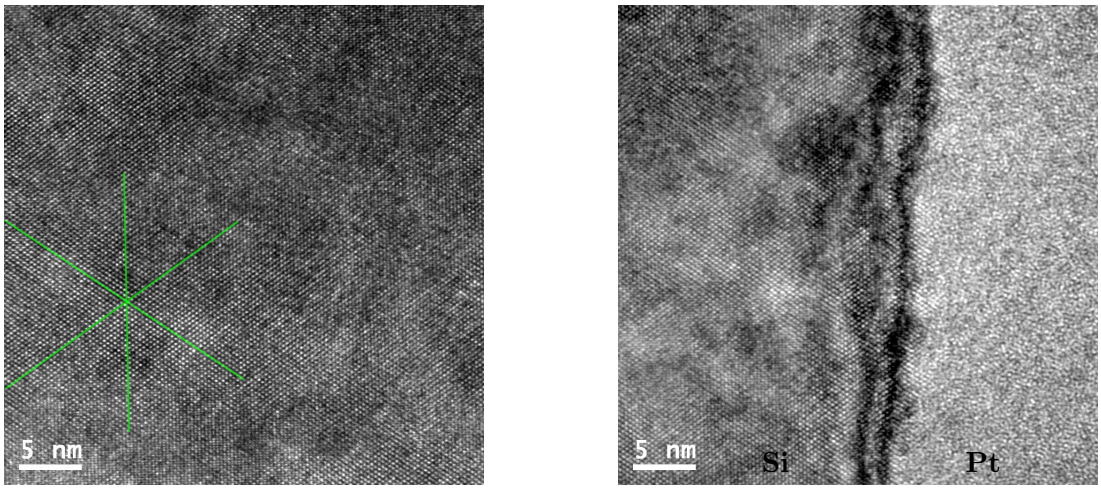

(a) Inner part of sample (b) Outer part of sample

Figure 5.12: HRTEM images of a sample processed at 50% of MLI at centered position of the FIB sample (left) and at sample's surface (right); amorphous Pt-layer results from FIB preparation

of the sample's surface is shown: Immediately below the Pt layer from the FIB preparation, the three-fold structure can be observed, substantiating that the re-solidified layer shows the high crystallinity throughout the whole volume. However, a change in the brightness is observed along the surface. The origin of this surface near, only a few nano meters thick layer is not clear so far. On the one hand it may be attributed to impurities which accumulate near the surface

due to a self-cleaning process during re-crystallization (discussed in more detail in ch. 5.2.2). On the other hand, a similar - though flatter structure is also observed for the sample annealed at less intensity, c.f. left border of fig. 5.11b. It may therefore be concluded, that this may be a typical surface effect, perhaps resulting from misalignment of the surface atoms or from the formation of oxides.

Figures 5.13a and 5.13b show the TED patterns corresponding to the fig.s 5.11c and 5.12a, respectively. For the sample annealed at low intensity, several spots can be observed that are aligned on diffraction rings. As this is typical for disordered or multi crystalline materials, this observation is in line with the observed ≈ 2nm primary particles. In contrast the TED image for the sample annealed at high intensity shows the diffraction pattern of a perfect {110}-oriented Si crystal, in agreement with the orientation of the lamella's plane. [Fuchs1990] As this diffraction pattern is observed throughout the whole sample it proves that the annealed thin film re-solidifies crystalline in the substrate's orientation.

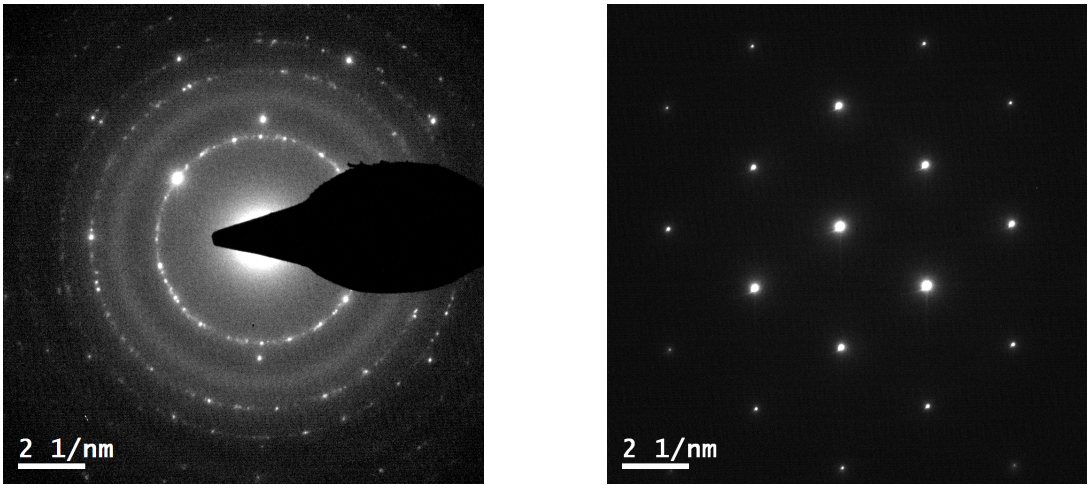

(a) 30% sample - multi crystalline (b) 50% sample - single crystalline

Figure 5.13: TED images of the 50% sample (right) and the thin film from the 30% sample (left)

Profilometry

The surface morphologies of annealed samples (15mm edge length) are characterized by 11mm long profilometer line scans in parallel with (x-direction) and perpendicular to (y-direction) the scan direction. Four samples are prepared using the standard parameters but varying the numbers of laser scans (see fig.s 5.14a and 5.16a).

Y-direction From fig. 5.14a a rather random bending of up to ≈ 5µm in y-direction is observed for the samples. However, it seems not to correlate with the numbers of scans. The reason for the bending may be measurements inaccuracies due to the relatively long scan distance on the one hand. On the other hand, it may be due to the heating procedure: As discussed using photography, the maximum temperature created by the laser depends on the position, which can lead to deformations during re-solidification due to stress / strain.

The upper graph of fig. 5.14a focuses on a length of 0.7mm of the lower graph. A superimposed ripple structure is found for all samples. While the amplitude changes up to 1.9µm, the

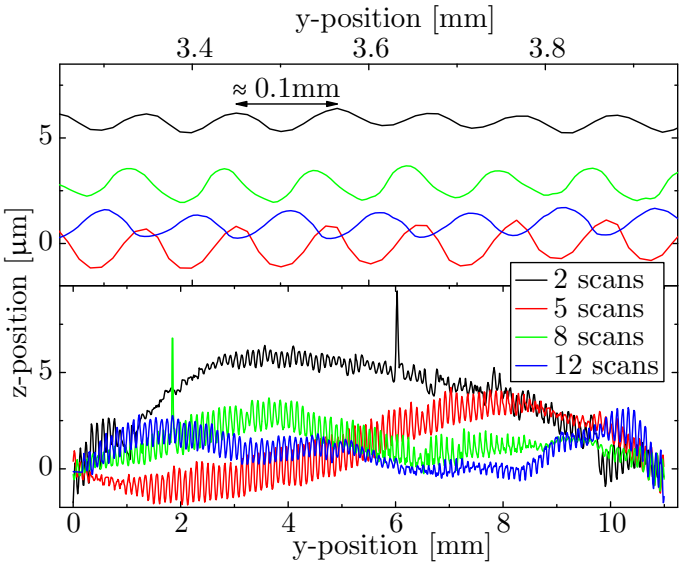

(a) Profilometer measurement in y-direction

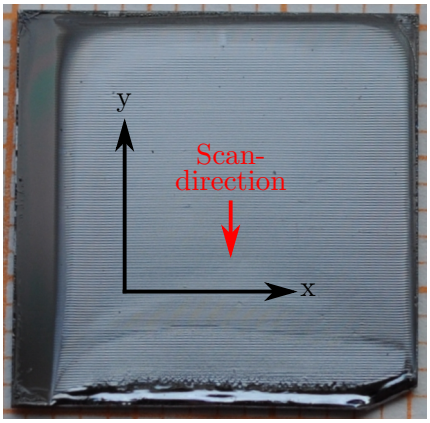

(b) Photograph of an annealed sample

Figure 5.14: Left: profilometer measurement of annealed samples: bending in y-direction
Right: photograph of an annealed sample (scanned only once, direction as indicated)

period is found to be ≈ 0.1mm and almost constant. Actually, this structure can be observed already with the bare eye, as the photograph in fig. 5.14b of a sample scanned by only one scan (starting from the top of the picture) demonstrates. A possible explanation for the build-up of these ripples is based on the following three assumptions:

1. Since the ripples are aligned along the scan direction it is expected, that the laser's positioning system shows a discontinuous movement, leading to variations in the melt depth.

2. Due to the crystallinity investigations presented before, it is assumed that crystallization takes place only at the interface between liquid and crystalline phase.

3. Further it is assumed that crystallization takes place only in {100}-direction[2].

Figure 5.15 schematically displays the assumed re-growing process: The yellow and blue areas symbolize the molten and crystallized material, respectively. The variation in melting depth is symbolized by a zigzag structure. During cool down, the crystal grows from the substrate in {100} direction. When the liquid-solid interface approaches the substrate's surface, the surface tension of the liquid Si results in the formation of a closed film of liquid Si on top of the crystallizing material. Consequently, the periodic melting depth is transcribed to the re-solidified surface.

X-direction In fig. 5.16a the profilometer scans in x-direction are presented. Obviously, the bending increases with the number of scans. To quantify this, a coefficient of bending B is calculated according to the formula:

$$B = \frac{\max(|z|)}{11\text{mm}} = \frac{h}{11\text{mm}} \tag{5.1}$$

[2]Since growth velocities of different orientations depend on the undercooling (not measured) it is hard to prove this assumption. [Cullis1984, Collins1977, Nagashio2005, Fujiwara2002, Izumi1997, Yang2012]

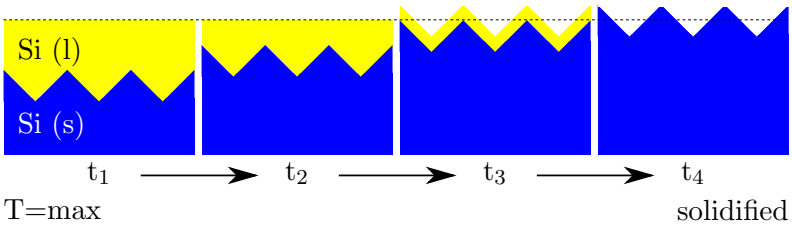

Figure 5.15: Scheme of the recrystallization process (t_i = time; T = temperature)

where $\max(|z|) = h$ is the maximum absolute value in profilometer measurement and the denominator represents the scan length. Plotting B versus the number of scans results in a linear

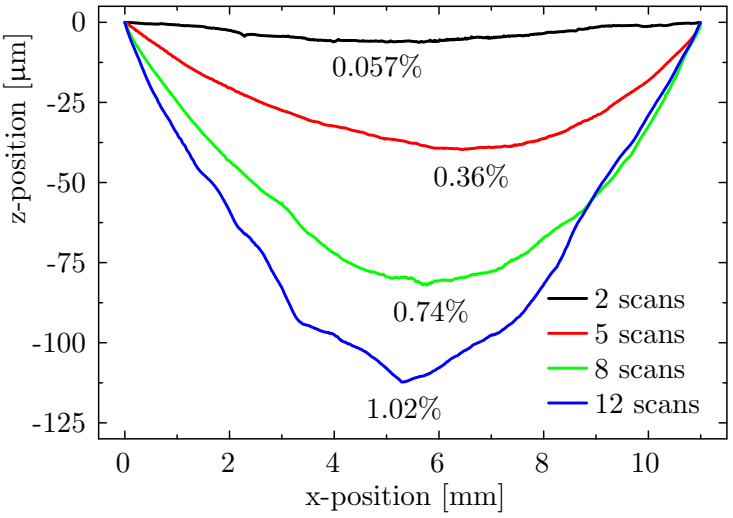

(a) Profilometer scan of IR annealed sample in x-direction

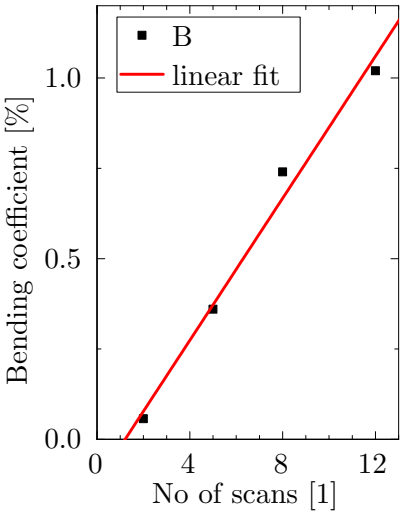

(b) Bending coefficient

Figure 5.16: Profilometer measurement of IR annealed sample along the x-direction

function (see fig. 5.16b). The data are fitted using a linear function with a slope of $\approx 0.1\%$/scan. According to the fit no wafer bending in x-direction is observed for one scan, which may be interesting for commercial applications. However, further investigations are performed at two or more scans, because of the improved sample homogeneity, as discussed e.g. for the photographs.

It is suggested that stress / strain occur during cool-down and create this bending. A possible explanation is given in the following: The scheme in fig. 5.17a shows a hot but already completely crystallized sample. While the lattice constant on bottom is that of room temperature, it is slightly increased on top in the hot region. After cool-down the lattice constants tend to reach the same length, c.f. fig. 5.17b. As the sides are unannealed, the re-solidifying volume is constricted in that dimension. To calculate the length difference Δl, a thermal expansion coefficient of $\alpha \sim 3 \cdot 10^{-6}\mathrm{K}^{-1}$ for Si at 300K, a temperature difference of $\Delta T = 1000°\mathrm{C}$ between hot (near the melting temperature of Si) and chilled material (almost room temperature) and a length of $l = 11\mathrm{mm}$ are assumed. [Gerthsen1963, Hull1999, ch. 4.2] This results in:

$$\Delta l = l \cdot \Delta T \cdot \alpha = 33\mu\mathrm{m} \tag{5.2}$$

To judge this value, h is calculated from this data: Therefore, the bent sample is approxi-

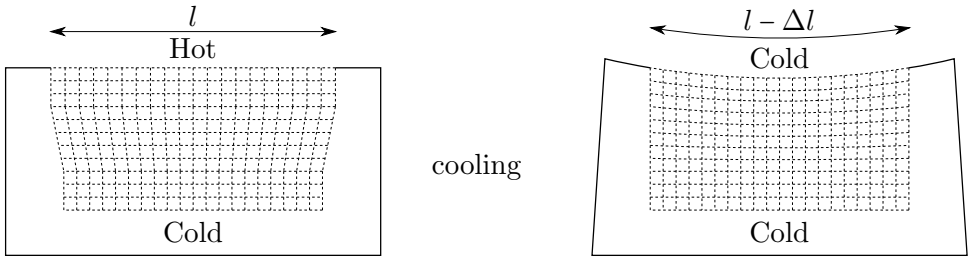

(a) Hot (b) Chilled

Figure 5.17: Schemes for the explanation of the bending along the y-axis

mated by a segment of a circle (see fig. 5.18). According to geometrical similarity considerations and the radian relation, the following equations are found:

$$\frac{l}{d+r} = \frac{l-\Delta l}{r} = \Phi \tag{5.3}$$

$$\Rightarrow r = \frac{\frac{d}{l}}{\frac{1}{l-\Delta l} - \frac{1}{l}} = \frac{d}{\frac{l}{l-\Delta l} - 1} \tag{5.4}$$

According to fig. 5.18 the following equation is found:

$$\zeta = r \cdot \cos\left(\frac{\Phi}{2}\right) \tag{5.5}$$

With this, an equation for h is derived:

$$\begin{aligned} h &= r - \zeta \\ &\overset{(5.5)}{=} r\left[1 - \cos\left(\frac{\Phi}{2}\right)\right] \\ &\overset{(5.3)}{=} r\left[1 - \cos\left(\frac{l-\Delta l}{2 \cdot r}\right)\right] \\ &\overset{(5.4)}{=} \frac{d}{\frac{l}{l-\Delta l} - 1} \cdot \left[1 - \cos\left\{\frac{\Delta l}{2 \cdot d}\right\}\right] \end{aligned} \tag{5.6}$$

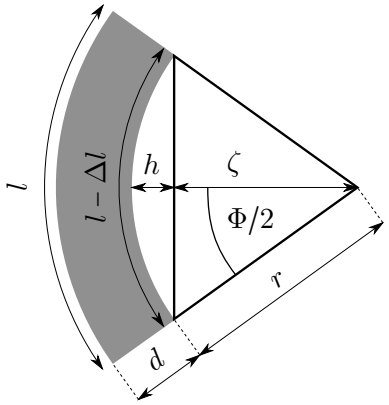

Figure 5.18: Scheme for calculation; the bent sample is coloured gray

Inserting the found values, a z-difference of $h = 86\mu m$ is calculated. Such big values are only reached for at least eight scans. The primary reason for the discrepancy may be a wrong temperature difference on the one hand: Considering the linear fit in fig. 5.16b, each scan results in an additional bending of $\approx 11\mu m$. Using the above calculations, a temperature of $T \approx 115°C$ must be present to realize this bending. On the other hand, an additional restoring force must be present during the annealing because of areas that are still solid while other areas do recrystallize.

Although this approach leads to rather good results, it has the drawback that it contradicts perfect single crystallinity as reasoned e.g. from fig. 5.12b. While fig. 5.17 sketched the lattices in the middle of the sample, those at the edges are not shown. By continuing the presented approach towards the edges, there have to be dislocations in the sample, esp. in the regions that have only been heated but have not been not melted. The contradiction may be a result of the melting depth: while the HR-TEM and TED investigations scanned an area of 100nm depth,

this high dislocation density region may be even deeper. That this melting depth is much bigger than a few 100nm is presented in the following section, presenting the results of an elemental analysis of such samples.

5.2.2 Elemental analysis

Time of flight secondary ion mass spectroscopy (TOF-SIMS, see ch. 4.2.2) is used to investigate the chemical structure of samples before and after IR laser annealing using the standard parameters. These investigations address the question, whether and how deep boron gets incorporated from the NPs into the Si substrate.

Boron distribution

In fig. 5.19 the surface-integrated signal for Si (red) and B (black) of an as deposited (filled symbols) and an annealed (open symbols) sample are presented. The Si signal does not change due to the annealing, which is plausible, as even the NPs mainly compose of Si. In contrast, the B distribution gets drastically changed: Before annealing an ≈ 500nm thick layer with a more or less constant intensity is found, followed by an abrupt drop in intensity down to the resolution limit. Using a relative sensitivity factor determined for B in a Si matrix, the former value is ascribed to B concentrations of $\sim 4 \cdot 10^{20}\mathrm{cm}^{-3}$. These results are in reasonable good agreement with the thickness of the coated film and the doping concentration of the NPs ($\sim 10^{21}\mathrm{cm}^{-3}$). The discrepancy in the film thickness to the one obtained by profilometry (400nm), as well as the increase of the measured SIMS intensity of the NP thin film towards the substrate are ascribed to measurement inaccuracies due to the porous structure of the NP film. After annealing, the B concentration exhibits a rapid drop within the topmost ≈ 1µm down to a concentration of $\sim 2 \cdot 10^{18}\mathrm{cm}^{-3}$ and decreases only slightly throughout the whole measurement range. These measurements show, that B is successfully incorporated in the c-Si substrate.

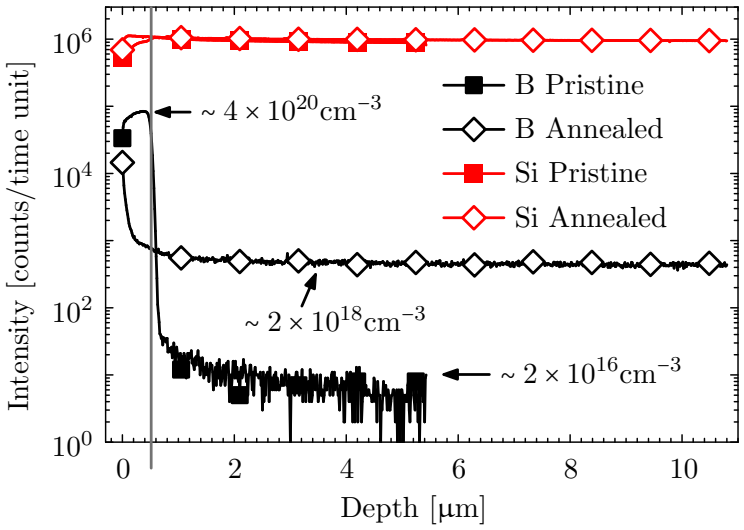

Figure 5.19: TOF-SIMS data: boron (black) and silicon (red), before (squares) and after (diamonds) laser annealing - the presented boron concentrations are estimated using a sensitivity factor

Due to the rather constant doping concentration solid state diffusion of B can be excluded:

Its diffusivity in c-Si at 1200°C is found to be $D_s = 1 \cdot 10^{-12}\mathrm{cm}^2\mathrm{s}^{-1}$. [Fair1975] Thus, for typical processing times of $\lessapprox$ 1min for each sample, a comparable dopant distribution would be impossible. Instead it is concluded that the NPs as well as a surface near layer melt during the laser processing, which is in agreement with the structural results from ch. 5.2.1. Due to the about eight orders of magnitude higher diffusion coefficient of B in liquid Si ($D_l = 2.4 \cdot 10^{-4}\mathrm{cm}^2\mathrm{s}^{-1}$) a homogeneous intermixing is much more reasonable. [Kodera1963] Additionally it is proposed, that convection inside the melt, driven by the temperature difference between liquid and solid Si, may contribute to the homogenizing of the B distribution. [Allmen1995, ch. 4.3.3]

The increase in B concentration towards the surface is expected to be a result of the high propensity of "self-refining" of Si: Regrowing materials like Si have the tendency to segregate impurities from the crystal boundary. [Allmen1995, ch. 4.2.2] The liquid Si in the melt is therefore expected to preferably solidify crystalline at the solid Si boundary, whereas B concentrates in the liquid and an increase towards the surface is obtained.

Estimation of the doping depth by SIMS measurements

By assuming that the total amount of B dopants remains the same before and after laser annealing, an upper limit of the doping depth can be derived. The SIMS profile of B is therefore approximated by a box function:

$$c_{init} \cdot d_{init} = const = c_{final} \cdot d_{final} \tag{5.7}$$

Here c and d represent the concentration and the depth and the subscripts $init$ and $final$ symbolize the as deposited and the annealed thin film, respectively. For the determined values a doping depth of $d_{final} = 100\mu\mathrm{m}$ is calculated.

This value seems very big, at least if PV applications are addressed. It therefore has to be mentioned that the doping concentration determined using the SIMS signal in combination with the relative sensitivity factor may be inaccurate by a factor of two or higher. In consequence a similar uncertainty in d_{final} is expected.

Oxygen distribution

SIMS is furthermore applied to investigate the distribution of oxygen (O) and O containing species in the sample. Due to the absence of a calibration standard or a sensitivity factor, the measured intensities cannot be converted into absolute concentrations. However, comparing the relative intensities is reasonable, since the measurements are performed under equal conditions. Figure 5.20 illustrates the results for a pristine (filled symbols) and an annealed (open symbols) sample, comparing the intensities of SiO_2 (black triangles) and O (blue circles) as representatives for O containing species as well as Si (red squares). The pristine sample is measured only down to a depth of 100nm, because only the thin film contributes to this data, whereas the c-Si is expected not to exhibit a significant amount of O. In contrast the annealed sample is measured down to a depth of 220nm, where the resolution limit determines the measurement data. Again, the Si intensity changes only slightly due to the annealing. Contrarily the profiles of SiO_2 and O show significant modifications: While a rather homogeneous distribution is found for both O species for the as deposited thin film, an almost exponential decrease is observed for the annealed sample within the analyzed depth.

By comparing the integrated SIMS signals (for the top most 100nm) before and after annealing, it is found that O containing species are reduced by a factor of 2 to 6. This can be

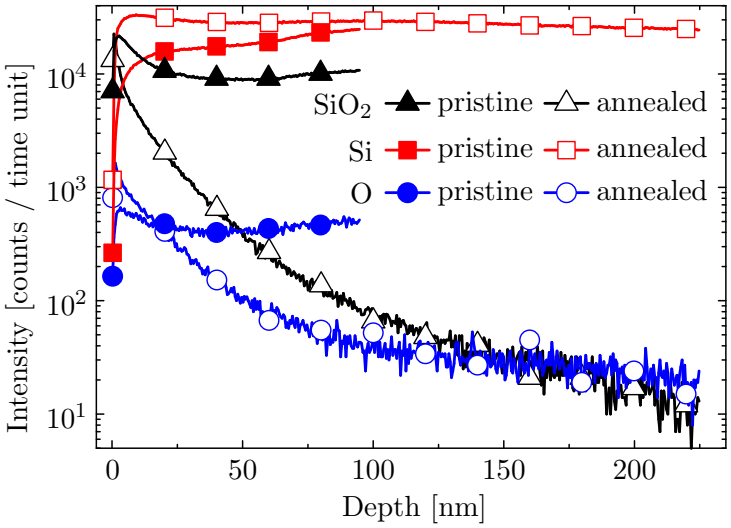

Figure 5.20: SIMS signal of SiO_2 (triangles), Si (squares) and oxygen (circles) as a function of the sputtering depth before (filled symbols) and after (open symbols) laser annealing

explained on the one hand by the formation of volatile compounds such as N_XO_y, SiO_X(g) or O_X during the processing or by the incorporation of O into the substrate. On the other hand this decay supports the "self-refining" hypothesis of the re-crystallizing Si as discussed for B.

However, the process does not create a homogeneous O distribution on the surface, as can be obtained from the image in fig. 5.21, displaying the oxide map of the first, analyzed layer (red points indicate O). Comparing this image with top view SEM images of an annealed sample (c.f. fig. 5.8) shows certain similarities, supporting the conclusion that the white regions in the SEM micrographs are O enriched areas.

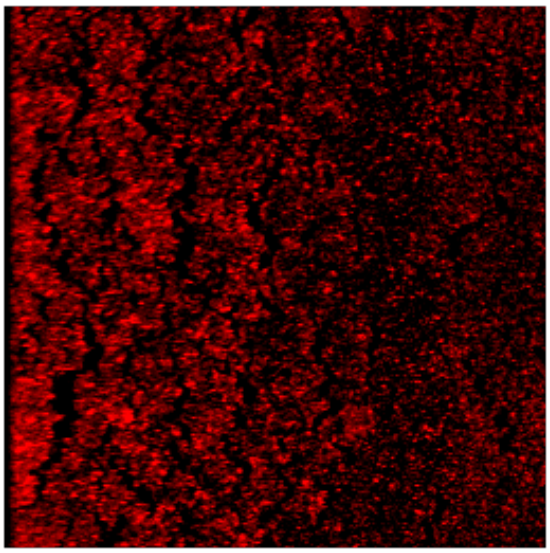

Figure 5.21: Surface O distribution determined by SIMS: Red indicates the presence of O

5.2.3 Electrical characterization

While SIMS measurements show, that B is incorporated by the annealing, in this section electrical conductance measurements of NP laser annealed, (formerly) intrinsic substrates are discussed in order to clarify, whether the incorporated B is electrically activated. For the characterization, 200nm thick Al contacts are deposited (c.f. ch. 4.1.3) on top of the re-solidified layer in four point geometry (see fig. 4.6a and related discussion). If conductivities are calculated, the difference factor of ≈ 3 (as discussed in ch. 4.2.3) is considered.

Feasibility of electrical doping by NP laser annealing

The conductances of a bare substrate (Si), an as deposited sample (Si+NPs) and samples annealed in argon (Ar) and nitrogen (N_2) are presented in fig. 5.22. The atmosphere is varied to check whether N gets incorporated and therefore leads to a compensation of B dopants. The bare substrate's conductance is measured to be $0.089\Omega^{-1}$. By coating the substrate with NPs, the conductance decreases by almost one order down to $0.014\Omega^{-1}$. Due to the high amount of insulating oxide interfaces in the thin film, the current preferably flows through the substrate and only a small fraction through the NP thin film, thus reducing the measured conductance significantly. [Stegner2008]

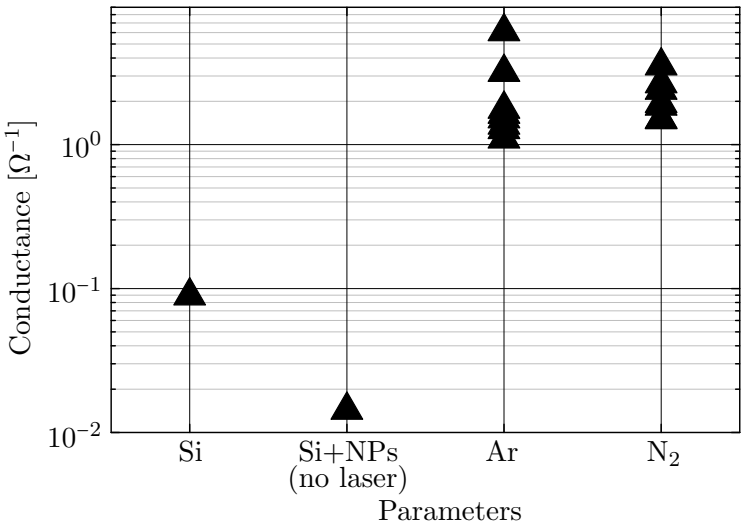

Figure 5.22: Conductance measurements for a bare substrate, an as deposited sample and IR laser annealed samples, created in argon (Ar) and nitrogen (N_2)

The processed samples show an increase of the conductance up to a mean value of $2.2\Omega^{-1}$. Consequently, at least a part of the incorporated dopants are electrically activated. However, the results from samples annealed in Ar and in N_2 do not show a significant difference. Consequently, if N is incorporated in the annealed material, the amount is much smaller than the B concentration.

Variation of laser intensity

The influence of the laser intensity of the main laser scan is investigated by changing it from 25% up to 50% of MLI. Square-cut, intrinsic samples are used. The resulting conductances for 15mm

and 10mm edge length samples processed in N and for 10mm edge length samples processed in Ar are presented in fig. 5.23.

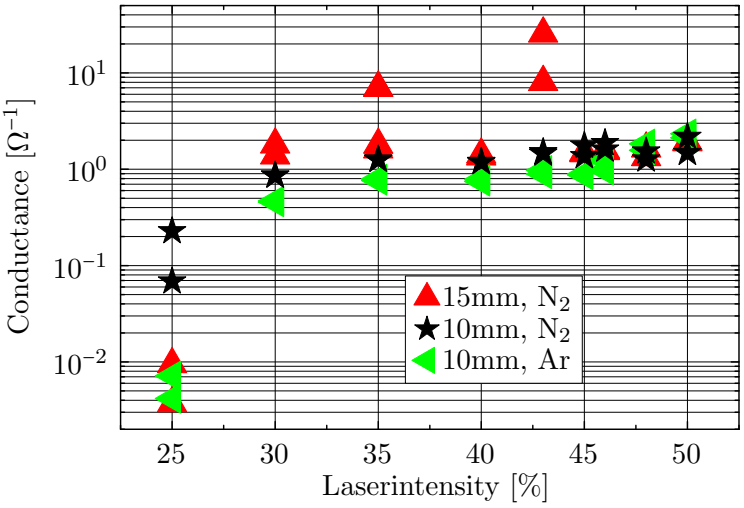

Figure 5.23: Conductance measurements of annealed samples varying the laser intensity

In general, for all samples and independent of the ambient atmosphere, a similar trend is observed: While the laser intensity seems not to be high enough at 25% to increase the sample's conductance, it jumps up to $\sim 1\Omega^{-1}$, if a laser intensity of $\geq 30\%$ is used. This value increases only slightly, for higher laser intensities.

For the high doping concentrations (see SIMS measurements) the observed increase in conductance for higher laser intensities can be a result from a deeper melting depth: A deeper melting results in a reduced doping concentration and thus to an increased mobility and conductivity. [Jacoboni1977, Caughey1967]

Estimation of the doping depth by conductance measurements

Taking into account the limitations discussed in ch. 4.2.3, conductivities of the samples are derived. Since the doping depth is unclear, by using the whole substrate thickness h_{wafer} = 525µm an effective (minimal) conductivity is assumed. Applying this method on the derived values gives $0.066\Omega^{-1}\text{cm}^{-1}$ for the Si-substrate and $4.5\Omega^{-1}\text{cm}^{-1}$ for the highest conductivity. The latter value corresponds to an effective doping concentration of $N_{eff} \approx 1 \cdot 10^{17}\text{cm}^{-3}$ and therefore differs by almost one order of magnitude to SIMS measurements, which is mainly attributed to the unknown doping depth used for calculation. [Bulucea1993] Further explanations for the difference are not electrically activated dopants or the inaccuracies of the SIMS measurements.

In order to estimate a limit of the diffusion depth the conductance measurements are interpreted as a result of a two-layer system. While one of them represents the doped layer of unknown thickness d_B and conductivity σ_B, the second layer represents the unmodified, intrinsic substrate of $d_{intr} = d_{subs} - d_B = 525\mu\text{m} - d_B$ thickness and with a conductivity of $\sigma_{intr} = 0.066\Omega^{-1}\text{cm}^{-1}$. Since the effective conductivity σ_{eff} contains both contributions it can be derived:

$$d_{subs} \cdot \sigma_{eff} = d_B \cdot \sigma_B + d_{intr} \cdot \sigma_{intr} \tag{5.8}$$

$$\Rightarrow \quad d_B = d_{subs} \frac{\sigma_{eff} - \sigma_{intr}}{\sigma_B - \sigma_{intr}} = 15.9\mu\text{m} \cdot \left(\frac{\sigma_{eff}}{\Omega^{-1}\text{cm}^{-1}} - 0.066 \right) \tag{5.9}$$

Here the doping concentration from SIMS measurements is used to estimate the conductivity of the doped region, i.e. $\sigma_B \approx 33\Omega^{-1}\text{cm}^{-1}$. [Bulucea1993]

For the samples processed at standard conditions (see fig. 5.22) effective conductivities are in between $\sigma_{eff,lo} = 0.58\Omega^{-1}\text{cm}^{-1}$ and $\sigma_{eff,hi} = 4.7\Omega^{-1}\text{cm}^{-1}$ with a mean value of $\sigma_{eff,mean} = 1.47\Omega^{-1}\text{cm}^{-1}$. This results in doping depths of $d_{B,lo} = 8.9\mu\text{m}$, $d_{B,hi} = 74\mu\text{m}$ and $d_{B,mean} = 23.1\mu\text{m}$, respectively. While $d_{B,lo}$ contradicts the SIMS measurements the others are in a possible range. Nevertheless, the values are much smaller than those obtained from SIMS measurements. The presumably major reason for it are the inaccuracies of the SIMS measurements.

An "intrinsic" substrates will always exhibit a residual doping of either p- or n-type. This is not measured for the used substrates. Thus, if the residual doping is of n-type, a space charge region exists. For this case, the estimate neglects two facts: On the one hand, the laser doped p-type region gets reduced due to the space charge region. But since the theoretical depletion width in the acceptor region for a pn-junction of the given doping concentrations of $N_A \approx 10^{18}\text{cm}^{-3}$ and $N_D \approx 3 \cdot 10^{14}\text{cm}^{-3}$ is below 1nm this is expected to be of little importance. [Sze2007, p. 83] On the other hand, for a contribution of the "intrinsic" region to the electrical current, the current would have to pass the space charge region twice: from p- to n-type material and vice versa. A significant current through the "intrinsic" substrate seems therefore rather keen. Nevertheless, the resulting maximum error is expected to be only in the range of 10%, as $\sigma_{eff,lo}$ and σ_{intr} differ by a factor of ≈ 10 and are the major contributions in eq. (5.9).

Estimation of the activated dopants

To make an estimation of the amount of electrically activated dopants, first the amount of maximally available dopants per area $n_{dope,NP}$ is calculated from the as deposited NP thin film:

$$n_{dope,NP} = d \cdot P \cdot N \approx 400\text{nm} \cdot 30\% \cdot 4 \cdot 10^{20}\text{cm}^{-3} = 4.8 \cdot 10^{15}\text{cm}^{-2} \tag{5.10}$$

Here d, P and N are the NP film thickness, its density and the NP doping concentration, respectively. The values of d and N used for the estimate are taken from profilometer and SIMS measurements, whereas the density is taken from literature. [Lechner2008]

Second, the concentration of electrically activated dopants is calculated, by assuming that the dopants are homogeneously distributed throughout the whole sample. For the samples processed at $\geq 40\%$, a mean conductivity of $1.47\Omega^{-1}\text{cm}^{-1}$ is calculated. According to fig. 3.1 this results in a doping concentration of $\approx 1 \cdot 10^{16}\text{cm}^{-3}$. [Bulucea1993] Hence for a thickness of 525µm, $n_{i-Si} \approx 1 \cdot 10^{15}\text{cm}^{-2}$ dopants are available.

Comparing both values with each other, the amount of dopants differs by a factor of 5. The difference can be interpreted as a reasonable agreement in regard of the inaccuracies of almost all values used to calculate the two concentrations and the imprecision of the calculations as discussed just before (p. 55) on the one hand. On the other hand, measurement inaccuracies, inactivity of dopants which are bond to other impurities and evaporation of dopants during the annealing process cannot be excluded.

Varying the number of scans

In fig. 5.24 the conductances of samples prepared at 35% of MLI and with the number of scans varied between 2 and 12, are shown. As a general trend, the conductance increases with the number of scans from $\approx 0.6\Omega^{-1}$ up to a best value of $\approx 10\Omega^{-1}$, whereas a plateau around $1.5\Omega^{-1}$ can be estimated between 5 and 9 scans.

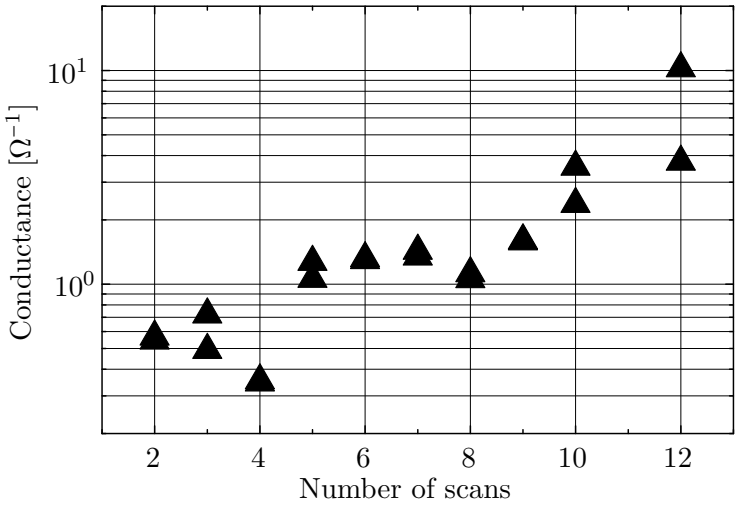

Figure 5.24: Conductance measurements of annealed samples varying the number of scans

One possible explanation for the increase may be that more scans result in an increased melting depth and therefore in a lower doping concentration of the annealed layer that leads to an increased mobility and conductivity. Another explanation is based on hypothesis of the formation of volatile oxygen groups. Accordingly, a repeated scan results in a better purified sample.

IR laser doping with n-type NPs

The experiments presented before have solely used p-type HWR NPs for deposition. However, the principle of NP laser doping has also been confirmed using n-type MWR NPs. Thus, IR laser doping using highly doped NPs is possible independent of the majority doping type in the respective NPs.

5.2.4 Realization of pn-junctions

To investigate whether the presented technique of laser doping is applicable to change the majority doping type p-type Si HWR NPs are laser annealed on n-type, one-side polished, {100}-oriented, $1.5 \times 1.5\text{cm}^2$ c-Si substrates, which exhibit a phosphorus doping concentration of $3 \cdot 10^{17}\text{cm}^{-3}$ and a thickness of 525µm. For NP deposition and laser annealing the standard parameters are used. Since the doping depth as well as the doping density of the substrates are too big for high efficiency PV applications, these devices are primarily considered to investigate the principle idea.

After annealing, 200nm thick Al contacts are evaporated by physical vapor deposition on the laser doped front and on the rear side to apply a voltage over the pn-junction. On the front a finger structure contact (see fig. 5.27b), covering an area of 30.66mm^2 and on the rear side a $12 \times 12\text{mm}^2$ contact is deposited. Using standard silver ink, the back side of each sample is glued on a metal plate which is contacted to the measurement equipment. On the front side an additional silver ink droplet is placed to improve front side contacting.

Current-voltage measurements

Fig. 5.25 shows the $I(U)$ characteristics in the dark (black triangles) and under AM1.5 light (green squares) of a pn-sample. For the data from the measurement in the dark, a clear rectifying behaviour is observed with an on / off ratio of 124 at $U = +/-1\text{V}$ and a reverse current of $\approx 2\text{mA}$ at $U = -1\text{V}$. This rectification proves, the feasibility to change the majority dopant type by the presented method. The rectifying behaviour is not a result from Schottky contacts of the deposited metal, as it is not observed for samples consisting of the substrate and evaporated contacts only. (Since a short circuit current of $80\mu\text{A}$ is measured also in the dark, it is concluded that some light must have been present during the measurement.)

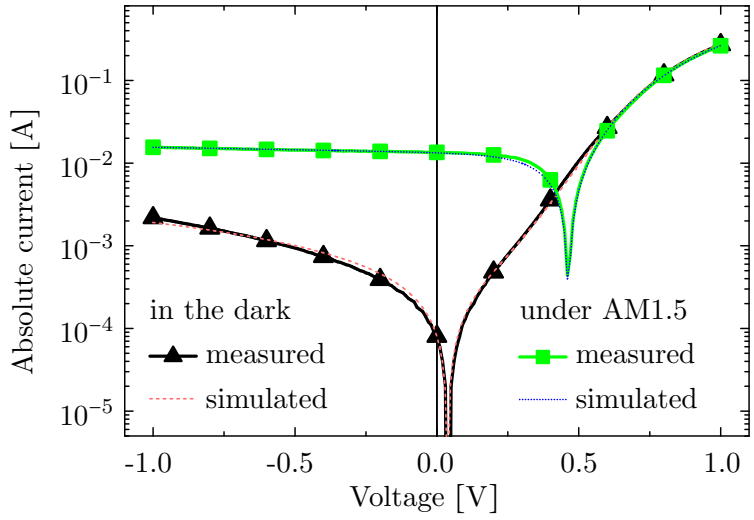

Figure 5.25: $I(U)$ characteristics of pn-sample in the dark (black triangles) and under AM1.5 illumination (green squares); red dashed and blue dotted lines: simulated graphs [Meseth2013a]

From the data obtained under illumination, a PV effect is measured, showing an open circuit voltage of $U_{oc} = 0.464\text{V}$, a short circuit current of $I_{sc} = 13.5\text{mA}$ and a fill factor of $FF = 53.5\%$. To make an estimate of the device efficiency, the PV active area is calculated by subtracting the contact area from the annealed area. This results in a short circuit current density of $J_{sc} = 7.94\text{mA/cm}^2$ and an efficiency of $\eta \approx 1.97\%$.

To get a better understanding of the device, both characteristics are fitted using the one-diode model, c.f. ch. 4.2.3. The resulting fit is in good agreement with the measurement, as can be seen from fig. 5.25. Table 5.2 presents the derived values.

The ideality factor n exceeds the limit by Sah, Noyce and Shockley of $1 \geq n \geq 2$. [Sah1957] According to Shah et al. the ideality factors of the pn-junction and additional rectifying heterojunctions or metal-semiconductor junctions in a diode have to be summed up. [Shah2003] The resulting overall ideality factor can therefore exceed two. [Zhu2009] However, since Schottky contacts can be excluded and a heterojunction seems inappropriate here, this explanation seems inadequate. A more reasonable explanation for the high n are defects in the material as a result from the annealing process like lattice imperfections due to the high temperature gradients or due to incorporated contaminations such as oxygen from the NPs. [Steingrube2011, Lee2010] They create interband states which can lead to transport paths and increase n. [Casey1996, Perlin1996]

According to Goetzberger et al. the derived shunt resistance is in a reasonably good range for a high efficiency solar cell. However, by reducing defects and contaminations it is expected

that it can be increased further. The series resistance, in contrast, has to be reduced below $0.5\Omega\text{cm}^2$. [Goetzberger1997, p. 93 f.] Besides purer material especially the contacting needs to be investigated to improve R_{ser}. The derived diode's reverse currents of 22µA and 167µA are a further indication of the non-ideal structure of this proof-of-principle device, esp. of the unpassivated surfaces.

Table 5.2: Values derived from one diode model for an IR laser annealed pn-sample

	in the dark	under AM1.5
ideality factor	$n = 3.18$	$n = 4.15$
series resistance	$R_{ser} = 0.83\Omega \triangleq 1.87\Omega\text{cm}^2$	$R_{ser} = 0.77\Omega \triangleq 1.73\Omega\text{cm}^2$
shunt resistance	$R_{shu} = 550\Omega \triangleq 1240\Omega\text{cm}^2$	$R_{shu} = 482\Omega \triangleq 1080\Omega\text{cm}^2$
reverse current	$I_0 = 22\mu\text{A}$	$I_0 = 167\mu\text{A}$
short circuit current	$I_{sc} = 80\mu\text{A}$	$I_{sc} = 13.5\text{mA}$

Voltage dependent capacitance measurements

In order to evaluate the build-in potential of the junction, $C(U)$ measurements are performed for a pn-sample, that is covered with squared contacts on both sides. The results are plotted as $C(U)$ and $C^{-2}(U)$ in fig. 5.26. The $C(U)$ measurement (graph on top) clearly indicates a voltage dependency of the capacitance in the range between $-2\text{V} \leq U \lessapprox 0.5\text{V}$, with a maximum at $U \approx 0.3\text{V}$. Thus, a bending of the energy bands is concluded.

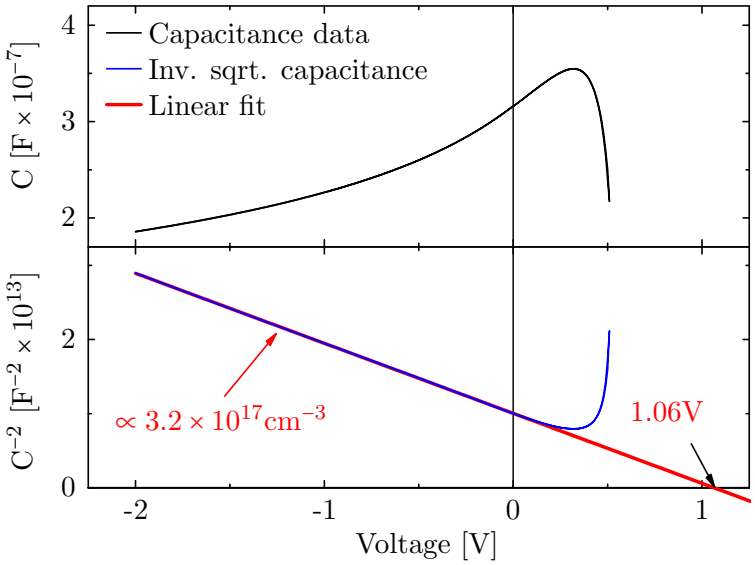

Figure 5.26: Voltage dependent capacitance ($C(U)$, top) and $C^{-2}(U)$ (bottom) characteristics of the pn-sample

According to ch. 4.2.3, $C^{-2}(U)$ the linear regime in the reverse-bias range is fitted by a linear curve and from the intercept $U_{bi} = 1.06\text{V}$ is derived. Further a substrate doping concentration of $N_D \approx 3.2 \cdot 10^{17}\text{cm}^{-3}$ is extracted from the slope, which is in agreement with the manufacturer's specifications. The value of U_{bi} is very close to the band gap of Si. Since the p- and the n-side

are highly doped, the Fermi-Energy is expected to be at the valence and the conduction band edge, respectively. Therefore, the derived value is in perfect agreement with theory.

According to standard semiconductor literature from the derived values and under the assumption of an abrupt pn-junction the doping concentration N_A of the doped layer can be determined [Sze2007, ch. 2.2.1]:

$$U_{bi} \approx \frac{k_B \cdot T}{e} \ln\left(\frac{N_D \cdot N_A}{N_i^2}\right) \tag{5.11}$$

$$N_A = \frac{N_i^2}{N_D} \exp\left[\frac{U_{bi} \cdot e}{k_B \cdot T}\right] = 2.2 \cdot 10^{20}\text{cm}^{-3} \tag{5.12}$$

with k_B, e, T and $N_i = 9.65 \cdot 10^9\text{cm}^{-3}$ being the Boltzmann constant, the elemental charge, the temperature in K and the charge carrier concentration of intrinsic Si at 300K, respectively. [Sze2007, Schwoerer2005, Altermatt2003] N_A significantly varies from the results obtained using SIMS measurements (c.f. ch. 5.2.2). Due to the high doping concentrations it is expected that the energy bands are degenerated. Since the formulas are based on a theory assuming non-degenerated samples, this simple theory seems to be inapplicable here.

OBIC characterization

In fig. 5.27a the short circuit current (I_{sc}) map of a $15 \times 15\text{mm}^2$ pn-sample processed with standard parameters is shown. It is determined by optical beam induced current (OBIC, c.f. ch. 4.2.3) measurement at 980nm laser illumination. The processing laser scan direction is horizontally, here. The colour bar at the right indicates the value of I_{sc}.

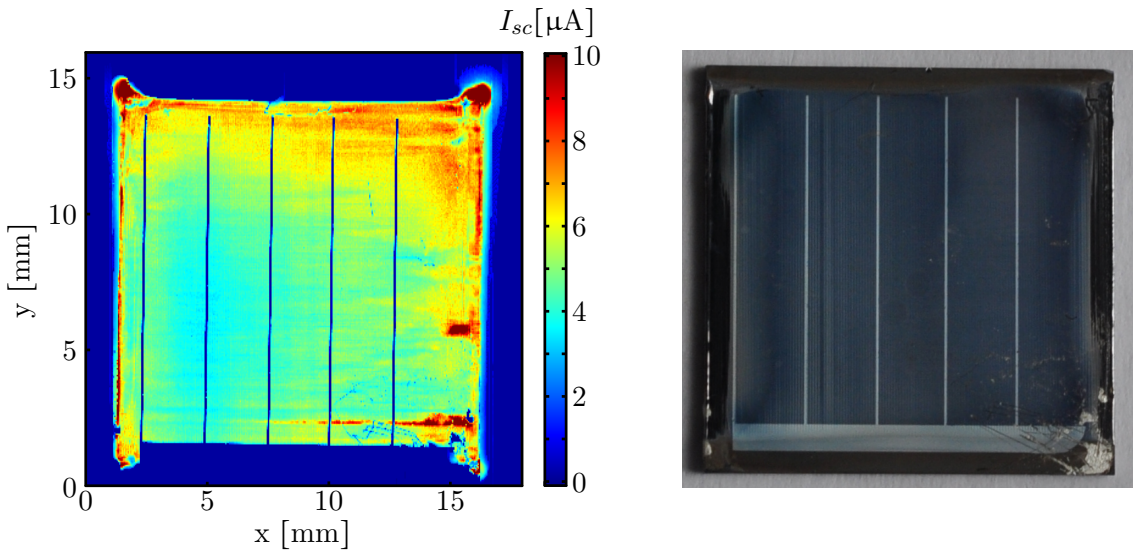

(a) OBIC-measurement (b) Photograph

Figure 5.27: OBIC measurement and photograph of IR annealed sample

I_{sc} strongly varies over the whole annealed area. On the one hand this is due to the finger contacts (deep blue), reflecting the light. On the other hand, an overall change is found: While at the left part of the image a more o less vertically aligned area of low I_{sc} ($\approx 4\mu$A) is observed, I_{sc} increases up to $\approx 8\mu$A at the upper and right part of the map. Since the annealing direction

is horizontally here, the origin of these inhomogeneities is assumed to be the inhomogeneous temperature distribution during the annealing process, as discussed in ch. 5.2.1. Thus, the melting depths vary over the sample's area, leading to different conversion efficiencies.

Apart from the annealed areas especially at the right and left top edges, areas of high I_{sc} are found. Although they are not irradiated by the annealing laser, a high I_{sc} is observed here, which is in contrast to the remaining, unannealed parts of the sample, showing no photo activity. This presence is a further evidence, that heat-constriction is obtained, when the annealing laser approaches the sample's edge (c.f. p. 41). From the photograph of this sample (see fig. 5.27b) and from additional cross sectional SEM images of similar edges (see fig. 5.28) such borders are found to be significantly deformed. However, it is unclear why I_{sc} is maximal here. One reason may be a better light absorption due to higher internal reflections.

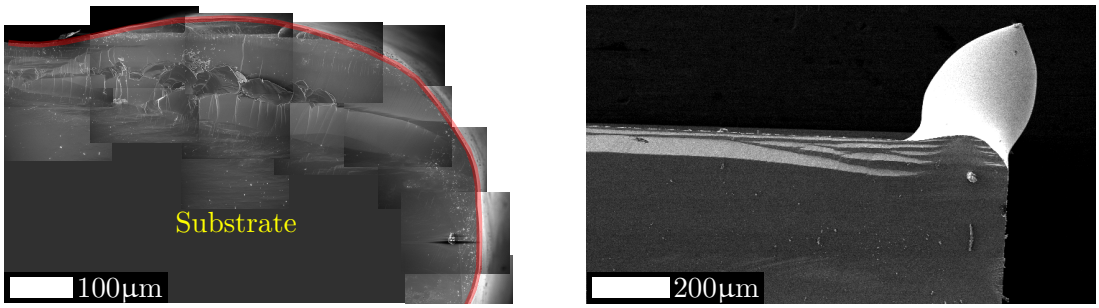

(a) Low laser annealing intensity (b) High laser annealing intensity

Figure 5.28: Melted sample borders due to IR laser annealing

Attempts to improve the photovoltaic devices

In this chapter first attempts to increase the PV power conversion efficiency η are presented. On the one hand the laser parameters and on the other hand, the amount of potentially available dopants are varied. In principle both attempts primarily try to improve the characteristics by a better control of the doping concentration in the annealed film.

Varying the laser parameters The dependence of the number of scans on the characteristic PV values is presented in fig. 5.29 for four samples. As an average trend all of the PV values increase, if the number of scans is increased from two to four, whereas a further increase does not show a significant improvement; instead it seems to saturate.

A reasonable interpretation for this observation is difficult to find, particularly with regard to the few measurement data. Nevertheless, similarities to the conductance measurements of IR-laser annealed NP films on c-Si are found, c.f. fig. 5.24, which saturate also in between five and eight scans. As suggested in ch. 5.2.3, an increased number of scans can result in a higher purity of the annealed material: Impurities may increasingly precipitate or evaporate and structural defects in the film can reduce. However, this does not explain, why U_{oc} reduces for the sample scanned eight times. Further, this way to increase the η seems inadequate because of the substrate bending and the estimated increase in melting depth observed for an increased number of scans.

Fig. 5.30 displays the characteristic PV values of samples created using the standard parameters, except that the laser intensity of the main scans is varied according to the abscissa.

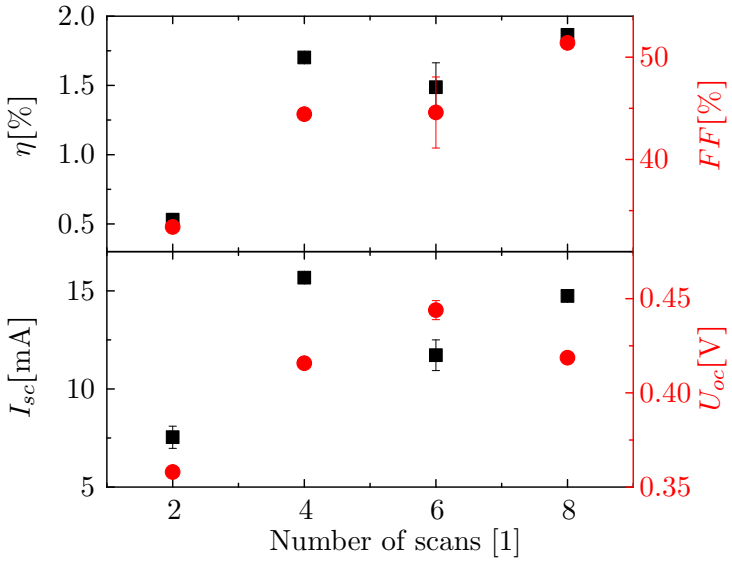

Figure 5.29: Characteristic PV values for varied amount of IR scans at max. intensity

Additionally the results obtained from $I(U)$ curve fitting (c.f. ch. 4.2.3) are shown. From this figure it is found that a maximum conversion efficiency of $\approx 2\%$ is achieved and that the maximum laser intensity plays only a minor role on the characteristic PV values, for laser intensities above 30% of MLI. For FF, I_{sc} and U_{oc} a measurable trend cannot be observed. Although not shown here, the variation between different sample batches seems to be higher than the one obtained here. It is concluded that an optimization which focuses primarily on the purity of the NPs results in an improve of the efficiency and of the deviations.

Varying the concentration of p-type NPs in the dispersion Fig. 5.31 shows the change of the characteristic PV values, if the amount of doped NPs is reduced by mixing it with nominally undoped ("intrinsic") NPs. Obviously by using only intrinsic NPs a PV device cannot be created. This is in agreement with PV theory, as the IR laser annealing of an intrinsic layer with a doped substrate leads to the formation of a less doped layer, but not to a PV pn-junction.

From the graph of η it can be concluded, that a p-type concentration of at least 25% is needed in order to create a working device. However, this does not give the absolute minimum amount of doped NPs in dispersion, as for these investigations, the concentration of doped NPs is not varied further between 25% and 0%. For a more detailed investigation it is supposed to change the dopant concentration in logarithmic steps.

For samples created with a dispersion of $\geq 25\%$ p-type NP all PV values are found to be in the same range. As discussed before, the variations between different samples are supposed to be governed by variations in the sample preparation.

5.2.5 Summary

This section demonstrates, that it is possible to dope c-Si by IR laser annealing of highly B doped HWR NPs. Chemical (SIMS) and structural (photography, SEM, XRD and TEM) investigations show, that the NPs as well as a surface near substrate layer melt during annealing and form a volume of homogeneous doping concentration. This liquefied layer re-solidifies crystalline and in the same orientation as the substrate. From SIMS and conductance measurements the thickness

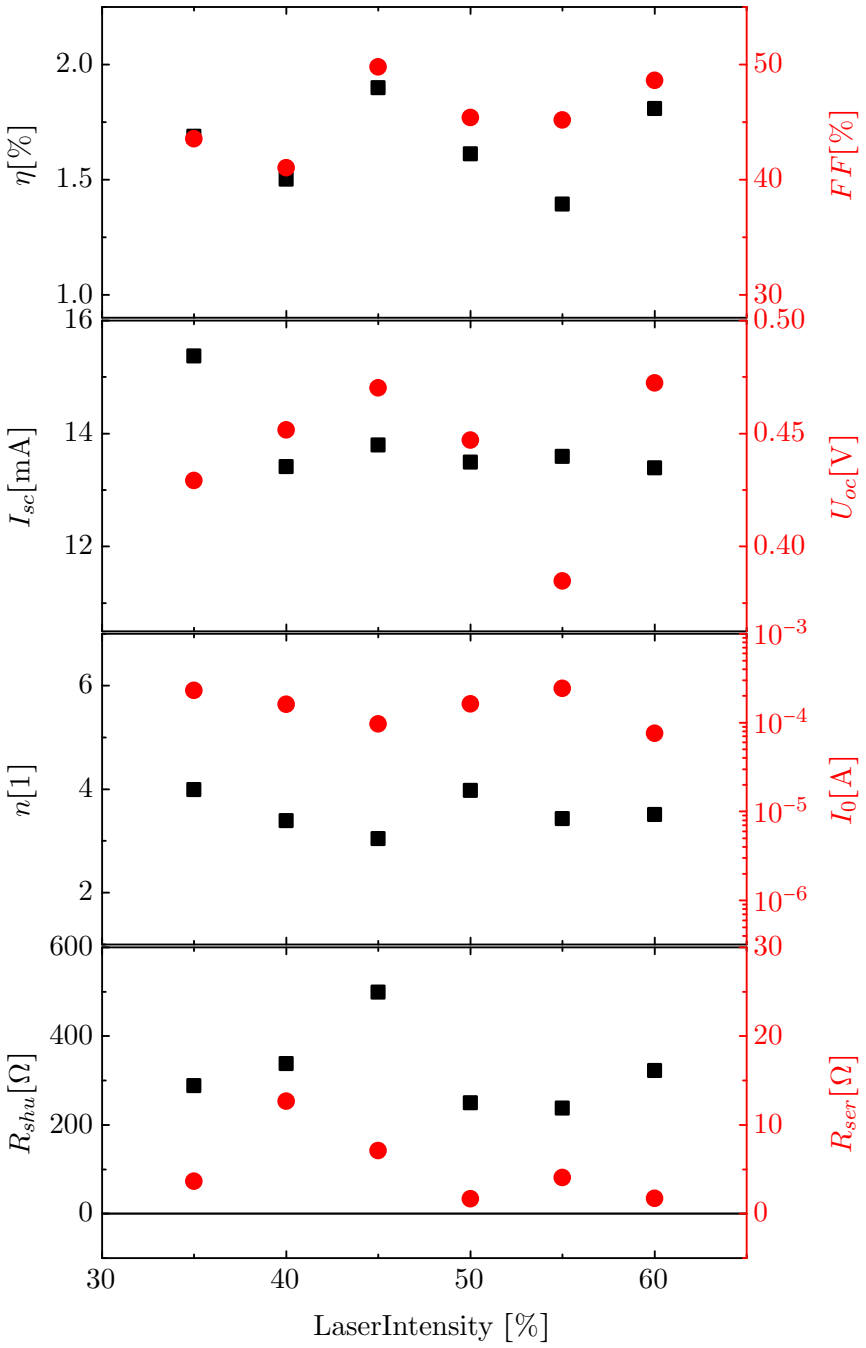

Figure 5.30: Characteristic PV values and results from one-diode fit for samples created by varying the maximum laser intensity; black (red) symbols belong to left (right) axes

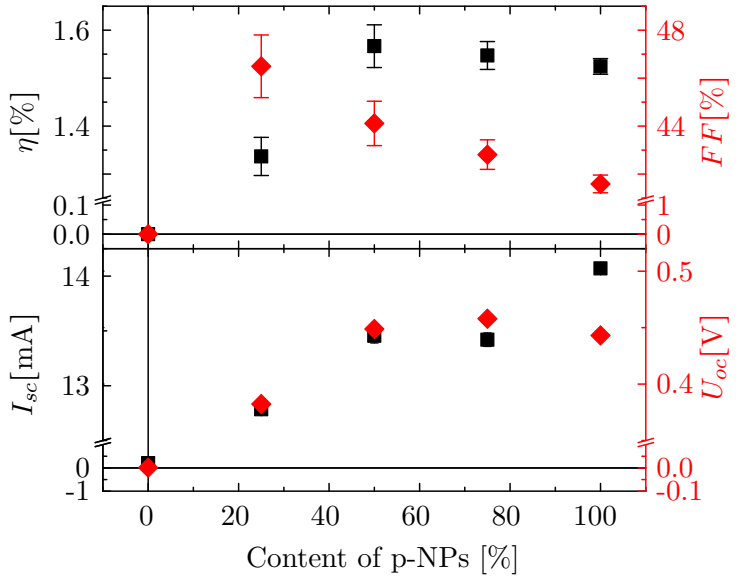

Figure 5.31: Characteristic PV values for varied compositions of the dispersion

d and the doping concentration N of this layer are estimated to be in between $\sim 100\mu m \geq d \geq 23\mu m$ and $2 \cdot 10^{18} cm^{-3} \geq N \geq 1 \cdot 10^{17} cm^{-3}$ for the standard parameters, respectively.

Further SIMS investigations show, that the amount of O and O precipitates from the NPs are reduced by a factor 5 – 6 due to the laser processing. This is ascribed on the one hand to the tendency of Si to segregate impurities during crystallization. On the other hand the reduction of O in the material may be due to the formation of volatile O groups or its evaporation. However, both effects lead to a self-refinement of the annealed layer.

From electrical conductance measurements, the fraction of electrically activated dopants is estimated to be only $\approx 20\%$. This loss may also be explained by the evaporation of dopants during the annealing. Otherwise, chemical or structural imperfections are another origin for electrical inactive dopants.

Although the estimated doping depth is much too thick for PV applications, pn-junctions are created by laser annealing of p-type NPs on n-type substrates in order to prove, whether in principle it is possible to change the majority doping type. These pn-junctions show on / off ratios of ≈ 120 and a PV effect with best conversion efficiencies of $\approx 2\%$. OBIC measurements show a rather inhomogeneous I_{sc} distribution, which is mostly ascribed to the inhomogeneous melting during the not optimized annealing process.

Since the bending of the samples along the laser line profile and the determined ripple structure along the scan direction are unfavorable, this technique is expected to be inadequate to create solar cells commercially. Instead the use of lasers with a shorter wavelength and / or short pulses are preferred in order to reduce the melting depth. Therefore, in the following section a UV laser is applied for laser annealing.

5.3 Ultraviolet laser annealing of Si NP thin films on c-Si

A pulsed 248nm UV laser with a line profile (for details see ch. 4.1.1) is used to laser anneal films of highly doped Si NPs on c-Si in order to dope the substrates. The smaller wavelength

results in a reduced absorption depth of only 5nm. Due to the pulsed nature of the used laser, also the heat diffusion length is reduced, c.f. fig. 2.11. Both properties are expected to reduce the melting / doping depth in comparison to the IR laser, which is favorable for a thin front side doping of a PV cell.

5.3.1 Sample preparation

For the experiments $1 \times 1\text{cm}^2$ c-Si substrates are used. If not stated otherwise, the sample preparation is performed by spin coating a 10wt.% p-type HWR NP dispersion on the polished surface of the substrates at 2 000r/min, followed by a 5min hot plate annealing at 125°C in air to remove residual solvents. The samples are then laser annealed. In order to ensure a laterally homogeneous irradiation the repetition frequency and the scan speed are set to $f = 100Hz$ and $v = 9.3$mm/min, respectively, which results in a distance of $\Delta x = 1.55$µm between neighbouring shots ($\approx 1/15$ of the laser's Gaussian width).

Optional aluminium contacts are formed by thermal evaporation, utilizing shadowing masks. For the backside, centered contacts of $8 \times 8\text{mm}^2$ are evaporated and for the annealed front side, a mask with a finger structure, covering an area of $A_{finger} \approx 14\text{mm}^2$ is used (see fig. 5.42). The oxygen content is reduced by hexafluorosilicic acid (HFS) steps at ≈ 90°C prior to and after NP deposition for 10min and 20s, respectively. (An investigation on the actual influence of these additional HFS steps is presented in the ch.s 5.3.2 and 5.3.4.)

5.3.2 Structural characterization

To investigate structural changes in the NP film and in the subjacent c-Si due to the annealing, samples are prepared at different laser intensities (c.f. table 5.3). Figure 5.32 shows top view and cross section SEM images of these samples. The scan direction for all samples is from left to right. Further, for the samples on top (+HFS) an HFS-treatment is performed; for those on bottom (-HFS) it is not.

Table 5.3: Sample identifications (ID), laser energy E_{sample} and energy density ϕ_{sample}

Sample ID	E_{sample}	ϕ_{sample}
noLT	—	—
loLT	0.89mJ	0.34J/cm^2
midLT	4.1mJ	1.6J/cm^2
highLT	9.7mJ	3.7J/cm^2

For both unannealed samples, the typical porous film structure is found. However, for the HFS etched sample (noLT+HFS) the surface appears to be comparatively uneven and the thickness is reduced by ≈ 50nm to ≈ 100nm, which is ascribed to the etching procedure. In top view a difference is observed only in the center. In contrast to the HFS etched, the HFS-untreated shows an almost radial change in brightness which is attributed to charging effects from the SEM measurements. Thus, it is concluded, that the HFS etched NP film exhibits a higher conductivity, which is ascribed to a reduced amount of SiO_X.

For the laser annealed samples it is found that the nanoparticulate structure increasingly reduces with higher laser intensities. This trend is independent of the HFS-treatment. Nevertheless differences are visible and are described in the following.

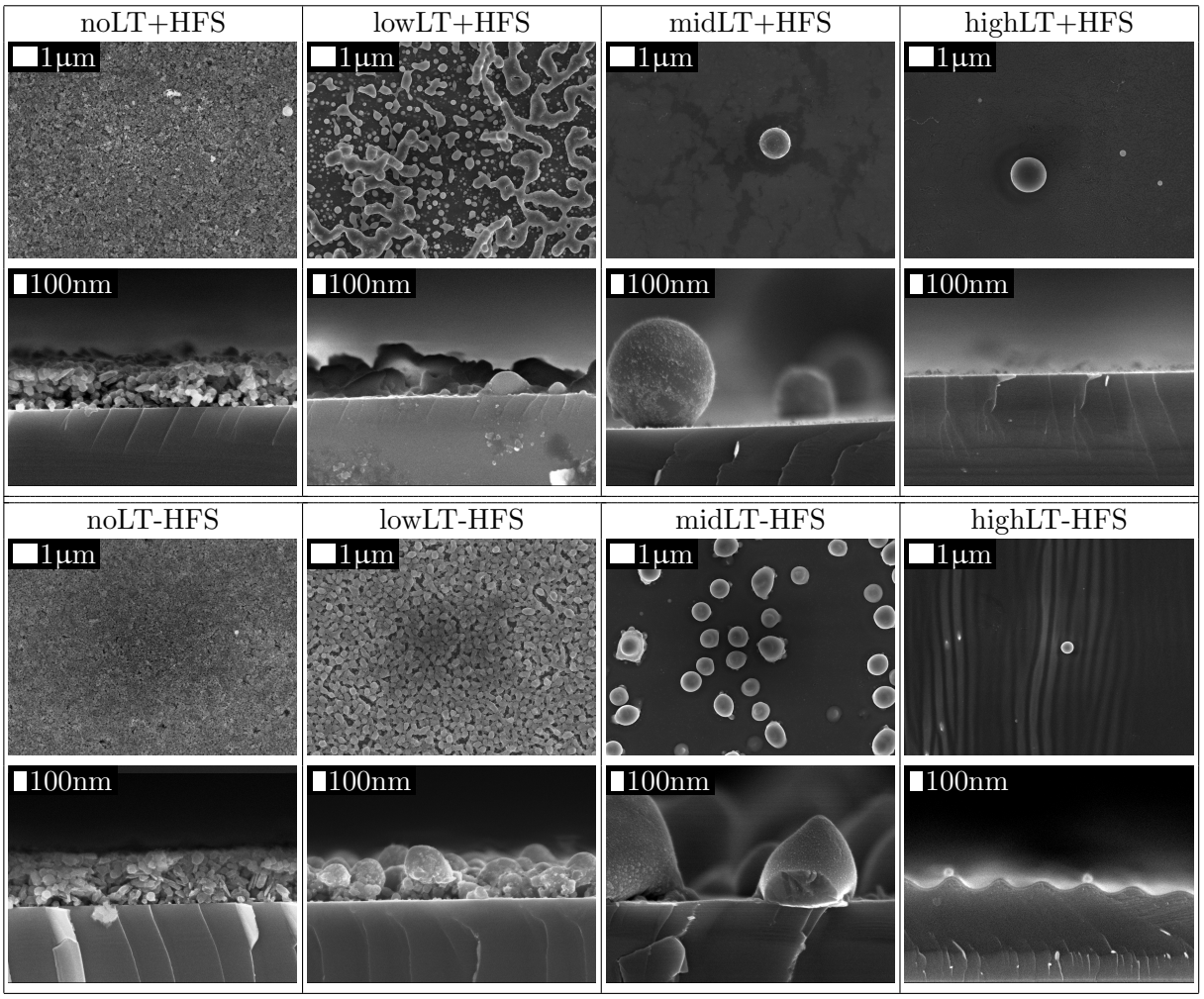

Figure 5.32: SEM images of annealed HWR NPs coated c-Si, treated with increasing laser intensities (table 5.3) and with (top) / without (bottom) HFS; annealing is performed from left to right

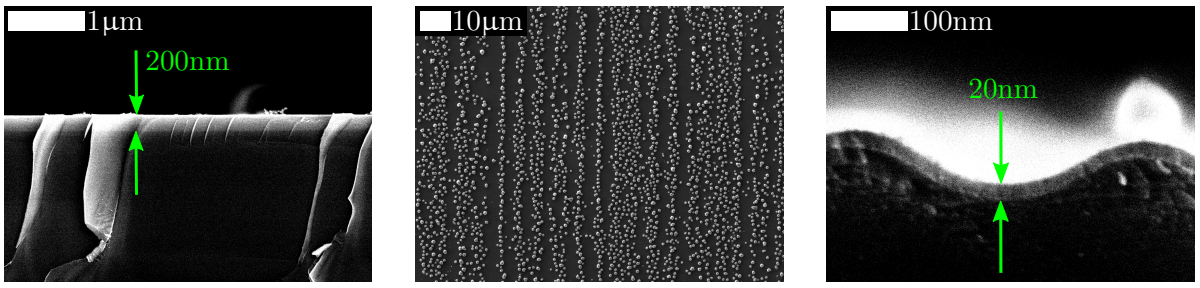

(a) midLT+HFS (b) midLT-HFS (c) highLT-HFS

Figure 5.33: SEM details of UV laser annealed samples:
(a): for cross sections of midLT+HFS a ≈ 200nm thick surface near film is found;
(b): top view image of midLT-HFS shows alignment of cones along the top-hat profile;
(c): cross section of highLT-HFS shows a ≈ 20nm thick layer below the surface

Samples processed with HFS-treatments For the sample lowLT+HFS all NPs are transformed into partially smeared out hemispheres and unordered networks. Consequently, the laser intensity is sufficient to melt the NP layer but not the substrate's surface.

For both higher intensities, a homogeneously flat surface is observed in cross sections. It is impossible to distinguish the substrate from the annealed NPs, suggesting an intermixing of the NPs and a surface near substrate layer. For midLT+HFS, a slight change in brightness is visible after the topmost ≈ 200nm. Fig. 5.33a, showing a cross section with highly increased contrast ratio, illustrates this feature much better. The intensity of the SEM signal is sensitive on the type of dopant in semiconductors (p-type material is predicted to result in a higher intensity) and scales linear with the logarithm of the doping concentration. [Perovic1995, Venables1998, Elliott2002, Tsurumi2013, Chee2011] Thus, one explanation for this change in intensity can be the result of a change of the majority dopant concentration.

For the top view images of the sample midLT+HFS frayed areas of different brightness are observed. Due to the similarity of the structure with the in-plane SIMS characterization of O containing species performed for the IR annealed samples, c.f. fig. 5.21, these areas are attributed to different surface O concentrations. Otherwise, due to the absence of frayed areas for highLT+HFS it is suggested that O is either incorporated in the re-solidified layer or evaporated during annealing. Further, the frayed areas in the top view image of that sample may also be a result from doping inhomogeneities, which possibly vanished for the higher laser intensities, c.f. top view SEM image of highLT+HFS.

Samples processed without HFS-treatment For the sample lowLT-HFS, hemispherically shaped structures on top of and an almost intact ≈ 100nm thick NP film of are observed. It is therefore concluded that the laser intensity is not high enough, to completely melt the NP layer.

In contrast, for the sample midLT-HFS the NPs must have completely molten, as the substrate is covered with menhir- or cone-like structures. As these cones are aligned along the laser's line profile (c.f. fig. 5.33b), it is concluded that the laser moves discontinuously, creating a locally varying amount of heat.

In cross section the cones exhibit a substrate dewetting with contact angles Θ of mainly $70° \geq \Theta \geq 110°$. For a few cones, the angle falls even below 45°. As these cones are only observed for the HFS untreated sample, they are concluded to be a result from oxides and from different surface energies of the melt and of the oxidized substrate surface: According to Young, the contact angle Θ_c of a liquid on a flat solid (see fig. 5.34) can be described by [Young1805]:

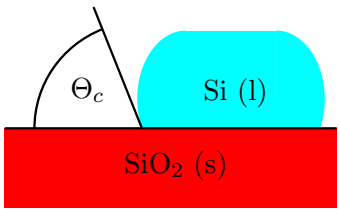

Figure 5.34: Scheme on Young's contact angle

$$\Theta_c = \arccos \frac{\zeta_s - \xi_{sl}}{\zeta_l} \qquad (5.13)$$
$$\zeta_s = \xi_{sl} + \zeta_l \cdot \cos \Theta_c$$

Here ζ_l and ζ_s symbolize the surface energies of the liquid and the solid (both in contact with air), respectively, and ξ_{sl} gives the interfacial energy density. For the case of liquid Si on SiO_2, the combination of $\xi_{sl} \sim 0.3 J/m^2$, $\zeta_l \sim 1.5 J/m^2$ and $\zeta_s \sim 0.75 J/m^2$ inhibits the formation of a closed film but favours the formation of islands, that dewet the surface with a contact angle of $\Theta_c \approx 73°$. [Danielson2006] The observed, average contact angles are more or less in line with Θ_c. Discrepancies are ascribed to the locally inhomogeneous chemical composition of the solid

layer and the molten NPs. Further, Tadmor has announced, that inhomogeneities in surface morphology can lead to a spread of the contact angle. [Tadmor2004]

Only for the highLT-HFS sample, no NPs or NP-agglomerates are observed. However, wave-like surface deformations along the laser's scan direction are observed. The periodicity varies in between 300nm and 500nm and the amplitude is not constant, either. One possible explanation for their build up is based on two assumptions: On the one hand, the locally fluctuating laser intensity creates a locally varying amount of heat and consequently of the melting depth. On the other hand due to the tendency of self-purification of Si and the segregation of impurities during re-crystallization (see discussion in the ch.s 5.2.2 and 5.2.1) an oxygen gradient towards the surface is expected to build up. Thus, the different thermal expansion coefficients of Si and SiO_2 are expected to create tension during cooling, which is suggested to create the wave like structures. [Tada2000]

Fig. 5.33c takes a closer look using a high contrast ratio at the cross section of highLT-HFS. A bright, 20nm thick layer is found on top of the wave structure, indicating a phase separation, substantiating the presented conclusion of oxygen segregation. Due to the most probable intermixing of the NP material with a substrate's surface near layer it seems implausible that this contrast is a result from dopant variations, as observed for the HFS treated sample highLT+HFS.

The absence of cones for the highLT-HFS sample does not contradict the presented explanation for the build-up of the cones for midLT-HFS. For the high laser intensity it is assumed that also a surface near layer melts, thus, forming a mixed liquid of molten NPs and substrate.

5.3.3 Conductance measurements

To clarify, whether electrically activated dopants are incorporated by the UV laser annealing technique and doping has therefore successfully been established, conductance measurements are performed with nominally undoped ("intrinsic") $10 \times 10\text{mm}^2$ Si samples ($\geq 500\Omega$cm, 525µm thickness, one side polished, one side as cut). These are coated with p-type HWR NPs on the polished side and laser annealed with attenuator angles in between 0° and 36° in steps of 4°. The samples are HFS treated before NP deposition and before laser treatment. For conductance measurements the standard four point measurement tool (see p. 32 and eq. (4.11)) is utilized. Fig. 5.35 depicts the resulting conductance measurements of two samples (red circles and green triangles) in comparison with a laser annealed bare substrate (black squares) and the laser energy at the sample's surface (turquoise line).

While the conductance measured for the uncoated sample is $(4.5 \pm 0.4) \cdot 10^{-5}\Omega^{-1}$ and is rather homogeneous for all angles, for the coated samples that are annealed at $\leq 36°$ neither a difference in conductance nor a change in colour can be observed, leading to the conclusion, that the laser intensity is not sufficient to melt the NPs. This is in line with the SEM observations of sample lowLT+HFS. (In contrast to the conductance measurements performed with as deposited samples in the IR laser chapter 5.2.3, the same conductance is measured for samples with and without NP deposition at the lowest laser intensity, because here the probes are pressed onto the sample, resulting in a penetration of the NP film.)

For smaller angles the conductance increases by more than two orders of magnitude up to $(7.8 \pm 1.2) \cdot 10^{-3}\Omega^{-1}$. This substantiates the conclusion from SEM measurements that the NPs and a surface near layer melt during annealing at sample energies of $E_{sample} \gtrsim 3$mJ.

Using the geometrical data and eq. (4.11), the substrate's resistivity is calculated to be $\approx 5\,000\Omega$cm, which corresponds to a doping concentration between 10^{12}cm^{-3} and 10^{13}cm^{-3}.

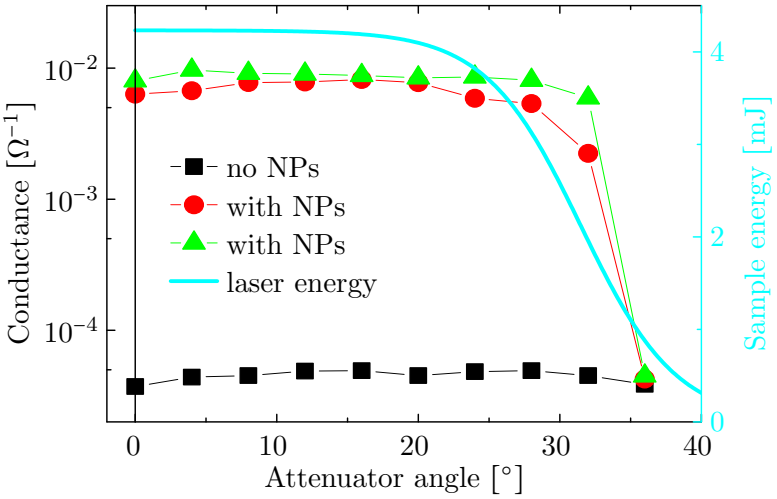

Figure 5.35: Conductances of annealed, bare (black squares) and p-type NP coated (red circles, green triangles), Si substrates and laser energy at the sample's surface (turquoise line)

[Sze2007] According to section 5.2.3 an effective sample resistivity of $\rho_{eff} = (30.5 \pm 4.7)\Omega$cm is derived which corresponds to an effective doping concentration of the whole sample of $\approx 5 \cdot 10^{14}$cm^{-3}. [Bulucea1993] (As in section 5.2.3 the residual doping type of the intrinsic substrates is not measured. Thus, for an opposite doping of substrate and laser doped layer it seems rather unrealistic that the "intrinsic" layer contributes to the current, because the current needs to flow through the space charge region twice.)

By comparing the activated and the available dopants, as discussed according to eq. (5.10), it is found that only $\approx 0.5\%$ are electrically activated. This immense reduction is ascribed on the one hand to the presumably small doping depth:

Under the assumptions that the $\approx$ 200nm thick, bright layer found in the SEM image (fig. 5.33a) is the doped layer and that only this layer contributes to the electrical current, the measured conductance results in a conductivity of $\sim 10^2\Omega^{-1}$cm^{-1} and - according to fig. 3.1 in a doping concentration of $\sim 10^{19}$cm^{-3} of this film. Integrating the dopants of this layer over its thickness results in $2 \cdot 10^{14}$cm^{-2}. According to this approximation, $\approx 5\%$ of the dopants are electrically active. (The increase by one order of magnitude is a result from the change in mobility between low and high doped Si.) Otherwise, Li and Thurber have announced for phosphorous doped Si and for doping concentrations between 10^{14}cm^{-3} and 10^{18}cm^{-3}, that the density of ionized dopants reduces for higher doping concentrations. [Li1977] The resulting reduction is assumed to be less than 1/10. Thus it seems implausible that these two effects are the only reason for this great difference. Another reason may be unintentional impurities or defects in the annealed layer which reduce the mobility significantly. This however invalidates the assumption that the annealed layer re-solidifies single crystalline.

The intention of the following passage is to estimate whether a significant amount of the Si NP material evaporates during annealing: If the volume V of the cone structures observed in SEM images for the sample midLT-HFS is approximated by the volume of a cone, i.e. $V = \pi \cdot r^2 \cdot h/3$, with $r = 0.6\mu$m being the radius of the circle at the bottom of the cone and $h = 1.0\mu$m being the height of the cone, a mean cone volume of 0.5μm^3 is calculated. In fig. 5.32, approximately 30 cones are visible in the top view micrograph, displaying an area of $\approx 100\mu$m^2. For the whole

$1 \times 1\text{cm}^2$ sample this leads to a cone volume of

$$1.08 \cdot 10^7 \mu\text{m}^3 \tag{5.14}$$

On the other hand, the volume of the as deposited NP film is calculated to be:

$$p \cdot h_{film} \cdot A = 30\% \cdot 400\text{nm} \cdot 1\text{cm}^2 = 1.2 \cdot 10^7 \mu\text{m}^3 \tag{5.15}$$

with p, h_{film} and A being the density of the NP film, its thickness and the area of the sample, respectively. [Lechner2008] Comparing eq. (5.14) and eq. (5.15) only a small difference is observed. Consequently, evaporation during annealing seems to be irrelevant. A significant evaporation could even more result in an accumulation of the boron, due to the different melting points and vapor pressures of silicon and boron. [Sharma2010] Finally, a fusion of the molten NPs with the substrate can be excluded for this sample (midLT-HFS).

Unfortunately, the electrochemical capacitance voltage (ECV) technique, (c.f. ch. 4.2.2 in order to measure the doping concentration and doping depth) has not been available for these samples.

5.3.4 Realization of pn-junctions

Conductance measurements have shown that it is possible to create an electrically doped Si layer by UV laser annealing of deposited highly doped Si NPs on c-Si. In order to measure the doping depth and to find out, whether it is furthermore possible to create a photovoltaic working device, np-samples (pn-samples) are prepared with this technique. Therefore, cleaned, B (P) doped c-Si substrates of $1 \times 1\text{cm}^2$ are coated with P doped MWR (B doped HWR) NPs before laser annealing. The substrates exhibit a thickness of 200µm (250µm) with a resistivity of $1\Omega\text{cm} - 20\Omega\text{cm}$ ($1\Omega\text{cm} - 30\Omega\text{cm}$). While for the pn-samples the standard HFS treatments are applied, the NP etching has not been performed for the np-samples, since for the n-type NPs most of the dopants are sited in the oxide shell, see ch. 3.1.1. By profilometry the thickness of the as deposited n-type thin film is determined to be only ~ 40nm, which is a result from the reduced NP concentration of the n-type dispersion of only ≈ 3wt.% and from the smaller size of the NPs.

Measurement of the doping depth

The doping profiles of three pn-samples, prepared with laser energies of E_{sample} = 2.1mJ, 4.1mJ and 6.6mJ are measured with ECV technique and the results are shown in fig. 5.38.

A drop of the doping concentration within the first ≈ 5nm from the maximum of $4 \cdot 10^{20}\text{cm}^{-3}$ for the 2.1mJ sample and $2 \cdot 10^{20}\text{cm}^{-3}$ for the other two samples down to a plateau of homogeneous doping concentration of $2 \cdot 10^{20}\text{cm}^{-3}$ and $1 \cdot 10^{20}\text{cm}^{-3}$ is observed, respectively. The drop is assumed to be a result from self-refinement (see IR laser annealed samples in ch. 5.2.2). The depths d_{const} of the plateaus are given in table 5.4 and in fig. 5.37 in dependence of E_{sample}. Due to the presence of the plateaus it is concluded that the incorporation is based on liquid state diffusion for all of the three samples. Consequently d_{const} indicates the lower limit of the melting depth which depends on E_{sample} as can be obtained from fig. 5.37. Convection cannot be excluded here, but due to the short pulse duration and the comparably small power it seems negligible.

After the plateaus the concentration drops to the substrate's doping of $\sim 5 \cdot 10^{15}\text{cm}^{-3}$, which is

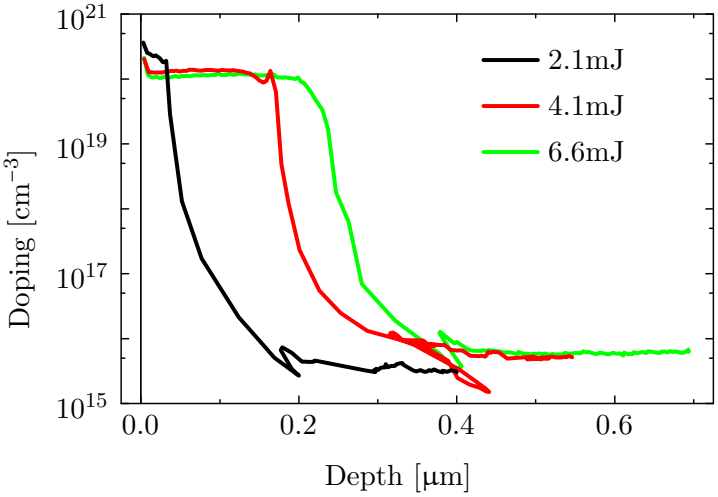

Figure 5.36: ECV measurements of pn-samples prepared with E_{sample} = 2.1mJ, 4.1mJ and 6.6mJ

Table 5.4: Results from ECV measurements: d_{const} is the max. depth of concentration above 10^{20}cm^{-3}, d_{max} represents the depth where the doping concentration falls below 10^{16}cm^{-3}, ($d_{drop} = d_{max} - d_{const}$) N_{total} gives the integrated dopant concentration

E_{prim}	d_{const}	d_{max}	d_{drop}	N_{total}	N_{total}/N_0
0mJ				$\sim 5 \cdot 10^{15}$cm^{-2}	100.0%
2.1mJ	32nm	173nm	141nm	$7.4 \cdot 10^{14}$cm^{-2}	15%
4.1mJ	164nm	336nm	172nm	$2.1 \cdot 10^{15}$cm^{-2}	42%
6.6mJ	199nm	378nm	179nm	$2.3 \cdot 10^{15}$cm^{-2}	46%

in line with the doping concentration of the substrate. Table 5.4 furthermore lists the maximum diffusion depth d_{max}, which is taken from the point, where the doping concentration falls below 10^{16}cm^{-3} and the dropping distance, i.e. the difference of both $d_{drop} = d_{max} - d_{const}$.

As the processing time is the same for all samples and since the values of $d_{drop} \approx 150$nm are more or less constant for all samples, the observed drop of the concentration can be an indication for solid state diffusion. However, a corresponding fit (not shown here) has resulted in abnormal high diffusion times or bad agreement. Therefore, it seems more plausible, that the observed drop is dominated by the proposed inhomogeneous melting depth along the scan direction, which consequently results in measurement values of intermediate doping concentration in the transitional region.

In fig. 5.37 a non-linear dependence of d_{const} on E_{prim} is observed. It is expected to be the result of the heat diffusion, that can be described best by a semi-infinite, three dimensional sample in the substrate, whereas the heat incorporation by the laser beam is better described by two dimensions. Consequently, the incorporated heat diffuses not only in direction of the laser beam, but in all three directions of the semi-infinite sample. These different dimensionalities are expected to become more important at higher laser intensities. However, so far a clear saturation is not observed for the three measurement points.

Further, energy loss by radiation from the surface of the semi-infinite sample cannot be excluded. Due to the discussed, most probable melting of the surface near layer, temperatures

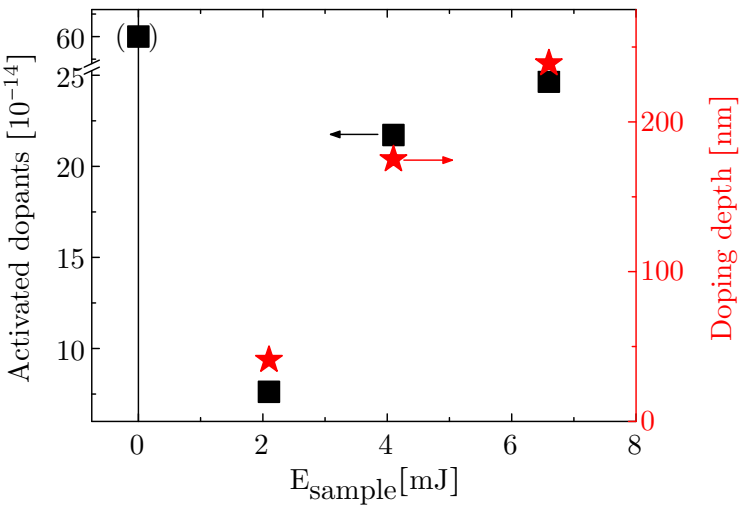

Figure 5.37: Integrated number of dopants and doping depth from ECV measurements

of $T \geq 1410°C$ must be present for some time during the annealing process. According to the Stefan-Boltzmann law, the heat loss by radiation is proportional to T^4, resulting in great losses here. [Allmen1995, p. 125] Nevertheless, since this is a dynamical, three dimensional process and a resulting calculation is not performed for the setup so far, it is hard to estimate the real influence of the radiation on the temperature distribution.

The ECV measurement is furthermore used to derive the fraction of activated per available dopant. For this the number of dopants per area, N_{total}, are calculated for each sample by integrating the doping concentration over the depth to the respective d_{max}. The results are presented in table 5.4 and in fig. 5.37. According to this N_{total} for the 2.1mJ sample is only $\approx 1/3$ of those of the other two samples.

This difference cannot be the result of a higher amount of dopant evaporation for the 2.1mJ sample. Instead it can be explained by the measurement method itself: By ECV measurements, the doping concentration only of electrically activated majority dopants is measured. Consequently, the incorporated heat is not sufficient to activate all dopants in the low intensity sample. However, due to the sensitivity of N_{total} on C, T and p the derived values of up to 46% have to be interpreted as a good approximation.

Otherwise, comparing the fraction of electrically activated dopants determined from ECV measurements and from conductance measurements, a difference of factor ~ 10 is found. Since the conductance measurements strongly depend on the mobility, which decreases for multi or micro crystalline Si (down to ~ $1cm^2/Vs$), the observed difference is a first indication that the re-solidified material may not be single-crystalline. [Finger1994, Chenga2002, Kandoussi2006] This is in contrast to the results of the IR laser annealing, which is due to the different preparation parameters (esp. duration and incorporated amount of heat).

Opto-electrical characterization of pn-samples

In this chapter, pn-samples and np-samples are investigated to clarify, whether they show an electrically rectifying behaviour and / or a PV effect. The samples are therefore characterized by illumination dependent $I(U)$ and by OBIC measurements. For electrical characterization, 200nm thick Al contacts are evaporated on both sides of each sample. The front contact is a

finger structure that covers an area of 14cm^2, the back contact is a square covering 8×8mm^2.

Current-voltage measurements Figure 5.38 A (B) shows the $I(U)$ characteristics of an np- (pn-) sample. In the graph, filled and open symbols represent the absolute current $|I(U)|$ measured in the dark and under standard AM1.5 illumination, respectively. For both samples, a rectifying behaviour with an on / off ratio of > 200 at $+/-1$V is observed in the dark, which proofs that the majority doping type is changed in the annealed layer.

Furthermore, a PV effect is measured for both samples. The characteristic parameters, η, FF, U_{oc} and I_{sc} are presented in the figure's left insets. Comparing both samples, the FF, U_{oc} and I_{sc} of the np-sample are 3% to 8% higher than those of the pn-sample, leading to an absolute power conversion efficiency increase of $\approx 0.7\%$ for the np-sample of 5.4%.

The illuminated $I(U)$ graphs are fitted using the Matlab fitting program (c.f. ch. 4.2.3). The calculated fits are included by a red and a blue dash-dotted line in fig. 5.38 A and B, respectively, and are in good agreement with the measured data. The parameters derived from the fit are given in table 5.5.

For both samples R_{shu} is in the kΩcm^2 range, showing that shunts - unless still present - do not play an important role for the energy conversion efficiency. [Goetzberger1997, p. 92 f.] According to *PVEducation.org*, nowadays shunt resistances are in the range of MΩcm^2 to kΩcm^2 and 0.5Ω. In contrast the values of $R_{ser} \approx 4\Omega$cm^2 are rather high and therefore show great potential for efficiency improvement, as typical values of commercial applications nowadays are between 0.5Ωcm^2 and 1.3Ωcm^2. [PV-EducationRshu, PV-EducationRser, Hoex2012] The reverse saturation currents of the diodes I_0 are determined to be 72μA and 104μA and are therefore very high, when compared with standard solar cells. [Goetzberger1997, p. 105 f.] Nowadays, for 1cm^2 samples, values between $\sim 10^{-7}$A and 10^{-11}A are already achieved. [Basu2013, Khan2010, Hoex2012] The ideality factors are determined to be $n \approx 3.4$ for both samples and can therefore not be explained by the Sah-Noyce-Shockley theory. [Sah1957]

Interpretation In order to optimize the presented diodes, in the following the main disadvantages and challenges determined from the measured and fitted data are discussed:

Contaminations

Due to the high R_{ser} a high amount of contaminants may be present in the sample. From SEM images it is already proposed, that oxygen is present even in the HFS etched, annealed layer (see discussion on frayed islands on the midLT+HFS sample in ch. 5.2.1). Otherwise, the chemical composition of the deposited NPs is not analyzed so far. Therefore, it cannot be excluded, that undesired contaminations are present in the NPs.

Metalization

The high values of R_{ser} and n are expected to be a result from the not optimized metal contacts. [Perez-Wurfl2009] As already discussed in ch. 5.2.4, non-Ohmic elements in a pn-device can increase the overall n. Due to the small doping concentration in the substrates, the metal-semiconductor interface on the back side are presumed to be responsible for the increase in n. It is therefore proposed to introduce a thermal annealing step after metal deposition or to create a back surface doping region (BSR) of the substrate's polarity.

Structural defects

The values I_0, n and U_{oc} can all be interpreted, such that structural defects are present in the sample: According to standard semiconductor literature, I_0 depends on the minority carrier diffusion length L or the carrier lifetime τ of the holes (p) and the electrons (n) in the respective

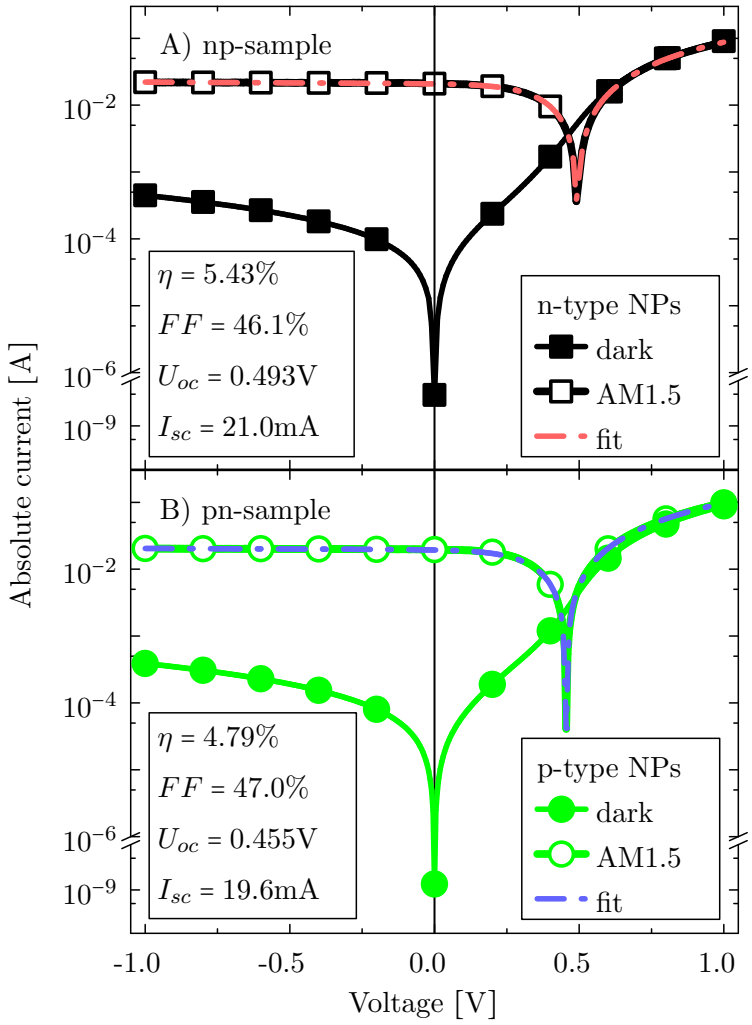

Figure 5.38: Illumination dependent $|I(U)|$ measurements of UV laser annealed pn-junctions: A) n-type NPs on p-type substrate B) p-type NPs on n-type substrate

Table 5.5: Derived values from one-diode fitting of np- and pn-samples: R_{ser} = series resistance, R_{shu} = shunt resistance, I_0 = diode's saturation current, n = diode ideality factor

Sample ID	NPs	c-Si	R_{ser}	R_{shu}	I_0	n
np-sample	n-type	p-type	4.2Ω ≙ 4.2Ωcm^2	884Ω ≙ 884Ωcm^2	72µA	3.35
pn-sample	p-type	n-type	4.0Ω ≙ 4.0Ωcm^2	1215Ω ≙ 1215Ωcm^2	104µA	3.36

region [Sze2007, p. 95]:

$$I_0 \propto \frac{1}{L_p} + \frac{1}{L_n} \propto \frac{1}{\tau_p} + \frac{1}{\tau_n} \approx \frac{1}{\tau} \tag{5.16}$$

Since the minority carrier lifetime is also inversely proportional to the concentration of defects [Goetzberger1997, p. 50 f.]:

$$N_{Dfct} \propto \frac{1}{\tau_n} \tag{5.17}$$

I_0 also depends on the defect concentration $I_0 \propto N_{Dfct}$. Thus, the high values of I_0 are attributed to defects. [Fahrenbruch1983, p. 90]

The measured $U_{oc} \leq 0.5$V is rather small for a Si PV cell. The following approximation shows, that defects can be one reason for it: U_{oc} is observed for $I = 0$A. Using the diode equation for an ideal, illuminated solar cell (see eq. (2.5)), this results in:

$$U_{oc} \propto \ln\left(\frac{I_{sc}}{I_0} + 1\right) \tag{5.18}$$

Thus, due to eq. (5.17) U_{oc} reduces with increasing N_{Dfct}.

Regarding the high ideality factor, Steingrube et al. have developed a model to describe ideality factors $n > 2$ if the defect concentration is high enough to form inter-bandgap energy bands (coupled defects). Due to the high defect concentration in such devices, the Shockley-Read-Hall recombination cannot be applied, here. [Steingrube2011, Shockley1952, Hall1952] Therefore, Steingrube et al. make instead use of the donor-acceptor-pair recombination via deep impurity bands. Applying their model to the presented data and using energy levels of donor (acceptor) like defects of $E_D = 100$meV ($E_A = 0$meV - both measured from midgap), results in high defect concentrations of $10^{19}\text{cm}^{-3} \lesssim N_{Dfct} < 10^{21}\text{cm}^{-3}$. Unfortunately, corresponding charge carrier lifetime measurements are not available, so far.

Improvements If the NPs are contaminated, their production and dispersion processes have to be investigated. Further, a back-surface region or / and a thermal annealing of the metal contacts is proposed to improve the metalization. Since structural defects can be present in the volume or at interfaces, a surface passivation, e.g. by SiO_2 or by SiN is proposed to reduce the number of surface defects. To reduce structural defects in the volume, which are present e.g. due to high temperature gradients during the laser annealing process, it is expected, that an optimization of the laser annealing process or / and a subsequent thermal annealing can reduce / heal these damages. [Ohmer2011a] However, the estimated value N_{Dfct} is in the range of the doping concentration measured using ECV measurements. It is therefore expected, that a high doping concentration is necessary to compensate the defects. Consequently, charge carrier recombination due to the high doping concentration seems to play an insignificant role.

Actually, it cannot be explained satisfactorily, why the efficiency of the np-sample is higher: On the one hand, the doping concentration of the annealed n-type NP layer is expected to be much lower, mainly due to the reduced film thickness and due to the reasons that about 95% of the P dopants are in the SiO_X, which are expected primarily not to diffuse into the Si, c.f. ch. 3.1.1. In consequence, the smaller doping concentration can reduce charge carrier recombination in the emitter (which is expected to be rather unimportant for the B doped Si). On the other hand, due to the same laser preparation, it is expected that a similar amount of

structural defects are present in the samples. Due to the reduced amount of dopants for the n-type NPs, less defects are compensated, which contradict previous conclusions. Consequently, a different contamination of the NPs or maybe experimental fluctuations seems more plausible.

Attempts to increase the photovoltaic efficiency

This section presents attempts to increase the power conversion efficiency of pn-samples: HFS etching is investigated in order to reduce the oxygen content in the annealed layer. The reduction of dopants in the NP layer is studied in order to investigate the importance of charge carrier recombination in the annealed layer. Finally, the realization of a back side doping region (BSR) is investigated in order to reduce recombination at the rear contact.

Effect of oxide removal To investigate the influence of the oxide on the PV efficiency, four pn-sample batches each consisting of three samples are created:

1. "without"
   Reference samples are prepared without any HFS treatment
2. "before"
   Substrates are HFS etched before NP coating
3. "between"
   Substrates are etched for 10min "before" NP coating; an additional etch "between" NP coating and laser annealing is varied from 10s to 2min
4. "after"
   Substrates are etched "before" for 10min and "between" for 20s; etching after laser annealing is varied in between 10s and 30min

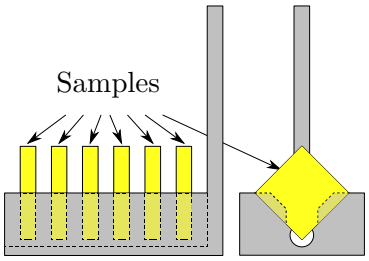

Figure 5.39: Scheme of HFS etching sample holder

For etching times ≤ 10s, the etching is performed by dipping the samples separately into the HFS using tweezers, leading to an incomplete exposure due to the (small) area covered by the tweezers. For longer etching times a sample holder is used, which is schematically displayed in fig. 5.39. With this, etching has become more time efficient but a perfect homogeneity of the sample etching is not ensured, either: On the one hand, HFS wetting is reduced in the area of the sample holders' lamellae (gray-yellow area in the right part of fig. 5.39), which are essential to align the samples. On the other hand, air bubbles randomly build up during the etching process and affix on the samples' surfaces, locally reducing the HFS exchange and its wetting.

The power conversion efficiencies of these samples are displayed in fig. 5.40 as a function of the respective etching times, while the black, red and green symbols give the measured values of each sample and the blue gives the arithmetical mean value with the standard variation indicated by the blue error bars. Further, the average value of each etch is indicated by red broken lines. Due to the small amount of samples of each batch, the determined mean values have to be interpreted as a trend.

For the reference batch without any HFS treatment the efficiency is measured to be 2.2% ± 0.2%. By etching the substrates the efficiency is increased to a mean value of 3.2% ± 0.5% with best values of up to 3.7%. However, by changing the etching time neither a significant trend on

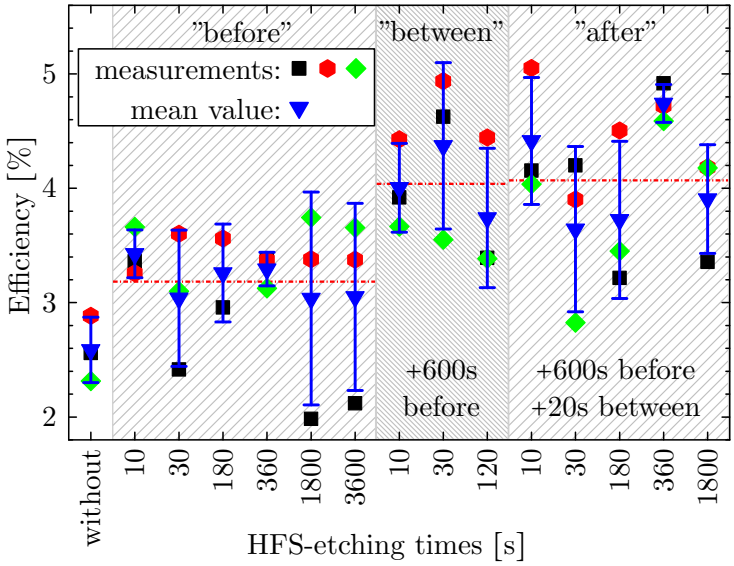

Figure 5.40: Power conversion efficiency in dependence on different HFS treatments

the efficiency nor on the standard deviation are found. It is therefore concluded, that the etching time "before" can be rather short, i.e. ~ 10s. So, in order to guarantee, to remove all SiO_X for further experiments, an etching time of 600s is chosen for substrate etching. Furthermore, it is subjectively observed that an etching of the substrate results in an improved adherence of the NP thin film.

By adding the etching step "between" NP coating and laser annealing, in general a further increase of the efficiency is observed, with a mean efficiency of $4.0\% \pm 0.6\%$ and a best efficiency of 4.9% at 30s. The etching time of this step is varied in a much smaller range, as the thickness of the NP layer decreases for an increased etching time. It can be explained on the one hand using fig. 5.41, sketching an NP film before and after the HFS etching: By removing the silicon oxide from the NPs, also the adhesion of the NPs to the substrate as well as to neighbouring NPs can be reduced, leading to an increased loss of particles, if the etching time is increased. On the other hand it is also possible, that NPs are wiped off. Although it is expected, that the oxygen is not completely removed, it is concluded, that its amount gets reduced by this method significantly.

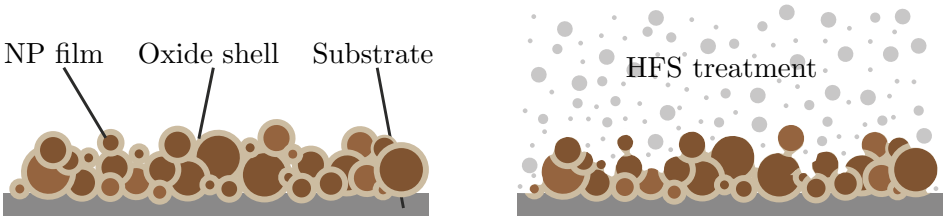

Figure 5.41: Scheme of HFS etching between NP deposition and laser annealing

Due to the tendency of Si to oxidize, it is expected that an oxide film establishes after laser annealing in air, which increases the electrical resistance between semiconductor and subsequently deposited metal contacts. Surprisingly the HFS treatment "after" laser annealing does not show a significant improvement of the efficiency. Since the HFS treatment results in a hy-

drogen passivation of the Si, which is stable much longer than the time to transfer the samples from the HFS treatment into the contact evaporation chamber, it is concluded that the interface between Si surface and Al are oxygen free. According to this result, segregation of oxygen to the surface due to self-refinement - as proposed from SEM images, is of minor importance for the cell's efficiency. It is measured to be $\eta = 4.1\% \pm 0.6\%$ in average and $\eta = 5.1\%$ for the best sample etched "after" for 10s.

Changing the dopant concentration in the dispersion Before, it is proposed that a reduction of the doping concentration in the annealed layer can result in a reduced charge carrier recombination, there. Here, the following two concepts are considered:

On the one hand the NP concentration in the dispersion can be reduced. As shown in fig. 5.4, for small concentrations this results in an incomplete coating. If the in-plane diffusion length of B atoms is similar to the doping depth obtained in ECV measurements ($\sim$ 200nm), dopants are not homogeneously distributed throughout the re-solidified volume. Consequently this attempt is discarded.

On the other hand, it is possible to mix undoped and doped NPs, creating dispersions and thus films of effectively reduced doping concentration[3]. Lechner introduced the definition "digitally doped" for this. [Lechner2008a, p. 29 f.] Samples are created from dispersions containing 10wt.% NPs, consisting of 100% (0%), 10% (90%) and 1% (99%) p-type (nominally undoped) HWR NPs. However, instead of an increase, the efficiency reduces down to almost zero for the less concentrated dispersions. In consequence, recombination due to a high dopant density seems to play only a minor role, whereas these experiments substantiate, that defect compensation by the dopants is essential to create an electrical pn-junction.

Back-surface doping A back surface region (BSR) is established on laser annealed pn-junctions by laser annealing of n-type NPs on the rear surface. The resulting, characteristic PV values are presented in table 5.6. All (even the standard deviations) prove the process to be successful, only for the series resistance a worsening by a factor of ≈ 2 is found.

One explanation can be found in the double-sided laser treatment, creating structural defects and contaminations on both sides of the sample. Since the current has to pass both regions, this leads to an increase of R_{ser}.

Table 5.6: Characteristics of pn-samples with (right column) and without additional BSR (left)

Value	Unit	p-NP|n-c-Si	p-NP|n-c-Si|n-NP
η	%	3.60 ± 0.70	5.94 ± 0.14
FF	%	41.2 ± 2.8	55.7 ± 1.1
U_{oc}	mV	436 ± 20	496 ± 4
J_{sc}	Am^{-2}	173 ± 14	188 ± 2
R_{shu}	$\mathrm{k\Omega cm}^2$	0.6 ± 0.18	2.36 ± 0.25
R_{ser}	$\mathrm{\Omega cm}^2$	1.88 ± 0.61	4.07 ± 0.03
n	1	3.42 ± 0.14	2.03 ± 0.13

Another explanation is based on the self-refining process of Si observed e.g. in the oxygen SIMS measurements of the IR laser annealed samples, c.f. ch. 5.2.2. A segregation of O, esp. of

[3]It is unclear, whether doped NPs are distributed homogeneously in such a film. Position dependent current measurements are needed therefore. Unfortunately, the OBIC's resolution is insufficient.

the not etched n-type NPs, during laser annealing to the annealed surface may create a highly resistive barrier.

Further, by implementing the BSR the ideality factor is reduced down to $n \approx 2$. This substantiates the former assumption that the metal contact at the back side of the prepared samples without BSR forms a Schottky-like contact. [Sah1957]

OBIC measurements

To investigate the in-plane homogeneity of the emitter layer, OBIC measurements (c.f. ch 4.2.3) are performed for a pn-sample using an incident wavelength of 750nm and a spatial resolution of 20µm. The measured data is used to create a two-dimensional image of the sample's spacial short circuit current I_{sc}, which is shown in fig. 5.42. The value of I_{sc} is given by the colour map on the right hand side.

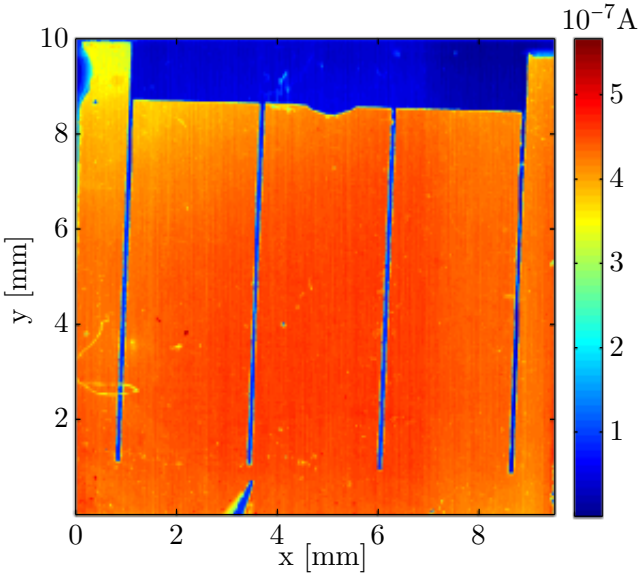

Figure 5.42: OBIC map of pn-sample: Besides the contacts (blue structure) a homogeneous colour is found; the scale bar is shown on the right

The contact fingers on the front can clearly be determined by the blue stripes. The metal inhibits photovoltaic action in this region. The blue spike at the bottom results from the sample holder. Further, an almost radial reduction in $I_{sc}(x, y)$ can be found, which is explained by the spin-coating procedure: While most of the surface is covered with a homogeneously thick layer, it is thicker near the borders and the corners, leading to these boundary effects. Taking a closer look at the measured data, vertical lines exactly aligned to the measurement's borders can be obtained which are a measurement artefact, c.f. ch. 4.2.3.

Last, in some areas it seems as if dust is found on the sample's surface. This may be a result from the laboratory's atmosphere, from unintentional scratches from the tweezers or even from the laboratory clothes. Taking into account these limitations, the laser treatment is found to result in a laterally uniformly doped layer. By comparing this result with the OBIC map of the IR laser annealed pn-sample (fig. 5.27a), the homogeneity of the UV laser annealed sample is clearly improved. This indicates once more that the UV laser treatment is preferable to IR laser annealing.

5.3.5 Summary

By pulsed UV laser annealing of Si NPs deposited on c-Si it is shown, that substrate doping is feasible. SEM and ECV measurements prove that the used laser energy is sufficient to completely melt the NPs and partially melt the substrate, leading to a rapid dopant diffusion in the liquid state. Doping concentrations above 10^{20}cm^{-3} and depths of at least 160nm are measured for samples prepared using the standard parameters.

It is further shown, that the oxygen plays an important role on the film formation: By HFS etching of the substrate and the NP film, the threshold laser intensity to create a closed, flat film reduces. Otherwise, for samples without HFS treatment and for high laser intensities, the samples' surface forms a wave like structure, which is supposed to build up because of self-purification effects and the different expansion coefficients of Si and SiO_2. This waved structure may be interesting for surface passivation or for a better light incorporation.

Opto-electrical characterizations of pn-samples created using p-type or n-type NPs in combination with complementary doped c-Si substrates have furthermore shown a rectifying pn-characteristic in the dark and a PV behaviour under AM1.5 illumination reaching efficiencies of 5.4%. It is expected that an anti reflection coating increases the efficiency by 35% to 45% up to $\eta \approx 7.5\%$. [Deutsch1981] From a one-diode-model fitting of the $I(U)$ characteristics, it is assumed that the metalization as well as contaminations and structural defects are the major reasons for the comparably low efficiency. However, OBIC measurements show a laterally homogeneous I_{sc} map as a result of a homogeneous in-plane doping.

First attempts are performed in order to increase the PV efficiency of the prepared devices. While the reduction of dopants in the NP layer is disadvantageous at the present stage, the removal of O from the NPs and the substrate's surface and a back-side doping turn out to be advantageous, pushing the efficiency up to almost 6%.

5.4 Conclusion

Highly doped NPs are deposited on c-Si by dispersion based spin coating. The necessary dispersions are created by milling the NPs in ethanol. Layer thicknesses of $\approx$ 400nm are realized with this.

Annealing these layers on c-Si using the IR laser unit results in a melting of the NPs and a surface near layer of the c-Si substrate. Deep doping depths d of $11\mu\text{m} \leq d \lesssim 100\mu\text{m}$ are determined using SIMS and from an approximation, respectively. Using XRD, TEM, TED and an anisotropic etching experiment, the re-solidified layer is found to be single-crystalline and of same crystal-orientation as the substrate.

Although a bending of the sample due to the laser annealing in principle disqualifies this method to create PV cells, pn-junctions are prepared to prove, whether this method is able to change the majority dopant type. These cells exhibit on / off ratios of ≈ 120 and PV efficiencies of up to $\eta \approx 2\%$, but a quite inhomogeneous planar I_{sc} distribution.

The application of a UV laser for annealing anneal is found to result in about two orders thinner doping depths of $\approx$ 200nm, which are favourable for PV applications. It is possible to create pn-junctions that exhibit power conversion efficiencies of up to $\eta \approx 5.4\%$, and almost 6% if a BSR is applied.

However, further improvements are expected, if the samples are thermally annealed in order to heal structural defects and if the NPs' oxygen shells is removed completely. The latter can be done on the one hand by chemistry, such as HF or HFS. On the other hand, it is in principle

also possible, to protect the NPs from oxidizing by performing all the production and handling steps in an inert atmosphere.

The actual process as such presents a very simple and presumably low-cost method to create a doping layer. Due to this simplicity it may be interesting already at the present state for industry. Therefore, it is proposed to investigate this method in order to create a doped, back surface region on semi-finished micro crystalline solar cells. First results of such investigations are presented in the following chapter.

Chapter 6

Nanoparticle laser doping of semi-finished PV cells

The investigations presented before show, that it is possible to dope c-Si by laser annealing of highly doped Si nanoparticles (NPs). Further in chapter 5.3.4 a back surface region (BSR) is successfully established using this technique. In the following fundamental experiments are discussed, that apply the presented method on multi crystalline Si (mc-Si) substrates to create a BSR. The primary goal of these experiments is to replace the Al as BSR dopant source: Since Al and Si have different heat-expansion coefficients the standard process of thermal diffusion of Al atoms, leads to wafer bowing. [Schneider2001, Bowden2000, Huster2005, Hartley2002] Bowing increases for reduced substrate thicknesses and therefore disqualifies the process for thinner mc-Si solar cell generations. Another goal is to anneal samples at the back side without harming already existing structures at the front.

For the experiments 250µm thick, mc-Si solar cells from Solland Solar of different production steps are used. Fig. 6.1 shows the scheme of a completely processed cell. The substrate material exhibits a typical B concentration in between 10^{15}cm^{-3} and 10^{16}cm^{-3} ("base", yellow in the scheme).

On the front side a phosphorous doping ("emitter", red) is realized by coating it with phosphorous acid followed by thermal diffusion. The P concentration drops within the topmost 300nm to 400nm from $2 \cdot 10^{21}\text{cm}^{-3}$ down to $\sim 10^{16}\text{cm}^{-3}$.

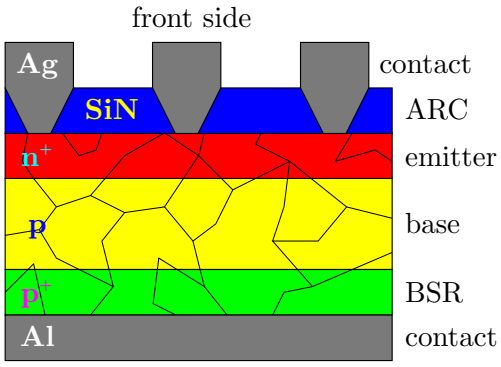

Figure 6.1: Scheme of a Solland PV cell

On top of the emitter, an anti reflexion coating ("ARC", blue) made of SiN with a refractive index of 2.1 ± 0.1 and a thickness of $(80 \pm 5)\,\text{nm}$ is established. Finally, silver (Ag) front contacts are printed from an Ag paste using a grid structure and subsequently fired to realize a contact to the emitter.

The back side is large-area coated with the aluminium (Al) paste "PASE-12" from the company Monocrystal, which is driven into the mc-Si in a co-firing step in order to form the back surface doping and the back surface contact. [PASE-12] Therefore, the wafers are transported through an oven existing of separate heating zones, with the last one heating the sample above

800°C for less than 10s.

For the experiments, $156 \times 156\text{mm}^2$ mc-Si sheets are cut into $10 \times 10\text{mm}^2$ samples that are cleaned in acetone and isopropanol as described in ch. 3.2.4. To establish a BSR substrates are used that exhibit a completely processed front side, but an unfinished back side, i.e. without Al paste steps. Here, they are named "semi-finished" cells. On this back side, thin films made of either NPs or Al are annealed, while the Al is used to create references. For annealing the presented laser units as well as a rapid thermal annealing unit (RTA, c.f. ch. 4.1.1) are used. Additionally, completely finished cells are used as benchmark.

The IR laser is found to be inappropriate for these experiments, since the determined and estimated doping depths d_B (c.f. ch. 5.2.3) are much too thick for a BSR. Nevertheless a few experiments are performed with it, proving the inapplicability. In contrast, the UV laser and the RTA are more useful because of the small doping depth $d_B \approx$ nm (see ch. 5.3.4) and the comparability with the original, commercial production process, respectively.

The chapter is divided primarily in three sections: In the first and second section, reference samples are discussed, that are prepared without any BSR and with an Al-BSR, respectively. In the third section the formation of a BSR by NP annealing is discussed. This is followed by a summary and a conclusion of this process and its applicability for cell fabrication.

6.1 Unannealed reference sample

To create reference samples without any BSR, on the back side of semi-finished samples a 200nm thick Al contact is deposited by thermal evaporation. The $|I(U)|$ characteristics in the dark and under AM1.5 illumination are presented in fig. 6.2. An exponential increase of the current cannot be observed; neither in the dark nor under illumination; instead the current saturates in both directions. Nevertheless, an electromotive force (EMF) with I_{sc} = 8.47mA, U_{oc} = +0.07V, FF = 25% and η = 0.17% is observed under illumination.

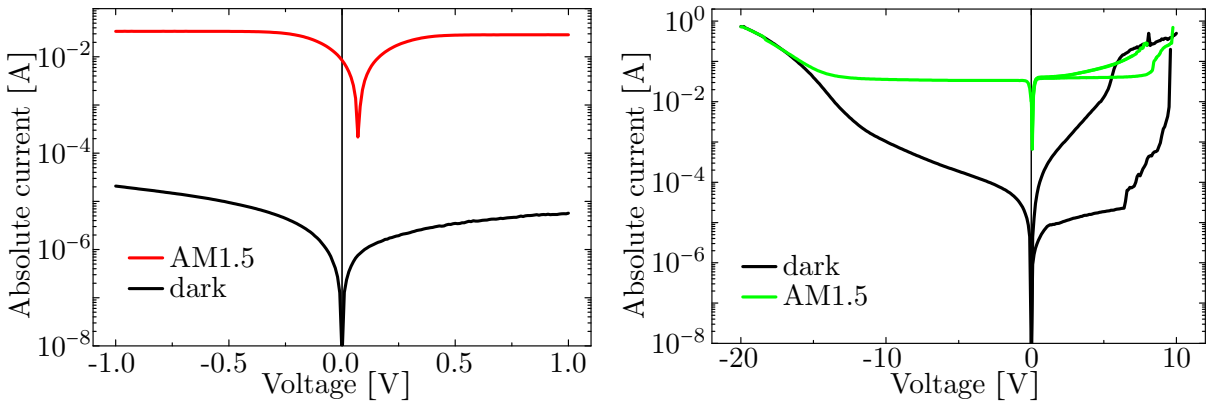

(a) Standard voltage region

(b) Maximum voltage region

Figure 6.2: $|I(U)|$ measurements of semi-finished Solland Solar cells without BSR; the applied voltage ranges vary for the left and the right graph

The non-exponential behaviour can be explained by two series-opposing diodes (2SOD - comparably to an npn-junction): For each voltage sign, one of the junction operates like a diode in reverse direction while the other operates in forward direction. Consequently, most of the

voltage drops over the back-biased junction and in the dark the current is dominated by the junction's reverse current. This assumption is supported by the measurements under illumination, showing constant absolute currents that are close to I_{sc} = 33.6mA of a cell completely finished by Solland Solar for both signs at $|U| \gtrapprox 0.5$V.

For the used samples this 2SOD behaviour can be the result of surface states on the rear surface. Usually these are cited in the middle of the band gap, leading to a band bending towards a lower energy. Schematically this is displayed in fig. 6.3. [Sze2007, p. 139 f.] Actually, this behaviour is neither the result of one sample only, nor is it the result from small voltages, as can be obtained by fig. 6.2b, showing the $|I(U)|$ characteristics of several similarly prepared samples over a bigger voltage range. Due to possible and irreversible breakdown under reverse bias in this high voltage range, each sample is measured only once and each measurement is started at 0V. Under illumination for both directions a stable saturation current of ≈ -33mA ($\approx +39$mA) is observed for $-0.5\text{V} \gtrsim U > -12\text{V}$ ($+0.5\text{V} \lesssim U < +2\text{V}(+8\text{V})$). The strong variation between different samples in fig. 6.2b on the other hand is expected to be a result from the used mc-Si substrate pieces, which can vary significantly from each other.

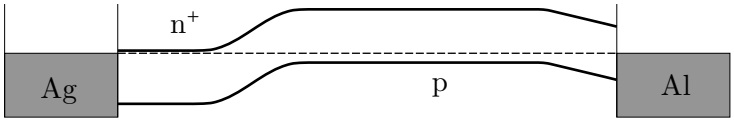

Figure 6.3: Energy band scheme of semi-finished cell with deposited Al contact (2SOD)

6.1.1 Improving the rear contact resistance

It is very implausible to use the obtained data as reference data, as it is much too low for a commercial solar cell. So, in order to determine a better reliable reference efficiency value, a rapid thermal annealing is added after the Al deposition. By this procedure it is expected that the contact resistance of the rear contact gets reduced.

The heat ramps (heating and cooling) are set such, that after 30s the respective maximum temperature is reached, which is hold for 1s. Since the eutectic temperature of the Al:Si-system is T_{eu} = 577°C, the maximum temperatures are changed in between 100°C and 600°C in steps of 100K, which is only slightly above T_{eu}. [Murray1984] Annealing is performed in a nitrogen flow. Fig. 6.4 shows the resulting $I(U)$ characteristics of two samples annealed at 400°C (black lines), one annealed at 500°C (red) and one at 600°C (green). Furthermore, the inset displays the derived efficiencies.

According to the $I(U)$ data after annealing at 400°C the 2SOD behaviour is still present, whereas it vanishes for ≥ 500°C. By further increasing the temperature, a reduction of the efficiency is obtained (see inset). This reduction may be a result of typical fluctuations of the used substrates (e.g. varying crystallite sizes). For an annealing temperature of $500°\text{C} < T_{eu}$ a best efficiency of $\eta = 12.6\%$ is obtained, which in the following is used as the reference efficiency without BSR.

6.2 Al as dopant source

In order to establish a BSR by Al alloying, Al films are deposited by physical vapour deposition or sputter deposition and are annealed using the UV laser or the RTA unit, respectively.

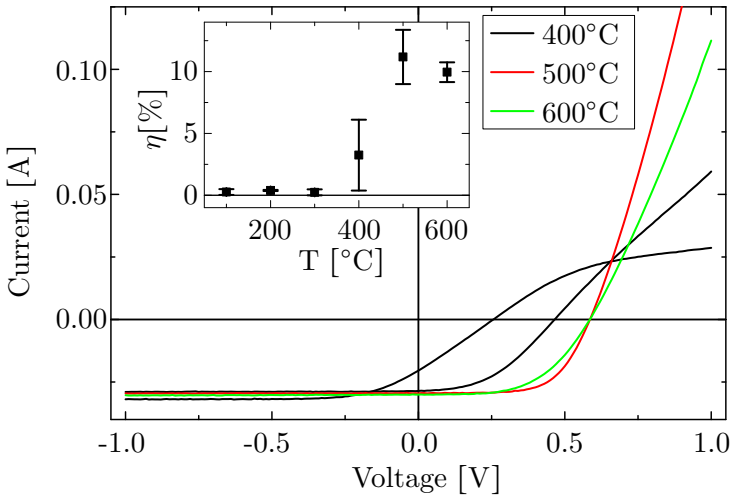

Figure 6.4: $I(U)$ measurements under AM1.5 illumination (lines) and derived efficiencies (symbols in inset) of semi-finished solar cells after contact annealing for 1s at different temperatures

6.2.1 Al-BSR by UV laser annealing

For the creation of a BSR by UV laser annealing of Al, the thickness of the deposited Al is varied between 0nm and 200nm. Subsequently these are UV laser annealed in a nitrogen flow using a primary energy of 6mJ, an attenuating angle of 30° ($\triangleq$ 850mJ/cm^2), a repetition frequency of 100Hz and a scanning velocity of 2.7mm/min. For electrical characterization 200nm thick 8×8mm^2 Al contacts are deposited on these samples by physical vapor deposition. (Three samples of each variation are prepared for better statistics.) The characteristic PV values J_{sc}, U_{oc}, n and FF of these samples are presented in fig. 6.5. To classify the results, the PV values of the reference sample without BSR (right, but one) and of a sample, that is completely processed by Solland Solar (right), are presented. For the latter $\eta = (14.7 \pm 0.1)\%$ is determined.

From the graph it is found, that already by laser annealing of the bare rear side (0nmAl+laser) the efficiency can be increased. This is due to the reduced 2SOD behaviour, which is explained by partial melting of the rear surface during annealing, which can lead to a reduction of defects there. However, by annealing of the Al layer a significant increase in all PV values is obtained, whereas the influence of the layer thickness is very small for the thicknesses used here.

Comparing the results with the reference samples, it is found that U_{oc} and I_{sc} are close to that of the completely processed sample. It is therefore suggested that a BSR establishes by laser annealing of the Al layer. However, due to the worse FF, η is limited to a maximum efficiency of 12.1%, which is 2.6% below the value of the completely processed sample and 0.5% below the reference sample without BSR (absolute percentages).

The reduction of FF is ascribed to an increased ideality factor, which can be a result of chemical or structural imperfections in the layer annealed layer, c.f. ch. 5.3.4. [Steingrube2011] To decrease the concentration of structural defects, thermal post-annealing is proposed, but for these samples care has to be taken in order not to shunt the emitter. Anyway, a difference between the front sides of annealed and unannealed samples is not observed; neither by the bare eye, nor by using SEM. It is therefore concluded, that this method does not significantly influence the front side.

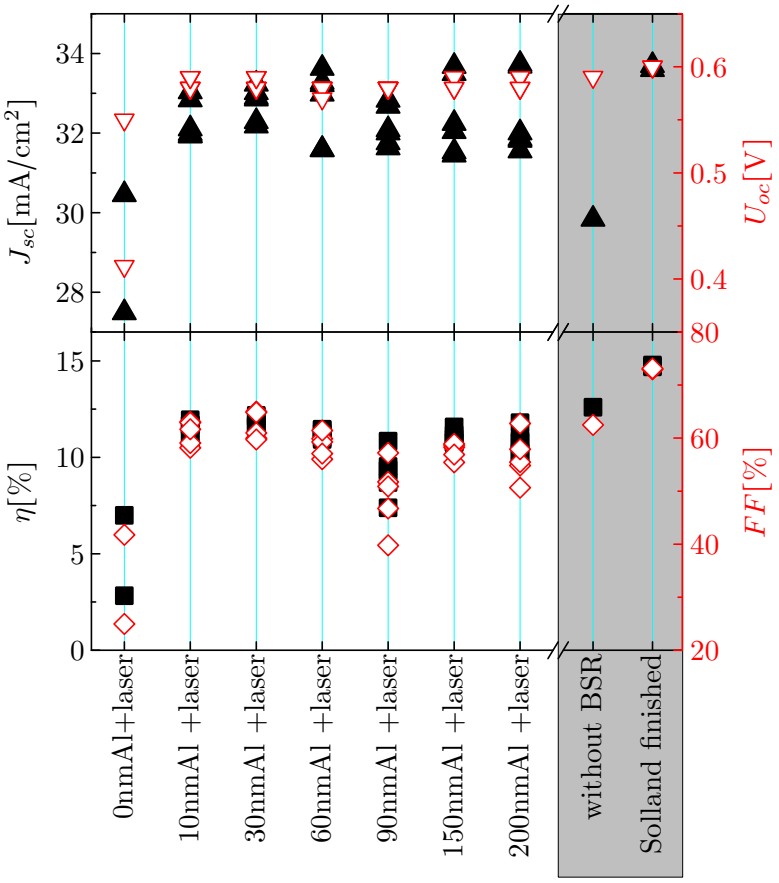

Figure 6.5: PV values of samples that are prepared by UV laser annealing for BSR creation; the Al layer thickness is varied; reference samples are added on the right

6.2.2 Al-BSR by rapid thermal annealing

For the creation of an Al-BSR by RTA, 1µm or 10µm thick $\approx 9 \times 9\text{mm}^2$ Al layers are deposited on the rear side of semi-finished cells by sputter deposition. Subsequently, these samples are annealed in the RTA unit in a vacuum with a base pressure of $\leq 10^{-4}$mbar. The temperature ramps (heating and cooling) are set to 50K/s and the maximum temperature of 800°C is hold for 10s. (The temperature is chosen in agreement with the standard process at Solland Solar.) The samples are then characterized by $I(U)$ measurements. The characteristic PV values are plotted in fig. 6.6; while the dark (light) gray samples mark the 1µm (10µm) thick Al contact samples. Further, the sample 20s-No2 is annealed for 20s, while the others are annealed for 10s. (It has to be mentioned that these investigations are from an initial stage.)

For all samples the 2SOD behaviour is vanished and a PV effect is measured. Nevertheless, differences are observed:

1. thicker Al layers lead to significant improvements in all PV values; the thinner Al layer may be too thin for these experiments, as the whole Al is alloyed in the Si and the concentration at the surface may be too small.

2. longer annealing times reduce the properties drastically; it is expected that for longer times the front contacts start to shunt the emitter region.

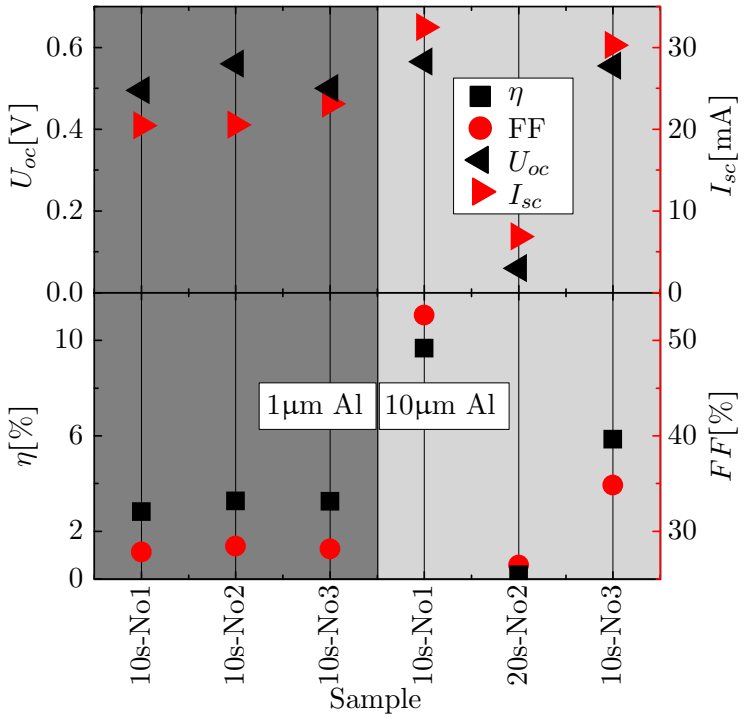

Figure 6.6: Characteristic PV values of semi-finished cells after RTA of the Al-BSR

For these very few samples, the best one reached η = 9.8%, FF = 52.6%, U_{oc} = 0.57V and J_{sc} = 32.6mA/cm^2, which is close to the Al laser doped ones.

6.3 NPs as dopant source

To replace the Al from the process, highly B doped HWR NPs are coated from a 10$wt.$% dispersion using 2000r/min and 2000r/(min · s) as spin coating parameters, on the rear surface and are annealed using the RTA or the UV laser unit. Due to the surface roughness, see fig. 6.7, which is supposed to be the result of an HF:HNO_3 wet chemical etching, the thickness of the NP film varies locally in between ≈ 200nm and ≈ 1.3µm. [Schultz2003, Hylton2006, ch. 3, esp. fig. 3.17c] After the respective annealing, 200nm Al contacts are evaporated on the annealed surface and the samples are characterized by illumination dependent $I(U)$ measurements.

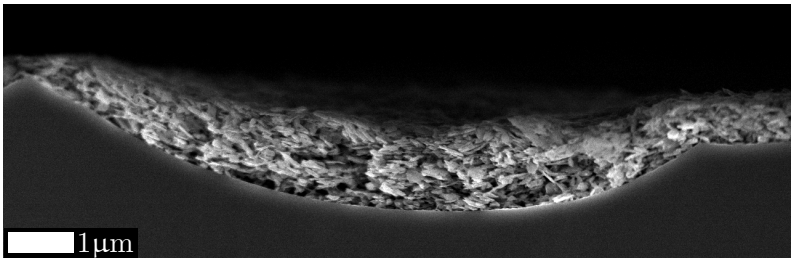

Figure 6.7: Cross sectional SEM image of HWR NPs deposited on mc-Si rear surface

6.3.1 NP-BSR by rapid thermal annealing

For RTA treatment of NP coated, semi-finished solar cells, the temperature ramps are set to 50K/s and a holding time of 10s is applied. In these first experiments the maximum temperature is changed in between 1200°C and 800°C. The efficiencies of the prepared samples are plotted in fig. 6.8.

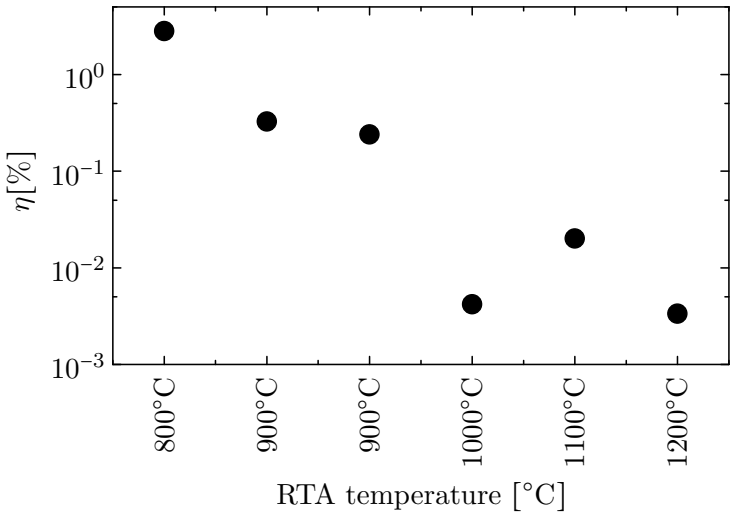

Figure 6.8: Power conversion efficiency of RTA NP-BSR semi-finished cells

A best efficiency of only ~ 2% is obtained for the sample annealed at 800°C. For higher annealing temperatures the efficiency decreases exponentially, disqualifying this process for further experiments. One reason for this decrease is found in the front side metalization, that increasingly shunts the emitter for higher temperatures. In order to exclude this shunting, for future experiments it is proposed to apply the presented processes to samples without a front side treatment.

6.3.2 NP-BSR by UV laser annealing

UV laser annealing of NP coated, semi-finished cells is done the same way as described in ch. 6.2.1. Figure 6.9 shows the resulting $I(U)$ characteristic (black scatter plots) in the dark (open circles) and under AM1.5 standard illumination (closed circles) in comparison with the characteristics of a sample completely processed by Solland Solar (red scatter plots).

Both graphs look rather similar, esp. I_{sc} and U_{oc} are close to each other. However, two important differences are obtained, reducing the efficiency: On the one hand the fill factor of the annealed sample is significantly lower, on the other hand the current at 1V is reduced by almost one order of magnitude leading to the conclusion that also the series resistance is increased significantly. One possibility for both reductions may be inhomogeneities, such as impurities from the NPs or structural defects due to the laser annealing process. However, an HFS treatment to remove the oxide from the NPs cannot be applied for these samples, because the front side preparation gets harmed by the etching.

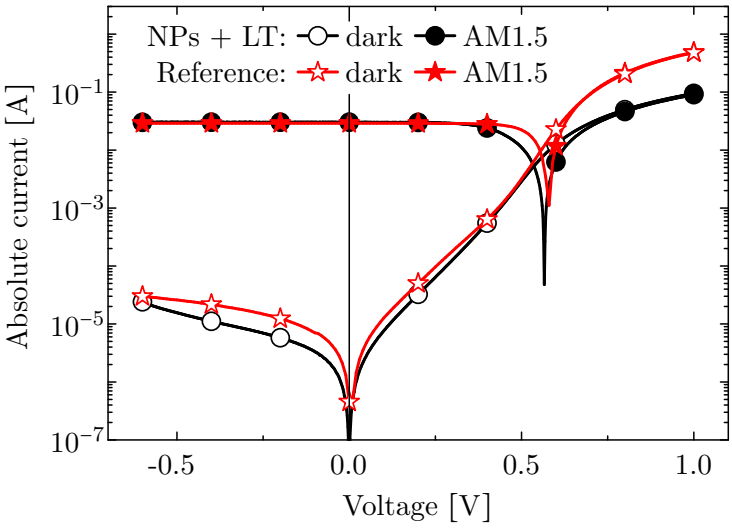

Figure 6.9: $|I(U)|$ measurements of a NP-BSR sample in comparison with a sample completely processed by Solland Solar

Variation of process parameters

Samples are created at varying coating parameters (see table 6.1 - last sample is coated twice at a rotational speed of 1000r/min to further increase the NP film thickness) and the characteristic PV values are presented in fig. 6.10.

Table 6.1: Labeling of NP annealed samples

sample name	NP-coating	UV-annealing
–NP –Laser	—	—
–NP +Laser	—	✓
+NP –Laser	2000r/min	—
+NP +Laser	2000r/min	✓
+NP(1k) +L	1000r/min	✓
+NP(4k) +L	4000r/min	✓
+NP2×(1k) +L	2×1000r/min	✓

Again it is found, that a laser annealing of the bare rear surface (–NP +Laser) leads to an improvement. In contrast, the deposition of NPs without a laser annealing results in comparable values as obtained without rear surface treatment, supposedly due to the bad contacting. By laser annealing these layers, an increase in the PV values is obtained. Actually, J_{sc} and U_{oc} approximate the values of the completely processed reference sample, but due to the reduced fill factors the best efficiency is only 12.2%. Anyway, a clear correlation of the spin coating parameters, i.e. the deposited NP film thickness on the PV values cannot be obtained.

Although the NP laser annealed samples do not show higher characteristic PV values than completely processed cells, the presented process may be interesting for solar cell manufacturers, because the thermal treatment of the rear surface is replaced by a laser annealing. In principle this can be designed to anneal designated areas, only. [Tucci2008] Nevertheless, a decent cost listing is not performed, for the processes presented here. Further, these results are quite similar

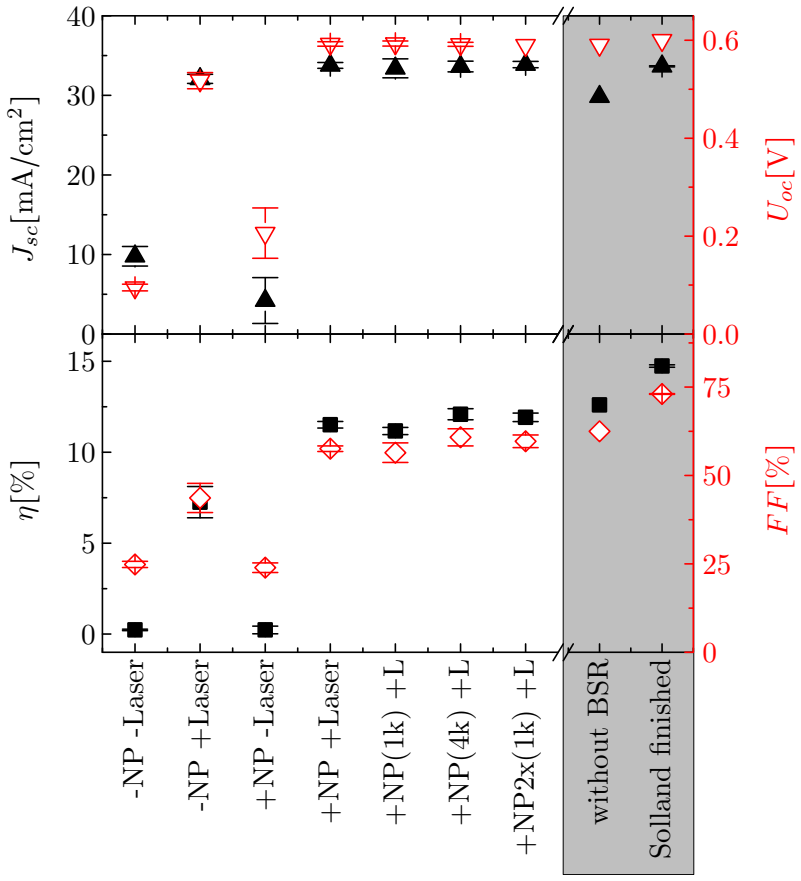

Figure 6.10: Characteristic PV values of annealed semi-finished cells (for labeling see table 6.1)

to those of the UV laser annealed Al thin films, c.f. ch. 6.2.1. Therefore it is concluded that on the one hand, the creation of a BSR by UV laser annealing of highly doped Si NPs is feasible. On the other hand, the results support the idea of laser induced structural defects.

6.4 Summary and conclusion

A BSR can be realized by UV laser annealing of Al films as well as NP layers without harming the front side significantly. However, so far the efficiency of the solar cells that are completely processed by Solland Solar are not reached. Therefore it seems rather inadequate to state, whether the prepared samples really have the potential to achieve or even exceed the PV values of the optimized Solland Solar process.

For most of the UV laser annealed cells I_{sc} and U_{oc} are comparable to the values obtained for the completely processed reference, whereas the fill factors differ by up to 20% (absolute) for both methods. This supports the assumption, that a high amount of defects are incorporated by the laser annealing at the back side and shows that for the applied process a thermal post-annealing may be important to improve the efficiency. Further, it is suggested to include an HF or HFS etching of the NP layer in order to reduce the oxygen content in it and therefore in the annealed thin film. Nevertheless, since no changes are observed at the front side a laser-post-processing of the back side is possible without harming the front.

Due to the simplicity of this method to realize doping and due to the possibility to realize

locally defined doping regions, e.g. for local back surface emitter cells, it may be interesting for future applications in PV production. Furthermore, these few and initial investigations show that doping is also possible on mc-Si substrates without destroying them.

Chapter 7

Spark-plasma sintering of Si nanoparticles

The experiments discussed in this chapter are performed in order to answer the fundamental question whether it is possible to create a pn-junction made of complementary doped Si nanoparticles (NPs) solely, which at best shows photovoltaic (PV) action, too. Microwave reactor (MWR) NPs (see ch. 3.1.1) with a mean size of (20 ± 10)nm and a boron or phosphorus doping of $\sim 5 \cdot 10^{20}\mathrm{cm}^{-3}$ are therefore sintered by spark plasma sintering (SPS, see ch. 4.1.2). The resulting samples are characterized structurally and electrically. [Meseth2012a, Becker2012] As these samples are created only from NPs, the investigations allow for a directer insight of the pn-junction of NPs. The chapter is finished with a discussion about the applicability of this process for PVs.

7.1 Sintering process

As discussed in ch. 4.1.2, for the SPS process NPs are filled in a graphite die and sintering is done by heating the powder up to 1050°C while a constant pressure is applied to it. For a typical SPS process fig. 7.1 shows the time dependency of

a) the relative z-position z of the compressing piston

b) the velocity v of the compressing die, i.e. the time derivative of z

c) the temperature T measured by the pyrometer

At the beginning and the end of the process (fig. 7.1 c)) a temperature of T = 400°C is displayed because the pyrometer cannot measure temperatures below T = 400°C. After the initial heating during the first ~ 5min a linear increase of 100K/min is found in between T = 500°C and the maximum temperature of T = 1050°C, which is held for 3min before cooling-down.

According to fig. 7.1 a) and b) two regions of compaction are found: At ≈ 2min it is attributed only to the applied pressure of the die, since the temperature at that early stage is much too small to create a significant change of the NP structure. The second compaction occurs at around 10min, which can be linked via fig. 7.1 c) to a temperature of $T \approx 900$°C. As discussed in ch. 2.2, the melting temperature of a particle is inversely proportional to its diameter. It is therefore expected that this second compaction is a result of NP melting which leads to a

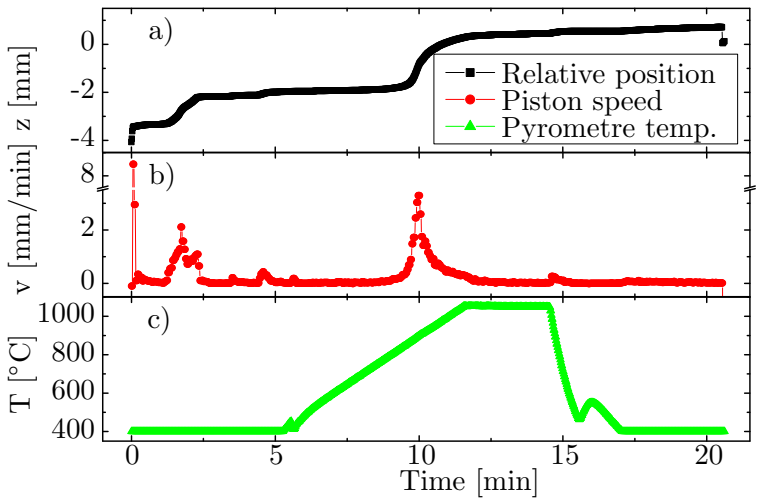

Figure 7.1: Typical SPS-process: a) relative position of piston; b) velocity of piston; c) temperature measured via pyrometer

microscopic coagulation of the NPs and due to the applied pressure from the SPS-unit to a further macroscopic compaction of the sample. [Becker2012b]

An additional explanation for the compaction is based on the NP oxide shell. As the shell is very similar to glass, it is reasonable that its viscosity decreases with the temperature. [Poole1949] Consequently, at high temperatures the oxide can flow into pores and compact the material. Further, it can also lead to a precipitation of the glass, which is observed in several experiments. [Schierning2011a]

For the characterization, the sintered samples are cut into pieces of $\approx 5 \times 14\text{mm}^2$, which are ground, polished and cleaned. The latter is performed by successive ultrasonic treatments in acetone, ethanol and isopropanol, each for 10min. For samples that are characterized electrically, electrodes of 1mm diameter and 200nm thickness are evaporated on the respective surfaces by physical vapor deposition (see ch. 4.1.3) at deposition rates of $(3.0 \pm 0.6)\,\text{Å/s}$. Metal used are either gold (Au) or silver (Ag), depending on the experiment and on the subjacent material.

In the following one pn-device and several unipolar devices are investigated, while the latter are made of either p-type or n-type Si MWR NPs, the pn-device is made by stacking a layer of n-doped Si MWR NPs on top of a layer of p-doped Si MWR NPs before sintering. At the end of the chapter a third type of device, the so called “pin”-device, is discussed (see fig.s and and corresponding discussions). This sample is prepared similar to the pn-device except that an intermediate layer consisting of a $\approx 1:1$ mixture of n- and p-type Si MWR NPs is inserted between the p- and the n-type layer. The idea is that dopants compensate each other in that area to create an almost intrinsic region and therefore to increase a possible space charge region between p- and i- as well as n- and i-type. But then again, it needs to be considered that the mixing of boron and phosphorous can also result in a higher density of impurities, changing the intrinsic properties of that layer significantly.

7.2 Structural and chemical investigations

In this section, the SPS samples are characterized structurally in order to clarify the microstructure and the chemical composition. The latter is done primarily to determine, whether a dopant

diffusion takes place in the junction region of the pn-sample. A significant diffusion can result in a charge carrier compensation, which can lead to an increased space charge region, which may be beneficial for PV applications. Structural investigations are performed by scanning electron microscopy (SEM) and chemical investigations are performed by electron dispersive x-ray (EDX) spectroscopy and by scanning potential Seebeck microscopy (PSM) measurements.

7.2.1 Scanning electron microscopy and energy dispersive x-ray spectroscopy

In fig. 7.2 SEM micrographs of the surface of the p-type region of an SPS pn-sample are shown, varying in the magnification. For the overview image (fig. 7.2a), darker dots of up to 100nm diametre and almost horizontally aligned lines are found on the surface on the one hand. The dots may be the result of locally higher sintering temperatures or a higher concentration of activated dopants. The lines are expected to be a result from the grinding and polishing procedures.

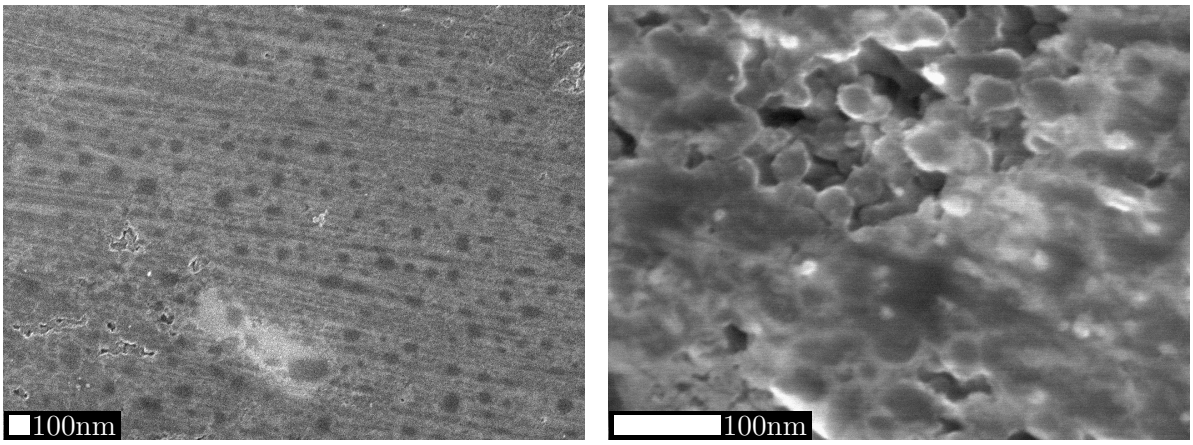

(a) Low magnification (b) High magnification

Figure 7.2: SEM micrographs of p-type area of an SPS pn-sample at different magnifications.

Further, cavities and holes are observed, which indicate that the SPS process is not optimized yet. Fig. 7.2b takes a closer look at one of these holes. A nano structure is found here, which is formed presumably by primary, as well as sintered, if not even fused NPs. Since the structures are found to be ≈ 50nm, i.e. ≈ 30nm bigger than the mean initial NP diameter, this image supports the idea of coagulation of smaller particles on bigger particles as proposed by Schierning et al. [Schierning2008]

Last, in fig. 7.2a below the center, a brighter structure is observed. By taking an SEM image of much lower magnification (see fig. 7.3) similar changes in brightness are observed throughout the whole cross section. In fig. 7.3, these structures are found to be tube-like and aligned vertically and mostly perpendicular to the applied pressure. To clarify the chemical nature of these structures, an EDX line scan is prepared along the blue line in the SEM micrograph. The result is shown in the upper part of fig. 7.3, displaying the elements O, P and S as black squares, red circles and green triangles, respectively. (Unfortunately, B cannot be detected with the used detector.)

Since no S is present in the sample, this signal is used to determine the background. By comparing the S to the P signal, it is found that the P signal shows an almost constant offset in between 0mm and ≈ 1.6mm with several spikes, whereas the signal drops to the background at

positions bigger than ≈ 1.6mm. In conclusion the p- and n-doped region seem to be separated still after the sintering.

In contrast, O is found throughout the whole investigated area, also exhibiting several spikes. The existence of O in the SPS sample is a result of the NP's shell. [Lechner2008, Stegner2009] By comparing the O spikes with the SEM picture, it is found that the described tube-like, bright structures are O enriched. According to investigations by Schierning et al. the particle's core-shell structure completely vanishes after the SPS process and the two phases Si and SiO_X separate from each other by viscous flow and form these tube-like structures. [Schierning2011a]

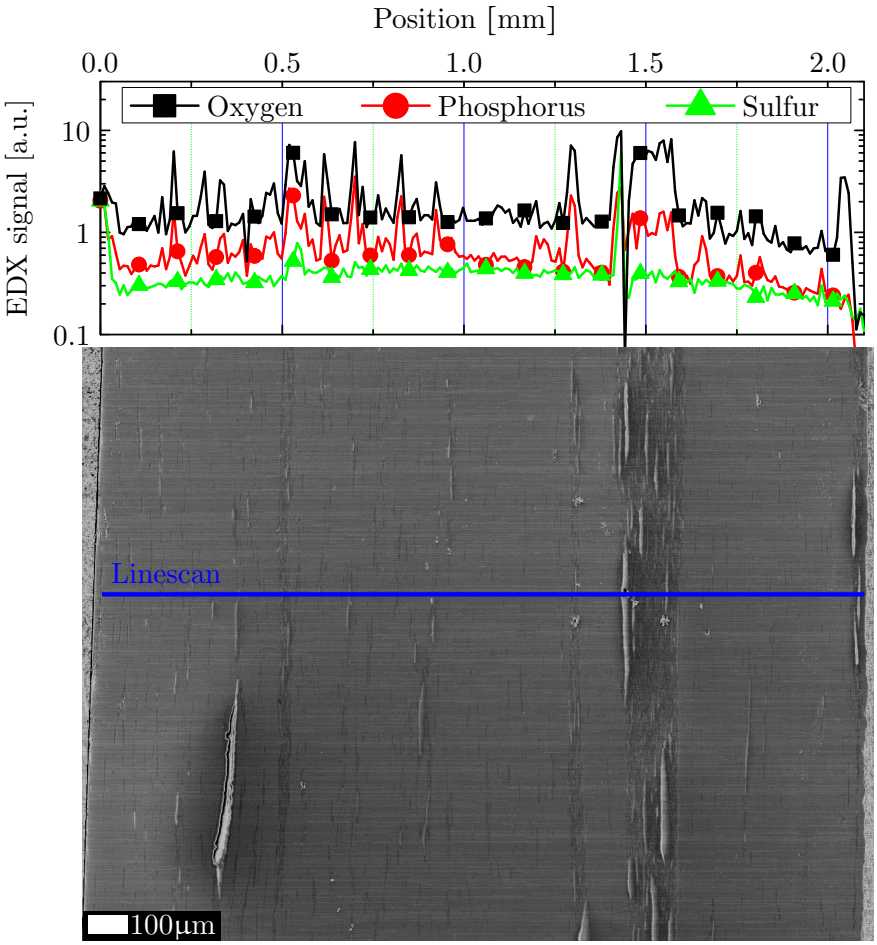

Figure 7.3: EDX scan of a SPS sample: vertical, white lines consist of a high amount of O

Comparing furthermore the signals of O and P shows that the spikes of both signals are sited at the same positions, leading to the conclusion that P concentrates at the oxides. A similar accumulation of phosphorus in SiO_X is observed in the oxide shell of n-type Si NPs, c.f. ch. 3.1.1.[Lechner2008, Stegner2009] Although, the solubility limit of P in Si of 2.4at.% at 1180°C is not reached here on the one hand and the P-Si bond is principally preferred to the P-O bond on the other hand, it is concluded that the concentration of P in the oxide does not significantly change due to the sintering. [Olesinski1985]

An explanation for this is found in the characteristic diffusion lengths of P in both materials: While in SiO_X it is 0.6nm for 1h at 900°C in Si it is ≈ 20nm. [Schierning2011a, Perego2010a] Consequently, P is bond very strong to the oxide and its small release even at high temperatures

is considered to be the limiting factor for the inhomogeneous P concentration. [Schierning2011a]

7.2.2 Scanning potential Seebeck microscopy

Although from EDX measurements do not show a significant diffusion or a mixing of the dopants near the pn-junction region, diffusion cannot be excluded, because of the spatial resolution of the EDX. Therefore, an SPS pn-sample is characterized by scanning potential Seebeck microscopy (PSM, c.f. ch. 4.2.2). The result is illustrated in fig. 7.4, showing the Seebeck coefficient for an area of $0.2 \times 1.4\text{mm}^2$ as a 3D-plot. The graph indicates two quite flat plateaus at $\Sigma \approx 100\mu\text{V/K}$ on the right and $\Sigma \approx -80\mu\text{V/K}$ on the left.

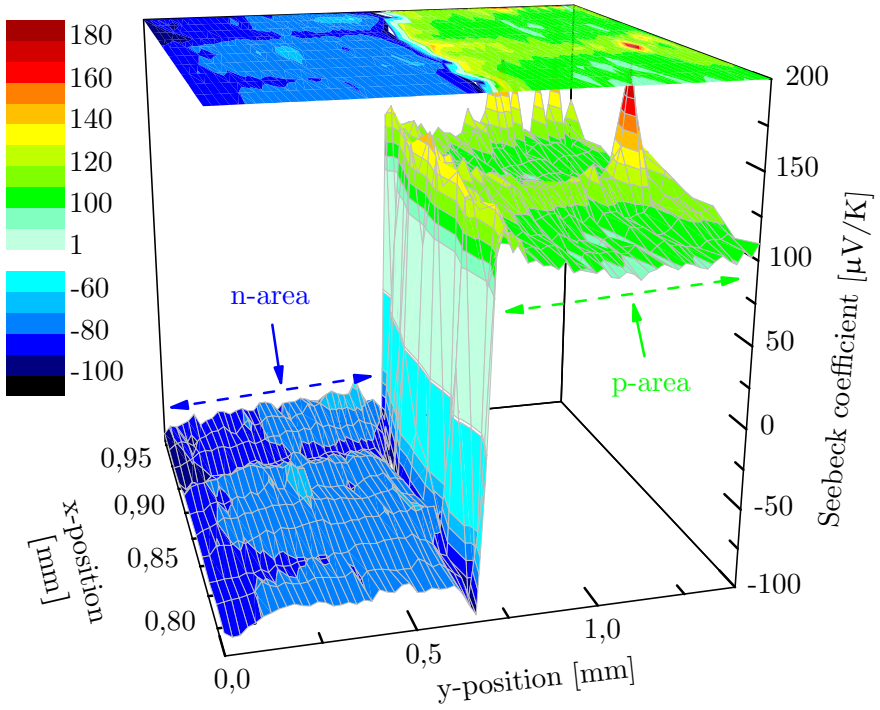

Figure 7.4: Microscopic scanning Seebeck measurement of a pn-device made by SPS

The plateaus can be identified as the n-type and p-type area due to the sign of the Seebeck coefficient. By applying eq. (4.6) the respective, concentrations of activated dopants are calculated to be $N_D = 1.2 \cdot 10^{20}\text{cm}^{-3}$ and $N_A = 2.6 \cdot 10^{19}\text{cm}^{-3}$, which are in the range of the initial doping concentration of the NPs. However, since for the calculation the effective masses of holes $m_h^* = 0.98 \cdot m_e$ and electrons $m_e^* = 0.49 \cdot m_e$ in c-Si are used, this of course may be one reason for inaccuracies.

The sharpness of the transition, confirms the assumption of small dopant diffusion during the sintering process. In order to take a closer look at the transitional region, fig. 7.5 displays a single scanning line of the 3D graph. Overshoots of $\approx 30\mu\text{V/K}$ are found in a width of $\approx 100\mu\text{m}$ on both sides. These are investigated in an article by Becker et al. [Becker2012] The authors used different models to fit the measured data.

According to these calculation, NPs intermix near the junction due to the mechanical filling procedure and melt during the sintering process. This leads to a dopant compensation in the transitional region of the sintered sample. Consequently, the regions are either n- or p-doped, only varying in the concentration. Due to the reduced effective number of dopants, the Seebeck

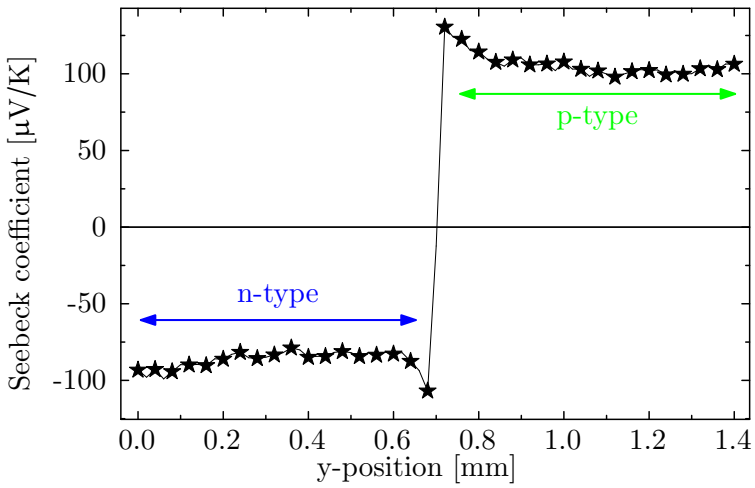

Figure 7.5: Representative single line scan in y-direction of fig. 7.4

coefficient increases in the transitional region, leading to the determined overshoots.

Thus, it is concluded that on the one hand a partial compensation takes place during the sintering process, which may be beneficial for PV applications. On the other hand, the dopant diffusion length is rather small and the effects from mechanical mixing are expected to be of major importance.

7.3 Electrical and opto-electrical characterization

In order to investigate the device's electronic behaviour, esp. whether the pn-samples behave like a PV diode. The samples are characterized electrically using capacitance-voltage ($C(U)$, c.f. ch. 7.3.1) and current-voltage ($I(U)$, ch. 7.3.2) measurements. To clarify, whether a PV effect is present, illumination-, temperature- and time-dependent $I(U)$ measurements are furthermore performed. Additionally an SPS pin-sample is analyzed using the optical beam induced current (OBIC, ch. 4.2.3) method.

7.3.1 Capacitance-voltage measurements

The $C(U)$ measurements of the the pn-sample are performed at a frequency of f = 1MHz and the result is shown in fig. 7.6. Although the increases in capacitance is only 3.78%, a non-symmetric dependence on the applied voltage is found. It is therefore concluded that an electronic band bending must be present in the sample, which is a first indication that a depletion region between n- and p-doped area is present.

However, from the $C(U)$ measurements it is neither possible to derive the built-in voltage U_{bi}, nor the dopant concentration N using the standard model, c.f. eq. (4.14). Respective calculations result in U_{bi} = 40V and $N = 6 \cdot 10^{14}\text{cm}^{-3}$, which are implausible. It is therefore concluded, that the simple model is not applicable here. The main reason may be the huge amount of chemical and structural imperfections.

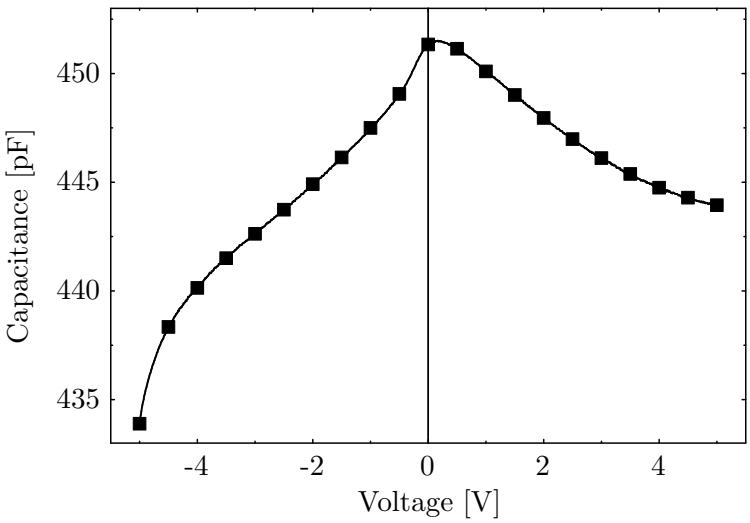

Figure 7.6: $C(U)$ measurements of SPS pn-sample

7.3.2 Current-voltage measurements

In order to substantiate, that an electrical band bending is present in the pn-sample, it is characterized using $I(U)$ measurements. The measured data is shown in fig. 7.7 as a scatter plot of black rectangles in comparison with the $I(U)$ characteristics of a uniformly n- (blue triangles pointing up) and a uniformly p-doped (green triangles pointing down) sample.

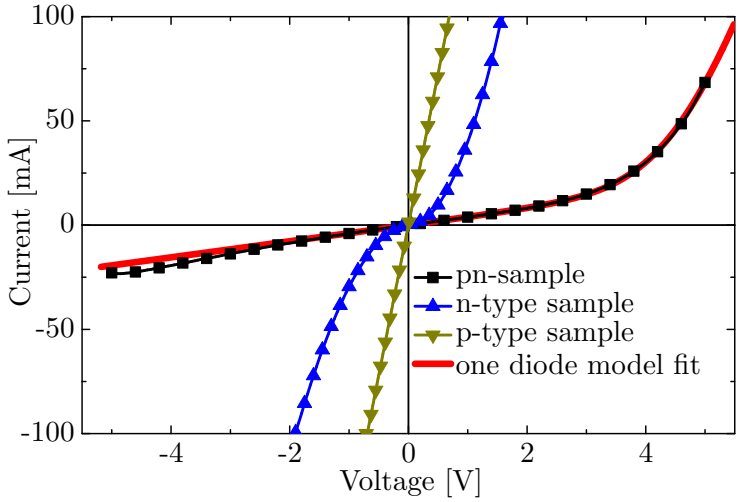

Figure 7.7: $I(U)$ graph of a pn- (black), a uniformly n-doped (blue) and a uniformly p-doped SPS sample without illumination; red line indicates a fit, from one diode model

The $I(U)$ characteristic of the pn-sample shows an exponential increase for voltages $U > 0\text{V}$ and an almost linear dependence for $U < 0\text{V}$ with an on / off ratio of 3.5 at $+5\text{V}/-5\text{V}$. Due to this rectification the existence of a space charge region between p- and n-doped areas and thus a band bending is concluded, substantiating the results from the $C(U)$ measurements.

In contrast to the pn-sample both uniformly doped samples show a symmetrical behaviour. This confirms that the rectification found for the pn-sample is not a result from Schottky contacts between the metal and the highly doped semiconductor material. Otherwise, the absence of the

Esaki-spike, which is typical for tunnel-diodes in forward direction is a supposed to be a result of the great amount of imperfections in the sample.

In order to find out, which processes limit the functionality of the pn-device, the $I(U)$ data of the pn-sample is fitted according to the standard one-diode model, c.f. ch. 4.2.3. For the following parameters:

- $R_{ser} = 9\Omega \triangleq 6.3\Omega\text{cm}^2$ (series resistance)
- $R_{shu} = 250\Omega \triangleq 175\Omega\text{cm}^2$ (shunt resistance)
- $n = 22$ (ideality factor)
- $I_0 = 17.5\mu\text{A} \triangleq 25\mu\text{A/cm}^2$ (saturation current)

the fit is found to be in good agreement with the measured data, showing that in principle the $I(U)$ characteristic can be described by a pn-diode. However, results are far away from a typical values for a pn-diode. The unusually high ideality factor is expected to be a result from the non-ideal resistances. The primary structural reasons for the small R_{shu} are tunneling mechanisms due to the reduced space charge region (only a few nm for such high doping concentrations) and the high concentration of defect states in the band gap. [Perez-Wurfl2009] Further, R_{ser} is supposed to be increased due to the high oxygen concentration, usually leading to a reduction of the electrical conductivity in Si.

Illumination dependence

Since $I(U)$ measurements show a diode like electrical behaviour for the pn-sample, illumination dependent $I(U)$ measurements are performed for the three samples to find out, whether a PV effect can be observed, too. For these experiments the white light of a high intense 1000W halogen lamp is used. The resulting $I(U)$ data are shown as scatter plots in fig. 7.8 as black squares (pn-sample), red triangles pointing upwards (n-type sample) and green triangles pointing downwards; with the dark (illuminated) measurement data as open (filled) symbols.

For both uniformly doped samples the $I(U)$ characteristics with and without illumination, are straight lines through the origin and vary only slightly from each other.

In contrast the $I(U)$ characteristic of the pn-sample shows a significantly different behaviour: While in the dark a line through the origin is measured, too, under illumination on the one hand the slope significantly increases. This is attributed to the increased conductivity in the heated sample due to the intense halogen lamp's illumination. On the other hand, an electromotive force (EMF) is measured in between $0\text{V} \leq U \leq 2\text{mV}$ with a short circuit current of $I_{sc} \approx 50\mu\text{A}$. If this EMF is characterized according to PV methods, a fill factor of $FF \approx 25\%$ and an efficiency of $\eta \approx 2 \cdot 10^{-7}\%$ are derived. However, due to the small efficiency it is unclear whether the primary origin for the observed EMF is found in a PVs. It is also possible, that a thermoelectric (TE) effect is responsible for it, as the high intense halogen lamp increases the temperature of the sample significantly. The following section aims to clarify this question.

7.3.3 Investigations on the origin of the observed electromotive force

Experiments are performed in order to find out, which effect to be the most prominent to create the observed EMF in the pn-sample under illumination.

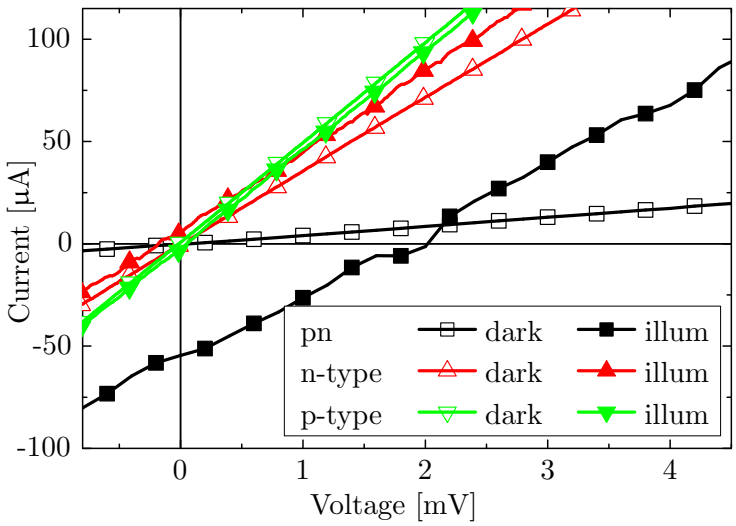

Figure 7.8: $I(U)$ characteristics of a pn- (black squares), a uniformly n-doped (red triangles pointing up) and a uniformly p-doped (green triangles pointing down) sample, measured in the dark (open symbols) and under illumination with a high intense halogen lamp

Time dependent short circuit current measurements

In a first experiment time dependent short circuit current ($I_{sc}(t)$) measurements of a pn-sample are conducted while it is ...

a) ... illuminated using the high intense halogen lamp

b) ... placed on a hot plate heated up to 45°C

both for 1.3s. In both cases, the energy (heat / photons) is incorporated rectangular to the junction interface and the contact is realized by clamping cables on the evaporated metal contacts. Both types of experiment are conducted in a simple way: For the light experiments the lamp is turned on and a metal plate, placed in between sample and lamp is removed and placed back after 1.3s. Regarding the hot plate experiments the sample is manually placed on and removed from the hot plate. $I_{sc}(t)$ measurements are performed using the Keithley SCS 4200 unit at a sample rate of ≈ 13ms. The resulting data is presented in fig. 7.9, showing a similar behaviour concerning the peak value on the one hand and the shape of the graph on the other hand, for the light (black scatter plot) and the hot plate (red scatter plot) experiment.

According to these results, the mechanism for the development of the I_{sc} does not necessarily depend on photons. Instead a temperature difference of max. 45°C – 24°C ≈ 20°C can create similar data. The used temperature difference seems plausible for the applied, high intense halogen lamp. Consequently, the probability is high that the observed EMF detected for the pn-sample under illumination of the high intense halogen lamp is dominated by the TE effect. However, the presence of a PV effect cannot be excluded from these experiments.

Optical beam induced current measurements

In a second experiment, optical beam induced current (OBIC) measurements are performed to determine, whether it is possible to separate the PV effect from the TE effect locally. Here, only

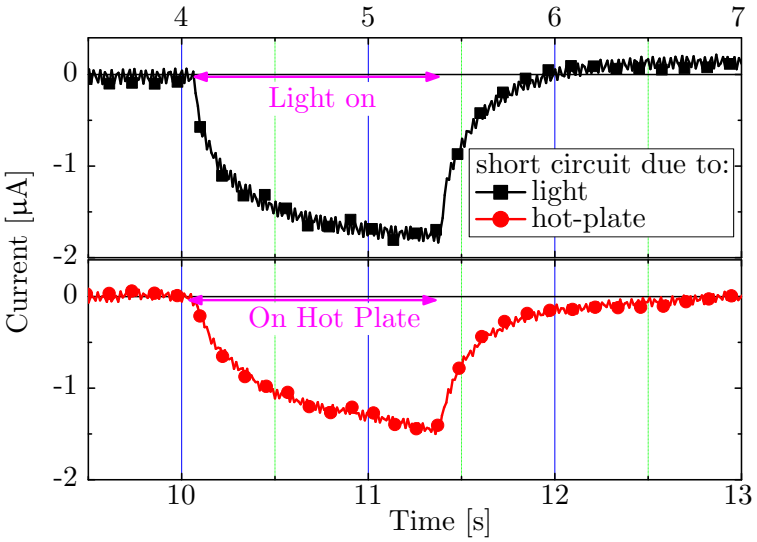

Figure 7.9: Time dependent short circuit of a pn-sample: illuminated for 1.3s with the high intense halogen lamp (top); placed for 1.3s on a 45°C hot plate (bottom)

the results of a pin sample are presented, as they are found to illustrate the observations clearer. Further the voltage is measured in stead of the current, because of a much higher precision.

Characterization of the pin sample by a PSM measurement In fig. 7.10a the PSM measurement of this sample is presented, showing almost flat plateaus of the Seebeck coefficients around $\Sigma = -/+120\mu V/K$ on the left and right with doping concentrations of $n = 6.5 \cdot 10^{-19} cm^{-3}$ and $p = 2.3 \cdot 10^{-19} cm^{-3}$, respectively. In the "intrinsic" region, the sign of Σ is negative, consequently more electrically active P- than B-dopants are found here. Further, the absolute value of Σ in that region is not constant along the y-direction but increases from $\Sigma(y \approx 0.5mm) \approx 200\mu V/K \triangleq 3.0 \cdot 10^{19} cm^{-3}$ near the n-type region to $\Sigma(y \approx 2.5mm) \approx 300\mu V/K \triangleq 1.6 \cdot 10^{19} cm^{-3}$ near the p-type region, with an accelerated gradient for $y > 2mm$. Again overshoots of $\approx 30\mu V/K$ are found at the interface between "intrinsic" and p-type region, c.f. ch. 7.2.2.

The explanation for the gradient of Σ along the y-axis may be found in the inhomogeneous temperature distribution during the sintering process. [Becker2012b] Due to the opposite majority charge carriers and Peltier heating or cooling, the pi-junction either cools down or heats up, depending on the direction of the current. The resulting temperature difference may affect the dopants, i.e. more dopants are activated at higher temperatures or can lead to a denser material, increasing the conductivity locally. Unfortunately, the direction of the current is not recorded, therefore the explanation cannot be proven. Otherwise, by applying the assumption by Becker at al. it is concluded that the current is directed from p-type to n-type material.

OBIC measurement For the OBIC measurement, a laser beam of 532nm wavelength is used to illuminate sample of $\approx 0.5 \times 1 \times 3mm^3$. A laser energy of 130μW is measured at the sample's surface by a calibrated photo diode and the step size between measurement points is set to 20μm. In order to increase the measurement accuracy (see ch. 4.2.3), here the open circuit voltage is measured using a Keithley 2182A nanovoltmeter. With this a position dependent photo-response map is created, which is displayed in fig. 7.10b.

According to the scale on the right, the measured voltage changes from 5μV at the n-type

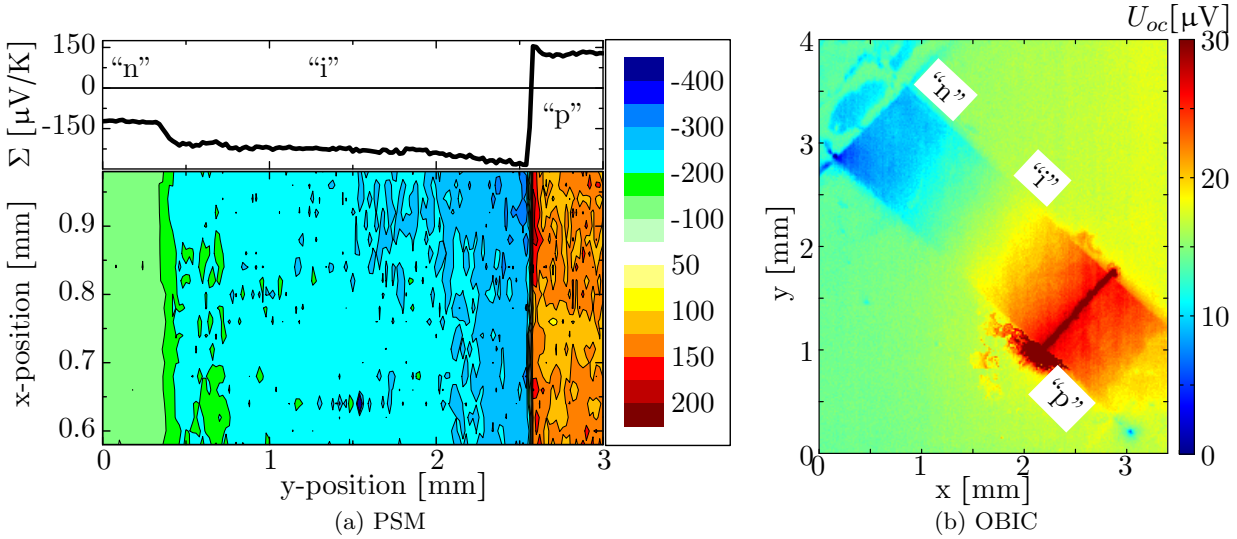

(a) PSM (b) OBIC

Figure 7.10: (a): PSM of pin-sample - top: mean value of the Seebeck coefficient (Σ); bottom: colour map of scanned area; right: colour bar indicating values of Σ
(b): U_{oc} map of same sample; the maximum (dark red) peaks up to 600µV

region (left top) to 30µV and then drops again down to ≈ 17µV at the p-type region (right bottom). It is concluded, that the rather linear increase and decrease are due to TE effects, as similar increases are obtained for pn-junctions from Patino-Lopez et al. [Patino-Lopez2004]

On the other hand, in this graph it is not indicated, that at the points of maximum intensity (dark red), the measured voltage peaks by more than one order of magnitude up to ≈ 600µV. These peaks, which are observed only near the pi-junction, which indeed is better named a p^+n-junction due to the measured majority charge carriers, are therefore suggested to be the result of PV action. Then again, Span et al. proposed that TE power can be generated by thermal generation of free charge carriers near pn-junctions. [Span2006, Span2007] This theory is validated experimentally by Becker et al. [Becker2013] Therefore, it is also possible that the peak near the pi-junction is a result only from the TE instead of the PV effect.

In consequence, also this measurement does not entirely clarify the question of the EMF's origin. The most possible explanation by date seems to be the superposition of both effects, while the PV effect seems to be very localized near pn-junctions, whereas the TE effect is observed over much longer distances.

7.3.4 Atmosphere dependency and electrical hysteresis behaviour

So far it is not mentioned, that the $I(U)$ measurements usually show a hysteresis with a higher absolute current after the respective, absolute maximum is reached. For the pin sample this is shown for the forward bias in fig. 7.11a. Here, the voltage is swept from −6V to +6V and back. (Above 100mA the compliance level is reached, the black, dashed arrow indicates the direction of the hysteresis using the example of the green graph.) The origin for the hysteresis is suggested to be the electrical current through the material, which leads to an increased temperature because of Joule heating and therefore to an increased conductivity.

Fig. 7.11a additionally shows another, so far not completely understood effect. The pin-sample is inserted into a pure nitrogen atmosphere and measured several times after insertion, as indicated in the legend. According to this graph the rectifying behaviour reduces in N_2

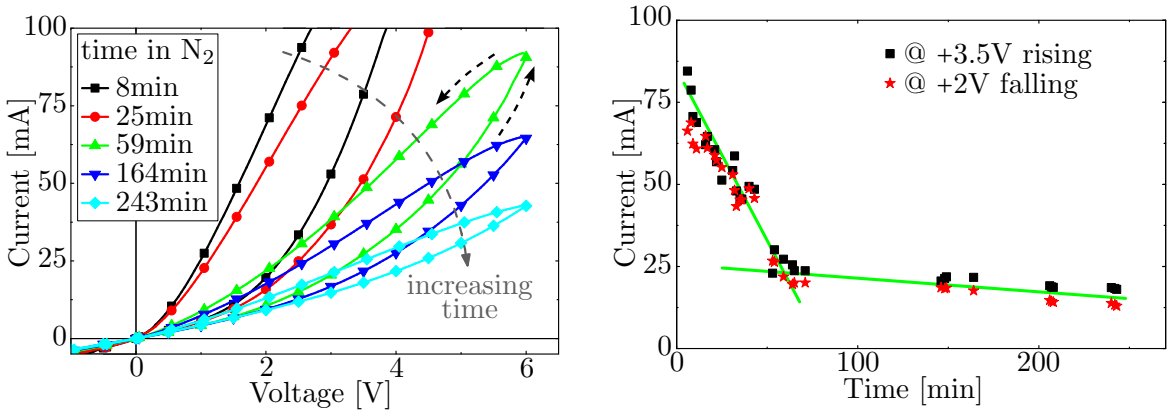

(a) $I(U,t)$ (b) $I(U = +3.5\text{V}/+2\text{V})$

Figure 7.11: Dependency of atmosphere on $I(U)$ characteristic of SPS-pin-sample

atmosphere. (The reduction is reversible, if the sample is returned to ambient air.)

To quantify this, the current values at +3.5V (+2V) for the increasing (falling) voltage are plotted in fig. 7.11b as black squares (red stars). Due to the inserted, green lines the degradation may be described by two effects linearly decreasing with different time constants. However, their origin is unclear so far.

The biggest difference between the N_2 atmosphere and ambient air are the O_2 and the water contents, which are reduced to a few parts per million (ppm). Regarding O, it seems implausible that it is responsible for this altering, because on the one hand, if SiO_X forms, O is bound strongly to it and high energies are needed to remove it. Although the O_2 concentration in the N_2 atmosphere is strongly reduced when compared with ambient air, it seems implausible that evaporation of O significantly takes place. On the other hand, if O would really be released from the samples, an enhancement in the conductivity is expected, but the contrary is observed here. Consequently, this assumption is unreliable.

Another hypothesis is based on the reduced water concentration in the N_2 atmosphere: It is reduced by dissociation of the water: while O gets chemically bound to an absorber, the H_2 is left in the residual atmosphere. It is expected, that the reduced amount of water in the sample does not lead to a reduction of the conductivity, just as for the O. But it is possible, that H_2 accumulates in the glove box's atmosphere, which might react with the SiO_X, forming SiO_XH_Y. With this the amount of free charge carriers can be reduced, leading to a possible reduction in the current, as observed here. However, this hypothesis is not verified yet, not least because the H_2 concentration cannot be monitored for the used glove box system.

7.4 Summary and conclusion

A pn-junction is created by SPS of p-type and n-type doped Si NPs. Structural SEM characterizations show a quite well but not homogeneous compaction of the NPs after the sintering. By combining SEM and EDX measurements, tube-like structures, which are found perpendicularly aligned to the direction of the applied pressure and current are identified as oxygen precipitates, which are highly enriched with P in the n-type region.

From EDX and PSM measurements it is assumed, that dopant diffusion during SPS occurs in distances of less than $\approx 80\mu\text{m}$. A separation of the n-type and the p-type areas is therefore

present also after the sintering process. However, according to calculations the particles melt and form a thin more or less compensated layer between the p- and the n-type side, leading to the assumption, that dopant diffusion in deed takes place.

Electrical measurements in the dark show, that a band bending and a depletion region are present in the pn-sample. By further performing $I(U)$ measurements under illumination with a 1000W halogen lamp a small electromotive force (EMF) is measured. However, its origin is not clear, so far. On the one hand by placing the pn-sample on a 45°C hot plate for 1.3s, a characteristic is observed which is similar to the characteristic if the sample is illuminated for the same time with the 1000W halogen lamp, pointing towards the TE effect to be the major effect. On the other hand, OBIC measurements show that the open circuit voltage between adjacent metal contacts highly increases, if the junction-region is illuminated. That is why it is suggested that a combination of both effects creates the EMF.

Another unsolved question is the observed dependency of the $I(U)$ characteristics on the atmosphere: If the pn-sample is placed in a pure nitrogen atmosphere, the rectifying nature reduces with time. While it is excluded, that O is responsible for this change, a possible explanation bases on the amount of hydrogen, which is expected to be increased in the glove box, forming SiO_XH_Y, which may be the origin for the reduced conductivity of the sample.

With the SPS technique it is possible to create bulk material with a nano structure. Consequently, this technique is found to be beneficial for thermoelectrics, as the structure and the defects can be helpful there. However, to apply SPS in order to create an absorbing layer of a PV cell seems to be inappropriate, as the high concentration of defects dramatically reduces the cell's efficiency to a negligibly small value. Further, a high amount of energy is needed to create these samples which are much too thick for standard PV applications - not to think of thin film PVs. Otherwise, to create samples of typical PV cell thickness is very hard to realize using SPS.

Therefore, in the following another approach using Si NPs for PV devices is investigated. The NPs are therefore laser annealed on non-conductive substrates to create PV devices made of Si NPs only.

Chapter 8

Laser annealing of NP films on insulating substrates

The long-term objective of the investigations presented here, is to create photovoltaic (PV) cells that exhibit an absorbing layer made only of Si NPs. The NPs are one possible vehicle towards rollable and thus low-cost PVs. Therefore in this chapter, preliminary results of laser annealed Si NPs on two insulating substrates (glass and Kapton®) are presented. Especially Kapton® is of great interest, as it is a flexible substrate and resists hydrofluoric acid.

8.1 Sample preparation

To investigate the possibility to create electrically conducting films from NPs, thin films of NPs are created on glass substrates by spin coating p-type NP dispersion. For spin coating the following standard parameters are chosen: 2 000r/min and 2 000r/(min · s), resulting in layer thicknesses of ≈ 400nm. These layers are laser annealed using the infra red (IR) or the ultra violet (UV) laser. If the IR laser is used, most substrates broke during the annealing process, and the conductances are too low to measure them. Therefore, the IR laser unit is rejected for further experiments on glass. Instead the UV laser unit (c.f. ch. 4.1.1) is found to be more applicable, because of the much smaller absorption length as well as the reduced thermal diffusion length.

The standard parameters for UV laser annealing are set to: repetition frequency f = 100Hz, velocity v = 8mm/min and E_{prim} = 6mJ and β = 36°. This results in a distance between neighbouring shots of Δx = 1.33µm and an energy at the sample's surface of each shot of E_{sample} = 0.75mJ, c.f. eq. (4.1).

An hexafluorosilicic acid (HFS) etching to remove silicon oxide from the NPs of the thin film is only applied for the experiments on Kapton® because for glass substrates, the whole NP layer immediately gets removed from it.

8.2 Laser annealing of nanoparticle films on glass

UV laser annealed NP layers on glass substrates are characterized structurally and electrically in this section. Further, first experiments to adjust the doping concentration of the NP layer are presented. Keeping in mind the future objective, at the end of this section a pin-device is created and characterized.

8.2.1 Structural investigations

Depending on the used parameters of the UV laser unit, a change in the transparency first to darker and for even higher intensities or lower velocities, to almost complete transparency is observed. Optical microscope investigations of completely transparent areas show a rough surface, as if glass slivers are removed from it due to (maybe explosive) evaporation of a surface near layer or due to splintering as a result of high stress or strain.

The samples are characterized structurally by scanning electron microscopy (SEM), x-ray diffraction (XRD) and transmission electron microscopy (TEM). The respective results are discussed in the following.

Scanning electron microscopy

Figure 8.1 shows top view SEM images of HWR NP layers on glass that are laser annealed at standard conditions but with E_{sample} being varied in between 0.27mJ and 2.21mJ. While E_{sample} = 0.27mJ is not sufficient to create a significant change in the layer's structure, by increasing E_{sample}, first the agglomeration of the NPs increases, then spheres form and thereafter grow in size. These observations are comparable with UV laser annealed Si NPs on c-Si without oxide removal, c.f. fig. 5.32 and discussion. For the samples prepared at highest intensities a smearing out of the spheres' borders, as if they wet the surface, is observed. However, a closed film is not observed.

Cross sectional SEM images of three samples prepared at E_{sample} = 0.46mJ, 1.17mJ and 2.21mJ are presented in fig. 8.2. While the NP layer of the sample prepared at 0.46mJ does not exhibit significant changes, when compared with unannealed samples, for the sample annealed at 1.17mJ hemispheres are observed on top of an inhomogeneous film, which is expected to consist of unannealed NPs. For the sample prepared at 2.21mJ the hemispheres are directly connected to the substrate with contact angles of $\Theta_c \approx 90°$. According to Young and Danielson, for liquid Si on SiO_2 a contact angle of $\Theta_c \approx 73°$ is calculated (see ch. 5.3.2). [Young1805, Danielson2006] The discrepancy between the observed and the predicted Θ_c may be a result of the hemispheres' composition, consisting of a significant fraction of oxygen. Consequently the surface energies differ from those used to calculate Θ_c. Surprisingly, a smearing out of the borders, as observed in top view images, is not found here.

In fig. 8.3 top view SEM micrographs of samples scanned 1, 8 and 16 times at standard conditions are presented. The nano structure network after 8 scans is found to be denser than after only 1 scan and less unannealed NPs are observed for this sample. The SEM analysis of the sample scanned 16 times, shows an increased amount of pores or holes. From these micrographs, it seems as if by increasing the number of scans, an increased amount of material is removed from the film, presumably by evaporation.

X-ray diffraction measurements

In order to investigate the structure of the annealed films, XRD measurements in Θ - 2Θ geometry are performed. Fig. 8.4 shows the results of six samples. An uncoated glass substrate (black graph) and a NP coated but unannealed sample (red) are used as reference samples. The preparation of the other samples varies in regard of the laser intensity and the amounts of scan repetitions as displayed in the legend. Furthermore, the Bragg angles of the 111, the 222 and the 331 reflection peaks of c-Si are indicated by vertical, gray lines. (Measurements are shifted in y-direction, for better comparability.)

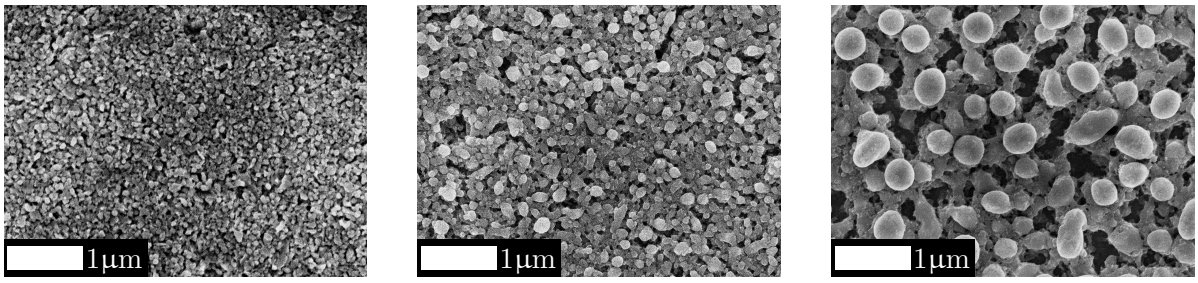

(a) E_{sample} = 0.27mJ (b) E_{sample} = 0.46mJ (c) E_{sample} = 0.75mJ

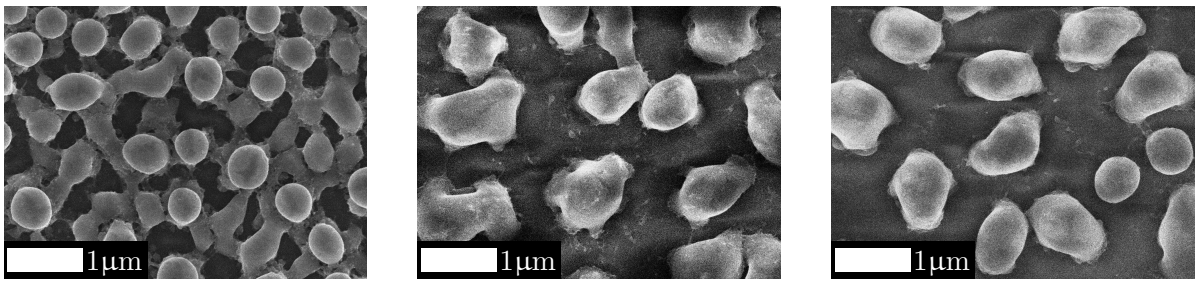

(d) E_{sample} = 1.17mJ (e) E_{sample} = 1.68mJ (f) E_{sample} = 2.21mJ

Figure 8.1: SEM images of UV laser annealed, HWR NP coated glass; laser energy is set according the subscripts

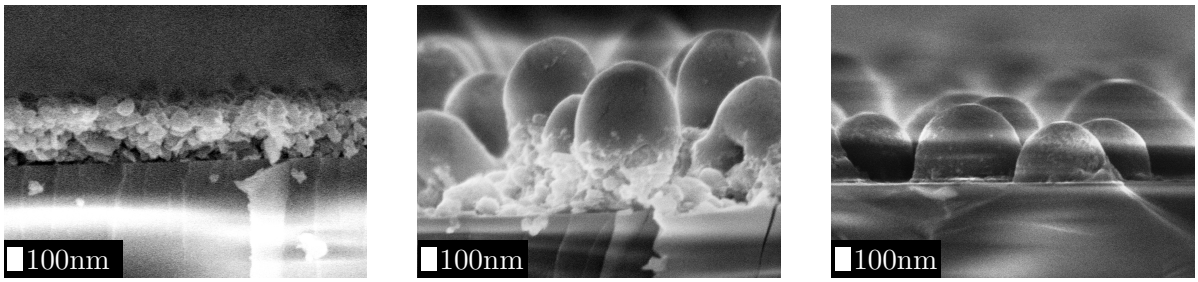

(a) 0.46mJ (b) 1.17mJ (c) 2.21mJ

Figure 8.2: Cross section SEM images of UV laser annealed, HWR NP coated glass; laser energy is set according the subscripts

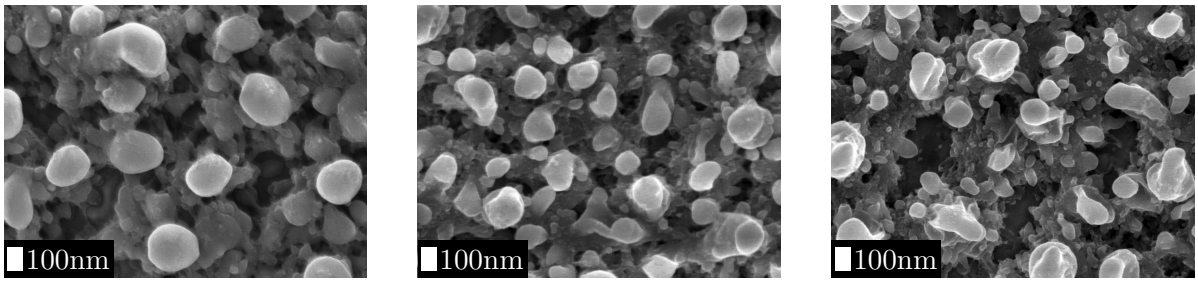

(a) 1×0.75mJ (b) 8×0.75mJ (c) 16×0.75mJ

Figure 8.3: SEM images of multiple scanned UV laser annealed HWR NP coated glass

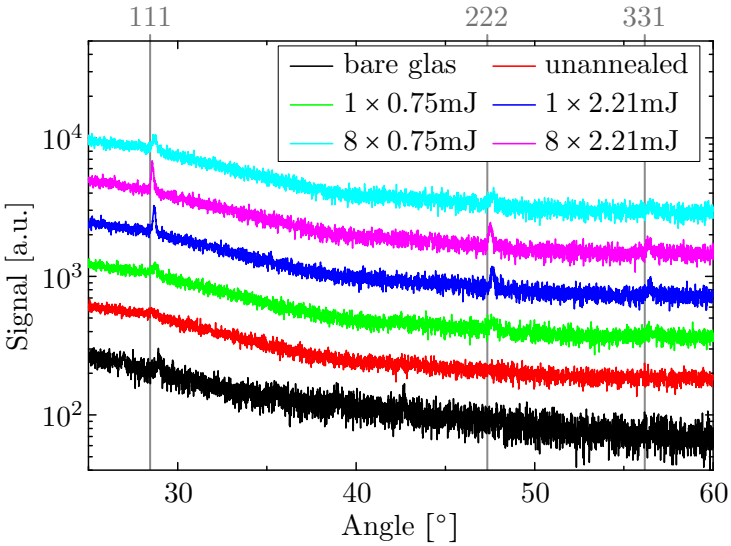

Figure 8.4: XRD measurements of UV laser annealed NPs on glass

A small peak near the 111-peak is already observed for the bare substrate. Since simple chalk-natron glass is used in the glass a small fraction of Si atoms can aggregate and form very small crystallites. For the as deposited sample this peak is almost vanished, which is expected to be a result from the small crystallites in the highly agglomerated HWR NPs (see TEM images in fig. 5.11). [Wiggers2001, Huelser2011]

For all annealed samples XRD peaks are observed near the three indicated reflexion angles. The constant difference of $(0.30 \pm 0.05)^\circ$ for all peaks is ascribed to a systematic positioning inaccuracy of the samples during the measurement.

Scherrer fits (see eq. (4.3)) of the 111-peaks are performed to estimate the respective crystallite sizes and the results are presented in table 8.1. From the data it is found, that for higher laser intensities bigger crystallites form. On the other hand, the number of laser scans seems to play only a minor role on the crystallite size, which is more or less in line with SEM observations of fig. 8.3. Further it confirms conclusions from Schierning et al. and ch. 7.2.1 that small crystallites aggregate on each other and form bigger crystallites. [Schierning2008]

Table 8.1: Crystallite sizes derived from XRD data using Scherrer formula

Sample	1 × 0.75mJ	8 × 0.75mJ	1 × 2.21mJ	8 × 2.21mJ
Crystallite size	32.2nm	32.1nm	50.1nm	55.5nm

Transmission electron microscopy measurements

The crystallite sizes determined from Scherrer fits do not agree with the SEM images, showing cones with diameters of several 100nm. To clarify this discrepancy, transmission electron microscope (TEM) images are prepared from a lamella that is cut out of a standard sample using the focused ion beam (FIB) technique. Fig. 8.5 shows a TEM micrograph of the lamella's face: Three cross cut hemispheres are observed in between the Pt layer (on top, from FIB preparation) and the glass substrate (bottom). Furthermore, between the hemispheres and the substrate an

inhomogeneous layer is found, which is determined to consist of rather unchanged NPs. The hemisphere on the left shows a diagonal crack, already in this magnification. It is unclear, where it originates from; possibly from FIB preparation but maybe it is a crystal twinning, that has built up during re-growth instead. However, the other hemispheres look homogeneous.

High resolution TEM images of the three hemispheres are shown in fig. 8.6. Regular, symmetrical structures of two- or three-fold symmetry are found in the micrographs. Transmission electron diffraction (TED) images of the three hemispheres in fig. 8.7 show perfect diffraction patterns without any diffraction rings. Both results substantiate the high crystallinity of the structures. Since the orientations of the three hemispheres are different: {001} for the left, {112} for the centered and {011} for the right hemisphere, they grow in random orientation.

The TED signal is furthermore used to derive the lattice constant of the respective reflexions. Table 8.2 presents the values in comparison with lattice constant from literature. [Batchelder1964] Although all values are in very good agreement with literature, deviations are found only to bigger distances. It is often observed that the lattice constants change for nano meter sized particles. [Kuznetsov2009, Goldstein1992] However, for Si a lattice contraction is usually observed. [Hofmeister1999, Yao2009] Besides, a systematic measurement inaccuracy or the high defect density may also be responsible for the small lattice mismatch. [Huelser2011]

Table 8.2: Lattice distances of the three analyzed hemispheres (= cones) derived from TED; the literature values are derived from [Batchelder1964]

Crystal direction	Left cone	Centered cone	Right cone	Literature
{220}	0.192nm	—	0.192nm	0.191nm
{400}	0.136nm	—	—	0.135nm
{111}	—	0.313nm	0.314nm	0.312nm
{311}	—	0.164nm	—	0.163nm
{200}	—	—	0.270nm	0.270nm

TEM micrographs show, that the hemispheres are almost completely filled with single crystalline Si. Consequently, the the crystallite sizes determined using XRD are a rough estimation, only.

8.2.2 Electrical characterization

In the following, conductance measurements of the UV laser annealed thin films are presented. The measurements are performed by the standard four point probe method using the pressed contacts (see fig. 4.6b and discussion). Only conductance results are presented here, as the calculation of a conductivity is inadequate due to the fluctuating thicknesses of the annealed layers.

Influence of laser intensity on conductance

The conductances of samples prepared at different attenuating angles, i.e. at different E_{sample} (see blue curve and right ordinate), and spin coating's rotational velocities, are presented in fig. 8.8.

From the graph as an overall tendency, it is found that for lower rotational speeds, an increased conductance is measured and that the conductance increases continuously with increasing angle up to 36° ($\hat{=}$ 0.75mJ) with a best value of $0.058\Omega^{-1}$. Considering the SEM images, it

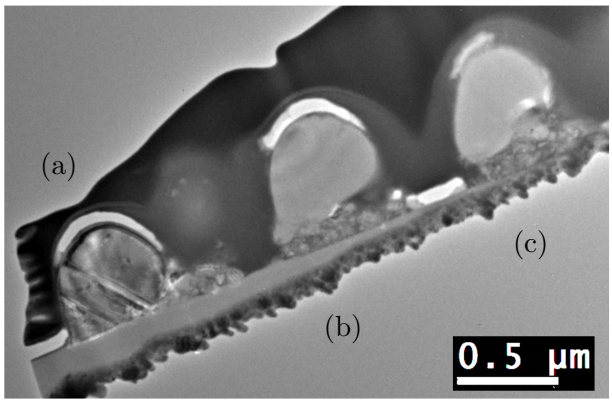

Figure 8.5: TEM overview of the FIB lamella

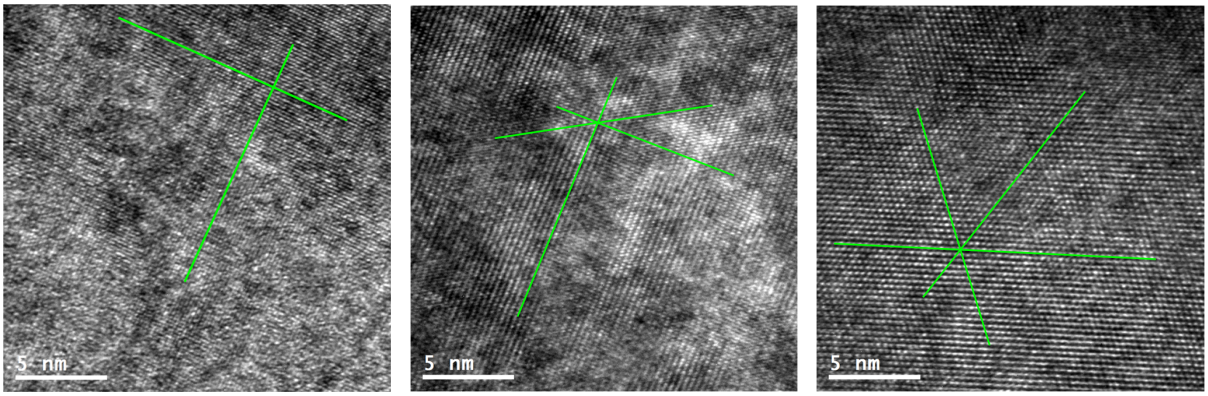

(a) (b) (c)

Figure 8.6: HR-TEM of cones (indices refer to fig. 8.5)

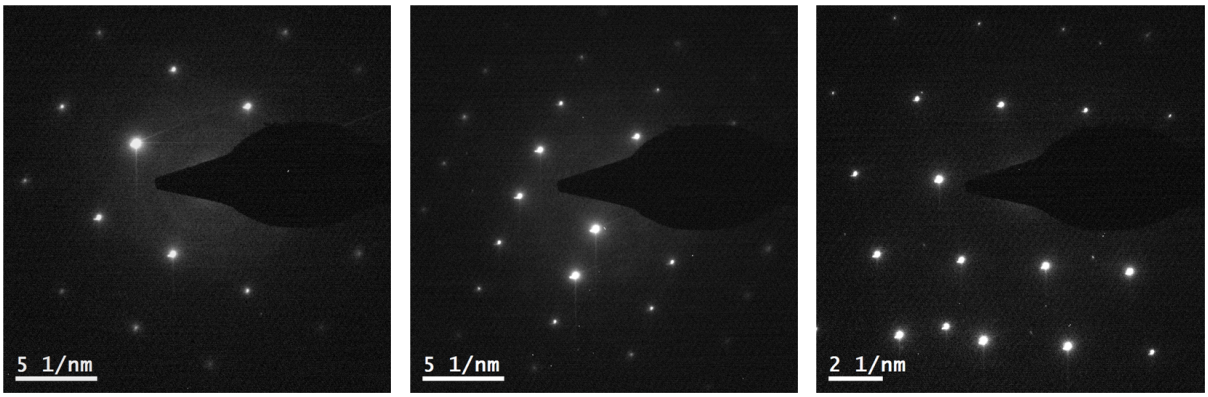

(a) {001}-orientation (b) {112}-orientation (c) {011}-orientation

Figure 8.7: TED of cones (indices refer to fig. 8.5)

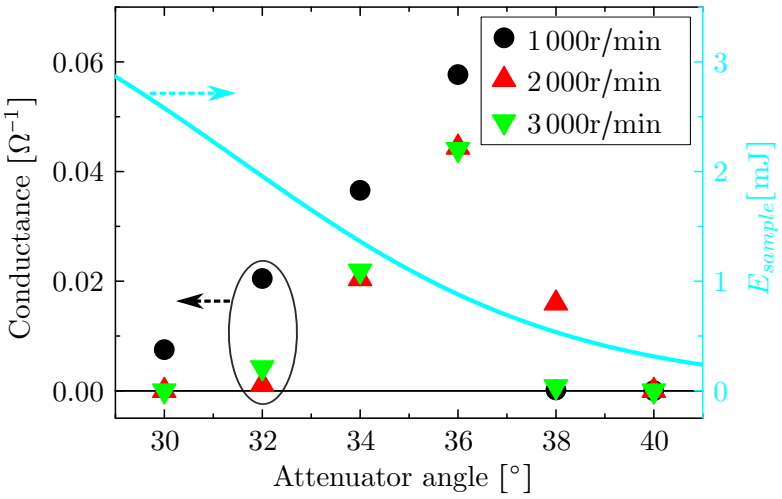

Figure 8.8: Conductance of UV laser annealed NPs on glass - Dependency of attenuator angle

is concluded that the degrading network character for increasing laser intensities leads to a decrease in the film's conductance for lower attenuator angles. For higher angles, the conductance abruptly drops by several orders of magnitude. This can also be explained by the SEM investigations which show, that low laser intensities result only in small changes of the film structure. The high amount of oxygen enriched interfaces is expected to inhibit a reasonable conductivity, here.

On the other hand it is surprising, that a conductance can be measured for attenuating angles $\leq 32°$ ($\triangleq E_{sample} \geq 1.68$mJ) as the corresponding SEM images show rather free standing hemispheres instead of a network. It is excluded that the electrical transport is based on a tunneling mechanism here, as the distanced between neighbouring hemispheres is several hundreds of nano meters and a current would have to pass at least $\approx 1\,000$ of these cones from injection to extraction. Since it is also implausible that the current flows through the glass substrate, it is proposed that still a few percolation paths exist between the hemispheres. These paths may not be caught by the SEM image, but since the electric field affects a much wider area they can contribute to a current.

Repeated laser annealing

Fig. 8.9 presents the conductances of three sample batches prepared with the standard parameters, except of the spin coating's rotational speed and the number of scan repetitions (legend and x-axis, respectively). As indicated by the blue guide-to-the-eye line, an almost linear increase is observed for all batches up to 8 scan repetitions, with a best value of $0.16\Omega^{-1}$. For the samples created by 16 scans, the conductance drops to an mean value of $0.085\Omega^{-1}$.

According to the SEM images in fig. 8.3 the denser film and the higher amount of annealed NPs is concluded to be the major reason for the increased conductance of the samples scanned up to 8 times. The high amount of pores for the sample scanned 16 times, in contrast, is expected to be the reason for the reduction in conductance. Again as an overall tendency the films prepared by the smallest rotational speed exhibit higher conductances.

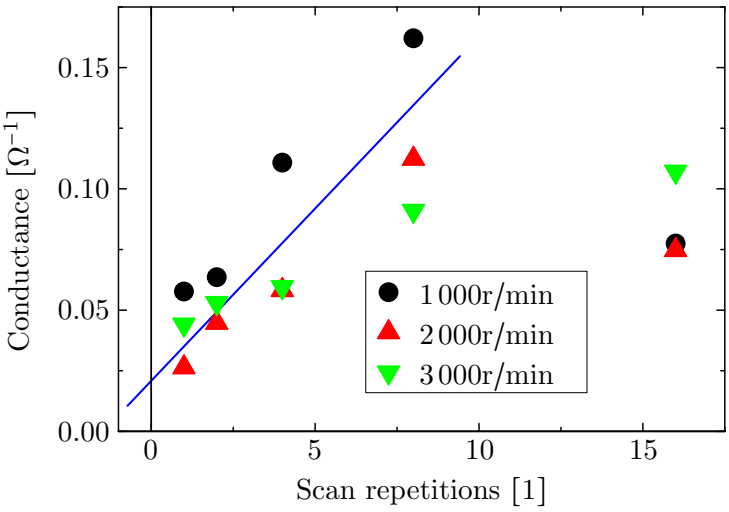

Figure 8.9: Conductances measured for repeated laser annealing

8.2.3 Adjusting the doping concentration

To create PV cells using only Si NPs as absorbing material it is necessary to be able to control the doping concentration. Here, the digital doping technique (see ch. 5.3.4) is applied: Dispersions of effectively reduced doping are prepared by mixing dispersions of p-type and undoped ("intrinsic") HWR NPs. [Lechner2008a, p. 29 f.] Such dispersions are spin coated on glass substrates and laser annealed using the standard parameters. Their conductances are plotted in fig. 8.10. An almost exponential increase from $\approx 0\Omega^{-1}$ to $0.047\Omega^{-1}$ is observed if the p-type content is increased from 0% to 100%.

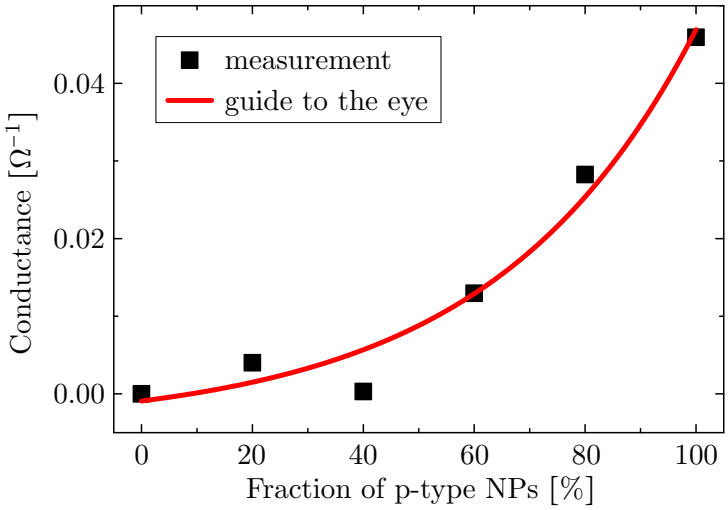

Figure 8.10: Conductance measured for digitally doped, annealed NP films

Lechner has also observed an increase of the conductivity of laser annealed Si NP layers with the doping concentration, however, he has found only a linear dependency. [Lechner2008a, p. 174] This difference may be attributed to the different measurement setups and preparation methods.

To investigate whether the digital doping technique also influences the temperature coefficient of the conductance, temperature dependent measurements of three annealed samples prepared according to the standard process but with 100%, 60% and 20% p-type NPs in intrinsic dispersion are measured in between 10K and 300K (450K) by two point measurements. The results are displayed in fig. 8.11.

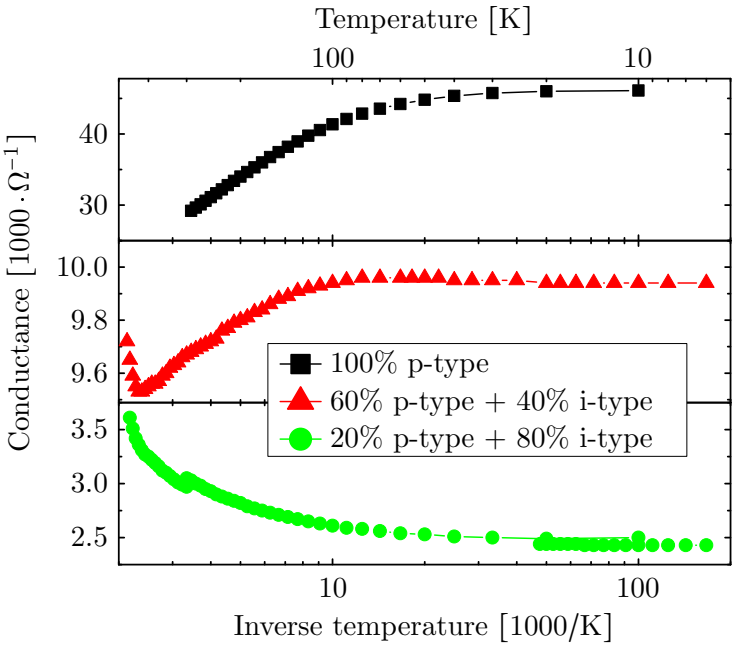

Figure 8.11: Temperature dependent conductance of digitally doped, annealed NP films

The sample prepared from 100% p-doped NP dispersion shows a decrease in conductivity for increasing temperatures. This behaviour is ascribed to the high doping concentration in the NPs, leading to a degenerated semiconductor of the annealed thin film.

By effectively reducing the amount of dopants in the device, the temperature coefficient changes from positive to negative. However, the conclusion that these layers can be described by the standard theory of low doped Si seems rather keen and further work on the crystalline structure and the doping concentration is necessary to make a decent, final statement. Nevertheless, this also proves that a reduction of the effective doping concentration in the NPs leads to a reduced doping in the annealed film, which is a promising result for the future aim of PV cells made of Si NPs as absorbing layer solely.

8.2.4 Creation of pin diodes

In a first approach to create a diode and hopefully a PV device using only NPs as the absorbing layer, a glass substrate is completely coated with 200nm of Al and layers of p-, i- and n-type NPs are coated and UV laser annealed using the standard parameters. Since the structural investigations show that annealed films are neither dense nor closed, each unipolar layer is processed 4 times (coating, annealing, coating, annealing...) to hopefully close the respective films. Further, an undoped NP layer (i-type) is sandwiched between n- and p-type to hopefully realize a larger depletion region and therefore a better charge carrier separation. Finally, an Ag front electrode is evaporated using a finger structure in order to perform illumination dependent

$I(U)$ characterization.

The finished sample exhibits a film thickness of ≈ 2µm, as the cross sectional SEM images in fig. 8.12a show. In top view SEM images (fig. 8.12b) a similar structure is observed as for the singly coated and annealed samples (see fig. 8.1), except that the substrate cannot be observed any more and that some of the hemispheres build spiking structures (the ends are bright in the micrograph). So far, it is not clear why these spiking structures build up.

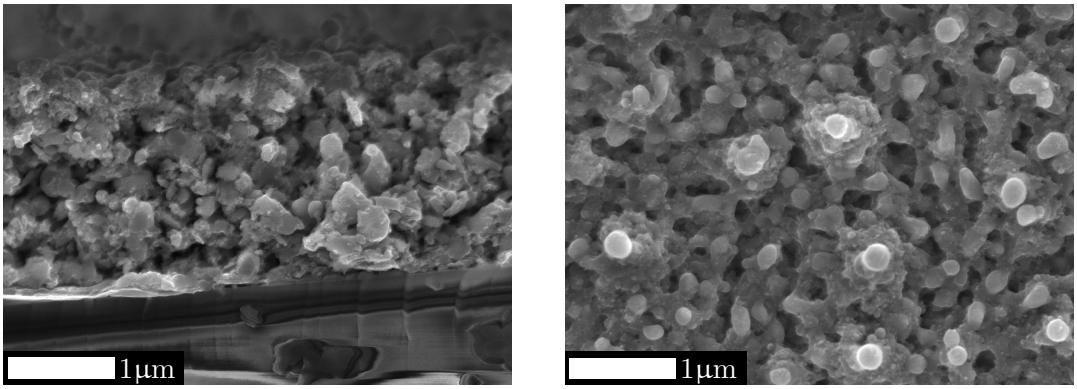

(a) Cross section (b) Top view

Figure 8.12: SEM of pin sample created by UV laser annealing of layers of NPs

The illumination dependent $I(U)$ characteristics of this sample are presented in fig. 8.13. Only a small rectifying behaviour is found with an on / off ratio of ≈ 2 at $+/-2$V. The small on / off ratio is an indication for a high amount of shunts in the device. On the one hand due to the high field strengths of ≈ 10^6V/m it is possible that the contacts shunt the material. On the other hand, defects or fluctuating dopant concentrations in the annealed layers can create a current path, shunting both contacts. Last, because of the high temperatures during the annealing, it is also possible that the NP layers and the underlying Al layer form a eutectic over the whole device. By this, a p-doped material gets created, that results in a simple, ohmic characteristic.

Under AM1.5 standard illumination a reduction of the absolute current is observed for the complete measurement range, which contradicts PV theory. The inset of fig. 8.13 shows a measurement of higher resolution between −1mV and +2mV. Here, an electromotive force (EMF) with a short circuit current of $I_{sc} \approx 7\mu$A and an open circuit voltage of $U_{oc} \approx 1.4$mV ($FF = 25\%$) is observed. A PV conversion efficiency of $\eta \approx 1.3 \cdot 10^{-6}\%$ can be calculated for it. Since the PV parameters are found to be in the same range as for the SPS pn-samples in ch. 7, it is again hard to decide whether the origin for the EMF is based on PVs or on thermoelectrics. Although the radiation is much smaller for the AM1.5 illumination, it is proposed that both effects are present throughout the measurement.

8.3 Laser annealing of NP films on flexible substrate

The structural investigations of the annealed NP layers on glass show hemispheres, which are more or less similar to results from ch. 5.3.2. Due to the corresponding results with and without HFS treatment, it is proposed that an oxide removing step can result in a closed film. Due to the etch resistance regarding HFS, in this section the flexible polyimide Kapton® is used as substrate. Sample preparation and laser annealing are performed as presented in ch. 8.1, but

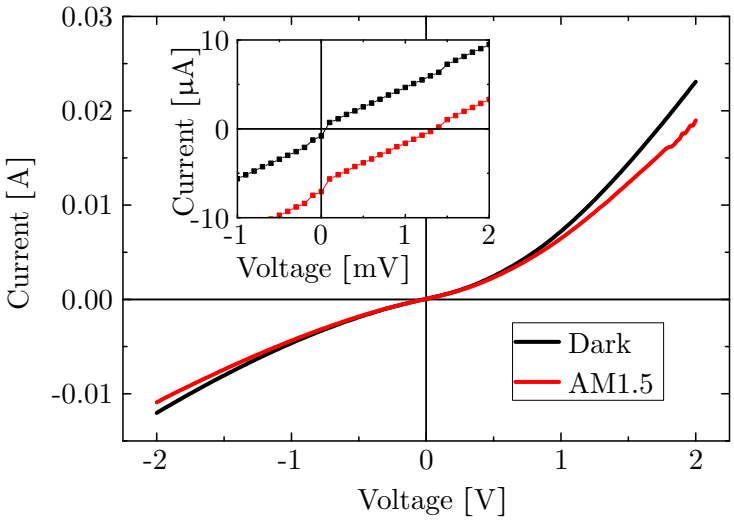

Figure 8.13: $I(U)$ characteristics of pin-sample; the inset shows a measurement performed at higher resolution around 0V

immediately before laser annealing, the samples are dipped in HFS at $\approx 90°$ for 10s in order to reduce the oxygen content in the NP layer.

8.3.1 Structural investigations

Fig. 8.14 shows two SEM images taken from one sample at different magnifications. For the higher magnified image (fig. 8.14a), a closed network is found throughout the whole image. Below the network, unannealed NPs are found. This leads to the conclusions that either the laser intensity is too low to melt the complete NP layer or that not enough oxygen is removed and therefore hemispheres form below the network. The latter may be a result from a too short HF dip. Thus, the HFS does not interpenetrate the whole NP layer (c.f. fig. 5.41 and corresponding discussion) and the different, resulting surface energies lead to the observed morphology.

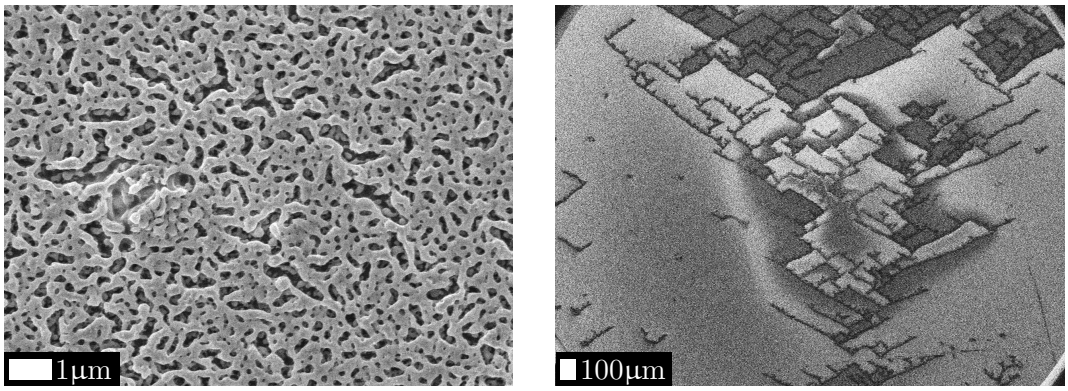

(a) Detailed image (b) Overview: cracks in layer

Figure 8.14: SEM images of UV laser annealed HFS etched HWR NPs coated on Kapton®

By comparing these images with images obtained for layers without HFS treatment (see fig. 8.1) it is found, that the reduced oxygen content in the film leads to the formation of a

denser network. This is assumed to be advantageous to create conducting layers and for an absorbing layer in PV applications. Nevertheless, a flat and completely closed layer is not achieved, so far and remains challenging.

From the overview SEM image in fig. 8.14b it is found that the network spreads over areas that are interrupted by almost rectangular borders. Further investigations of intentionally scratched Kapton® substrates show that these lines are present due to scratches in the substrate. Consequently, a more careful treatment of the substrates is expected to reduce them.

8.3.2 Electrical characterization

In order to determine whether the HFS treatment improves the electrical properties of the annealed films, two sample batches are prepared; one with and one without HFS treatment. Within each batch the scanning velocity:

$$v(\mathrm{i}) = \frac{250\mathrm{mm/min}}{2^{\mathrm{i}}} \tag{8.1}$$

is changed from i = 0 to i = 5 in steps of i = 1 and the attenuating angle is varied from 37° to 40° in steps of 1°. Smaller angles are not used here, as this results in a complete removal of the NPs. Fig. 8.15 illustrates the resulting conductances determined by the standard four point measurement using the tips, c.f. ch. 4.2.3. (For most samples, the conductances are too small to measure it using the Keithley 4200 SCS unit. Thus, only a fraction of the prepared samples is displayed in the log-log plot.)

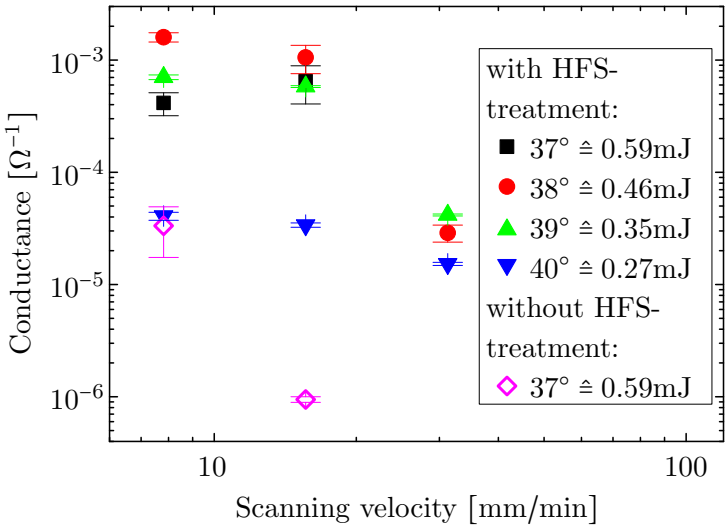

Figure 8.15: Conductances of laser annealed NP films on Kapton® - varied HFS treatment and annealing parameters

As an overall trend, the HFS treatment leads to a significant improvement in the conductivity by more than one order of magnitude. It is concluded, that this is a result of the different structures of the HFS etched and the not etched samples (for the latter a similar structure as for the glass substrates samples is assumed). Nevertheless, a conductance is also measured for the HFS untreated sample (see pink diamonds), leading to the conclusion that it is possible to create conducting films without HFS treatment on Kapton® in principle. In this case, however,

higher laser intensities are needed to achieve comparable values.

The significant increase in conductivity due to the oxide removal step shows once more that the oxygen shell of the NPs is a major bottleneck regarding the creation of functionalised, electrically conductive films using Si NPs. Consequently, for the realization of PV devices made only of NPs as absorbing layers, it is proposed to always include this step or to prevent NPs from oxidizing.

Regarding the conductance measurements it has to be mentioned, that at high currents, i.e. ~ 1mA a current path is visible by the naked eye, see fig. 8.16. After the respective measurement the glowing path can also be observed in the annealed structure. This is unlikely for the photon emission due to electroluminescence and therefore a melting of the annealed layer along the current path, i.e. the glowing path, is proposed.

Figure 8.16: Glowing observed at high currents in four point measurement

8.4 Summary and conclusion

Si NPs are coated on glass substrates and subsequently UV laser annealed in order to create semiconducting films. SEM micrographs show that for an increased laser intensity, the NPs first agglomerate, then form networks, then build hemispheres, which at even higher laser intensities separate from each other. The hemispheres are found to be crystalline, but conductance measurements show that the "network samples" exhibit a better electrical conductance. A first pin-diode made of Si NPs shows only an on/off ratio of ≈ 2 for $+/-2$V and an EMF which is similar to the one observed for the pn-sample made by spark plasma sintering, c.f. ch. 7.3.2. Thus, the results show that further experimental work is needed in order to realize a device with satisfactory properties. For future PV applications the successfully applied digital doping technique, i.e. the mixing of doped and undoped NP dispersions to reduce the effective doping, may be a helpful tool.

To reduce the silicon oxide content in the NP film, the HF resistant substrate Kapton® is used. Structural investigations of annealed NPs films on Kapton® show, that the HFS treatment leads to a network with bigger connecting arms. The conductance of these samples is determined to be at least one order of magnitude higher than without HFS etching, which is expected to be a result from the reduced oxygen content in the thin film and the higher closeness of the layer. However, a completely closed layer, which is essential for a not-shunting, absorbing layer for PV applications, is not realized so far.

Future experiments have to focus primarily on creating a closed, dense layer made of NPs. The HFS etching is found to be advantageous for the films on Kapton®, however, it seems inapplicable for PV applications, because the electrodes on which NPs need to be deposited are also etched by HF; even if they are made of noble metals. Different ways to remove the

silicon oxide from the NPs have to be considered instead. In a first experiment to remove the oxygen shell before deposition, the NP dispersion is treated with HF. Unfortunately, the NPs have coagulated and it has been impossible to create even a homogeneous, flat NP film. Consequently, it is proposed to move all production processes involving NPs (NP production, creation of dispersions, deposition and laser annealing as well as the handling in between the steps) in an inert atmosphere, to prevent the formation of oxides on the NPs.

Another way to overcome the challenges regarding the metalization may be the lift-off of the annealed layer's network followed by a metal coating of the lift-off surface. However, new processes need to be established at the Institute of Technology for Nanostructure for this, which are related primarily with funding of equipment and staff, that is hard to get at the moment.

Chapter 9

Final conclusion

In this thesis silicon (Si) nanoparticles (NPs) are investigated regarding their applicability for photovoltaics (PVs), esp. for the future's goal to create thin film PV cells, with the absorber made of Si NPs solely. In a first step towards this goal highly phosphorus or boron doped Si NPs (typical concentrations: $\sim 10^{20}\mathrm{cm}^{-1}$) are used as a dopant vehicle to create PV active pn-junctions on Si substrates. The NPs are dispersed in ethanol using a mill. The dispersion is coated on the respective substrate by spin coating and the film is laser annealed using an infrared (IR, $\lambda = 808$nm) continuous wave or a 5ns pulsed ultra violet (UV, $\lambda = 248$nm) laser.

Although doping is achieved for both laser units, the doping depths vary significantly for the lasers: For the IR laser, depths of $\sim 100\mu$m are evaluated from secondary ion mass spectroscopy measurements, which is much too thick for PV applications. The thickness is a result of the deep absorption depth in Si for this wavelength. For the UV laser unit the much shorter absorption depth and the pulsed nature of the laser result in doping depths of ≈ 200nm, as determined using capacitance voltage measurements. This thickness is much more desirable for PV applications.

From OBIC measurements of IR and UV laser annealed samples it is concluded that the latter exhibit a significantly increased in-plane doping homogeneity. The difference is attributed to the different heat incorporations: While for the IR laser an inhomogeneous heat distribution during the annealing process builds up, for the short pulses and the comparably low repetition frequency (~ 100Hz) of the UV laser, the heated volume equilibrates with the residual volume. Thus, immediately before each shot, similar temperature distributions are expected for the UV laser unit - contrarily to the IR laser unit.

All cells are fabricated without any anti reflexion treatment. Nonetheless, the best cell with a p-type front side doping, a lightly n-doped c-Si substrate and an n-type back side doping shows a conversion efficiency of $\eta \approx 6\%$.

Because of the determined efficiency and due to the slopes of the measured current-voltage ($I(U)$) graphs, a huge amount of defects is expected in the annealed layer. In principle they can have chemical or structural reasons. Since most of the handling is done in air, all NPs exhibit an oxygen shell of a few nm, which needs to be prevented or removed. Further, a decent chemical analysis of the NPs is proposed to judge, whether their purity is sufficient for PV applications. Due to the mismatch between implanted and activated dopants determined from conductance measurements, it seems furthermore possible that the re-solidified layer is not single crystalline. To determine these structural defects, it is suggested to perform transmission electron microscopy or charge carrier life time measurements. Further, a secondary ion mass spectroscopy of UV laser annealed samples can clarify this discrepancy. To reduce structural defects, thermal annealing after the laser annealing is proposed. Finally, structures to reduce

light reflection and an improved contacting are expected to boost the conversion efficiency and close the gap to standard and record cells.

To replace the Al from the standard back surface region alloying process, the NP UV laser doping technique is applied to multi crystalline Si (mc-Si) solar cells without back surface treatment. So far, the efficiency of cells completely factory-finished cells ($\eta = (14.7 \pm 0.1)\,\%$) is not achieved with the NP UV laser doping process (best cell: $\eta = 12.2\%$). This may be due to the much better development of the factory cells. Nevertheless, it seems that this process may be an interesting alternative, as the front side is not affected by the laser annealing. For further experiments it is proposed to use cells that do not exhibit any front side contacts, as subsequent thermal or HF- / HFS-treatments are possible then.

Finally, first attempts towards the realization of PV devices made only of Si NPs as the absorbing layer are presented. In a first experiment, a pn-junction is created by spark plasma sintering (SPS) of an n-type NP layer on top of a p-type NP layer. For this device a diode-like $I(U)$ behaviour is observed in the dark and a very small electro motive force (EMF) is measured under illumination. Although the observed rectification is a first indication that it may be possible to reach the future's goal, the most possible explanation for the small EMF is a superposition of thermoelectric (TE) and PV effects. However, since samples created by SPS are much thicker than the penetration depth of the light, this proof of principle method is inappropriate to create PV devices.

In a second batch of experiments, Si NPs are UV laser annealed on insulating glass and Kapton® substrates. Conductive layers are realized with this method. Unfortunately, they are not completely closed, but it is found, that a reduction of the oxygen in the NP thin film results not only in an enhanced electrical conductance but also in a denser morphology of the annealed layer. To remove the oxygen, etching is inapplicable if the NPs are deposited on metal contacts or conductive oxides, as the contacts get harmed, too. Thus a pin-junction is created on Al coated glass but without any HF or HFS treatment. In the dark, a poor rectifying behaviour (on / off ratio is 2 at $+/-2$V) and under standard AM1.5 illumination a similar EMF as the SPS pn-junction are observed. Again, it is unclear whether the primary origin is based on PVs, TEs or even something else.

It is expected that the most challenging part and maybe even the bottleneck towards the future's goal of a Si NP thin film PV cell is the removal / prevention of the oxygen from the NP layer. One possible method is to perform all steps from production to the final device in one inert space. This, however, means a great financial investment for an experiment which is very uncertain to be successful or not - even more in a time of low financial support for PV research. Another method is to equip the actual places such that handling can be done in inert atmospheres and to transfer the samples in inert atmospheres between the different places. This, however, would need a huge amount of time and would be pedestrian, when compared to the actual process, but may give a first hint, whether the great investment may be fruitful or not.

In summary, PV devices are fabricated using Si NPs. It is also possible, to realize conductive layers made of Si NPs solely. The established UV laser annealing technique seems therefore to be an interesting choice towards the future goal of thin film PV cells made of Si NPs solely.

List of abbreviations

Acronyms

AM1.5	Air mass coefficient of 1.5 (terrestrial irradiance at a solar zenith angle of 48.2°)
ARC	Anti reflexion coating
a-Si	Amorphous silicon; also: α-Si
BSR	Back surface region
c-Si	Crystalline silicon
cw	Continuous wave, i.e. continuously radiating
ECV	Electrochemical capacitance-voltage measurements
EDX	Energy dispersive x-ray spectroscopy
E-M	Electro magnetic field
EMF	Electromotive force
FIB	Focused ion beam
FWHM	Full width at half maximum
HF	Hydrofluoric acid
HFS	Hexafluorosilicic acid; chemical formula: H_2SiF_6
HWR	Hot wall reactor
IQE	Internal quantum efficiency
IR	Infra red
mc-Si	Multi crystalline silicon
MLI	Maximum laser intensity
mpp	Subscript for maximum power point properties
MWR	Micro wave reactor
NIR	Near infra red

NP	Nanoparticle
OBIC	Optical beam induced current
OBIV	Optical beam induced voltage
PSM	Scanning potential Seebeck microscopy
PV	Photovoltaic
RTA	Rapid thermal annealing
SEM	Scanning electron microscope
SIMS	Secondary ion mass spectroscopy
SPS	Spark plasma sintering - in literature different names like “current-activated pressure-assisted densification”, “DC-current sintering” or “field assisted sintering” are used, too.
TCO	Transparent conductive oxide
TE	Thermoelectric
TED	Transmission electron diffraction
TEM	Transmission electron microscope
TOF	Time of flight
UV	Ultra violet
VB	Valence band
VIS	Visible (spectral range)
XPS	X-ray photoelectron spectroscopy
XRD	X-ray diffraction

Quantity symbols

α	$\frac{1}{\mathrm{m}}$	Absorption coefficient
a_{abs}	m	Absorption length
β	°	Angle of the UV laser unit's attenuator
C	F	Capacitance
χ_a	m	Surface roughness
D_l	$\frac{\mathrm{m}^2}{\mathrm{s}}$	Liquid diffusivity of atoms or impurities etc.
D_s	$\frac{\mathrm{m}^2}{\mathrm{s}}$	Solid diffusivity of atoms or impurities etc.
D_T	$\frac{\mathrm{m}^2}{\mathrm{s}}$	Thermal diffusion constant.
e	C	Elemental charge
$\tilde{\epsilon}$	1	Complex refraction index: $\tilde{\epsilon} = \epsilon_{\Re} + \imath\epsilon_{\Im} = \epsilon_r + \frac{\imath \cdot \sigma}{\epsilon_0 \cdot \omega}$
ϵ_0	$\frac{\mathrm{A} \cdot \mathrm{s}}{\mathrm{V} \cdot \mathrm{m}}$	Dielectric constant / permittivity of the vacuum
$\epsilon_{\Im}$	1	Imaginary part of complex refraction index
ϵ_r	1	Relative dielectric constant / permittivity of a material
$\epsilon_{\Re}$	1	Real part of complex refraction index
E_g	eV	Bandgap
E_{prim}	J	Primary energy of one pulse, at the exit of the excimer laser unit
E_{sample}	J	Energy of one pulse at the sample's surface ($E_{sample} = Tr(\omega) \cdot E_{prim}$)
ϕ_{sample}	$\frac{\mathrm{J}}{\mathrm{m}^2}$	Energy density of one pulse at sample surface ($\phi_{sample} = \frac{E_{sample}}{A_{eff}}$)
FF	1	Fill factor
h	$\mathrm{J} \cdot \mathrm{s}$	Planck's constant; $h = 6.626 \cdot 10^{-34}$Js
η	%	Power conversion efficiency of a PV cell
I	A	Electric current
I_0	A	Diode's saturation current
I_D	A	Diode's current
I_{sc}	A	Short circuit current
J_{sc}	A	Short circuit current density

κ	$\frac{\mathrm{kg}\cdot\mathrm{m}}{\mathrm{s}^3\cdot\mathrm{K}}$	Thermal conductivity
k_B	$\frac{\mathrm{J}}{\mathrm{K}}$	Boltzmann's constant
λ	m	Wavelength
m_e	kg	Electron mass
N	$\frac{1}{\mathrm{m}^3}$	Doping concentration (acceptors: N_A; donors: N_D)
n	1	Diode's ideality factor
$\tilde{n}$	1	Complex refraction index: $\tilde{n} = n_{\Re} + \imath n_{\Im}$
$n_{\Im}$	1	Imaginary part of complex refraction index
$n_{\Re}$	1	Real part of complex refraction index
Irr	$\frac{\mathrm{W}}{\mathrm{m}^2}$	Irradiance
P	W	Power
q	C	Charge
ω	Hz	Frequency of the light
ρ	$\Omega\cdot\mathrm{m}$	Resistivity
R	Ω	Resistance
R_{ser}	Ω	Serial resistance in the equivalent circuit of diode models
R_{shu}	Ω	Parallel resistance in the equivalent circuit of diode models
Σ	$\frac{\mathrm{V}}{\mathrm{K}}$	Seebeck coefficient
σ	$\frac{1}{\Omega\cdot\mathrm{m}}$	Electrical conductivity
T	K	Temperature
Θ_c	$^\circ$	Contact angle, c.f. fig. 5.34
Tr	%	Transmitted part of a light beam
U	V	Voltage
U_{bi}	V	Build in voltage
U_D	V	Diode's voltage
U_{oc}	V	Open circuit voltage
U_{TE}	V	Thermoelectric voltage

List of Figures

List of Tables

Bibliography

[4JETTechnologies] GmbH 4JET Technologies. Laser solutions for solar. online, 2012.

[Agency2010] EuropeanEnvironmentAgency. Tracking progress towards Kyoto and 2020 targets in Europe. EEA Report 7, European Environment Agency, October 2010. ISSN 1725-9177.

[Ahn2012] S. Ahn, D. J. Hwang, H. K. Park, and C. P. Grigoropoulos. Femtosecond laser drilling of crystalline and multicrystalline silicon for advanced solar cell fabrication. *Applied Physics A*, 108(1):113–120, July 2012.

[Allmen1995] M. v. Allmen and A. Blätter. *Laser-Beam Interactions with Materials: Physical Principles and Applications*, volume 2. Springer, Berlin, 1995.

[Altermatt2003] P. P. Altermatt, A. Schenk, F. Geelhaar, and G. Heiser. Reassessment of the intrinsic carrier density in crystalline silicon in view of band-gap narrowing. *Journal of Applied Physics*, 93(3):1598–1604, February 2003.

[Andrae1999] G. Andrä, J. Bergmann, F. Falk, E. Ose, and Stafast; H. Laser induced crystallization of amorphous silicon films on glass for thin film solar cells. *Physica Status Solidi (a)*, 166(2):629–634, January 1999.

[Ardani2011] K. Ardani and R. Margolis. 2010 solar technologies market report. Technical report, National Renewable Energy Laboratory (NREL), 2011.

[Arizpe-Chavez2000] H. Arizpe-Chavez, R. Ramirez-Bon, F. J. Espinoza-Beltran, O. Zelaya-Angel, J. L. Marin, and R. Riera. Quantum confinement effects in CdTe nanostructured films prepared by the RF sputtering technique. *Journal of Physics and Chemistry of Solids*, 61(4):511–518, April 2000.

[Ashcroft2007] N. W. Ashcroft and D. N. Mermin. *Festkörperphysik*, volume 3. Oldenbourg Wissenschaftsverlag, 2007.

[Atwater2010] H. A. Atwater and A. Polman. Plasmonics for improved photovoltaic devices. *Nature Materials*, 9:205–2013, March 2010.

[Baeuerle2000] D. Bäuerle. *Laser Processing and Chemistry*. Springer, 3 edition, 2000.

[Balaz2008] P. Baláz. *Mechanochemistry in Nanoscience and Minerals Engineering*, volume 1. Springer Verlag, 2008.

[Basu2013] P. K. Basu, Z. Hameiri, D. Sarangi, J. Cunnusamy, E. Carmona, and M. B. Boreland. 18.7% efficient inline-diffused screen-printed silicon wafer solar cells

with deep homogeneous emitter etch-back. *Solar Energy Materials and Solar Cells*, 117:412–420, October 2013.

[Batchelder1964] D. N. Batchelder and R. O. Simmons. Lattice constants and thermal expansivities of silicon and of calcium fluoride between 6° and 322°K. *Journal of Chemical Physics*, 41(8):2324–2330, 1964.

[Becker2012] A. Becker, G. Schierning, R. Theissmann, M. Meseth, N. Benson, R. Schmechel, D. Schwesig, N. Petermann, H. Wiggers, and P. Ziolkowski. A sintered nanoparticle p-n junction observed by a Seebeck microscan. *Journal of Applied Physics*, 111(5):054320, 2012.

[Becker2012b] A. Becker, S. Angst, A. Schmitz, M. Engenhorst, J. Stötzel, D. Gautam, H. Wiggers, D. E. Wolf, G. Schierning, and R. Schmechel. The effect of Peltier heat during current activated densification. *Applied Physical Letters*, 101(013113):013113, 2012.

[Becker2013] A. Becker, R. Chavez, N. Petermann, G. Schierning, and R. Schmechel. A thermoelectric generator concept using a p-n junction: Experimental proof of principle. *Journal of Electronic Materials*, 42(7):2297–2300, 2013.

[Becquerel1839] A. E. Becquerel. Mémoire sur les effets électriques produits sous l'influence des rayons solaires. *Comptes rendus hebdomadaires des séances de l'Académie des Sciences*, 9:561–567, 1839.

[Behrenberg2012] D. Behrenberg, S. Franzka, N. Petermann, H. Wiggers, and N. Hartmann. Photothermal laser processing of thin silicon nanoparticle films: on the impact of oxide formation on film morphology. *Applied Physics A*, 106(4):853–861, October 2012.

[Beneking1991] H. Beneking. *Halbleiter-Technologie*. B. G. Teubner, Stuttgart, 1991.

[Bet2006] S. Bet and A. Kar. Laser forming of silicon films using nanoparticle precursor. *Journal of Electronic Materials*, 35(5):993–1004, May 2006.

[Birkholz2005] M. Birkholz. *Thin Film Analysis by X-Ray Scattering: Techniques for Structural Characterization*, volume 1. Wiley-VCH, 2005.

[Bitzer2013] L. Bitzer, M. Meseth, N. Benson, and R. Schmechel. A new adaptive light beam focusing principle for scanning light stimulation systems. *Review of Scientific Instruments*, 84(2):023707, 2013.

[Bock2008] R. Bock, P. P. Altermatt, and G. Schmidt. Accurate extraction of doping profiles from electrochemical capacity voltage measurements. In *Proceedings of the 23rd European Photovoltaic Solar Energy Conference and Exhibition*, number 2CV.4.56, pages 1510–1513, 2008.

[Boucle2007] J. Bouclé, P. Ravirajan, and J. Nelson. Hybrid polymer-metal oxide thin films for photovoltaic applications. *Journal of Materials Chemistry*, 17:3141–3153, 2007.

[Bowden2000] S. Bowden, F. Duerinckx, J. Szlufcik, and J. Nijs. Rear passivation of thin multicrystalline silicon solar cells. *Opto-Electronics Review*, 8(4):307–310, December 2000.

[Boyd1984] I. W. Boyd, T. D. Binnie, J. I. B. Wilson, and M. J. Colles. Absorption of infrared radiation in silicon. *Journal of Applied Physics*, 55(8):3061–3063, April 1984.

[Bozel2006] M. Bozel. *Springer Handbook of Electronic and Photonic Materials*, chapter 23 - Gallium Arsenide, pages 499–536. Springer Science+Business Media, Inc., 2006.

[Buffat1976] P. Buffat and J.-P. Borel. Size effect on the melting temperature of gold particles. *Physical Review A*, 13(13):2287–2298, June 1976.

[Bulucea1993] C. Bulucea. Recalculation of Irvin's resistivity curves for diffused layers in silicon using updated bulk resistivity data. *Solid-State Electronics*, 36(4):489–493, 1993.

[Buuren1993] T. van Buuren, T. Tiedje, J. R. Dahn, and B.M. Way. Photoelectron spectroscopy measurements of the band gap in porous silicon. *Applied Physical Letters*, 63(21–22):2911–2913, November 1993.

[Bux2009] S. K. Bux, R. G. Blair, P. K. Gogna, H. Lee, G. Chen, M. S. Dresselhaus, R. B. Kaner, and J.-P. Fleurial. Nanostructured bulk silicon as an effective thermoelectric material. *Advanced Functional Materials*, 19(15):2445–2452, 2009.

[Casey1996] H. C. Jr. Casey, J. Muth, S. Krishnankutty, and J. M. Zavada. Dominance of tunneling current and band filling in InGaN/AlGaN double heterostructure blue light-emitting diodes. *Applied Physical Letters*, 68(20):2867–2869, May 1996.

[Caughey1967] D. M. Caughey and R. E. Thomas. Carrier mobilities in silicon empirically related to doping and field. *Proceedings of the IEEE*, 55(12):2192–2193, December 1967.

[Chee2011] A. K. W. Chee, R. F. Broom, C. J. Humphreys, and E. G. T. Bosch. A quantitative model for doping contrast in the scanning electron microscope using calculated potential distributions and monte carlo simulations. *Journal of Applied Physics*, 109(1):013109, January 2011.

[Cheng2013] P. Cheng, Y. Li, and X. Zhan. A DMF-assisted solution process boosts the efficiency in P3HT:PCBM solar cells up to 5.31%. *Nanotechnology*, 24(48):484008, November 2013.

[Chenga2002] I-C. Chenga and S. Wagner. Hole and electron field-effect mobilities in nanocrystalline silicon deposited at 150°C. *Applied Physics Letters*, 80(2):440–442, January 2002.

[Chirila2011] A. Chirila, S. Buecheler, F. Pianezzi, P. Bloesch, C. Gretener, A. R. Uhl, C. Fella, L. Kranz, J. Perrenoud, S. Seyrling, R. Verma, S. Nishiwaki, Y. E. Romanyuk, G. Bilger, and A. N. Tiwari. Highly efficient Cu(In,Ga)Se_2 solar cells grown on flexible polymer films. *Nature Materials*, 10:857–861, 2011.

[Collins1977] R. L. Collins. Growth parameters for large diameter float zone silicon crystals. *Journal of Crystal Growth*, 42:490–492, 1977.

[Couchman1977] P. R. Couchman and W. A. Jesser. Thermodynamic theory of size dependence of melting temperature in metals. *Nature*, 269:481–483, October 1977.

[Cruz-Orea1994] A. Cruz-Orea, J. J. Alvarado-Gil, H. Vargas, F. Sanches-Sinencio, and F. Macias-Santiesteban. Photoacoustic monitoring of the thermal expansion coefficient of amorphous silicon on glass. *AIP Conference Proceedings*, 378:295–299, 1994. The 8th Latin American congress on surface science: Surfaces , vacuum, and their applications.

[Cullis1984] A. G. Cullis, N. G. Chew, H. C. Webber, and D. J. Smith. Orientation dependence of high speed silicon crystal growth from the melt. *Journal of Crystal Growth*, 68(2):624–638, September 1984.

[Cullis1991] A. G. Cullis and L. T. Canham. Visible light emission due to quantum size effects in highly porous crystalline silicon. *Nature*, 353:335–338, 1991.

[Danielson2006] D. T Danielson, D. K. Sparacin, J. Michel, and L. C. Kimerling. Surface-energy-driven dewetting theory of silicon-on-insulator agglomeration. *Journal Of Applied Physics*, 100(8):083507, 2006.

[Dassow2000] R. Dassow, J. R. Köhler, Y. Helen, K. Mourgues, O. Bonnaud, T. Mohammed-Brahim, and J. H. Werner. Laser crystallization of silicon for high-performance thin-film transistors. *Semiconductor Science and Technology*, 15(10):L31–L34, July 2000.

[Deegan1997] R. D. Deegan, O. Bakajin, T. F. Dupont, G. Huber, S. R. Nagel, and T. A. Witten. Capillary flow as the cause of ring stains from dried liquid drops. *Nature*, 389:827–829, 1997.

[Deutsch1981] T. F. Deutsch, J. C. C. Fan, G. W. Turner, R. L. Chapman, D. J. Ehrlich, and R. M. Osgood. Efficient Si solar cells by laser photochemical doping. *Applied Physics Letters*, 38(3):144–146, February 1981.

[Deutsch1982] M. Deutsch and M. Hart. Wavelength, energy shape, and structure of the CuKα_1 x-ray emission line. *Physical Review B*, 26(10):5558–5567, November 1982.

[Devlen1992] R. I. Devlen and E. A. Schiff. Optically detected photocarrier transport in amorphous silicon: a review. *Journal of Non-Crystalline Solids*, 141:106–118, 1992.

[Dharmadasa2002] I. M. Dharmadasa, A. P. Samantilleke, N. B. Chaure, and J. Young. New ways of developing glass/conducting glass/CdS/CdTe/metal thin-film solar cells based on a new model. *Semiconductor Science and Technology*, 17(12):1238–1248, December 2002.

[Dietmueller2009] R. Dietmueller, A. R. Stegner, R. Lechner, S. Niesar, R. Pereira, M. S. Brandt, A. Ebbers, M. Trocha, H. Wiggers, and M. Stutzmann. Light-induced charge transfer in hybrid composites of organic semiconductors and silicon nanocrystals. *Applied Physics Letters*, 94(11):113301, 2009.

[Dingle1974] R. Dingle, W. Wiegmann, and C. H. Henry. Quantum states of confined carriers in very thin $Al_xGa_{1-x}As$-GaAs-$Al_xGa_{1-x}As$ heterostructures. *Physical Review Letters*, 33:827–830, September 1974.

[ERKC2009] Energy Research Knowledge Centre. A nano approach to high efficiency photovoltaics: Novel SWNT nanoparticle composites for solar cell applications. Technical report, European Commission, 2009.

[EU-Commission2011] EU-Commission. A roadmap for moving to a competitive low carbon economy in 2050. Communication from the commission to the european parliament, the council, the european economic and social committee and the committee of the regions 112, European Commission, Brussels, March 2011.

[Edwards2008] M. Edwards, J. Bocking, J. E. Cotter, and N. Bennett. Screen-print selective diffusions for high-efficiency industrial silicon solar cells. *Progress in Photovoltaics: Research and Applications*, 16:31–45, 2008.

[Ehrlich1980] D. J. Ehrlich, R. M. Osgood, and T. F. Deutsch. Laser-induced microscopic etching of GaAs and InP. *Applied Physics Letters*, 36(8):698–700, 1980.

[Ekimov1985] A. I. Ekimov, Al. L. Efros, and A. A. Onushchenko. Quantum size effect in semiconductor microcrystals. *Solid State Communications*, 56(11):921–924, December 1985.

[Elliott2002] S. L. Elliott, R. F. Broom, and C. J. Humphreys. Dopant profiling with the scanning electron microscope-a study of Si. *Journal of Applied Physics*, 91(11):9116–9122, June 2002.

[Ellmer1992] K. Ellmer, A. Mertens, A. Rockoff, J. Rohrich, and W. M. Vysek. Range parameters and annealing behavior of $250-1500$keV high-energy boron and phosphorus implantations into silicon. *Nuclear Instruments & Methods in Physics Research Section B-Beam Interactions with Materials and Atoms*, 62(4):431–437, January 1992.

[Emma2010] P. Emma, R. R. Akre, J. Arthur, R. Bionta, C. Bostedt, J. Bozek, A. Brachmann, P. Bucksbaum, R. Coffee, F.-J. Decker, Y. Ding, D. Dowell, S. Edstrom, A. Fisher, J. Frisch, S. Gilevich, J. Hastings, G. Hays, P. Hering, Z. Huang, R. Iverson, H. Loos, M. Messerschmidt, A. Miahnahri, S. Moeller, H.-D. Nuhn, G. Pile, D. Ratner, J. Rzepiela, D. Schultz, T. Smith, P. Stefan, H. Tompkins, J. Turner, J. Welch, W. White, J. Wu, G. Yocky, and J. Galayda. First lasing and operation of an angstrom-wavelength free-electron laser. *Nature Photonics*, 4:641–647, 2010.

[EnergyAndClimateDep2012] Department of Energy & Climate Change. *Electricity Generation Costs*. Department of Energy & Climate Change, 2012.

[Engel2012] M. Engel, F. Kunze, D. C. Lupascu, N. Benson, and R. Schmechel. Reduced exciton binding energy in organic semiconductors: Tailoring the coulomb interaction. *Physica Status Solidi - Rapid Research Letters*, 6(2):68–70, February 2012.

[Engel2013] M. Engel, D. Schaefer, D. Erni, N. Benson, and R. Schmechel. Reduced coulomb interaction in organic solar cells by the introduction of inorganic high-k nanostructured materials. *Physics Status Solidi A*, 210(9):1712–1218, 2013.

[Fahrenbruch1983] A. L. Fahrenbruch and R. H. Bube. *Fundamentals of Solar Cells - Photovoltaic Solar Energy Conversion.* Academic Press, Inc. (London), 1983.

[Fair1975] R. B. Fair. Boron diffusion in silicon-concentration and orientation dependence, background effects, and profile estimation. *Journal of The Electrochemical Society - Solid-State Science and Technology*, 122(6):800–805, June 1975.

[Finger1994] F. Finger, P. Hapke, M. Luysberg, R. Carius, H. Wagner, and M. Scheib. Improvement of grain size and deposition rate of microcrystalline silicon by use of very high frequency glow discharge. *Applied Physics Letters*, 65(20):2588–2590, November 1994.

[FirstSolar2012] First solar annual report, 2012.

[Foerster2013] J. Förster. *Untersuchung des Temperaturkoeffizienten und anderer Materialeigenschaften von Laser-ausgeheilten amorphen Silizium- und Silizium-Germanium-Schichten*, volume 1. Shaker, 2013.

[Fogarassy1981] E. Fogarassy, R. Stuck, J. J. Grob, and P. Siffert. Silicon solar cells realized by laser induced diffusion of vacuum-deposited dopants. *Journal of Applied Physics*, 52(2):1076–1082, February 1981.

[Fthenakis2008] V. M . Fthenakis, H. C. Kim, and E. Alsema. Emissions from photovoltaic life cycles. *Environmental Science and Technology*, 42(6):2168–2174, 2008.

[Fuchs1990] E. Fuchs, H. Oppolzer, and H. Rehme. *Particle beam microanalysis.* VCH, Weinheim, 1990.

[Fujiwara2002] K. Fujiwara, K. Nakajima, T. Ujihara, N. Usami, G. Sazaki, H. Hasegawa, S. Mizoguchi, and K. Nakajima. In situ observations of crystal growth behavior of silicon melt. *Journal of Crystal Growth*, 243(2):275–282, August 2002.

[Gerthsen1963] C. Gerthsen and H. O. Kneser. *Physik*, volume 7. Springer-Verlag, 1963.

[Gittleman1979] J. I. Gittleman, E. K. Sichel, H. W. Lehmann, and R. Widmer. Textured silicon: A selective absorber for solar thermal conversion. *Applied Physics Letters*, 35(10):742–744, November 1979.

[GlobalSolar2012] Inc. Global Solar Energy. PowerFLEX BIPV - 250/275/300W. Product information sheet, Global Solar Energy, Inc., 2012.

[Gloeckler2013] M. Gloeckler, I. Sankin, and Z. Zhao. CdTe solar cells at the threshold to 20% efficiency. *IEEE Journal of Photovoltaics*, 3(4):1389–1393, October 2013.

[Goetzberger1997] A. Goetzberger, B. Voß, and J. Knobloch. *Sonnenenergie: Photovoltaik*, volume 1. Teubner Studienbücher, 2 edition, 1997.

[Goldstein1992] A. N. Goldstein, C. M. Echer, and A. P. Alivisatos. Melting in semiconductor nanocrystals. *Science*, 256(5062):1425–1427, June 1992.

[Goldstein1996] A. N. Goldstein. The melting point of silicon nanocrystals: Submicron thin-film structures derived from nanocrystal precursors. *Applied Physics A*, 62(1):33–37, 1996.

[Graetzel1985] M. Grätzel and F. P. Rotzinger. The influence of the crystal lattice structure on the conduction band energy of oxides of titanium(IV). *Chemical Physics Letters*, 118(5):474–477, August 1985.

[Granek2009] F. Granek. *High-Efficiency Back-Contact Back-Junction Silicon Solar Cells*. Dissertation, Albert-Ludwigs Universität Freiburg, Fraunhofer ISE, 2009.

[Green2014] M. A. Green, K. Emery, Y. Hishikawa, W. Warta, and E. D. Dunlop. Solar cell efficiency tables (version 43). *Progress in Photovoltaics: Research and Applications*, 22(1):1–9, January 2014.

[Greenham1996] N. C. Greenham, X. Peng, and A. P. Alivisatos. Charge separation and transport in conjugated-polymer/semiconductor-nanocrystal composites studied by photoluminescence quenching and photoconductivity. *Physical Review B*, 54(24):17628–17637, December 1996.

[Gur2005] I. Gur, N. A. Fromer, M. L. Geier, and A. P. Alivisatos. Air-stable all-inorganic nanocrystal solar cells processed from solution. *Science*, 310(5747):462–465, October 2005.

[Hall1952] R. N. Hall. Electron-hole recombination in germanium. *Physical Review*, 87(2):387–387, July 1952.

[Hartley2002] O. N. Hartley, R. Russell, K. C. Heasman, N. B. Mason, and T. M. Bruton. Investigation of thin aluminium films on the rear of monocrystalline silicon solar cells for back surface field formation. In *Proc. Conf Photovoltaic Specialists Conf. Record of the Twenty-Ninth IEEE*, pages 118–121, 2002.

[Hasegawa2010] M. Hasegawa, K. Hirata, T. Saitoh, T. Takayama, T. F. E. Sugimura, S. Tsujii, A. Tani, and T. Fuyuki. Laser doping technique using continuous wave laser in multi-crystalline silicon solar cell process. In *Proc. 35th IEEE Photovoltaic Specialists Conf. (PVSC)*, pages 003154–003157, 2010.

[Hedstroem1993] J. Hedström, H. Ohlsen, M. Bodegard, A. Kylner, L. Stolt, D. Hariskos, M. Ruckh, and H.-W. Schock. ZnO/CdS/Cu(In,Ga)Se, thin film solar cells with improved performance. *Conference Record of the 23rd IEEE Photovoltaic Specialists Conference, 1993.*, 23:364–371, 1993.

[Heikes1961] R. R. Heikes and R. W. Ure. *Thermoelectricity : science and engineering*. Interscience Publishers, 1961.

[Helgesen2010] M. Helgesen, R. Søndergaard, and F. C. Krebs. Advanced materials and processes for polymer solar cell devices. *Journal of Materials Chemistry*, 20:36–60, 2010.

[Hikita2010] Y. Hikita and H. Y. Hwang. *Thin Film Matal-Oxides*, chapter 5 - Complex Oxide Schottky Junctions, pages 169–204. Springer Science+Business Media, 2010.

[Hodes1987] G. Hodes, A. Albu-Yaron, F. Decker, and P. Motisuke. Three-dimensional quantum-size effect in chemically deposited cadmium selenide films. *Physical Review B*, 36(8):4215–4221, September 1987.

[Hoeger2012] I. Höger, A. Gawlik, G. Andrä, and F. Falk. Thickening of thin laser crystallized silicon films by solid phase epitaxy for photovoltaic applications. *Journal of Crystal Growth*, 364:164–168, February 2013.

[Hoex2012] B. Hoex, W. Zhang, and A. G. Aberle. Advanced characterisation of silicon wafer solar cells. In *Energy Procedia - International Conference on Materials for Advanced Technologies 2011, Symposium O*, volume 15, pages 147–154, 2012.

[Hofmeister1999] H. Hofmeister, F. Huisken, and B. Kohn. Lattice contraction in nanosized silicon particles produced by laser pyrolysis of silane. *European Physical Journal D: Atomic, Molecular and Optical Physics*, 9(1–4):137–140, December 1999.

[Huelser2011] T. Hülser, S. M. Schurre, H. Wiggers, and C. Schulz. Gas-phase synthesis of nanoscale silicon as an economical route towards sustainable energy technology. *KONA Powder and Particle Journal*, 29:191–206, 2011.

[Hull1999] Y. Okada, H.-M. Kagaya, T. Soma, M. N. Wybourne, and M. R. Bronzel. *Properties of crystalline silicon*, volume 1. INSPEC publication, 1999. Großartiges Nachschlagewerk! Bib.: 43 XWQ 2912.

[Huster2005] F. Huster. Aluminium - back surface field: Bow investigation and elimination. *Proceedings of the 20th EU PVSEC Barcelona, Spain*, 2005(2AO.2.1):635–638, June 2005.

[Hylton2006] J. D. Hylton. *Light coupling and light trapping in alkaline etched multicrystalline silicon wafers for solar cells.* PhD thesis, University of Utrecht, 2006.

[Isshiki2006] M. Isshiki and J. Wang. *Springer Handbook of Electronic and Photonic Materials*, chapter 23 - II - VI Semiconductors for Optoelectronics: CdS, CdSe, CdTe, pages 829–842. Springer Science+Business Media, Inc., 2006.

[Izumi1997] T. Izumi. Model analysis of segregation phenomena for silicon single crystal growth from the melt. *Journal of Crystal Growth*, 181:210–217, 1997.

[Jacoboni1977] C. Jacoboni, C. Canali, G. Otiaviani, and A. Alberigi Quaranta. A review of some charge transport properties of silicon. *Solid-State Electronics*, 20(2):77–89, February 1977.

[Joergensen2012] M. Jørgensen, K. Norrman, S. A. Gevorgyan, T. Tromholt, B. Andreasen, and F. C. Krebs. Stability of polymer solar cells. *Advanced Materials*, 24(5):580–612, February 2012.

[Kandoussi2006] K. Kandoussi, A. Gaillard, C. Simon, N. Coulon, T. Pier, and T. Mohammed-Brahim. Improved microcrystalline silicon TFTs. *Journal of Non-Crystalline Solids*, 352(9-20):1728–1731, June 2006.

[Kawai2013] M. Kawai. High-durability dye improves efficiency of dye-sensitized solar cells. Technical report, Nikkei Electronics, February 2013.

[Kayes2011] B. M. Kayes, H. Nie, R. Twist, S. G. Spruytte, F. Reinhardt, I. C. Kizilyalli, and G. S. Higashi. 27.6% conversion efficiency, a new record for single-junction solar cells under 1 sun illumination. In *Photovoltaic Specialists Conference (PVSC), 2011 37th IEEE*, pages 4–8, 2011.

[Khan2010] F. Khan, S. N. Singh, and M. Husain. Effect of illumination intensity on cell parameters of a silicon solar cell. *Solar Energy Materials and Solar Cells*, 94(9):1473–1476, September 2010.

[Kittel2005] C. Kittel. *Einführung in die Festkörperphysik*. Oldenbourg Wissenschaftsverlag GmbH, 14th edition, 2005.

[Kodera1963] H. Kodera. Diffusion coefficients of impurities in silicon melt. *Japanese Journal of Applied Physics*, 2(4):212–219, April 1963.

[Koster2008] L. J. A. Koster, V. D. Mihailetchi, M. Lenes, and P. W. M. Blom. *Performance Improvement of Polymer: Fullerene Solar Cells Due to Balanced Charge Transport*, chapter 10, pages 283–298. Wiley-VCH Verlag GmbH & Co. KGaA, 2008.

[Kosyachenko2010] L. Kosyachenko. *Solar Energy*, chapter 6 - Efficiency of Thin-Film CdS/CdTe Solar Cells, pages 105–130. InTech, 2010.

[Koynov2006] S. Koynov, M. S. Brandt, and M. Stutzmann. Black nonreflecting silicon surfaces for solar cells. *Applied Physics Letters*, 88(20):201307, May 2006.

[Koynov2007] S. Koynov, M. S. Brandt, and M. Stutzmann. Black multi-crystalline silicon solar cells. *Physica Status Solidi - RapidResearchLetters*, 1(2):R53–R55, March 2007.

[Krause2002] O. Krause, H. Ryssel, and P. Pichler. Determination of aluminum diffusion parameters in silicon. *Journal of Applied Physics*, 91(9):5645–5649, May 2002.

[Kroon2008] R. Kroon, M. Lenes, J. C. Hummelen, P. W. M. Blom, and B. De Boer. Small bandgap polymers for organic solar cells (polymer material development in the last 5 years). *Polymer Reviews*, 48(3):531–582, 2008.

[Kunert2013] B. C. Kunert. Herstellung und charakterisierung von laser-bearbeiteten siliziumnanopartikel schichten. Master's thesis, University of Duisburg-Essen, January 2013.

[Kunze2012] F. Kunze and S. Meyer. Excimer laser crystallization of p-doped silicon nanoparticulate thin films for photovoltaic applications. Master project report, Nanostructures and Technology; Electrical Engineering and Information Technology; Faculty of Engineering; University of Duisburg-Essen, Jluy 2012.

[Kuznetsov2009] A. Y. Kuznetsov, R. Machado, L. S. Gomes, C. A. Achete, V. Swamy, B. C. Muddle, and V. Prakapenka. Size dependence of rutile TiO_2 lattice parameters determined via simultaneous size, strain, and shape modeling. *Applied Physics Letters*, 94(19):193117, May 2009.

[Lechner2008] R. Lechner, A. R. Stegner, R. N. Pereira, R. Dietmueller, M. S. Brandt, A. Ebbers, M. Trocha, H. Wiggers, and M. Stutzmann. Electronic properties of doped silicon nanocrystal films. *Journal of Applied Physics*, 104(5):053701, September 2008.

[Lechner2008a] R. Lechner. *Silicon Nanocrystal Films for Electronic Applications*. PhD thesis, TU München, Walter Schottky Institut, October 2008.

[Lee2010] K. B. Lee, P. J. Parbrook, T. Wang, J. Bai, F. Ranalli, R. J. Airey, and G. Hill. The origin of the high ideality factor in AlGaN-based quantum well ultraviolet light emitting diodes. *Physica Status Solidi B*, 247(7):1761–1763, June 2010.

[Li1977] S. S. Li and W. R. Thurber. The dopant density and temperature dependence of electron mobility and resistivity in n-type silicon. *Solid-State Electronics*, 20:609–616, 1977.

[Logan1967] M. A. Logan. Sheet resistivity measurements on rectangular surfaces - general solution for four point probe cnversion factors. *The Bell System Technical Journal*, 46(10):2277–2322, December 1967.

[Luque2005] A. Luque and S. Hegedus. *Handbook of Photovoltaic Science and Engineering*. Wiley, 2005. Authors ch.5: Ceccaroli, B. and Lohne, O. Authors ch.6: Rodriguez, H. and Guerrero, I. and Koch, W. and Endrös, A. L. and Franke, D. and Häßler, C. and Kalejs, J. P. and Möller, H. J.

[Mandelkorn1973] J. Mandelkorn and J. H. Lamneck. A new electric field effect in silicon solar cells. *Journal of Applied Physics*, 44(10):4785–4787, 1973.

[ManzAG2012] Manz AG. MANZ M-GES101 CIGS power station module. Product information sheet, Manz AG, 2012.

[Maskil1988] N. Maskil and M. Deutsch. Structure and wavelength of the Cu Kα_2 x-ray emission line. *Physical Review A*, 37(8):2947–2952, April 1988.

[Matsumoto1990] S. Matsumoto, S. Yoshioka, J. Wada, S. Inui, and K. Uwasawa. Boron doping of silicon by ArF excimer laser irradiation in B_2H_6. *Journal of Applied Physics*, 67(12):7204–7210, June 1990.

[McConnell2004] R. McConnell. Next-generation technologies in the USA. *Semiconductors*, 38(8):971–974, August 2004.

[Meseth2012a] M. Meseth, P. Ziolkowski, G. Schierning, R. Theissmann, N. Petermann, H. Wiggers, N. Benson, and R. Schmechel. The realization of a pn-diode using only silicon nanoparticles. *Scripta Materialia*, 67(3):265–268, August 2012.

[Meseth2013] M. Meseth, B. C. Kunert, L. Bitzer, F. Kunze, S. Meyer, F. Kiefer, M. Dehnen, H. Orthner, M. Kummer, H. Wiggers, N.-P. Harder, N. Benson, and R. Schmechel. Excimer laser doping using highly doped silicon nanoparticles. *Physica status solidi (a)*, 210(11):2456–2462, November 2013. submitted.

[Meseth2013a] M. Meseth, K. Lamine, M. Dehnen, S. Kayser, W. Brock, D. Behrenberg, H. Orthner, A. Elsukova, N. Hartmann, H. Wiggers, T. Hülser, H. Nienhaus, N. Benson, and R. Schmechel. Laser-doping of crystalline silicon substrates using doped silicon nanoparticles. *Thin Solid Films*, 548:437–442, December 2013.

[MicroChemicals2012] MicroChemicals. Silicon wafers. Printed medium, MicroChemicals GmbH, Nicolaus-Otto-Strasse 39, Ulm, Germany D-89079, 2012.

[Moore1965] G. E. Moore. Cramming more components onto integrated circuits. *Electronics*, 38(8):114–117, April 1965.

[Mortimer1976] C. E. Mortimer. *Chemie*, volume 2. Georg Thieme Verlag Stuttgart, 1976.

[Murray1984] J. L. Murray and A. J. McAllister. The Al-Si (aluminium-silicon) system. *Bulletin of Alloy Phase Diagrams*, 5(1):74–84, February 1984.

[NETZSCH2007] NETZSCH. *Micro- & MiniSerie*. NETZSCH, NETZSCH Feinmahltechnik GmbH Sedanstraße 70 Postfach 14 60 D-95088 Selb/Bayern, 19.3.2007 edition, March 2007.

[NREL2013] NREL. Best research-cell efficiencies. Technical report, NREL, 2013.

[Nagashio2005] K. Nagashio and K. Kuribayashi. Growth mechanism of twin-related and twin-free facet Si dendrites. *Acta Materialia*, 53:3021–3029, 2005.

[Narayan1978] J. Narayan, R. T. Young, and R. F. Wood. p-n junction formation in boron-deposited silicon by laser-induced diffusion. *Applied Physical Letters*, 33(4):338–340, August 1978.

[Nguyen2013] K. N. Nguyen, P. Basset, F. Marty, Y. Leprince-Wang, and T. Bourouina. On the optical and morphological properties of microstructured black silicon obtained by cryogenic-enhanced plasma reactive ion etching. *Journal of Applied Physics*, 113:194903, 2013.

[Niesar2009] S. Niesar, R. Dietmueller, H. Nesswetter, H. Wiggers, and M. Stutzmann. Silicon/organic semiconductor heterojunctions for solar cells. *Physica Status Solidi A*, 206(12):2775–2781, 2009.

[Nozawa2012] T. Nozawa. Mitsubishi chemical claims efficiency record for organic thin-film PV cell. Technical report, Nikkei Electronics, June 2012.

[ORegan1991] B. O'Regan and M. Grätzel. A low-cost, high-efficiency solar cell based on dye-sensitized colloidal TiO_2 films. *Nature*, 353:737–740, October 1991.

[Ochoa1996] O. R. Ochoa, C. Colajacomo, and E. J. Witkowski. Quantum confinement effects on the photoluminescence spectra of cdte nanocrystallites. *Solid State Communications*, 98(8):717–721, 1996.

[Ogane2009] A. Ogane, K. Hirata, K. Horiuchi, Y. Nishihara, Y. Takahashi, A. Kitiyanan, and T. Fuyuki. Laser-doping technique using ultraviolet laser for shallow doping in crystalline silicon solar cell fabrication. *Japanese Journal of Applied Physics*, 48(071201):071201, July 2009.

[Ohmer2011a] K. Ohmer, Y. Weng, J. R. Köhler, H. P. Strunk, and J. H. Werner. Defect formation in silicon during laser doping. *IEEE Journal of Photovoltaics*, 1(2):183–186, December 2011.

[Olesinski1985] R. W. Olesinski, N. Kanani, and G.J. Abbaschin. The P-Si (phosphorus-silicon) system. *Bulletin of Alloy Phase Diagrams*, 6(2):130–133, 1985.

[PASE-12] Monocrystal Inc. *Aluminium Conductor Paste for Solar Cells.* Monocrystal Inc., Kulakovy pr. 4/1 Stavropol 355035 Russia.

[PV-EducationRser] PVEducation.com. Series resistance. Published online, February 2014. (http://pveducation.org/pvcdrom/solar-cell-operation/series-resistance).

[PV-EducationRshu] PVEducation.com. Shunt resistance. Published online, February 2014. (http://pveducation.org/pvcdrom/solar-cell-operation/shunt-resistance).

[Patino-Lopez2004] L.-D. Patino-Lopez, A. Salhi, S. Dilhaire, S. Grauby, J.-M. Rempoux, S. Jorez, and W. Claeys. Thermal study of PN thermoelectric couple by laser induced Seebeck EMF measurement. *Superlattices and Microstructures*, 35(3–6):375–387, March–June 2004.

[Peiner1995] E. Peiner, A. Schlachetzki, and D. Krüger. Doping profile analysis in si by electrochemical capacitance voltage measurements. *Journal of the Electrochemical Society*, 142(2):576–580, 1995.

[Perego2010a] M. Perego, C. Bonafos, and M. Fanciulli. Phosphorus doping of ultra-small silicon nanocrystals. *Nanotechnology*, 21:025602, 2010.

[Pereira2007] R. N. Pereira, A. R. Stegner, K. Klein, R. Lechner, R. Dietmueller, H. Wiggers, M. S. Brandt, and M. Stutzmann. Electronic transport through Si nanocrystal films: Spin-dependent conductivity studies. *Physica B: Condensed Matter*, 401–402:527–530, December 2007.

[Perez-Wurfl2009] I. Perez-Wurfl, X. Hao, A. Gentle, D.-H. Kim, G. Conibeer, and M. A. Green. Si nanocrystal p-i-n diodes fabricated on quartz substrates for third generation solar cell applications. *Applied Physical Letters*, 95(15):153506, 2009.

[Perlin1996] P. Perlin, M. Osinski, P. G. Eliseev, V. A. Smagley, J. Mu, M. Banas, and P. Sartori. Low-temperature study of current and electroluminescence in InGaN/AlGaN/GaN double-heterostructure blue light-emitting diodes. *Applied Physical Letters*, 69(12):1680–1682, September 1996.

[Perovic1995] D. D. Perovic, M. R. Castell, A. Howie, C. Lavoie, T. Tiedje, and J. S. W. Cole. Field-emission sem imaging of compositional and doping layer semiconductor superlattices. *Ultramicroscopy*, 58(1):104–113, April 1995.

[Petermann2011] N. Petermann, N. Stein, G. Schierning, R. Theissmann, B. Stoib, M. S. Brandt, C. Hecht, C. Schulz, and H. Wiggers. Plasma synthesis of nanostructures for improved thermoelectric properties. *Journal Of Applied Physics D: Applied Physics*, 44(174034):174034, April 2011.

[Poole1949] J. P. Poole. Low-temperature viscosity of alkali silicate glasses. *Journal of The American Ceramic Society*, 32(7):230–233, 1949.

[Proot1992] J. P. Proot, C. Delerue, and G. Allan. Electronic structure and optical properties of silicon crystallites: Application to porous silicon. *Applied Physical Letters*, 61(16):1948–1950, October 1992.

[Rauer2011] M. Rauer, R. Woehl, K. Ruhle, C. Schmiga, M. Hermle, M. Horteis, and D. Biro. Aluminum alloying in local contact areas on dielectrically passivated rear surfaces of silicon solar cells. *IEEE Electron Device Letters*, 32(7):916–918, July 2011.

[Rezek1999] B. Rezek, C. E. Nebel, and M. Stutzmann. Polycrystalline silicon thin films produced by interference laser crystallization of amorphous silicon. *Japanese Journal of Applied Physics*, 38(10A):L1083–L1084, October 1999.

[Ribeiro1995] R. M. Ribeiro, W. Margulis, C. A. F. Leite, I. Guedes, L. Misoguti, and V. S. Bagnato. Nonlinear optical response of hydrogenated amorphous silicon films studied by laser induced transient gratings. *Applied Physical Letters*, 66(9):1089–1091, February 1995.

[Ruby2001] D. S. Ruby and Zaidi; S. H. Metal catalyst technique for texturing silicon solar cells, 2001.

[Rupp2011] K. Rupp and S. Selberherr. The economic limit to Moore's law. *IEEE Transactions on Semiconductor Manufacturing*, 24(1):1–4, February 2011.

[Sagadevan2013] S. Sagadevan. Recent trends on nanostructures based solar energy applications: a review. *Reviews on Advanced Materials Science*, 34(1):44–61, October 2013.

[Sah1957] C.-T. Sah, R. N. Noyce, and W. Shockley. Carrier generation and recombination in p-n junctions and p-n junction characteristics. *Proceedings of the IRE*, 45(9):1228–1243, September 1957.

[Sah1995] C.-T. Sah. *Fundamentals of solid-state electronics*. World Scientific, Singapore, 1995.

[Salvadeo2012] P. A. Salvadeo, Á. C. Veca, and R. C. Lopez. Historic behavior of the electronic technology: The wave of Makimoto and Moore's law in the transistor's age. In *2012 VIII Southern Conference on Programmable Logic (SPL)*, pages 1–5, Bento Gonçalves, Rio Grande do Sul, Brazil, 2012.

[Sameshima1987] T. Sameshima, S. Usui, and M. Sekiya. Laser-induced melting of predeposited impurity doping technique used to fabricate shallow junctions. *Journal of Applied Physics*, 62(2):711–713, April 1987.

[Sameshima2005] T. Sameshima, H. Watakabe, N. Andoh, and S. Higashi. Pulsed laser crystallization of very thin silicon films. *Thin Solid Films*, 487(1–2):63–66, September 2005.

[Scardera2011] G. Scardera, D. Poplavskyy, M. Burrows, and S. Shah. Methods of using a silicon nanoparticles fluid to control in situ a set of dopant diffusion profiles, January 2011.

[Schierning2008] G. Schierning, R. Theissmann, H. Wiggers, D. Sudfeld, A. Ebbers, D. Franke, V. T. Witusiewicz, and M. Apel. Microcrystalline silicon formation by silicon nanoparticles. *Journal of Applied Physics*, 103(8):084305, 2008.

[Schierning2011a] G. Schierning, R. Theissmann, N. Stein, N. Petermann, A. Becker, M. Engenhorst, V. Kessler, M. Geller, A. Beckel, H. Wiggers, and R. Schmechel. Role of oxygen on microstructure and thermoelectric properties of silicon nanocomposites. *Journal of Applied Physics*, 110(11):113515, 2011.

[Schneider2001] A. Schneider, C. Gerhards, F. Huster, W. Heu, M. Spiegel, P. Fath, E. Bucher, R. J. S. Young, A. G. Prince, J.A. Raby, and A. F. Carroll. Al BSF for thin screenprinted multicrystalline Si solar cells. *Proceedings of the 17th EU PVSEC Munich, Germany*, 2001:1768–1771, 2001.

[Schroder2006] D. K. Schroder. *Semiconductor Material and Device Characterization*. John Wiley & Sons, 3 edition, 2006.

[Schubert2003] D. W. Schubert and T. Dunkel. Spin coating from a molecular point of view: its concentration regimes, influence of molar mass and distribution. *Materials Research Innovations*, 7(5):314–321, October 2003.

[Schultz2003] O. Schultz, G. Emanuel, W. Glunz, and G. P. Willeke. Texturing of multicrystalline silicon with acidic wet chemical etching and plasma etching. In K. Kurokawa, B. Kazmerski, L. L. McNelis, M. Yamaguchi, C. Wronski, and W. C. Sinke, editors, *Proceedings of 3rd World Conference on Photovoltaic Energy Conversion, 2003*, volume 2, pages 1360–1363, 2003.

[Schwesig2011] D. Schwesig, G. Schierning, R. Theissmann, N. Stein, N. Petermann, H. Wiggers, R. Schmechel, and D. E. Wolf. From nanoparticles to nanocrystalline bulk: percolation effects in field assisted sintering of silicon nanoparticles. *Nanotechnology*, 22(13):135601, February 2011.

[Schwoerer2005] M. Schwoerer and H. C. Wolf. *Organische Molekulare Festkörper*. Wiley-VCH, first edition, 2005.

[Seidel1990] H. Seidel, L. Csepregi, A. Heuberger, and H. Baumgärtel. Anisotropic etching of crystalline silicon in alkaline solutions. *Journal of the Electrochemical Society*, 137(11):3612–3626, November 1990.

[Seidel1990a] H. Seidel, L. Csepregi, A. Heuberger, and H. Baumgärtel. Anisotropic etching of crystalline silicon in alkaline solutions. *Journal of the Electrochemical Society*, 137(11):3626–3632, November 1990.

[Sha2011] W. E. I. Sha, W. C. H. Choy, Y. G. Liu, and W. C. Chew. Near-field multiple scattering effects of plasmonic nanospheres embedded into thin-film organic solar cells. *Applied Physics Letters*, 99(11):113304, 2011.

[Shah2003] J. M. Shah, Y.-L. Li, T. Gessmann, and E. F. Schubert. Experimental analysis and theoretical model for anomalously high ideality factors (n>>2.0) in AlGaN/GaN p-n junction diodes. *Journal of Applied Physics*, 94(4):2627–2630, 2003.

[Sharma2010] B. L. Sharma. *CRC Handbook of chemistry and physics*, volume 90. CRC Press, 2010.

[Shieh2011] J. Shieh, S. Ravipati, F.-H. Ko, and K. (K.) Ostrikov. Plasma-made silicon nanograss and related nanostructures. *Journal of Applied Physics D: Applied Physics*, 44(17):174010, April 2011.

[Shockley1949] W. Shockley. The theory of p-n junctions in semiconductors and p-n junction transistors. *Bell System Technical Journal*, 28(3):435–489, July 1949.

[Shockley1952] W. Shockley and W. T. Read. Statistics of the recombinations of holes and electrons. *Physical Review*, 87(2):835–842, September 1952.

[Shockley1961] W. Shockley and H. J. Queisser. Detailed balance limit of efficiency of p-n junction solar cells. *Journal of Applied Physics*, 32(3):510–520, 1961.

[Shukla2011] M. Shukla and N. Brahme. Improved efficiency of MEH-PPV:PCBM solar cells by the use of ZnS nano-particles. *Polymere Bulletin*, 67:709–718, 2011.

[Smith2011] M. J. Smith, Lin Y.-T., Sher M.-J., M. T. Winkler, E. Mazur, and S. Gradecak. Pressure-induced phase transformations during femtosecond-laser doping of silicon. *Journal of Applied Physics*, 110(5):053524, 2011.

[Smits1958] F. M. Smits. Measurement of sheet resistivities with the four-point probe. *The Bell System Technical Journal*, 37(3):711–718, May 1958.

[Snyder2008] G. J. Snyder and E. S. Toberer. Complex thermoelectric materials. *Nature Materials*, 7(2):105–114, February 2008.

[Span2006] G. Span, M. Wagner, S. Holzer, and T. Grasser. Thermoelectric power conversion using generation of electron-hole pairs in large area p-n junctions. In *2006 International Conference on Thermoelectrics*, 2006.

[Span2007] G. Span, M. Wagner, T. Grasser, and L. Holmgren. Miniaturized TEG with thermal generation of free carriers. *physica status solidi (RRL)*, 1(6):241–243, November 2007.

[Stanbery2002] B. J. Stanbery. Copper indium selenides and related materials for photovoltaic devices. *Critical Reviews in Solid State and Materials Sciences*, 27:73–117, 2 2002.

[Stegner2008] A. R. Stegner, R. N. Pereira, K. Klein, R. Lechner, R. Dietmueller, M. S. Brandt, and M. Stutzmann. Electronic transport in phosphorus-doped silicon nanocrystal networks. *Physical Review Letters*, 100(2):026803, January 2008.

[Stegner2009] A. R. Stegner, R. N. Pereira, R. Lechner, K. Klein, H. Wiggers, M. Stutzmann, and M. S. Brandt. Doping efficiency in freestanding silicon nanocrystals from the gas phase: Phosphorus incorporation and defect-induced compensation. *Physical Review B*, 80(16):165326, October 2009.

[Steingrube2011] S. Steingrube, O. Breitenstein, K. Ramspeck, S Glunz, A. Schenk, and P. P. Altermatt. Explanation of commonly observed shunt currents in c-Si solar cells by means of recombination statistics beyond the Shockley-Read-Hall approximation. *Journal of Applied Physics*, 110(1):014515, 2011.

[Stephens1977] R. B. Stephens and G. D. Cody. Optical reflectance and transmission of a textured surface. *Thin Solid Films*, 45(1):19–29, August 1977.

[Stratakis2013] E. Stratakis and E. Kymakis. Nanoparticle-based plasmonic organic photovoltaic devices. *Materials Today*, 16(4):133–146, April 2013.

[Strevel2013] N. Strevel, L. Trippel, C. Kotarba, and I. Khan. Improvements in CdTe module reliability and long-term degradation through advances in construction and device innovation. *Photovoltaics International*, 22:66–74, December 2013.

[Swanson2006] R. M. Swanson. A vision for crystalline silicon photovoltaics. *Prrogress in Photovoltaics: Research and Applications*, 14(5):443–453, June 2006.

[Sze2007] S. M. Sze and K. K. Ng. *Physics of Semiconductor Devices*. Wiley, 3rd edition, 2007.

[Tada2000] H. Tada, A. E. Kumpel, R. E. Lathrop, J. B. Slanina, P. Nieva, P. Zavracky, I. N. Miaoulis, and P. Y. Wong. Thermal expansion coefficient of polycrystalline silicon and silicon dioxide thin films at high temperatures. *Journal of Applied Physics*, 87(9):4189–4193, 2000.

[Tadmor2004] R. Tadmor. Line energy and the relation between advancing, receding, and young contact angles. *Langmuir*, 20(18):7659–7664, June 2004.

[Tiedtke2009] K. Tiedtke, A. Azima, N. von Bargen, L. Bittner, S. Bonfigt, S. Düsterer, B. Faatz, U. Frühling, M. Gensch, C. Gerth, N. Guerassimova, U. Hahn, T. Hans, M. Hesse, K. Honkavaar, U. Jastrow, P. Juranic, S. Kapitzki, B. Keitel, T. Kracht, M. Kuhlmann, W. B. Li, M. Martins, T. Nuñez, E. Plönjes, H. Redlin, E. L. Saldin, E. A. Schneidmiller, J. R. Schneider, S. Schreiber, N. Stojanovic, F. Tavella, S. Toleikis, R. Treusch, H. Weigelt, M. Wellhöfer, H. Wabnitz, M. V. Yurkov, and J. Feldhaus. The soft x-ray free-electron laser FLASH at DESY: beamlines, diagnostics and end-stations. *New Journal of Physics*, 11(023029):1–16, February 2009.

[Tsurumi2013] D. Tsurumi and K. Hamada. Dopant mapping of semiconductors with scanning electron microscopy. *Sumitomo Electric Industries Technical Review*, 77:141–146, October 2013.

[Tucci2008] M. Tucci, E. Talgorn, L. Serenelli, E. Salza, M. Izzi, and P. Mangiapane. Laser fired back contact for silicon solar cells. *Thin Solid Films*, 516(20):6767–6770, 2008.

[USEnergyAdmin2013] U.S. Energy Information Administration. *Levelized Cost of New Generation Resources in the Annual Energy Outlook 2013*. U.S. Energy Information Administration, 2013.

[Ukawa2010] K. Ukawa, Y. Kanda, T. Sameshima, N. Sano, M. Naito, and N. Hamamoto. Activation of silicon implanted with phosphorus and boron atoms by infrared semiconductor laser rapid annealing. *Japanese Journal Of Applied Physics*, 49(076503):076503, 2010.

[Valdes1954] L. B. Valdes. Resistivity measurements on germanium for transistors. *Proceedings of the IRE*, 42(2):420–427, February 1954.

[Venables1998] D. Venables, H. Jain, and D. C. Collins. Secondary electron imaging as a two-dimensional dopant profiling technique: Review and update. *Journal of Vacuum Science & Technology B*, 16(1):362–366, January/February 1998.

[Wang2011a] Y. Wang, L. Wang, and D. H. Waldeck. Electrochemically guided photovoltaic devices: A photocurrent study of the charge transfer directionality between CdTe and CdSe nanoparticles. *Journal of Physical Chemistry C*, 115:18136–18141, 2011.

[Watanabe2012] A. Watanabe. Laser sintering of si and ge nano- and microparticle films toward solar cells by solution process. In F. G. Bachmann, W. Pfleging, K. Washio, J. Amako, W. Hoving, and Y. Lu, editors, *Proceedings of SPIE - Laser-based Micro- and Nanopackaging and Assembly VI*, volume 8244, 2012.

[Wautelet1990] M. Wautelet. Size effect on the melting (or disordering) temperature of small particles. *Solid State Communications*, 74(11):1237–1239, 1990.

[Wautelet1991] M. Wautelet. Estimation of the variation of the melting temperature with the size of small particles, on the basis of a surface-phonon instability model. *Journal of Applied Physics D: Applied Physics*, 24(3):343–346, 1991.

[Wiggers2001] H. Wiggers, R. Starke, and P. Roth. Silicon particle formation by pyrolysis of silane in a hot wall gasphase reactor. *Chemical Engineering and Technology*, 24(3):261–264, March 2001.

[Wuerfel2005] P. Würfel. *Physics of Solar Cells - From Basic Principles to Advanced Concepts*. Wiley-VCH Verlag GmbH & Co. KGaA, 2005.

[Yang2012] X. Yang, K. Fujiwara, R. Gotoh, K. Maeda, J. Nozawa, H. Koizumi, and S. Uda. Crystal and faceted dendrite growth of silicon near (100). *Acta Materialia*, 60:3254–3267, 2012.

[Yao2009] D. Yao, G. Zhang, G.-Q. Lo, and B. Li. Impacts of size and cross-sectional shape on surface lattice constant and electron effective mass of silicon nanowires. *Applied Physics Letters*, 94(11):113113, March 2009.

[Young1805] T. Young. An essay on cohesion of fluids. *Philosophical Transactions of the Royal Society of London*, 95:65–87, January 1805.

[Young1980] R. T. Young, R. F. Wood, J. Narayan, C. W. White, and W. H. Christie. Pulsed laser techniques for solar cell processing. *IEEE Transactions on Electron Devices*, 27(4):807–815, April 1980.

[Zhang2011] C. Zhang, J. Zhang, Y. Hao, Z. Lin, and C. Zhu. A simple and efficient solar cell parameter extraction method from a single current-voltage curve. *Journal of Applied Physics*, 110(6):064504, 2011.

[Zhu2009] X.-Y. Zhu, Q. Yang, and M. Muntwiler. Charge-transfer excitons at organic semiconductor surfaces and interfaces. *Acc Chem Res*, 42(11):1779–87, 2009.

[Ziolkowski2006] P. Ziolkowski, G. Karpinski, D. Platzek, C. Stiewe, and E. Müller. Application overview of the potential seebeck microscope. *Proceedings of the 25th International Conference on Thermoelectrics*, 25:684–688, August 2006.

List of publications

Published articles

1. A. Becker, G. Schierning, R. Theissmann, M. Meseth, N. Benson, R. Schmechel, D. Schwesig, N. Petermann, H. Wiggers, and P. Ziolkowski. A sintered nanoparticle p-n junction observed by a Seebeck microscan, *Journal of Applied Physics*, 111(5):054320, 2012.

2. M. Meseth, P. Ziolkowski, G. Schierning, R. Theissmann, N. Petermann, H. Wiggers, N. Benson, and R. Schmechel. The realization of a pn-diode using only silicon nanoparticles, *Scripta Materialia*, 67:265, 2012.

3. L. Bitzer, M. Meseth, N. Benson, and R. Schmechel. A new adaptive light beam focusing principle for scanning light stimulation systems, *Review of Scientific Instruments*, 84:023707, 2013.

4. M. Meseth, B. C. Kunert, L. Bitzer, F. Kunze, S. Meyer, F. Kiefer, M. Dehnen, H. Orthner, M. Kummer, H. Wiggers, N.-P. Harder, N. Benson, and R. Schmechel. Excimer laser doping using highly doped silicon nanoparticles, *Physica status solidi (a)*, 210(11):2456–2462, 2013.

5. M. Meseth, K. Lamine, M. Dehnen, S. Kayser, W. Brock, D. Behrenberg, H. Orthner, A. Elsukova, N. Hartmann, H. Wiggers, T. Hülser, H. Nienhaus, N. Benson, and R. Schmechel. Laser-Doping of Crystalline Silicon Substrates using Doped Silicon Nanoparticles, *Thin Solid Films*, 548:437–442, 2013.

6. CENIDE. Nano Ganz Gross – Nano Goes Big, *CENIDE image brochure*, p. 9, 2013.

7. Universität Duisburg-Essen. Fakultät für Ingenieurwissenschaften – Faculty of Engineering, *Forschungsbericht - Fakultäten – Research Report - Faculties* p. 127, 2012.

Conference contributions

1. M. Meseth, P. Ziolkowski, N. Benson, G. Schierning, R. Theissmann, H. Wiggers, and R. Schmechel, *Potential of Nanocystalline Silicon in Photovoltaic Applications*, Talk, Science to Business - GRK Summer School, 8.7.2010, Marl, Germany.

2. M. Meseth, N. Benson, H. Wiggers, and R. Schmechel, *Si nanoparticles for photovoltaic applications*, Poster, NETZ Vollversammlung, 9.11.2010, Duisburg, Germany.

3. M. Meseth, *Detectors and Photovoltaic Cells from Nanoparticles*, Talk, Internal Meeting GRK 1240: Presentations by GRK 1240 Members, 3.12.2010, Duisburg, Germany.

4. M. Meseth, P. Ziolkowski, N. Petermann, G. Schierning, H. Wiggers, R. Theissmann, N. Benson, and R. Schmechel, *Potential of silicon nanoparticles for photovoltaic applications*, Talk, DPG Spring Meeting, Session HL 79: Photovoltaics: Mainly Silicon, 17.3.2011, Dresden, Germany.

5. M. Meseth, K. Lamine, A. Sandmann, H. Orthner, P. Cadiz-Bedini, H. Wiggers, N. Benson, M. Winterer, and R. Schmechel, *Laser Treatment of Si-Nanoparticles for Photovoltaic Applications*, Talk, Science to Business - GRK Summer School, 20.7.2011, Marl, Germany.

6. M. Meseth, K. Lamine, S. Kayser, W. Brock, H. Orthner, A. Yelsukova, M. Bartsch, A. Beckel, H. Wiggers, H. Nienhaus, N. Benson, and R. Schmechel, *Laser doping of c-Si using highly doped Si nanoparticles*, 2012 spring meeting of the european MRS, Symposium Y: Advanced materials and characterization techniques for solar cells, 17.5.2012, Strasbourg, France.

Acknowledgements

The work was funded by the DFG within the Research Training Group (Graduiertenkolleg) 1240 Nanotronics and by the Ministry of Research and Education within the NanoEnergieTechnikZentrum (Ziel2.NRW) Project.

I deeply thank Prof. Dr. R. Schmechel for giving me the chance to work at his chair, for fruitful discussions and for the supervision during experimental work and writing, as well as for the preparation of the report about this thesis.

I greatly appreciate the willingness of Prof. Dr. F.-J. Tegude to prepare the report about this thesis.

Further, I thank Dr. N. Benson for his trust in me as the first member of his group, for the supervision during my work at the NST, including experimental questions, paper corrections, discussions and for his support in so many ways. He initiated my personal growth, which I hereby deeply acknowledge.

The results presented here are this numerous, because on the one hand, many students helped me: A. P. Cadiz-Bedini, S. Dülme, C. Kunert, F. Kunze, K. Lamine, S. Meyer and A. Schmitz (alphabetical order). I thank you all so much for great work and hope, that you will all make your ways satisfactory. On the other hand, I had great support in the lab and by discussions from the members of the PVs group of the NST, i.e. M. Engel, L. Bitzer (special thanks for many discussions on topics on physics) and M. Caninenberg, from the members of Dr. G. Schierning's thermoelectrics group, i.e. A. Becker, M. Engenhorst, V. Kessler, N. Stein and R. Chavez, and from C. Busch and from D. Kiesler. Further, I thank M. Dehnen for solving so many questions on chemistry and especially for creating the NP dispersions, C. Kleinert and F. Bensel for multiple technical support, like fast realizations of urgent orders at the university's work shops, A. Trampe for his work and help on finances and Dr. R. Theismann for the introduction to the SEM and for subsequent support.

All the experimental work was possible only due to the availability of the NPs. We received them free of charge from the work group of Dr. H. Wiggers of the Institute for Combustion and Gas Dynamics, Duisburg. Especially Dr. H. Orthner and N. Petermann I thank for NP production and support.

Further, I appreciate so much the numerous help regarding sample production and analysis:

- *University of Duisburg-Essen*
  I acknowledge the provision of laboratories, equipment such as the work shops, where several tools like the processing chamber used for the laser sample preparation were prepared.

- *LIMO*
  I acknowledge the support of the IR and the UV lasers.

- *Solland Solar*
  I thank R. Derix for the support of many semi-finished and completely finished solar cells.

- *Institute of Electrical Power Transmission*
  I thank esp. Dipl.-Ing. P. Hammerschlag-Büttner for providing space in their facilities for the IR laser unit in a fast and uncomplicated way.

- *Faculty of Physics, Duisburg*
  From the work group of Prof. Dr. A. Lorke, I thank A. Beckel and M. Bartsch for exhaustive FIB preparations; from the work group of Prof. Dr. H. Nienhaus, I thank Dr. D. Krix for XPS measurements.

- *Faculty of Chemistry, Essen*
  From the work group of PD. Dr. N. Hartmann I thank esp. D. Behrenberg for fruitful co-work and help regarding the anisotropic etching experiments.

- *Nano Particle Process Technology group of Prof. Dr. M. Winterer*
  Besides his efforts regarding the Research Training Group I thank Prof. Dr. Winterer for the uncomplicated access to the XRD equipment. Further I thank A. Sandmann for help and support with the DLS measurements and Mr. A. Kompch for help regarding XRD measurements and their interpretations.

- *ICAN / A. Elsukova*
  I thank for the (HR-)TEM investigations.

- *Pyrosensor*
  I thank Dr. W. Bohrmeyer for the uncomplicated, free of charge support of an intensity sensor for the UV laser. (Schulstr. 15, 15366 Neuenhagen b. Berlin)

- *The German Aerospace Center (DLR)*
  especially Dr. P. Ziolkowski I thank for the Seebeck potential microscope measurements.

- *Tascon and ION-TOF GmbHs*
  I am thankful for the SIMS measurements, that are performed by Tascon GmbH for ION-TOF GmbH.

- *Institute for Solar Research Hameln (ISFH)*
  I thank especially F. Kiefer of Prof. Dr. N.-P. Harder's work group for ECV measurements.

Finally, I thank Prof. Dr. G. Krost for being my ombudsman and his discrete help during dire straits.